

PROCEEDINGS

National Conference on

CONDITION MONITORING

(Theme: Condition Monitoring & Industry 4.0)

NCCM - 2023

27 - 28 April
2023



Jointly Organised by



Naval Science and Technological Laboratory
DRDO, Ministry of Defence, GOI
Visakhapatnam-530027



Condition Monitoring Society of India (CMSI)
(Regd. No: 45061/ 2003)
Visakhapatnam-530027

Proceedings

**NATIONAL CONFERENCE
ON
CONDITION MONITORING
(NCCM-2023)**

April 27-28, 2023

Organised by



**CONDITION MONITORING SOCIETY OF INDIA
&
NAVAL SCIENCE & TECHNOLOGICAL LABORATORY
Visakhapatnam, India**



The papers published in the National Conference on Condition Monitoring (NCCM-2023) are protected under copyright. No part of the proceedings protected under the copyright may be reproduced in any form by any means, electronic or mechanical including photocopying without prior written permission from the copyright owner.

(C) Copyright of the proceedings

PRESIDENT
Condition Monitoring Society of India
Visakhapatnam

PREFACE

Condition Monitoring Society of India is a non profit professional body of practising Engineers, Scientists and Personnel involved in the field of industrial maintenance. The society primarily aims at growth of the science of condition monitoring of machines, equipment and systems of India. Condition Monitoring Society of India was established in 2003 with R&D scientists, academicians and maintenance engineers forming the core strength. The society was established on 25 August 2003 at Naval Science and Technological Laboratory (NSTL), Visakhapatnam with Dr. V Bhujanga Rao (currently Chairman of KIMS Research Foundation Centre, Hyderabad) as the founder President and Dr. M. Ananda Rao as founder General Secretary. The society has two grades of membership namely, Individual Life members and Institutional Life members. The society has grown over the past two decades. Twenty Nine Industries, Academia and R&D organisations have become the Institutional members of Condition Monitoring Society of India so far. CMSI brings out a quarterly News letter “MONITOR” to disseminate the latest trends in condition monitoring among the professionals in the country and abroad. The society’s website www.comsoi.org provides for publishing online news and online interaction among members. The Executive council of the society meets annually to discuss the progress of activities of the society. Annual meets are held to foster interaction among the members and technical talks are organised during these meets. Vijayawada, Durgapur, Hyderabad, Jamshedpur and Chennai local chapters have been formed under the aegis of CMSI.

CMSI organised eight National Conferences on Condition Monitoring (NCCM-2006- Visakhapatnam, NCCM-2009-Visakhapatnam, NCCM-2012-Pune, NCCM-2013-Bengaluru, NCCM-2014-Chennai, NCCM-2015-Visakhapatnam, NCCM-2017-IGCAR, Kalpakkam and NCCM-2019-Vijayawada) since its inception. International conferences on Condition Monitoring ICCM-2011, ICCM-2016 & ICCM-2021 were conducted by CMSI in association with GITAM University at Visakhapatnam and Tata Steel, Jamshedpur. Several experts including Prof. BVA Rao, Dr. V Ramamurti, Dr. V Bhujanga Rao, Sri. BK Das, Sri. MP Srivastava, Sri. RK Biswas, Dr. Naresh Tandon, Dr. Amiya R Mohanty and Dr. Rajiv Tiwari among others delivered invited talks during these conferences. Apart from this, CMSI organised, several short term courses and workshops in association with CII, AICTE, ISTE and others. All these events were attended by a large number of engineers, scientists and students.

Dr. V Bhujanga Rao endowment lecture was instituted from 2012 onwards. The first endowment lecture was delivered by Prof. BKN Rao, an internationally acclaimed expert on Condition Monitoring. Second Lecture was delivered by Dr. V Ramamurti (Retd) Professor of IIT, Chennai. Subsequently, Dr. Kota Harinarayana, Dr. PS Goel, Prof. Raj Kumar Roy, Dr. Amaresh Chakrabarti, Professor of IISc, Bangalore, Dr. A R Mohanty, Professor of IIT Kharagpur and Dr. Nalinakash S Vyas, Professor of IIT Kanpur delivered Dr. V Bhujanga Rao Endowment lectures. CMSI Centre was setup and First Student Chapter of CMSI was launched on 14 Mar 2013 at Andhra University, Visakhapatnam. Later, student chapters were launched at NITTE Bangalore, Hindustan University-Chennai, GVP College of Engineering, Visakhapatnam, GVP Degree & PG Studies, Visakhapatnam and NSRIT-Visakhapatnam. With the co-operation of industries, academic institutions and R&D Laboratories across the country, CMSI is set to scaled greater heights in years to come.

As a part of CMSI's endeavour to highlight growing importance of Condition Monitoring, a two day National Conference of Condition Monitoring (NCCM 2023) is being organised during April 27-28, 2023 at Naval Science and Technological laboratory (NSTL), Visakhapatnam. A number of Condition monitoring experts/practising specialists from various organisations, institutes and industries are expected to participate in the conference. The conference provides a platform for interaction on state of art Condition Monitoring strategies being followed worldwide. It also provides an opportunity to deliberate on latest trends in the field of condition monitoring. The conference aims to discuss future trends in thermography, wear debris analysis etc that are being employed in the industry for predictive maintenance and hence these proceedings are being brought out so as to disseminate the knowledge that is being shared in the conference.



Er. PVS Ganesh Kumar
Outstanding Scientist
President, CMSI

CONTENTS

SNo	Title	Page No
I	Keynote Address	
01	Condition monitoring - A foundation for industry 4.0 - <i>Dr. V. Bhujanga Rao</i>	09
II	Invited Talks	
IT-01	Machinery Diagnostics and Vibration Technology, Scenario in Industry 4.0, Challenges and Opportunities Ahead - <i>Dr. Tarapada Pyne</i>	11
IT-02	Rotating Machinery Fault Detection by Vibration Signature Analysis - <i>Dr. Kamal Kishore J Uke</i>	13
IT-03	Reaching Out Condition Monitoring Systems to Our Msmes - It can be their Saviour - <i>Dr. Rana Dutta</i>	14
IT-04	Seven Stages in The Life of A Rotating Equipment and Their Influence on the Vibration Analysis - <i>Shri. Ganti Subba Rao</i>	15
IT-05	Application of Active Magnetic Bearing for Fault Suppression and Identification in the Moderate and High Speed Rotors - <i>Dr. Rajiv Tiwari</i>	16
III	Contributed Papers	
C-01	AI/ML based Performance Characteristics Predictions of Centrifugal Pumps - <i>Ashish Sharma, Rajiv Tiwari, and Niranjana Sahoo</i>	18
C-02	Diagnosing the Healthy or Defective State of a Centrifugal Pump based on Vibration, Pressure and Current data using a Deep Learning Algorithm - <i>Shivam Gautam and Rajiv Tiwari</i>	27
C-03	Prediction of Remaining Useful Life for Running Gear System of an Armoured Fighting Vehicle - <i>Hafeezur Rehaman, Srinivasan. G, Vetrivelan D, Akilandeswari.P, Balaguru.V, and Balamurugan.V</i>	37
C-04	Remote Monitoring of Mining Dump Truck Operation using Engine Vibration - <i>Nagesh Dewangan, Amiya Ranjan Mohanty</i>	46
C-05	Root Cause of High Vibration in A Vertical Circulating Water Pump And Its Remedial Suggestion - <i>Biplab Swarnakar, Sourav Kansabanik, Swarup Kumar Laha and Kamalkishor Uke</i>	56
C-06	Vibration And Acoustic Signal Monitoring of High-Speed Bearings for Electrical Vehicles - <i>Ajiket Patil, Madhav Bavu, Gautam Susarla and B. Venkatesham</i>	64
C-07	Case Study on Defect Rectification of an External Gear Pump Through Vibration Monitoring - <i>S Jagadish Kumar and M P Patmase</i>	72
C-08	Condition Monitoring of Rigid Shaft Supported on Foil Bearings With Defects in Supporting Bump Foil - <i>Balaji Sankar, and Dr. Sadanand S Kulkarni</i>	80
C-09	A Comprehensive Case Study on Tripping of VFD Motor Driven AFC Fan & 3-Stage Centrifugal Air Compressor on High Vibration - <i>Padmakar Jaiswal, and G.V.S.S.K Varma</i>	89
C-10	Eliminating The Problem of Frequent Tripping of Main Reversing Mill Motor of Cold Rolling Mill - <i>Sudip Kumar Mukherjee, Saurav Ghosh and Malay Choudhury</i>	94

C-11	Vibration Analysis – An Ideal Tool to Detect Early Signs of Locomotive Wheel Axle Bearing Deterioration - <i>Hemant Bari, Atul Deshpande and Suhas Patil</i>	102
C-12	Analysis of Incorrect Condition Predictions Leads to Corrective Action For Understanding Monitoring Defects & Instrument Limitations - A Case Study - <i>Dr. Rana Dutta, B. Koteswar Rao and Janaki Ranjan</i>	107
C-13	Latest Trends In Condition Monitoring of Rotating Equipment - <i>Padmakar Jaiswal</i>	116
C-14	Experimental Evaluation of Modal Damping to Assess Onset of Flutter In Aero-Engine Blades - <i>Manish Kumar, Giridhar RK and Sanjay Barad G</i>	124
C-15	A Case Study On Condition Monitoring and Accuracy Assessment of Coordinate Measuring Machine - <i>Ravi George, Suneel Kumar, and B Chiranjeevi</i>	135
C-16	Health Monitoring of Gear Box By Wear Debris Analysis Practices and case Study From Strip Processing Line - <i>Naval K Prasad and Premangshu Saha</i>	144
C-17	Intelligent Approach For Compound Fault Detection in Rolling Element Bearing Using Sound Signals - <i>Mohamad Atif Jamil, Sidra Khanam and Md Asif Ali Khan</i>	152
C-18	Reliability Improvement of Exciter Gearbox At Sinter Plant - <i>Aditya Jain, T.Thirumurugan G.R.P Singh, N. Rajesh Kumar and Himangshu S. Mandal</i>	161
C-19	Data Driven Based Solution For Condition Monitoring of Continuous Galvanizing Line Motors Using Time Series Data - <i>Gaurav Lal, Namrata, D N Sharma, Priya Ranjan Mahaptra, Arghya Deb and Sanjeev Kumar</i>	171
C-20	Hydraulic System Failure Prediction through Data Science Models - <i>Prasant Kumar, Sanjeev Kumar, Digvijay Narayan Sharma, hari Darshan Singh and Gyan Prakash</i>	185
C-21	Dynamic Behaviors of a Functionally Graded Rotating Shaft- Bearing System With Nonlinear Supports - <i>Bala Murugan S</i>	195
C-22	Crack Localization In Composite Plates By Intersection of first three normalized Mode Shape Curves From Experimental Modal Analysis - <i>V Deepak Raj Kumar, S. Rama Krishna and M. Tarun</i>	204
C-23	Development of A Machine Learning Based Random Forest Model for Localization of Crack in the Composite Beams - <i>T Rahul Mani Dutta, L. Ram Ganesh, S. Rama Krishna and J. Satish</i>	212
C-24	Monitoring of Power Generation For Vortex-Induced Vibrations of a Single Cylinder Using Ansys Fluent - <i>Johny Shaida Shaik, Srinivasa Rao. Putti and Nikhil Chaitanya Angajala</i>	220
C-25	Vibration Analysis Of An Underwater Pipeline Conveying Fluid With Varying Cross-Section - <i>Bala Murugan S, R.K. Behera and Prajjwal Anuragi</i>	229
C-26	Performance Enhancement of Functionally Graded Mems Accelerometer for Condition Monitoring Using Artificial Neural Network - <i>Uttam Kumar Kar, J. Srinivas</i>	238
C-27	Condition Monitoring of Ship Structures Using Stress- Strength Model - <i>V Srinivasa Rao</i>	247

Keynote Address

Dr. V Bhujanga Rao,
Founder and Patron,
Condition Monitoring Society of India, Visakhapatnam

Abstract

Innovations in digital technology like the IoT, AI, VR / AR, digital twin and 3D printing are fuelling the Industry 4.0 revolution to achieve higher efficiency goals in all industrial processes and plant operations. "Smart factory" or Industry 4.0 environments connect systems to build an "intelligent network" of machines and processes, viewing every aspect of the operation as a potential profit centre. There is a digital layer that sits on top of the mechanical and human operations, and this digital layer is constantly monitoring, interpreting, reporting on, and in some cases directing the actions of the physical machine layer. This digital layer is created on the basis of Condition Monitoring methodology making condition monitoring as an essential gateway to Industry 4.0 to realize new business value. Industry 4.0-style plant or smart factory requires automating data capture ecosystem reflecting the health, safety, risk of damage of machinery or equipment which helps prevent down time. Once the most useful asset data for condition monitoring has been identified, the system must use predictive / cognitive data analytics and direct that data into a platform where it can be aggregated, integrated with data from other operational systems, and then compared against machine performance which enhances the ability to control and optimize processes, cut costs, drive new innovations, virtualise experiments with digital twins etc.

Invited Talks

Machinery Diagnostics and Vibration Technology: Scenario in Industry 4.0, Challenges and Opportunities Ahead

Dr. Tarapada Pyne

Chief Knowledge Officer & Director, Center for Reliability and Diagnostics, Mumbai

Founder Secretary & Director General, Council of Vibration Specialists, Mumbai

SUMMARY OF THE TALK

Condition Monitoring (CM) and associated maintenance strategy Condition Based Maintenance (CBM)/ Predictive Maintenance (PdM) have evolved over the decades in types, in application coverage, in diagnostic and prognostic suitability and not new to us today.

The importance of these predictive techniques, applied independently or jointly, in the health monitoring and assessment of assets (machines or humans), has already been proven. Each technology, related hardware or software, has matured over the decades, as per the depth of analysis required to arrive at the root causes of the anomalies; to satisfy the diagnostic requirements in the handling of health data, both quantitative and qualitative; and to interface the requirements of industry-specific reliability and maintenance performance indices. So, the monitoring and prediction tasks, in terms of their applicability, have traced a learning curve. However, unfortunately, industries have not been able to reap the results to the extent the proven technologies are capable of providing, possibly due to the mismanagement of knowledge in the inter-disciplinary fields of reliability and diagnostics.

CBM through vibration diagnostics is widely used, given the fact of defect vs. symptoms relationship being unique, the ease of access to learning the technology of vibration analysis supported by machinery correction methodologies related to this parameter. It is also observed that around 70 - 80% of assets anomalies may be rightly predicted by the use of vibration information. It is to be remembered at the same time that tracking of one health parameter and analysing the same is not good enough for timely prediction of any health issues of the machinery.

In this talk, the speaker attempts to bring out, in brief, the lessons learnt so far from the ineffective usage of the various proven CM technologies; and the present claims made by the overhyped asset analytics in the age of digitalization and the consequent global industrial disruptions. While narrating the current scenario, the challenges being faced/ to be encountered in near future, the speaker places emphasis on the opportunities available today in India (Today's CBM Destination!) keeping the diagnostic-interests and expectations of the owners of industrial assets at first place, and then concludes the topic with some encouraging notes on the all-round merits of CBM/PdM.

The entire talk is expected to cover the following possible heads:

1. Introduction to the World of CBM/ PdM

- Concept
- Plant Reliability & CBM
- Technologies - Causes Vs Consequences
- Addressing PF Curve/ Maintenance Strategies (criteria of right fit of technologies)

2. Scenario Today

- Good and encouraging state (Awareness/ Hype/ Love for AI, ML/ Jobs/ Market survey/ corporate marriages).
- Bad where lies the **Challenges** (Disintegration/ Isolated Approach, RCA & Design/ Re-Engineering, PdM Status (Old Vs New Assets), Education & Training (Formal & Non-formal), Service Providers, PdM & Energy saving efforts).
- Govt/ OEMs/Institutional role as a whole.

3. Opportunities

- Industrial Benefits (its visible and omnipresent).
- Market Growth & Job Opportunity
- Education & Training / Indian Experts/ Various Platforms/ Seminars
- Education and Training (Formal & Non-formal/ Govt/ Non-Govt/ Service Providers & MSME efforts/ OEMs/ Independent Bodies/ Research Institutions.....)
- Growth of Innovative Indian Products/ Start-ups
- Market / Players in the field / Indian-ness/ Make in India
- Govt Role in encashing the current growth market.

4. CBM/ PdM in Industry 4.0

- Industrial disruptions - **Claims Vs. Expectations**
- Technology suitability Vs Impact on Machine health prediction
- Electronics vs. Mechanical/ Physical Expectations vs. Software vs. Data transfer media & cloud Vs asset owner's needs.
- Prospect of Simulation & Digital Twins – Confidence level in Surveillance/ Knowledge Gaps/ Knowledge-Risk/ Knowledge Strength in performance monitoring.

5. Conclusion

In conclusion, emphasis is given on the imminent growth of CM technologies and therefore the benefits and hence no looking back. What BEST the diagnostic fraternity should opt at this junction is briefed again not only in health monitoring, but also in energy savings, in energy harvesting, in equipment and process waste management, in selection of prime movers/ drivers, in maintenance and in built-in design thinking of CBM process. Lastly but not the least in skills development and knowledge management.

Rotating Machinery Fault Detection by Vibration Signature Analysis

Dr. Kamalkishor J. Uke

Senior Principal Scientist

CSIR- Central Mechanical Engineering Research Institute, Durgapur

Abstract

A machine seldom breaks without a warning. The signs of impending breakdown are almost present long time before the catastrophic breakdown. Therefore, objective of condition monitoring is to provide information that will keep machinery operating longer at the least overall cost. Vibration, bearing temperature, pressure and lubricating oil condition are some of the accessible parameters that can be measured at varying intervals.

Vibration signals define the dynamic properties of a machine including various faults in machine like bearing stability, unbalance, coupling misalignment, looseness and rubs etc. Vibration characteristics also provide early indication of defects on components such as rolling element bearings and gears.

All machines under dynamic condition produce vibration and some unwanted noise. These vibrations are nothing but the transformations of one form of energy to the other, which can be represented in the form of wave and is commonly known as vibration signatures. These vibration signatures carry most of the information of dynamic conditions of a machine including the faults.

Full utilization of vibration characteristics for analysis and monitoring requires measuring amplitude, frequency and phase. With some exceptions, amplitude is the primary indicator of the quality of condition that is how long a machine can operate. Frequency content and phase identify the specific defects; components affected and in some cases, also indicate quality.

Vibration monitoring is the most versatile technique for condition monitoring. Noise and vibration are the signals of machinery trouble. Vibrations are due to many causes inside the equipment that vibrates or may be induced or transmitted from sources outside. Measurement of vibration and its analysis enable us to predict the actual fault and take suitable action much before the breakdown of the machinery. If the measurement falls within the stipulated norm, the equipment can be allowed to operate. It is therefore essential to establish the norms. Regular records & signature analysis coupled with experience are essential for exact diagnosis.

For vital machines, vibration signatures may be obtained immediately after installation. The analysis can then be carried out periodically as well as after every maintenance. The analysis may also be carried out when the overall vibration level shows some abnormal changes. Displacement, velocity or acceleration amplitude may be used for measurement of vibration signatures of machine depending upon the prominence of the frequency components of the vibration signal. Velocity response is generally used for almost equal emphasis on all frequencies. Some of the vibration signals can be identified at certain expected frequency, which are discussed later in this paper. This paper will discuss in details how to identify different faults in rotating machines by vibration signature analysis.

Reaching Out Condition Monitoring Systems to Our MSMEs - It can be Their Saviour – Few Case Studies

Dr. Rana Dutta ,

Consultant, TPM & CBM

Electrosteel Castings Limited, Srikalahasthi Works, Rachagunneri ,AP

Abstract

Condition Monitoring systems are normally dominant in major industries only as the tools and the engineers handling them are both highly expensive. The tight budget of our micro, small and medium enterprises (MSME) can ill afford these expenses after meeting their operational expenses. The author had an opportunity to be a maintenance consultant to few of our MSMEs across the country. During consultancy it was realised that one of the aspects that affect many MSME's turnover are the frequent breakdowns of their machineries and wasteful process of plant maintenance. It was also observed that most of the failures could have been prevented with simple application of condition monitoring tools. The reluctance of using the condition monitoring tools by the MSMEs were found to be two-fold. Firstly, the initial cost of condition monitoring tool and secondly but most important the general apathy of those who are responsible for the plant upkeep for the fear that these tools will make their job redundant. The challenge lay in how to overcome these mental as well as financial barriers and reach out the benefits of the condition monitoring to these enterprises. It could be their saviour for low productivity due to machine failures. Case studies shows that with proper counselling and shop floor demonstration the challenge can be resolved and CBM be made one of the saviours for many of our flagging MSMEs.

“Seven Stages in the life of a Rotating Equipment” and their influence on the Vibration Analysis

Shri. Ganti Subba Rao

Vibration Consultant, Rajahmundry

Abstract

Carrying out analysis and finding solution for a vibration problem of a small motor driven fan of few Kilowatts capacity or a large gas turbine of 210 MW could be equally challenging. This is most likely due to the fact that the actual seed (root cause) for vibration problem might have been shown (entered) at any of the various stages of the life of the equipment. Logically, there appears to be seven stages in the life of any rotating equipment and they are:

1. Design
2. Engineering
3. Manufacturing
4. Installation
5. Commissioning
6. Operation
7. Maintenance

Whether the analysis and solution shall be simple or complicated depend upon the stage at which the problem was initiated.

Typically, a field vibration analyst might not be not be adequately equipped with necessary tools and expertise to resolve the vibration problems if they are due to any design / engineering / manufacturing / Installation issues.

Either OEM experts or consultant specialists of respective fields are required to address the problem.

Many of the field vibration analysts do not have an understanding of the “seven stages” concept and the limitations thereof in analyzing the vibration problem.

This talk discusses the above with relevant inputs from real world case studies. However, due to confidentiality of the data, only salient details of the case studies shall be presented.

Key words: *Rotating Equipment, Seven Stages, Vibration Analysis, Root Cause,*

Application of Active Magnetic Bearings for Fault Suppression and Identification in the Moderate and High-Speed Rotors

Prof. Rajiv Tiwari

*Department of Mechanical Engineering, Indian Institute of Technology, Guwahati,
Guwahati-781039, Assam, India*

Abstract

The paper presents application of active magnetic bearings (AMBs) for the moderate and high-speed rotors for its fault suppression and identification [1]. Initially, some application of AMBs in aerospace application will be reviewed. Conventional identification techniques require external excitation (either known or unknown) to the system, and based on input-output information the system and fault parameters are identified. However, with AMBs instead a suppression force is used. The new philosophy of fault suppression and identification in rotating machinery will be introduced in very abstract way. Then some model-based research performed on this topic will be presented, which includes balancing of high-speed rotors with virtual trial unbalances at slow runs [2]; quantification of misalignment with virtual trial misalignments [3-4]; quantification of transmission error in geared rotor system [5], etc. will be briefly presented. In the end some future direction in the field will be presented [6].

Keywords: *Active Magnetic Bearings Flexible Rotor Balancing; Cracked Rotor; Geared Rotor; Misaligned Rotors; Virtual Trial Unbalance and Misalignments.*

REFERENCES

- [1] Tiwari R. *Rotor Systems: Analysis and Identification*. CRC press, Boca Raton, USA; 2017.
- [2] Gyan R. and Tiwari R. On-site high-speed balancing of flexible rotor-bearing system using virtual trial unbalances at slow run. *International Journal of Mechanical Sciences*, 2021: 183, 105786.
- [3] Prabhat K. and Tiwari R. Finite element modelling, analysis and identification using novel trial misalignment approach in an unbalanced and misaligned flexible rotor system levitated by active magnetic bearings. *Mechanical Systems and Signal Processing*, 2021: 152, 107454.
- [4] Srinivas S., Tiwari R. and Kannababu C. Modeling, Analysis, and Identification of Parallel and Angular Misalignments in a Coupled Rotor-Bearing-Active Magnetic Bearing System. *ASME, Journal of Dynamic Systems, Measurement, and Control*, 2021: 143 (1), 011007.
- [5] Majumder G. and Tiwari R. Transverse vibration of geared-rotor integrated with active magnetic bearings in identification of multiple faults. *ASME, Journal of Dynamic Systems, Measurement, and Control*, 2021: 143 (9), 091003
- [6] Srinivas S., Tiwari R. and Kanna babu C. Application of active magnetic bearings in flexible rotor dynamic systems—A state-of-the-art review. *Mechanical Systems and Signal Processing*, 2018: 106, 537-572.

Contributed Papers

AI/ ML-Based Performance Characteristics Predictions of Centrifugal Pumps

Ashish Sharma, Rajiv Tiwari, Niranjan Sahoo

*Department of Mechanical Engineering, Indian Institute of Technology Guwahati,
Guwahati-781039, Assam, India*

Abstract

Deviation of pump characteristics, i.e. the pump head, power, and efficiency from normal trends should be considered as a condition monitoring factor, and can be used for predictive maintenance which justifies the best time for overhauling of pumps. The effective operation of pumps in diverse technical fields depends on centrifugal pump characteristics at various operating speeds. Therefore, a unique method considering the centrifugal pump intrinsic operating characteristics has been proposed to solve this problem and anticipate the pump characteristics. In this study, Pump characteristics were evaluated to calculate functional curves, such as the pump head versus discharge, power versus discharge, and efficiency versus discharge at different ranges of speed varying from 900 rpm to 2520 rpm to find out the most efficient operating speed of the pump. The best efficiency point was evaluated for each speed. Artificial Neural Networks (ANN) and different machine learning algorithms are used to predict the performance characteristics of centrifugal pumps. Training and testing data were obtained from experimental studies. The best training algorithm is determined. The model performs as anticipated, according to all projected performance parameters for a centrifugal pump. Complex, time-consuming, and expensive experimental research is required to identify the head, efficiency, and effective power consumption of various types of pumps. This approach can be used to forecast pump performance with a centrifugal pump at different speeds without conducting experiments.

Keywords: *Centrifugal Pump, Pump Characteristics, Machine Learning, Artificial Neural Network*

Introduction

Centrifugal pumps are rotor-dynamic devices that move liquid to a higher head by spinning a set of impeller blades. Using a centrifugal pump, the liquid is accelerated to the impeller's exterior ring, where motor energy is transformed into kinetic energy. The quantity of energy transferred to the liquid is reflected in the velocity at the vane or impeller point. The liquid travels at a higher velocity at the vane tip and is given off more energy when the impeller rotates more quickly or is larger. Since many industrial activities depend on non-redundant components, a decline in pump performance or a malfunction has an impact on how well the system works as a whole. Because of their exceptional efficiency, broad range of capacity and head options, uniform flow rate, ease of operation, and cheap maintenance costs, Centrifugal Pumps are frequently used in industry. Their usual working speed range is between 1000 and 3000 rpm, and they operate in harsh environments. They guarantee the smooth operation of the process and are essential components of many manufacturing facilities [1]. It is crucial to understand how centrifugal pump problems arise in order to spot them and take appropriate action to stop the unavoidable consequences. The premature failure or performance degradation of the pump system could have a significant financial impact on the functioning of the complete unit. In addition to the economics, the operator's

safety is in jeopardy. Early fault identification is therefore essential to prevent the device from failing catastrophically. Although qualitative analyses of vibration patterns are highly beneficial and contain a wealth of information about the flaws, they are susceptible to interpretation mistakes made by humans [1]. Centrifugal Pump as conventional machine of energy conversion, with low energy consumption, low cost and compact structure, in industry, agriculture and life has wide range of applications. Low speed centrifugal pumps are especially crucial in the petrochemical, irrigation and draining, aircraft, and other industries. According to statistics, 22% of the world's energy supply is used by pumping systems. However, the poor working efficiency of low-speed centrifugal pumps, which prevents them from using the majority of the energy, makes it urgently necessary to enhance pump performance in order to boost the efficiency of energy conversion

The typical curves of centrifugal pumps depict the laws and relationships governing each parameter, and the pump performance expression is crucial to the manufacturing process. Two significant parameters among the centrifugal pumps efficiency parameters are the amount of flow (Q) and the pump head (H). The stability of the centrifugal pump function and the range of flow regulation is directly impacted by the shape of the H-Q curves. Additionally, a speed-based variable torque number is required for this pump. The torque increases by a factor of four when the speed is twice because it is simply proportional to the square of the speed. The characteristic curve of the centrifugal pump is determined by the design intention and actual test at a certain speed. The three characteristic curves of flow v/s head, flow v/s efficiency, and flow v/s power are measured by the pump manufacturer before leaving the factory. The pump's head and discharge rate are represented by the ordinate and abscissa, respectively. A particular centrifugal pumps flow and head curve is a downwardly curved line, showing that the pump head decreases and the flow rises. It is possible to choose and employ pumps based on the centrifugal pumps typical curve, which depicts the change law of the pump's fundamental performance. Different pumps have unique distinctive curves, and the apparatus maker will supply you with this information. Every pump, strictly speaking, has a unique distinctive shape. A collection of the head, shaft power, and efficiency numbers that correlate to any flow point can be located on the pump characteristic graph. Working conditions, which refer to a collection of working conditions at the greatest productivity point, are the normal name for this set of related factors. The state is referred to as the finest state. Despite the differences in the characteristic curves of the various kinds of centrifugal pumps, they all share a similar pattern of change.

Literature Review

According to several academic studies, the impeller, volute, and diffuser design parameters, which have an impact on the characteristics of fluid flow inside the turbo machine system, determine the efficacy of centrifugal pumps. The number of blades, vane angle setting, and blade width are all part of the impeller design. The diameter of the base, the breadth of the volute, the vane setting angle of the tongue, and the throat area are the principal design elements of the volute [2]. The characteristics of the pump were assessed on different blade outlet angles in a recent experimental study. It is one of the important centrifugal pump design factors that have an impact on the internal flow field and overall pump efficiency. It has a sizable impact on the efficacy and head pump. Wider blade departure angles improve overall pump performance [3]. Today's research focuses on obtaining pump characteristics for household use or evaluating the performance of centrifugal pump variations under various operating circumstances. A centrifugal pumps performance evaluation under

various operating circumstances is effectively investigated [4]. This study seeks to quickly and accurately predict centrifugal pumps' energy performance, including their head, power, and efficiency. The theoretical loss model is combined with the back propagation neural network, which is a physics-informed neural network and can predict accurate results with a small sample size, to create a hybrid neural network based on the different geometrical parameters and operational circumstances. [5]. The performance of a centrifugal pump can be calculated theoretically using internal and external energy loss equations that are both scientific and empirical. For varying impeller geometry and pump rotational speed, calculated data on pump head, efficiency, and power were produced and compared with experimental data. For pump head, a very excellent agreement between the two sets of data is found [6]. Developed hybrid neural networks that incorporates the theoretical loss model into the back propagation neural network and then automatically determines the node number of hidden layers is proposed to predict the energy performance (i.e., the head, power, and efficiency) of centrifugal pumps based on the various geometrical parameters and operating conditions [7]. Devised a method for Cavitation detection based on ultrasonic phase demodulation. The support vector machine was fed with the features retrieved from demodulated data. An accuracy of 98% was achieved [8]. The study offers an empirically verified optimization procedure for radial flow centrifugal pumps operating in turbine mode. The optimization procedure described here is intended to be used with prediction models to forecast a pump's turbine mode characteristics and selection models to choose the best pump for turbine-mode operation. Prior prediction uncertainties are reduced by the optimization routine, particularly in the low specific speed region [9]. Based on the hydraulic specifications of the pump, particularly the specific speed that identifies the type of the runner and, subsequently, its hydraulic behaviour, a new method was developed to forecast the Best efficiency point of a Pump as Turbine. The more effective pump works as a turbine in greater h and q when two pumps with the same specific speeds are compared, it has been demonstrated. However, a pump with a larger impeller operates more effectively at the same particular speeds [10]. Analysed the flow rate and pressure build-up in a pipe when a centrifugal pump is operating at a fixed speed. A straightforward and low-cost test rig is created to approximate residential water distribution, or housing application. In order to monitor and analyse pump performance, including water pressure, water flow rate, pump power, and pump speed, the approach is then experimentally validated [11]. They showed that Cavitation increases the typical oscillation frequency at specific locations in a centrifugal pump. Before and after cavitations, the five-stage diffuser centrifugal pumps oscillation was measured and analysed. The surface of the flow path components are affected by the high-speed micro-jet produced by Cavitation, which raises the oscillation characteristic frequency. [12]. They examined the pressure pulsation at the pump intake and exit using numerical modelling and experimental research to determine the evolution of the cavitations. Apart from the selection of method of collecting data and debating which physical signal (or their combination) will give better confidence in results, the domain in which the data is present before it is used for feature extraction also matters [13].

Measurement Procedure

A centrifugal pump may operate in a wide range of situations, but not all of them will result in effective and satisfying performance. How the data is displayed presents one of the primary challenges for the examination of centrifugal pump operational performances. A precise determination of the mass flow processed by the centrifugal pump is possible with the experimental test setup shown in Fig. 1. A switch valve that permits the use of a closed loop circuit is installed in the plumbing system. Throttle valve controls the flow rate. Pump

was made to operate at a set of different speeds. A variable frequency drive is used to run the induction motor from 900 rpm (15 Hz) to 2520 rpm (42 Hz) in steps of 300 rpm (5 Hz). Flow rate, suction and discharge pressure, are measured at seven different flow rates for each rpm.. Flow rate is measured with the help of flowmeter. Input power demand of pump-set is measured using electronic standard energy meter. In pump there are two pressure taps, one for the discharge and another one for the suction. These taps are connected to their corresponding pressure gauges. Pressure taps are closed subsequently to cause the variation in pressure in suction and discharge line. Equations 1, 2, 3, and 4 were used to determine the centrifugal pump head, hydraulic power, and efficiency after all values had been measured. The performance profiles were then found.

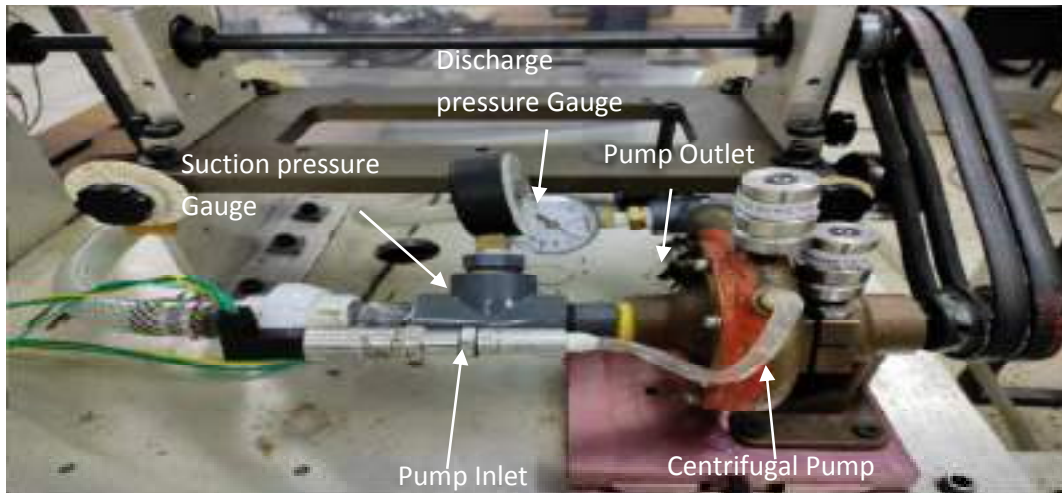


Fig. 1 Centrifugal pump Test Rig

The current study focuses on examining three performance metrics at different speeds, including head pump, hydraulic power, shaft power and efficiency. All of those parameters in centrifugal pumps are typically described by equations 1) to 4).

After obtaining the discharge and suction pressure during the pump test, the pump head is computed using the following equation:

$$H_p = \frac{1}{g} \left[\left(\frac{p}{\rho} + gz \right)_d - \left(\frac{p}{\rho} + gz \right)_s \right] = \frac{P_d - P_s}{\rho g} \dots \dots \dots (1)$$

where, P_d is the discharge pressure at pump outlet (N/m^2), P_s is the suction pressure at inlet (N/m^2), ρ is the fluid density(kg/m^3), g is the acceleration due to gravity.

The hydraulic power given to the fluid is given by,

$$P_{out} = \rho Q g H_p \dots \dots \dots (2)$$

The efficiency of pump is defined as the ratio of output power delivered to water to input power consumed by motor, it is given by,

$$\eta = \frac{P_{out}}{P_{shaft}} = \frac{\rho Q g H_p}{P_{shaft}} \dots \dots \dots (3)$$

Input power of three phase induction motor is dependent on phase angle, current and voltage, it is given by,

$$P_{shaft} = \sqrt{3} * V * I * \cos\Phi * \eta_{Motor} \dots\dots\dots (4)$$

Where, V is the voltage; I is the current and ϕ is the phase angle.

Fig.2 shows the prediction flow diagram i.e. from flow of input data to prediction of pump characteristics. Dataset was generated after series of experiments. Pump Characteristics were calculated from above equations. Data set was split into Training and Validation datasets. Various machine learning and deep learning algorithms were trained for prediction. All the models were evaluated on validation data set.

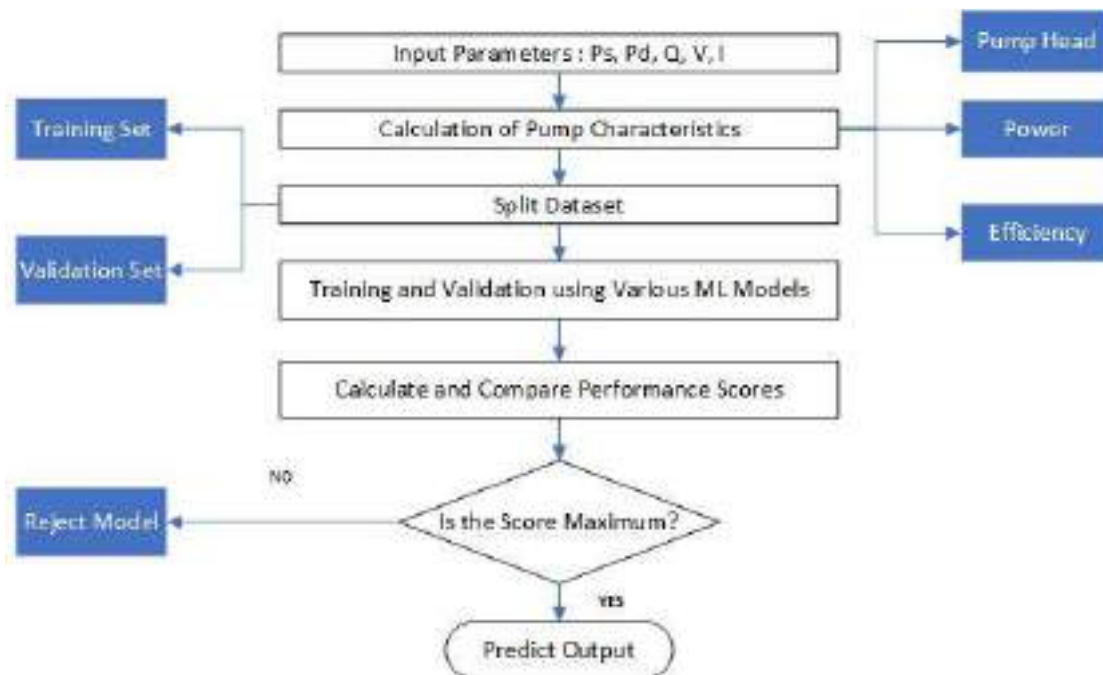


Fig. 2 Prediction Flow Diagram

Results

Table 1 shows the data findings from the experimental rig testing, including the water pressure, flow rate, and other factors at 1800 rpm. Values of each parameter are taken for 7 different flow rates at each set of rpm.

N(RPM)	P _s (Kpa)	P _d (Kpa)	Discharge (m ³ /s)	voltage(V)	Current(Amp)
1800	-9.542	36	0.0018	222.5	1.33
1800	-12.001	43.2	0.0017	221.47	1.32
1800	-13.234	48.6	0.0015	221.68	1.28
1800	-13.876	50.4	0.0011	222.5	1.25
1800	-14.987	54	0.0008	222.55	1.22
1800	-16.237	59.4	0.0006	222.99	1.18
1800	-19.976	63	0	221.77	1.18

Table1. Input parameters at 1800 rpm

N(RPM)	Pump Head(m)	Output power (W)	Input power(W)	Efficiency (%)
1800	4.64	81.98	328.03	24.99
1800	5.63	93.84	324.05	28.96
1800	6.3	92.75	314.53	29.49
1800	6.55	70.7	308.3	22.93
1800	7.03	55.19	300.96	18.34
1800	7.71	45.38	291.67	15.56
1800	8.45	0	289.76	0

Table 2. Pump Characteristics at 1800 rpm

Table2 contains centrifugal pump-set test data papers that list all of the pump-set's flow, head, power, and efficiency parameters at 1800 revolutions per minute. The characteristic curves for the pump set were derived from the computations at 5 various sets of rpm, ranging from 1800 rpm to 2520 rpm at a 180 rpm interval.

Table 3 shows the data findings from the experimental rig testing, including flow rate, Pump head, Power and efficiency at 5 different rpm at an interval of 180 rpm. All these parameters are benchmarked against established affinity laws i.e.

$$\left(\frac{Q}{ND^3}\right)_1 = \left(\frac{Q}{ND^3}\right)_2 \dots\dots\dots(5)$$

$$\left(\frac{gh_p}{N^2D^2}\right)_1 = \left(\frac{gh_p}{N^2D^2}\right)_2 \dots\dots\dots(6)$$

$$\left(\frac{P}{\rho N^3D^5}\right)_1 = \left(\frac{P}{\rho N^3D^5}\right)_2 \dots\dots\dots(7)$$

Where Q is discharge, D is impellor diameter, N is rpm, h_p is pump head and P is power.

N(RPM)	Discharge (m ³ /s)	Pump Head (m)	Input Power (W)	Efficiency (%)
2520	0.0033	8.99	929.952	64.77
2340	0.0028	7.97	728.511	54.11
2160	0.0024	6.95	571.876	45.16
1980	0.0021	5.65	440.256	36.53
1800	0.0018	4.64	328.03	24.99

Table 3. Parameters at 5 different rpm

Figure 3,4,5 shows the variation of Pump head, Input power and efficiency versus Discharge at 5 different rpm.

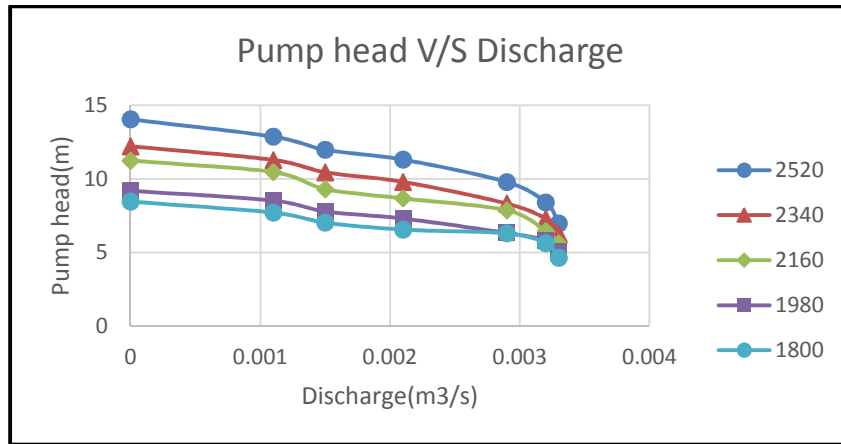


Fig.3 Variation of Pump Head w.r.t Discharge

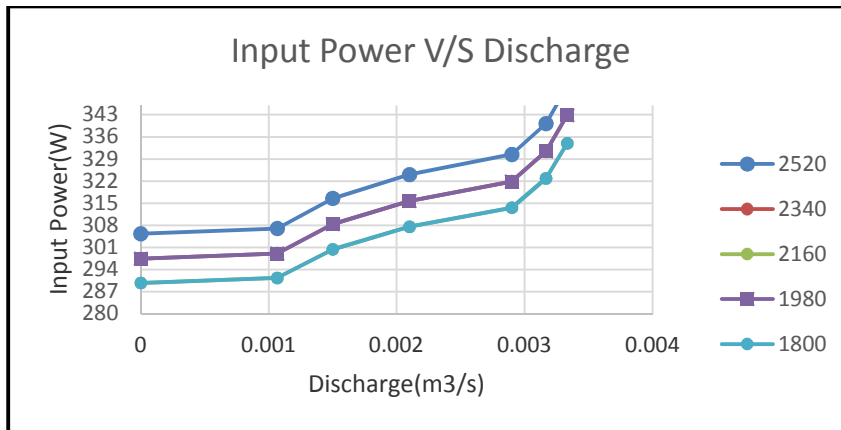


Fig.4 Variation of Input Power w.r.t Discharge

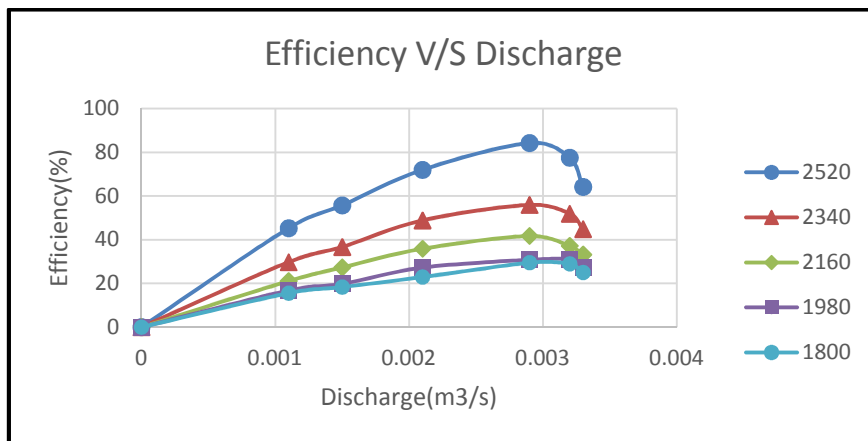


Fig.5 Variation of Efficiency w.r.t Discharge

Pump data set was generated from experiments. Data set consists of 70 rows and 10 columns. Various machine learning algorithms and artificial neural network was used to

predict the pump characteristics. Performance scores of all algorithms were evaluated and linear regression comes to be the best performing algorithm.

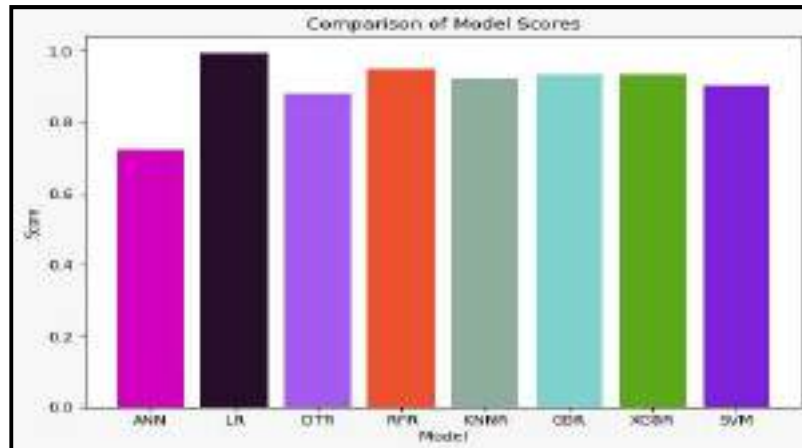


Fig. 6 Performance scores of algorithms

Conclusion

In this work, experimental procedure was developed to calculate the performance of the centrifugal pump at different set of rpm. It has been found that pump efficiency increases with increase in speed and it was found to be maximum (84%) at 2520 rpm. Pump input power and pump head also increases with increase in speed. Pump head decreases with increase in flow rate. Maximum shut-off head was found to be 14m at 2520 rpm. Power input slightly increases with flow rate. Pump efficiency increases upto maximum, known as best efficiency point and then decreases with flow rate. Several machine learning and deep learning algorithms are used to predict the pump characteristics. Among all algorithms, linear regression performs best with the accuracy score of 99%. The non-linear dataset may have a linear relationship between the independent and dependent variables in a certain range or under certain conditions. In such cases, the linear regression model may be appropriate for predicting the dependent variable within that range or under those conditions.

References

1. **Tiwari, R.:** Rotor Systems: Analysis and Identification. CRC Press Boca Raton, USA. (2017)
2. **Fu, L., Zhu, X., Jiang, W., Li, G.:** "Numerical investigation on influence of diffuser vane height of centrifugal pump." *International Communications in Heat and Mass Transfer*. **82**, 114–124 (2017).
<https://doi.org/10.1016/j.icheatmasstransfer.2017.02.014>
3. **Ding, H., Li, Z., Gong, X., Li, M.:** "The influence of blade outlet angle on the performance of centrifugal pump with high specific speed." *Vacuum*. **159**, 239–246 (2019). <https://doi.org/10.1016/j.vacuum.2018.10.049>
4. **Ale, B.B., Shrestha, S.O.B.:** "Experimental Study on Performance Characteristics of a Pem Fuelcell." *Journal of the Institute of Engineering*. **7**, 31–39 (1970).
<https://doi.org/10.3126/jie.v7i1.2060>
5. **Li, X., Chen, B., Luo, X., Zhu, Z.:** "Effects of flow pattern on hydraulic performance and energy conversion characterisation in a centrifugal pump."

- Renewable Energy*. **151**, 475–487 (2020).
<https://doi.org/10.1016/j.renene.2019.11.049>
6. **Kara Omar, A., Khaldi, A., Ladouani, A.**: “Prediction of centrifugal pump performance using energy loss analysis.” *Australian Journal of Mechanical Engineering*. **15**, 210–221 (2017). <https://doi.org/10.1080/14484846.2016.1252567>
 7. **Huang, R., Zhang, Z., Zhang, W., Mou, J., Zhou, P.**: “Energy performance prediction of the centrifugal pumps by using a hybrid neural network.” **213**, (2020)
 8. **Ping, X., Yang, F., Zhang, H., Zhang, J., Zhang, W., Song, G.**: “Introducing machine learning and hybrid algorithm for prediction and optimization of multistage centrifugal pump in an ORC system.” *Energy*. **222**, (2021).
<https://doi.org/10.1016/j.energy.2021.120007>
 9. **Singh, P., Nestmann, F.**: “An optimization routine on a prediction and selection model for the turbine operation of centrifugal pumps.” *Experimental Thermal and Fluid Science*. **34**, 152–164 (2010).
<https://doi.org/10.1016/j.expthermflusci.2009.10.004>
 10. **Derakhshan, S., Nourbakhsh, A.**: “Experimental study of characteristic curves of centrifugal pumps working as turbines in different specific speeds.” *Experimental Thermal and Fluid Science*. **32**, 800–807 (2008).
<https://doi.org/10.1016/j.expthermflusci.2007.10.004>
 11. **Jilani, A., Razali, A.**: “Variable Speed Pump Performance Characteristics for Domestic Application.” *MATEC Web of Conferences*. **225**, (2018).
<https://doi.org/10.1051/mateconf/201822502005>
 12. **Wang, K., Wang, C., Xia, C., Liu, H., Zhang, Z.**: “Experimental measurement of cavitation-induced vibration characteristics in a multi-stage centrifugal pump.” *Journal of Chemical Engineering of Japan*. **51**, 203–209 (2018).
<https://doi.org/10.1252/jcej.17we191>
 13. **Rakibuzzaman, M., Kim, K., Suh, S.H.**: “Numerical and experimental investigation of cavitation flows in a multistage centrifugal pump.” *Journal of Mechanical Science and Technology*. **32**, 1071–1078 (2018).
<https://doi.org/10.1007/s12206-018-0209-6>

Diagnosing the Healthy or Defective State of a Centrifugal Pump Based on Vibration, Pressure and Current Data using a Deep Learning Algorithm

Shivam Gautam, Rajiv Tiwari

Department of Mechanical Engineering, Indian Institute of Technology Guwahati, Guwahati 781039, Assam, India

Abstract

Throughout operating condition, centrifugal pumps may suffer due to operationally developed faults, likely to result in a disruption in long - term operation. As a result, tracking the health of the centrifugal pumps is crucial for avoiding unwelcome stoppages, which might result in the failure of the overall system. This study uses data from several types of sensors collected over a frequency range based on the cavitation hydraulic phenomenon to assess the health or fault of the pump. Data from the healthy pump and the impeller fault pump is considered. The pump ran at various levels of obstruction and frequency to collect data from vibration signals, motor current signals, and pressure signals based on time domain. At various obstruction levels and pump rotation frequencies, detection based on binary classification using the deep learning algorithm is provided as binary classification outperformed in any other algorithm such as kernel SVM, random forest, etc. Multiple statistical attributes are extracted from this data and fed into an artificial neural network (ANN) model and predicting the condition of pump. Moreover, for data classification, hyperparameters are tuned to optimized the model result. The methodology's robustness, as well as that of the developed and tuned model, is also tested and presented to demonstrate their dependability. The proposed failure detection methodology was found to be very efficient during observation. Cavitation is the hydraulic phenomenon used.

Keywords: *Centrifugal pump; Healthy or Faulty state; Machine Learning; Artificial Neural Network*

1. Introduction

The most common type of hydraulic rotating equipment for home, industrial, medical, and agricultural usage is the centrifugal pump (CP). CP main purpose is to move liquid and deliver it to a high head. The liquid enters through the suction pipe, travels to the impeller eye and goes through a number of impeller blades. Due to the centrifugal force generated by the impeller rotating blades, liquid is propelled radially outward and is then forced into a casing before exiting into the piping system below. In several industrial areas, hard particles of various types of pollutants may be present in the liquid being pumped. Impurities may clog the pipe, which results in unstable pump flow. Pump malfunctions could halt the plant's process flow or reduce its efficiency, failing to produce the desired results. Furthermore, if the defects are not addressed at the appropriate stage, the life of the pumps is drastically reduced. Therefore, it is essential to identify the different types of problems by the examination of their signatures. Most CP defects can be divided into three categories: (i) Mechanical causes, such as worn bearings, bent shafts, unbalanced rotors, and loose parts; (ii) system causes, such as partial or plugged strainers, clogged impellers or suction lines, and installation errors; and (iii) operational causes, such as cavitation,

speed and flow issues, and insufficient immersion of the suction pipe. Manufacturing or operational flaws could be to blame for bearing issues.[1]

Leaks and obstructions, as well as flow interruptions or mechanical flaws (such as burst impellers, bearing issues, and bent rotors), are the most frequent causes of CP defect. Suction obstruction issues might result from utilising contaminated working fluids or from damaging the pipe's surface. Such flow obstructions cause the flow rate to decrease and secondary flow, or recirculation, to appear. As flow separation widens, vortices form, which causes a drop in local pressure and the appearance of vapour bubbles. Also, the creation of bubbles in centrifugal pumps is not desirable because it reduces the head that is being created and leads to holes at the surfaces of the pumps due of the creation of micro-jets. Treating CP failures as separate problems is therefore not viable. One defect can make another defect due to dynamic flow of water and low pressure phenomenon i.e. cavitation and if a defect is already exist than it can make the situation worse by creating the number of more defects. As a result of the ensuing flow instabilities, this causes unpleasant vibrations. Maintenance strategies are readily available to maintain the assets in the sectors.[2]

Ranawat[3]evaluated the accuracy and efficiency of Support Vector Machines (SVMs) and Artificial Neural Networks (ANNs) techniques and compared their performance to identify the most suitable technique for fault diagnosis in centrifugal pumps. Furthermore, this paper also proposed the use of various signal processing techniques, such as wavelet transform and empirical mode decomposition, for feature extraction from the pump vibration signals. The use of these techniques allows for better classification of faults, which enhances the accuracy of fault diagnosis. Hasan[4]Proposed a framework that combines scalogram-based imaging and deep learning for more accurate fault diagnosis in centrifugal pumps, which can reduce downtime and maintenance costs. The framework uses deep learning algorithms and scalogram-based imaging to diagnose various centrifugal pump defects, such as misalignment, unbalance, and bearing problems. Wang et. al [5]postulated the use of a combination of Computational Fluid Dynamics (CFD) and optimized the design of a centrifugal pump and evaluated the effects of design parameters on pump performance. The proposed approach offers a more efficient and accurate way of optimizing design parameters for improved pump efficiency.

Gangsar and Tiwari [6]evaluated the use of wavelet-based features, current, and SVM algorithms to diagnose faults in induction motors under various operating conditions. The effectiveness of SVM algorithms for defect diagnosis was assessed under different load levels and speeds. Panda and Tiwari [7]The study suggests using SVM methods based on vibration measurements and signal processing techniques such as wavelet decomposition and principal component analysis to anticipate problems and evaluate the effectiveness of SVM algorithms in predicting flow obstructions and cavitation with varying conditions and severity. Kumar et. al [8] utilized multi-source data and a deep learning algorithm to determine intake pipe blockage levels in centrifugal pumps at a range of speeds results in a more precise and effective approach of recognising blockages than existing techniques.

According to the literature, to identify obstructions, vibration, pressure, and motor line signals have not yet been merged. There are still few studies dealing with locating faulty or healthy state of CP. Hence, all the elements motivate researchers to investigate state of the CP.

This study is separated into the upcoming sections as follows: Section 2 discusses the experimental setup and data capture. Section 3 explained of data classification methods is covered. Section 4 highlights steps for NN model and the state of CP. Section 5 presents the final conclusions.

2. Description of the experimental design and procedure

The Machine Failure Simulator was used to conduct the experiment on a centrifugal pump. The pump was mounted on a fixed base and powered by a double-belt pulley system with a 3-phase induction motor. The pump had leak-proof fittings and a manual modulating valve to control water flow. Data are captured at a rate of 5000 samples/s with 5000 samples/dataset for each defective condition. The pump was run at speeds from 30 to 60 Hz with varying levels of blockage at a gap of 5 Hz is achieved through a mechanical modulation valve with six equal intervals marked on it so that varied levels of blockage can be achieved by regulating the valve at various intervals. No clogging is used in B0, B1 shows 16.7% clogging, B2 shows 33.3% clogging, B3 shows 50% clogging, B4 shows 66.6% clogging, and B5 shows 83.33% clogging.

Accelerometers: To analyse acceleration, a pump was equipped with two triaxial accelerometers (refer to Figure 1(a)) with sensitivities of 101, 101.1, and 101.4 mV/g (accelerometer-2) and 100.3, 100.7, and 101.4 mV/g (accelerometer-1) in the x, y, and z axes, respectively. *Pressure Transducers:* Two pressure transducers (refer to Figure 1(b)) from "Nitech," a sensitive silicon chip, are used to measure the pressure of liquids. When the pressure sensors are functioning within the operational range (0-60 psi), current fluctuation can be used to understand the response from the sensors (4–20 mA). *Current sensing probes:* "The Key sight 1146B" current probes were used to record the current line reading. Current probes can measure currents between 100 mA and 10 A rms. *Data Acquisition System (DAQ):* For high accuracy frequency domain measurements, the NI PXI -4472 dynamic signal acquisition module has 8 channels while the NI PXI -6251 dynamic signal acquisition module has 16 channels. The 16 channels of the NI PXI -6251 and the eight channels of the NI PXI -4472 both digitise input signals simultaneously across a DC to 45 kHz bandwidth.

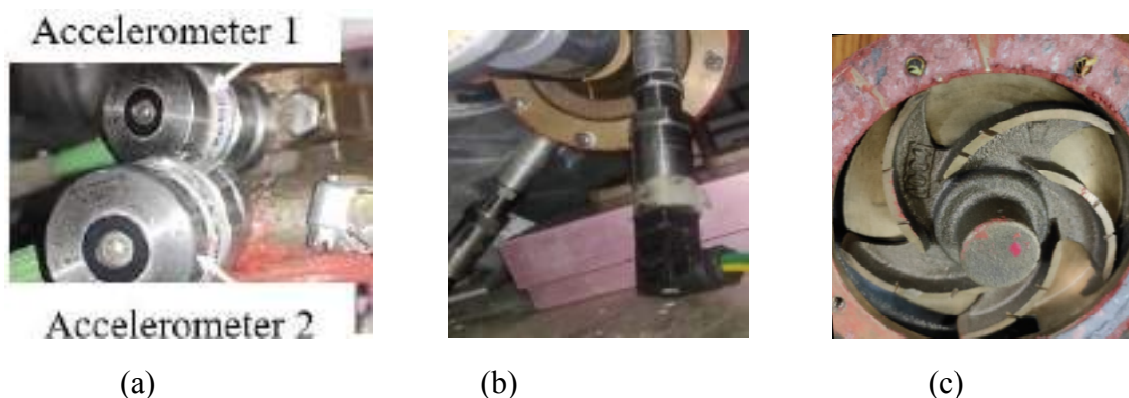


Figure 1: (a) Tri-axial accelerometers glued to the pump casing and bearing housing (b) High- and low-pressure transducers mounted on the pump (c) Impeller fault

2.1 An overview of the experiment

An experiment was run on the MFS to gather data at different levels of flow blockage. Data gathering was carried out for each combination of pump running speed and block level. In order to get comprehensive information about the defect, three distinct measurements acceleration, fluid pressure, and motor line current were taken using several sensors, including accelerometers, pressure transducers, and current probes. Figure 2 depicted the experimental setup.

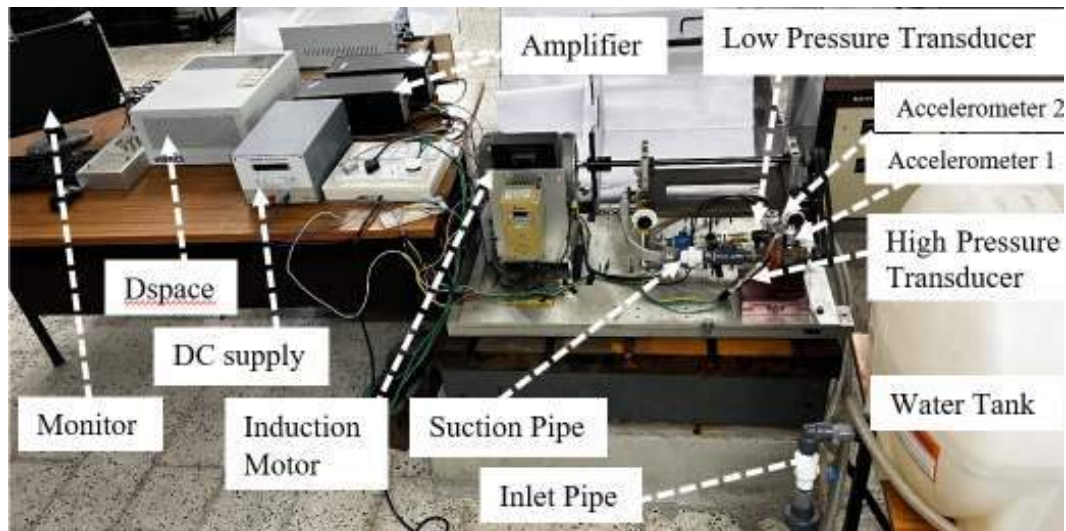


Figure 2: Experimental set-up

2.2 Evaluating Procedure

For fault diagnostics, vibration, pressure, and current signatures were used. Data acquisition system (DAQ) was set up using Control Desk software. The 5000 samples were collected at a sampling rate of 5000 samples per second for a time domain measurement. There were 150 seconds of data collection. 5000 x 150 non-overlapping data points were collected for each sensor.

The information was saved in distinct DAQ measurement files in.csv files for each disturbance at various centrifugal pump speeds and was recorded on the system hard drive. The details of DAQ are given in Table 1. The time domain data can then be transformed using a variety of methods into any domain. Sequentially mounted on the MFS were a healthy pump, a pump with a defective impeller, and a pump with a defective cover plate. Figure 1(c) displays an impeller defect fault. The cover plate fault has several pits on it and the impeller plate has cuts on the blades; these are thought to have occurred when high-pressure bubbles burst and impacted the metal wall as tiny jets. A suction blockage defect with six severity levels was included for each of these three pump problems. The pump was run at a variety of speeds during each pump state. The induction motor was run on a variable frequency drive in stages of 300 rpm from 1800 rpm (30 Hz) to 3600 rpm (60 Hz) (5 Hz). For fault diagnostics, vibration, pressure, and current signatures were used. Data were gathered at 5000 samples per second and 5000 samples makes one dataset for each

defective situation. While collecting the data, the data is gathered for 150 seconds and hence a total of 150 dataset were gathered for each fault situation.

Table 1: Data Acquisition System outlines

Blockage levels	B0 (Full Flow), B1 (1/6 obstruction), B2 (1/3 obstruction), B3 (1/2 obstruction), B4 (2/3 obstruction), B5 (5/6 obstruction)
Frequency	30, 35, 40, 45, 50, 55, 60 Hz
Quantity of all fault conditions	$6 \times 7 = 42$
Sets of measurements for each combination of obstacle and frequency	150
sample timings	5000
Timeframe for a single data collection	1 sec
Data collection time for each failure combination	150 sec

2.3. Declaration of Fault Set

In this study, a total of 18 different CP fault circumstances have been taken into account. Healthy pumps without obstructions (HP0), healthy pumps with blockages at the suction end (HPb), impeller faults without blockages (IF0), and impeller faults with blockages at the suction end (IFb), where $b = 1, 2, 3, 4, 5$. By bracketing the fault circumstances into the appropriate classes with these conditions, fault sets can be produced. There are two classes, one of which is in a healthy state and the other of which has the faulty state. Table 2 provides an explanation of the both fault sets.

Table 2: Fault classification sets description

Fault Set	Classes (labels)
1	Class 1: HP0, HP1, HP2, HP3, HP4, HP5 Class 2: IF0, IF1, IF2, IF3, IF4, IF5

3. Methodology for data classification

This study uses supervised learning to classify faults at various frequencies using pressure, acceleration, and current lines. Supervised learning classifies data based on different traits, creating a function connecting input and output. Deep learning uses neural networks to process data and extract sophisticated features. In deep learning, input x is passed through hidden layers to extract important data, and the output layer predicts the class of the input. The expression for z is as follows:

$$z = w^T x + b \quad (1)$$

Where x is the input, w and b are the weight and bias vectors, respectively, with T representing the transpose. Use "Rectified linear unit" (ReLU) activation function to compute vector function z in hidden layers, then apply bias and weight to obtain output in the next hidden layer, and use Sigmoid activation function in the output layer for binary class classification. The sigmoid function is a mathematical function commonly used in artificial neural networks as an activation function. It maps any input value to a value between 0 and 1, and is defined as

$$f(x) = 1 / (1 + e^{-x}) \quad (2)$$

The sigmoid function is useful in modelling decision making or probability-based scenarios, where the output represents the likelihood of a certain event occurring. The binary loss function which is used in binary classification and it compares the predicted probability of the positive class to the target label of 0 or 1. Binary loss functions include binary cross-entropy and measures the difference between the predicted probability and actual label. Binary cross-entropy loss function is expressed as

$$H_p(q) = -\frac{1}{N} \sum_{i=1}^N y_i \log(p(y_i)) + (1 - y_i) \log(1 - p(y_i)) \quad (3)$$

where $p(y)$ is the expected probability for each of the N locations, and y is the label. The open-source Python (Jupyter) deep learning libraries "Keras" and "Scikit learn" are used in this study.

4. Observations and Opinions

This study aims to use multiple sensor data to perform multiclass classification and recognize the severity of block utilization. To avoid excessive duplication in input data, only six statistical features are selected from raw sensor data. The selection of these features is not predetermined and can vary based on the defect and data being analysed. The six features considered are mean, standard deviation, mode, entropy, kurtosis, and skewness, which cover different aspects of the data.

4.1 Performance of separately and combined features

To make processing faster and more efficient, meaningful information can be extracted from raw data by considering statistical features such as standard deviation, variance, mean, median, mode, kurtosis and skewness. In this study, different algorithms including Kernel SVM and Random Forest were used to test the performance of these individual features at two different speeds (30 Hz, 60 Hz) and their average. Figure 3 (a, b) illustrates that the average of the random forest technique is superior to the kernel SVM. Results showed that Random Forest performed better than other algorithms, particularly. Therefore, the Random Forest model was selected for further feature calculations with 10 estimators and entropy criterion.

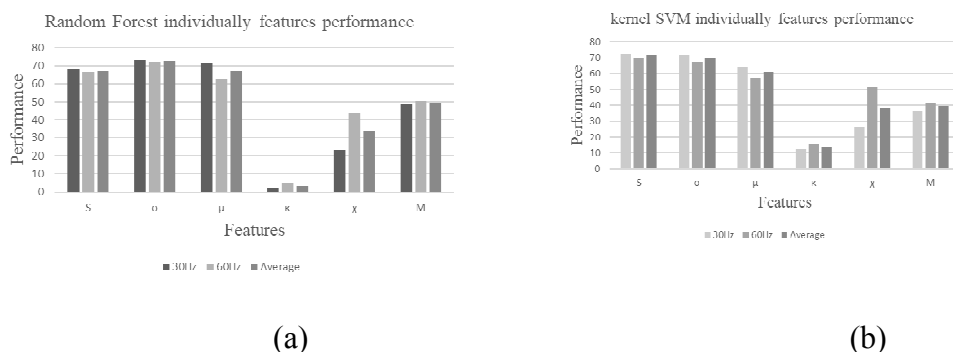


Figure 3: Classifier accuracies for several statistical features on average and at two different frequencies (a) Random Forest algorithm used to identify the performance of different feature at three different frequencies. (b) Kernel SVM algorithm used to identify the performance of different feature at three different frequencies.

The standard deviation was the best statistical feature, with mean and entropy also showing good performance. These features were used to calculate blockage severity accuracy. Accuracy was lower at low frequency (30 Hz) but vary with high frequency (60 Hz). It is due to slight signal pulsation variations, while higher frequency led to more bubbles forming and affecting defect severity. The combination of standard deviation and mean provides the best accuracy among all statistical features. The performance of the classifier also increases with increasing frequency, and two best feature combinations of mean and standard deviation are shown in Figure 4(a). For further three features taken into account i.e. mean, entropy and standard deviation to get more precious

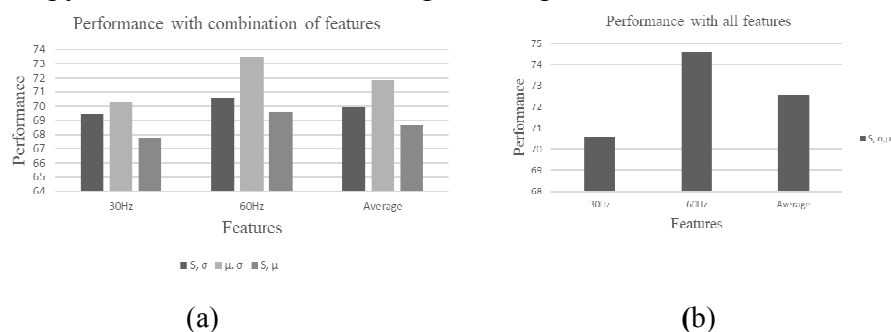


Figure 4: Classifier performance versus Frequency (a) using multiple features (b) using all the features

After analysing all three features (mean, entropy and standard deviation), Figure 4(b) shows that accuracy increases with frequency, indicating that cavitation severity improves accuracy. High accuracy indicates significant signal variation due to many bubble formations (i.e., cavitation generation), while low accuracy shows normal signal fluctuation. The combination of mean, entropy and standard deviation provides the best accuracy among all statistical features. Therefore, mean, entropy and standard deviation are selected for the remainder of the study. To enhance the quality of performance of both individual and combined characteristics, different features can be used and one might examine the inverse of standard deviation.

4.2. Classification algorithms for blockage severity

This study compares several classification techniques, including XGBoost, Decision Tree, K-Nearest Neighbours, Random Forest, and Artificial Neural Network to determine the best algorithm for a given input. The study uses data from all operating frequencies, including pressure signals, vibration signals, and motor current signals. The results of the study are presented in Figure 5(a), which shows the accuracy of each algorithm. After tuning, the neural network is found to be the best classifier, with a fault set accuracy of 85.90%. The study then used the tuned neural network to predict the state of CP, which are classified into two classes. Section 4.3 describes the steps for tuning the neural network, which is then used to predict blockage severity.

4.3. Steps for tuning the Artificial Neural Network

The tuning process involves iterative experimentation with the model. The study found that using three hidden layers with 100, 50, 15 neurons in each layer respectively and a Softmax activation function at the output layer produced the best results. The study also found that using Relu activation in the hidden layers and 100 epochs with 50 mini batch sizes optimized model performance. To avoid over fitting, dropout regularization method used.

Various training testing ratios were tested in neural networks to determine the best classification accuracy, including 25:75, 30:70, 50:50, 80:20, and 90:10. After evaluating all the ratios, the study found that the 80:20 training testing ratio produced the best results shown in figure 5(b).

To train the weights and biases of each neuron in a neural network, optimization algorithms are used to reduce the cost function. This study considered several optimization methods, such as stochastic gradient descent (SDG), RMS prop, Adadelata, Adam, and Nadam. After testing all of them, Nadam was found to perform the best and was used for the study as shown in figure 5(c). Proper initialization of network weights is critical to prevent gradients from vanishing or exploding, which can affect how the network is trained. This study considered various weight initialization methods, such as Lecun Uniform, Glorot Normal, Glorot Uniform, He Normal, and He Uniform in which Lecun Uniform performed best in all as shown in figure 5(d). The choice of activation function is crucial in creating any neural network, as it can impact how well the model learns from the training dataset. For binary class classification problems like this one, the output layer typically uses the Sigmoid activation function. However, when it comes to the activation function for hidden layers, it is important to test different options to find the most suitable one for the application. This study considered various activation functions, including Softplus, Relu, Tanh, Sigmoid, Hard-sigmoid activation function, to determine the most appropriate one for the given problem in which Relu performed best as shown in figure 5(e).

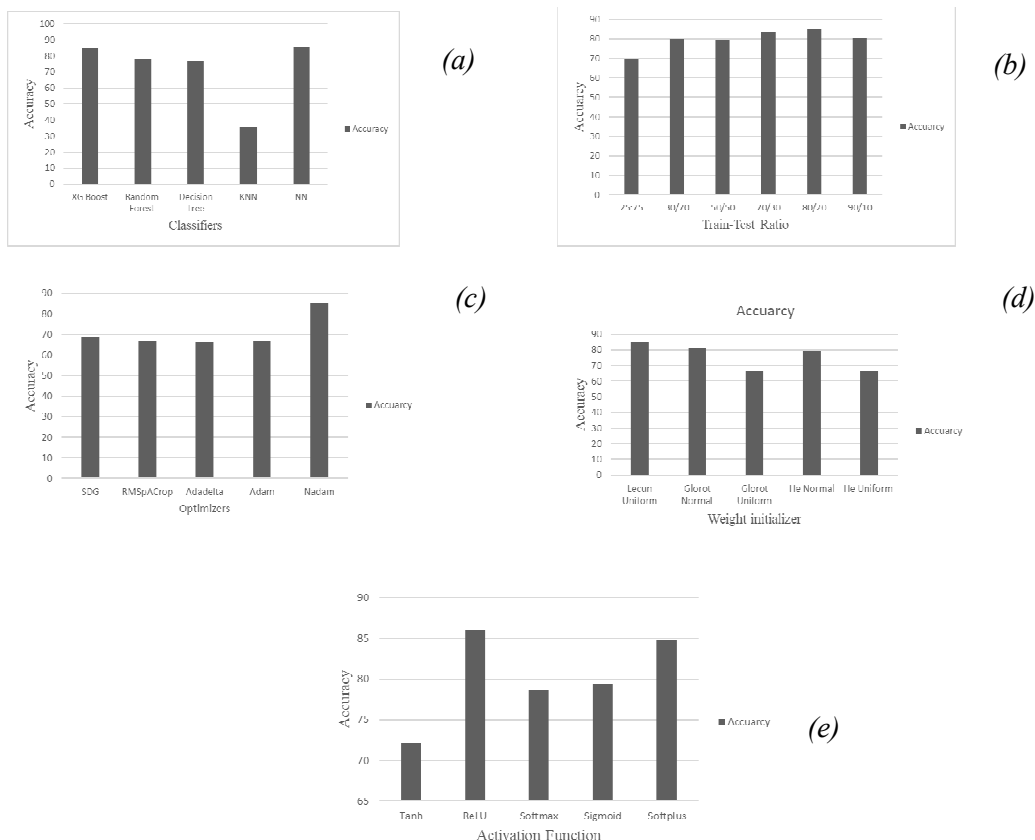


Figure 5: Performance while making the Neural Network

(a) Different classification algorithm at their tuned states in which Neural Network performs best (b) Selection of train-test ratio in which 80:20 ration found best (c) Selection of optimization algorithm in which Nadam executes best (d) Selection of weight initializers in which Lecun Uniform shows best performance (e) Selection of activation function in which Relu found best.

4.4. Test of healthy or defective state of CP

Table 3 displays the confusion matrix for the model's performance on all feature blockage. The confusion matrix is a $C \times C$ matrix that evaluates the classification model's effectiveness, with C representing the total number of target classes. It compares the predicted values generated by the machine learning model with the actual target values.

Table 3: Confusion matrix for all combined features at two different classes

Actual Level	Predicted Levels	
	7498	14
2081	5268	

It can be seen from the confusion matrix that all 12766 instances have been correctly classified by the model.

5. Conclusion

We provide effective deep learning-based centrifugal pump malfunction diagnostics using time-domain multiple sensor data. It is quite likely that a pump obstruction, which is progressive in nature, is what causes cavitation and causes the shutdown. So, it is crucial to find state of C-Pas early as possible. Two states, one is healthy and other is impeller faulty state were considered. All the input features are continuous variables while the output is represented as [1 0] for Healthy, [0 1] for Impeller Faulty for cavitations. The condition of a centrifugal pump can be determined using a simple method that uses features including mean, standard deviation, entropy, skewness, kurtosis, and mode. Several features were extracted from the raw data and different algorithms were used to classify them, and bar charts were used to compare the outcomes. Out of all features, individually standard deviation outperformed and, in the combination, standard deviation, mean and entropy outperformed in all. It is found that total 12766 predication were correct with the accuracy of 85.90% using the tuned model. This accuracy can be improved by gathering more number of dataset, use different features of the training data in the learning phase and the inverse of standard deviation feature can also used. ReLU is used in the hidden layer while the Sigmoid function is applied to the output layer. The ultimate mini batch size is found 50 and epoch is 100. The classification accuracy and confusion matrix inferred to the accelerometer sensor, motor current sensor, and pressure sensor data indicated that all these signals can be used to determine state of the CP. The results also show that collecting data from multiple sources is always advantageous. The same data classification technique may be utilized to examine various other traits derived from same sensor data for monitoring of the obstruction.

References

- [1] Tiwari, R. (2017). Rotor Systems: Analysis and Identification CRC Press: Boca Raton, USA, <https://doi.org/10.1201/9781315230962>
- [2] Tabar MTS, Majidi SH, Poursharifi Z (2011) "Investigation of recirculation effects on the formation of vapor bubbles in centrifugal pump blades". World Academy of Science, Engineering and Technology, January 2011, 73:521–526

- [3] N. S. Ranawat, P. K. Kankar, and A. Miglani, "Fault diagnosis in centrifugal pump using support vector machine and artificial neural network," *Journal of Engineering Research (Kuwait)*, vol. 9, pp. 99–111, 2021, doi:10.36909/jer.EMSME.13881.
- [4] Hasan, M. J., Rai, A., Ahmad, Z., & Kim, J.-M. (2021). "A Fault Diagnosis Framework for Centrifugal Pumps by Scalogram Based Imaging and Deep Learning," *IEEE Access*, 1–1. doi:10.1109/access.2021.3072854
- [5] C. N. Wang, F. C. Yang, V. T. T. Nguyen, and N. T. M. Vo, "CFD Analysis and Optimum Design for a Centrifugal Pump Using an Effectively Artificial Intelligent Algorithm," *Micromachines*, 2022, Taiwan, doi: 10.3390/mi13081208.
- [6] P. Gangsar and R. Tiwari, "Diagnostics of mechanical and electrical faults in induction motors using wavelet-based features of vibration and current through support vector machine algorithms for various operating conditions," *Journal of the Brazilian Society of Mechanical Sciences and Engineering*, volume 41, no. 2,12 January 2019,Guwahati, Assam, India, doi: 10.1007/s40430-019-1574-5.
- [7] A. K. Panda, J. S. Rapur, and R. Tiwari, "Prediction of flow blockages and impending cavitation in centrifugal pumps using Support Vector Machine (SVM) algorithms based on vibration measurements," *Measurement: Journal of the International Measurement Confederation*, Guwahati, Assam, India volume 130, 2018, doi: 10.1016/j.measurement.2018.07.092.
- [8] D. Kumar, A. Dewangan, R. Tiwari, and D. J. Bordoloi, "Identification of inlet pipe blockage level in centrifugal pump over a range of speeds by deep learning algorithm using multi-source data," *Measurement: Journal of the International Measurement Confederation*, volume 186, Guwahati, Assam, India September,2021, doi: 10.1016/j.measurement.2021.110146.

Prediction of Remaining Useful Life for Running Gear System of an Armoured Fighting Vehicle

**Hafeezur Rahman. A , Srinivasan. G , Vetrivelan. D , Akilandeswari. P ,
Balaguru.V & Balamurugan.V**

Combat Vehicles R&D Establishment (CVRDE), DRDO, Avadi, Chennai-54

Abstract

Armoured fighting vehicles are a class of vehicles intended to operate both on road and cross country which are designed with the fundamental philosophy of firepower, mobility, survivability, EM suite and situational awareness. With such multitude of systems integrated on these platforms, artificial intelligence and prognostics and health monitoring (PHM) play a key role in maintaining the platform with combat fitness. This paper deals with the prognostics and health monitoring of one such system namely the Running Gear (RG) system of an armoured fighting vehicle.

First and foremost, the system, its functions and its operating environment are introduced followed by the need to do health monitoring. Subsequently, the methodology to do PHM for the subject system is explained in detail. Also, the sensors chosen to carryout prognostics and health monitoring on the RG system are introduced followed by their mounting and data acquisition. Finally, this paper explains in detail the methodology for determining the remaining useful life (RUL) of RG system, the tangential benefits accruing due to the same for the services followed by the way forward for similar platforms.

Keywords: *running gear system, health monitoring, prognostics, data acquisition, combat vehicle, accelerometers*

Introduction

Armoured fighting vehicles (AFV) are a class of vehicles protected with heavy armour capable of withstanding diverse threats starting from kinetic energy to chemical energy projectiles with an accurate firepower and a matching mobility. These class of vehicles fulfill a wide variety of mission objectives such as tactical offensive, fire support to ground forces, amphibious assault, troop transport, artillery coverage, mortar coverage, air defence, reconnaissance, explosive ordinance disposal, repair & recovery, bridge laying etc. Of these roles, the tactical offensive is the most decisive in the determining combat effectiveness of the land forces in which, the mechanised infantry has a pivotal role. For such a mechanised infantry, the Main Battle Tank (MBT) platform forms the backbone of the fighting forces.

Traditionally these platforms were designed keeping in mind the conventional warfare philosophy or the iron triangle of firepower, mobility and protection¹. Such an iron triangle underwent minor changes with the introduction of un-conventional warfare by non-state actor's post 9/11² and the recent Russia-Ukraine war. The net result of these recent combat developments is the modification of the conventional iron triangle into an iron pentagon³. This change is a direct result of the introduction of artificial intelligence (AI) & prognostics and health monitoring (PHM) technologies in a large scale not only in design and development but also in platform maintenance. This assumes significance as the recent

developments have shown that platform maintenance issues have a great bearing on combat effectiveness. The traditional maintenance approach for AFVs include repair & overhaul on a fixed time basis based on the life data provided by the designers or original equipment manufacturers (OEMs). This type of maintenance based on a certain level of performance degradation without input from any sensors is a blind proactive maintenance. By inclusion of sensors in the system, this problem is obviated and the system utilized for an extended period by determining a remaining useful life (RUL) criterion which leads to a condition-based maintenance (CBM) or predictive maintenance. This paper tries to address these challenges through a study, wherein a prognostics and health monitoring (PHM) approach is evolved for a RG system of an AFV and thereby a RUL criterion determined.

Maintenance methodology

The maintenance methodology in vogue is based on an envisaged service life of 30 yrs for an AFV platform and its variants. The intervention period for determining medium repair and overhaul is shown below.

Intervention for maintenance	Periodicity as per maintenance philosophy (whichever is earlier)	
	Duration in yrs	Distance in kms
Medium Repair - 1 (MR-1)	10	2400
Overhaul - 1 (OH-1)	16	3700
Medium Repair - 2 (MR-2)	23	5400
Overhaul - 2 (OH-2)	29	6700
Medium Repair - 3 (MR-3)	35	7900

Table.1. Intervention period for maintenance of Class ‘A’ Vehicles⁴

Prognostics & Health monitoring (PHM)

The PHM approach to maintenance relies on monitoring the condition of a system in order to detect anomalies and on the ability to diagnose the health of critical components. An ultimate goal is to develop a prognosis of a faulted component’s Remaining Useful Life (RUL) and an associated functional impact on the system so that appropriate maintenance can be scheduled and life extension achieved as shown in Fig.1 below. The maturation of technologies in the areas of: measurement sensors, signal processing theory, digital processing hardware, dynamic system simulation, multi-sensor data analysis, and approximate reasoning have made condition based maintenance CBM & RUL prediction possible⁵. Thus, the prognostics shifts the maintenance into the “predict and prevent (PAP)” paradigm⁶.

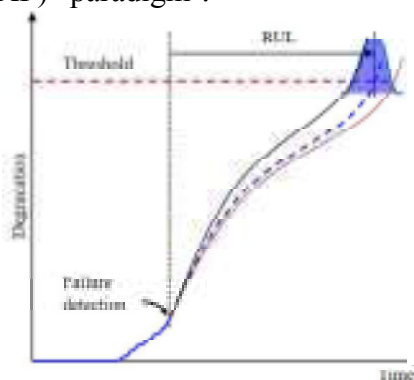


Fig.1. Prognostics approach

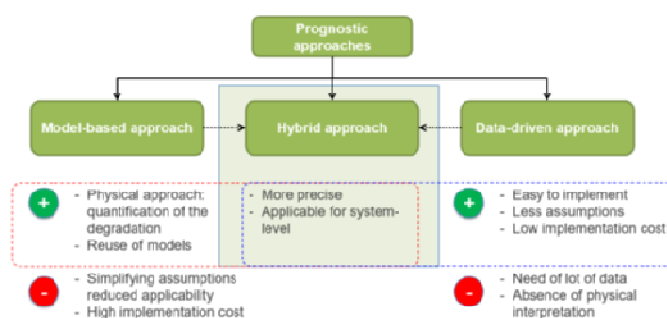


Fig.2. Different PHM approaches⁷

A typical PHM methodology consists of three approaches as shown in Fig.2. For the present study for a RG system, data-driven approach is selected. In this paper, a four-step maintenance assessment approach is proposed which consists of critical component analysis, right sensor selection, prognostics feature evaluation and prognostics methodology with determination of RUL for the system.

Running gear system of AFV

The running gear system for an AFV is shown in Fig.3. It consists of the drive sprocket, tracks, suspension, top roller, bump stops and track adjuster. This system in an AFV has four purposes. The primary purpose is to dissipate the pressure exerted on the ground due to higher mass of these platforms, the others include providing the required traction for the platform and offer superior ride comfort for the crew and provide better ride handling. Whereas, the sprocket converts the power from the vehicle transmission to driving torque, it is converted to the required tractive effort or the propelling force by the track through the interaction with the terrain. The track also provides the overall pressure dissipation to prevent sinkage of the AFV in soft soil. Although different types of tracks such as the single-pin bush, double-pin bush, band tracks are available, the double-pin bush track is often preferred.

The most critical item in the running gear system is the suspension. It has multiple roles in an AFV namely, support vehicle body or hull, provide lateral & longitudinal stability, selective distribution of pressure on ground, adjust for terrain irregularities and provide crew comfort. Further the suspension also protects the vehicle components & cargo from vibration damage, provide traction contact with ground through the track, transmit driving & braking torques, provide obstacle crossing capabilities, provide means for changing course and provide a stable gun platform⁸. Although, contemporary AFVs have both torsion bar and hydro-pneumatic suspension, the present study will focus only on a running gear system with hydro-pneumatic suspension.

To prevent the track whipping at high speeds thereby damaging the track guards of the structure and the suspension, support rollers are provided known as top rollers. In addition, to mechanically arrest the suspension travel beyond a point stoppers are provided known as bump stops. Finally, to prevent track shedding a mechanism known as track adjuster is provided which provides a constant track tension a grease actuated piston mechanism.



Fig.3. Running gear system for Main Battle Tank

Critical Snags in RG system

To determine the parameters that need to be monitored to formulate an effective PHM strategy, a history of critical snags that have occurred historically is studied. Whereas, the Type-I snags affect the immediate mobility of the AFV, the Type-II snags does not affect the mobility immediately and the system can be used but with prolonged usage, life is degraded considerably.

Snag	Description	Location	Root cause Analysis	Diagnosis
Type I	Axle arm not responding to given wheel input	Suspension	Axle arm weld failure at bearing interface	Frequency analysis
Type I	Bogie wheel wobbling	Suspension	Seal failure resulting in no lubrication and bearing failure	Frequency analysis or Thermocouple
Type I	Top roller wobbling	Top roller	Seal failure resulting in no lubrication and bearing failure	Frequency analysis
Type I	Abnormal noise during motion	Suspension	Connecting rod & crank failure	Frequency analysis
Type I	Track whipping	Near track adjuster	Grease Piston stuck in cylinder	Pressure sensor
Type I	Abnormal noise during motion	Near track adjuster	Seal failure resulting in no lubrication and bearing failure	Frequency analysis
Type I	Abnormal heating on damper & cylinder surface	Suspension	Seal exhibiting higher friction and higher misalignment between casing & cylinder	Thermocouple or IR camera
Type II	Bogie wheel not retracting	Suspension	Gas / Oil leakage from casing or filling valve	Pressure & Angle sensor

Table.2. Root cause analysis of major & minor snags

A cursory of the root cause analysis above reveals that three sensors namely accelerometer, pressure and temperature sensors are adequate to evolve the PHM methodology for the RG system.

Bearing health monitoring

Vibration analysis is the most common condition monitoring technique recommended for bearing condition. Here the acceleration spectrum is captured at specific points using accelerometers and techniques such as Fast Fourier Transform (FFT) applied to display a frequency spectrum, problems can be identified using distinct frequency components. By trending vibration periodically from the RG system, it is possible to detect and diagnose incipient damages so that maintenance can be planned and executed along with determining RUL. To exactly determine the bearing condition specific frequency of interests are calculated namely the ball pass frequency outer (BPFO, outer race defect), ball pass frequency inner (BPFI, inner race defect), ball spin frequency (BSF, rolling element defect) and fundamental train frequency (FTF, cage defect) as shown below. In the

equations below, N_B is the number of rolling elements, RPM is the shaft rotation speed in rev/min, B_D is the rolling element diameter in m, P_D is the pitch diameter in m and β the contact angle in deg.

During the first stage, the defects appear in the ultrasonic frequency range as shock or spike energy and life of the bearing is 10-20% of its L_{10} life. At stage two side bands appear and the life is 5-10% of its L_{10} life. In stage three BPFO, BPFI, BSF & FTF appear and the life deteriorates to 1-5% of its L_{10} life. During the final stage, random vibration in the form of a noise floor appear that lead to general condition of looseness and replacement. Based on this approach, the bearing frequencies of interest for a typical taper roller bearing on the suspension wheel hub is given in Table.3 below.

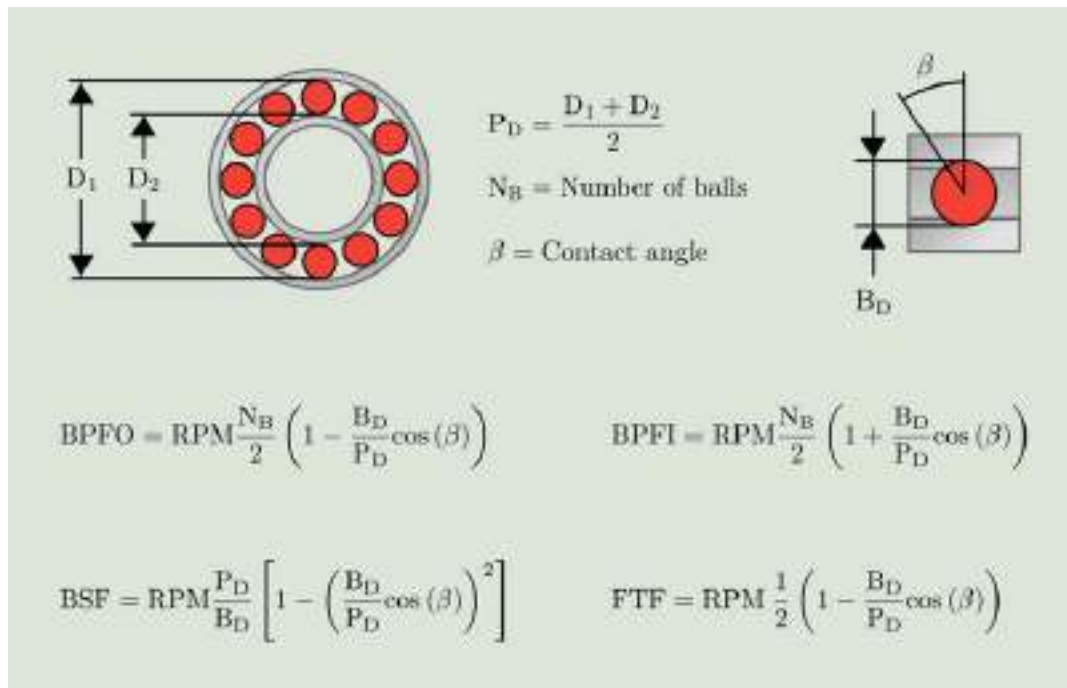


Fig.4. Rolling element bearing defect frequencies⁹

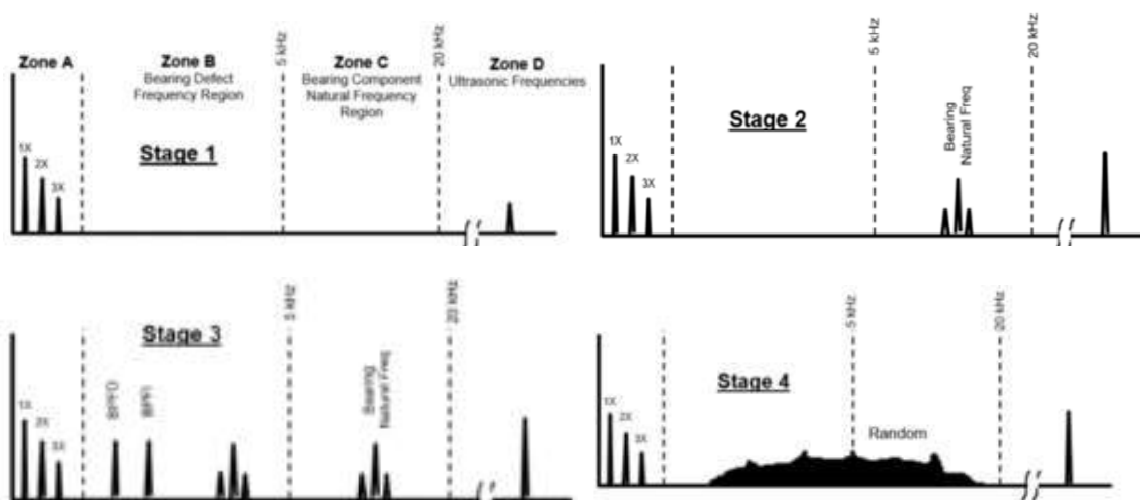


Fig.5. Four stages of bearing health monitoring¹⁰

Mk-IA, AHSU HUB BEARING - Taper Roller Bearing - 30220A						Impact rates f (Hz)						
Sl No	Vehicle Speed (kmph)	Vehicle Speed "V" (m/s)	RPM "N"	Running frequency RPS (fr) "IX" in Hz	Wheel Radius m	No of Roller	Roller Dia "mm"	Pitch Dia "mm"	Cos β (15°)	For outer race Defect Hz	For Inner Race Defect Hz	For Ball Defect Hz
1	5	1.38889	36.8266	0.613777	0.36	20	20.1	140	0.9659	5.2866	6.9889	4.1928
2	10	2.77778	73.6532	1.227553	0.36	20	20.1	140	0.9659	10.5732	13.9779	8.3857
3	15	4.16667	110.4798	1.84133	0.36	20	20.1	140	0.9659	15.8598	20.9668	12.5785
4	20	5.55556	147.3064	2.455107	0.36	20	20.1	140	0.9659	21.1464	27.9557	16.7714
5	25	6.94444	184.133	3.068883	0.36	20	20.1	140	0.9659	26.4330	34.9446	20.9642
6	30	8.33333	220.9596	3.68266	0.36	20	20.1	140	0.9659	31.7196	41.9336	25.1571
7	35	9.72222	257.7862	4.296437	0.36	20	20.1	140	0.9659	37.0063	48.9225	29.3499
8	40	11.1111	294.6128	4.910213	0.36	20	20.1	140	0.9659	42.2929	55.9114	33.5428
9	45	12.5	331.4394	5.52399	0.36	20	20.1	140	0.9659	47.5795	62.9003	37.7356
10	50	13.8889	368.266	6.137767	0.36	20	20.1	140	0.9659	52.8661	69.8893	41.9285
11	55	15.2778	405.0926	6.751543	0.36	20	20.1	140	0.9659	58.1527	76.8782	46.1213
12	58	16.1111	427.1886	7.119809	0.36	20	20.1	140	0.9659	61.3247	81.0715	48.6370

Table.3. Bearing frequencies of interest for a suspension bearing

Pressure & Temperature monitoring

Along with the bearing CBM, pressure and temperature of the HSU are also monitored. The pressure inside the HSU is measured with a reduction in gas pressure causing Type-II defects. However, if prolonged use it may lead to severe damage of the floating pistons. Similarly, higher seal friction, cylinder ID scoring or misalignment can cause temperature raise which can be monitored to check for threshold.

Sensors suite & CBM Kit for RG system

The sensor suite to be positioned in the HSU & track adjuster is shown in Fig.6. To mount the sensors suitable brackets are incorporated to conform to requirements¹¹.

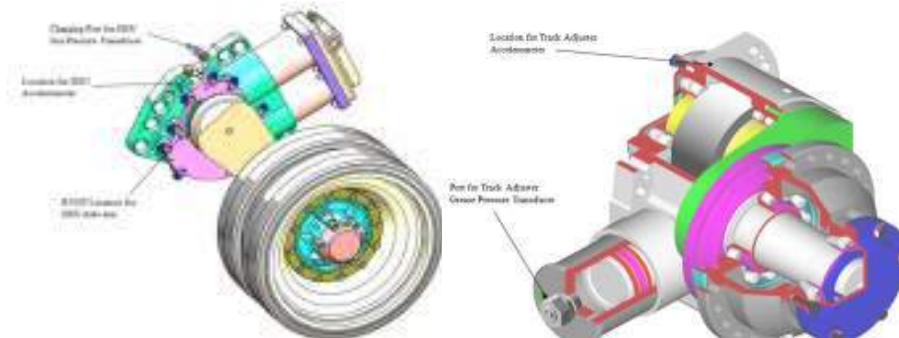


Fig.6. Sensor suite for suspension & track adjuster

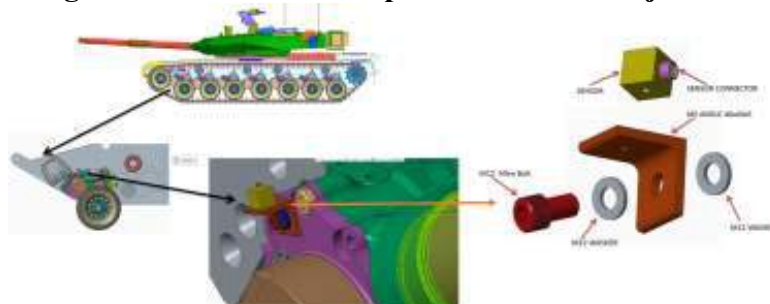


Fig.7. Accelerometer mounting for HSU

The overall sensor suite for the RG system is mounted on the AFV as shown in Fig.8 and the on-board PHM kit can be positioned. Alternatively, a portable kit for performing CBM on the RG system can also be provided as shown in Fig.9.



Fig.8. Overall sensor suite mounting including harness routing



Fig.9. Onboard & Portable PHM Kit for RG System inside AFV

Data acquisition & analysis approach for RG PHM

The data acquisition and analysis approach for the study is shown in Fig.10 below. The first step in the process is the fitment of sensors on the AFV at designated locations. Then, vehicle is run at designated speeds such as 10, 20, 30 kmph etc., to determine fundamental frequency. The sampling rate is set to optimum to prevent memory overload. In addition, the thresholds for bearing defect frequencies, pressure and temperature are set as given in Table.4. If a serious defect is detected, a data alert and warning message is logged for course correction. In case, the defect is non-serious, the corresponding RUL determined and message displayed in terms of hrs. Based on the smallest RUL of the sub-systems, the maintenance schedule is planned accordingly.

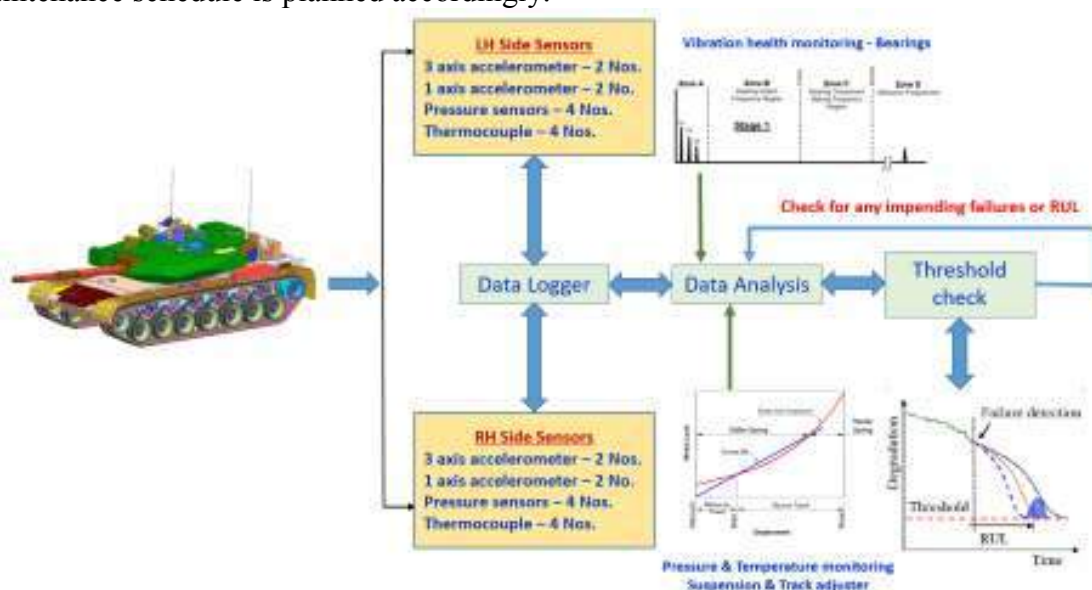


Fig.10. Data collection & analysis methodology for RG system

Parameter	Life hrs/km	Threshold	Threshold breached	RUL
Bearing Frequencies (Wheel hub)	L ₁₀ hrs	Spikes (gSE)	Y	881.3 hrs
			N	4406 hrs
		BPFO, BPFI, BSF, FTF	Y	440.6 hrs
			N	4406 hrs
Gas pressure	km	90 bar (min)	Y	200 km
			N	< 40 km
Skin temperature (on cylinder)	km	90 deg C (max)	Y	350 km
			N	3500 km

Table.4. Remaining useful life for RG suspension at 30 kmph (ref)

The above analysis pertains to the RUL for suspension at a particular vehicle speed of 30 kmph. To arrive at a meaningful analysis, all such RUL values at maximum and minimum speed ranges be estimated. Similarly, for the track adjuster the RUL is estimated as per the above methodology. Further, from the above analysis it is evident that when the FFT detects a spike then the threshold is set at 20% of the L10 life for a specific bearing which becomes its RUL. In addition, when the suspension gas pressure drops to less than 90 bar the system can be operated to only 10% of its life (RUL), beyond which damage to pistons are expected. Similarly, when the skin temperature reaches beyond 90 deg C the system can be operated to only 10% of its life (RUL), beyond which damage either to cylinder or pistons is expected.

Conclusion

The methodology for predicting the remaining useful life of a running gear system for an AFV is presented. Although, different approaches to PHM exists, the data driven model is chosen due to available experimental data. Based on the snags observed both during vehicle trials and in-house testing, critical parameters namely bearing life, pressure and temperature are chosen. In addition, the mounting or interfacing details of these sensors on the AFV is also explained. Also, the methodology to acquire data, threshold setting and RUL estimation in case of a breach of threshold are discussed in detail. The only drawback of this methodology is the mounting of sensors and data capture during vehicle running due to the severe vibration, temperature and sand & dust environment which is challenging. Finally, considering the availability of these platforms, the advantages that accrue due to this PHM methodology far outweigh its challenges and hence can be explored in other similar systems.

References

1. Tery, T.W., Jackson, S.R., Ryley, C.E.S., Jones, B.E. et al., Fighting Vehicles (London: Brassey's, 1991).
2. Zahn, B.R. The future combat system: Minimizing risk while maximizing capability. US Army War College, Pennsylvania, 2000.
3. South Asia Defence Strategic review, Vol 16, Issue 2, May-June 2022
4. Report No. 36 of 2016, Working of Army Base Workshops, Report of CAG Union Government (Defence Services-Army), India
5. Begg, C, Merdes.T, Byington.C.S, Maynard.K.P., Mechanical System Modeling for Failure Diagnosis and Prognosis, Maintenance and Reliability Conference (MARCON 99), Gatlinburg, Tennessee, May 10-12, 1999.

6. Cheng-liang Liu, Jay Lee, Liang Gong, Yixiang Huang, Prognostics and Maintenance for Mechanical Systems in Harsh Environment, *Advances in Mechanical Engineering* Volume 2013, Article ID 121340, 2 pages, <http://dx.doi.org/10.1155/2013/121340>.
7. Vepa Atamuradov, Kamal Medjaher, Pierre Dersin, Benjamin Lamoureux. et al., Prognostics and Health Management for Maintenance Practitioners - Review, Implementation and Tools Evaluation, *International Journal of Prognostics and Health Management*, ISSN 2153-2648, 2017.
8. AMCP 706-356, Automotive Suspensions, US Army Material Command, Washington, 1967.
9. Saruhan.H, Sandemir.S, Cicek.A, Uygur.I, Vibration Analysis of Rolling Element Bearing Defects, Volume 12, Issue 3, pg.384-395, June 2014.
10. Pawel Lecinski, Bearing Problems-Fault Frequency & Artificial Intelligence Based Methods, www.reliabilityconnect.com.
11. ISO 5348-1998, Mechanical Vibration & Shock-Mechanical Mounting of Accelerometers, International Organization for Standardisation, www.iso.org.

Remote Monitoring of Mining Dump Truck Operation using Engine Vibration

Nagesh Dewangan, Dr. Amiya Ranjan Mohanty

*Department of Mechanical Engineering,
Indian Institute of Technology Kharagpur, Kharagpur, India*

Abstract

Industry 4.0 is a unifying word for numerous ideas and innovations, including cloud computing, artificial intelligence, smart factories, cyber-physical systems, and the internet of things. All industries are transitioning to a more digital and networked world with its implementation. The coal mining industry, which must address upcoming productivity and operation monitoring challenges, finds it extremely relevant. So, industry 4.0 is executed in coal mines and mining dump truck operations are estimated by incorporating various sources of information and investigation. In this paper, a new approach for determining dump truck operations remotely is presented. The proposed method is based on acquiring and storing vibration at the engine block while simultaneously performing mining operations and transferring them to cloud storage. By remotely accessing these acquired signals, time domain features and frequency spectrum are calculated. The calculated values are filtered using Kalman filter to remove noise terms and get a smooth curve. Thus, smoothed curves provide a visualization of truck operations: motion and idling when related to time-stamps of operation. Further, truck operations are evaluated by tracking levels and duration of stagnant values using statistical features and frequency domain analysis of engine vibration signal. The approach is demonstrated by performing remote data acquisition from actual mining operations and analysing, which describes vibration observed on the engine block as truck operation and time interval for idling are determined for estimating the fuel consumption.

Keywords: *Mining industry, dump truck operation, engine block vibration, cloud storage, time domain features, Kalman filter, frequency domain analysis.*

1. Introduction

Industries have been emerging over a period of time. Several sectors are creating intelligent industrial units that require less human interaction from raw materials to finished products. This is made feasible by sophisticated computers, networked devices, and information that is shared globally [1]. This principle combined together is the core of industry 4.0. The production mode of every enterprise is shifting from digital to intelligent due to the fast growth of electric and electronic technology, and information technology [2]. Manufacturing, service-based, and product-based industries are using a combination of these technologies to increase their production. It is not about increasing productivity but increasing productivity, profitability, flexibility, safety, and ecology as shown in Figure 1 [3]. Industry 4.0 is the widespread adoption of industry best practices across an organization's activities, assisted by IT systems to promote rapid decision-making for increased productivity and quality. A component of the worldwide shifts in the production sector's paradigm development towards Industrial 4.0 is digital and smart factory 4.0. With the help of production processes and technological advancements, the industry has advanced significantly.

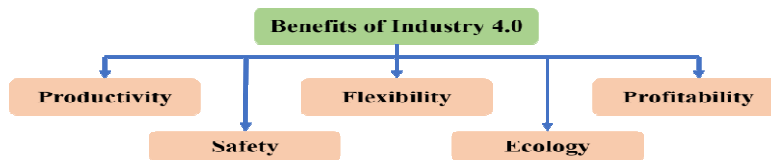


Figure 1: Benefits of Industry 4.0

One of the important industries is mining. Mining industry is among the top drivers of socioeconomic and human growth. For its operations to be optimal and successful, a mining business requires immediate insight into its production, quality, cycle times, machine status, and other key operational factors [4]. However, mining dump truck, which is one of the most important part of coal mines for production, are very costly equipment in crores and operating these heavy machines are also very costly. Therefore, it is very crucial to monitor dump truck operation. The need of fuel, whose consumption has a substantial impact on the cost of mining operations and accounts for 30.26 percent of total costs, is one of the key elements in mining operation activities [5]. On one hand, Consumption of fuel is highly affected by condition of truck, road condition and operator behaviour. But on the other hand, truck operation can also affect fuel consumption. A mining truck has to perform a lot of operations while in mines as shown in Figure 2. For that it has to do movement on mine road and then wait in queue to its turn for loading. And some of the time its keep waiting or standing while engine kept running, which consume a lot of fuel.



Figure 2: Mining dump truck operations

Moreover, a dump truck consumes a lot of fuel for operating which depends upon the type of truck used and payload in mines [6]. But for off-highway truck, which is used in Sonapur Bazari mines of CIL, consumes approximately 36-96.5 litres/hour. And amount of fuel consumption increases as previously discussion scenarios. Thus, monitoring of dump truck operation could help in reducing consumption of fuel. Additionally, there has been more focus toward condition monitoring of mining machines using condition-based monitoring (CBM) [7] [8]. Vibration monitoring is a kind of CBM approach where vibration data from vibrating portions of machines is collected using measuring equipment i.e., accelerometers mounted on them [9].

Accelerometers mounted on the engine block of mining dump truck allow for kind of information about the vehicles' remote monitoring to be gathered via vibration monitoring. This technique has been used on several mining machines whereas time-domain analysis has been used for feature calculation [10] [8]. Root mean square (RMS), is pre-dominantly used as time domain feature in previous research works for condition monitoring [11]. But RMS value from vibration has not been used for remote monitoring.

Vibration from engine block of dump truck varies while in motion and idling with engine running and both are very different with respect to RMS value, standard deviation (SD) and

variance. From comparing rms value, sd and variance provide dump truck operation. Thus, utilization of vibration on engine block will provide a remote monitoring of dump truck operation. Moreover, by tracking engine firing frequency in frequency domain analysis with different road conditions helps in identifying dump truck operation.

2. Mining Dump Truck

A mining dump truck, also known as a dumper, is used to transport demolition waste, sand, gravel, and other construction materials in addition to coal. Mining dump trucks often have open-box beds, which are hinged at the rear and have hydraulic rams to lift the front. This function enables material in the bed to be deposited to the ground at the dumping site behind the vehicle. The weight capacity of trucks ranges between 50,000 kg to 500,000 kg. A truck with a 94000 kg payload off-highway is chosen for the experiment. It is 746 kW engine power combining a seven-speed automatic transmission system. In this configuration, the truck's top speed is around 65 kph. Further, truck parameters are included in the table below. Mining dump truck selected for experiment is shown below in figure 1 and specifications are given in table 1.



Figure 3: Mining dump truck

Table 1: Mining dump truck Specifications

Gross machine operating weight	164000 kg
Payload	94000 kg
Engine Power	Diesel
Gross Power	746 kW
Transmission	7 Forward - 1 Reverse
Engine Configuration	V-8, 4-Stroke-Cycle Diesel
Rated Speed	1800 rpm

Fuel consumption in this model of dump truck varies for different load duties, i.e. 36-53 litres/hour for low duty, 53-73.8 litres/hour for medium duty, and 73.8-96.5 litres/hour for high duty [5]. So, dump truck consumes fuel according to operating mode such as idling or motion.

3. Experimental Method

3.1. Accelerometer Positioning

Vibration monitoring is performed on the mining dump truck using vibration sensor mounted on truck at engine block. Mounting is done such that it must not leave out its place while truck is in motion. For this purpose, a mounting of accelerometer has to be with studs. Using the stud mounting, accelerometer is mounted on engine block in horizontal truck motion direction. Sensor location in truck is shown in Figure 4.

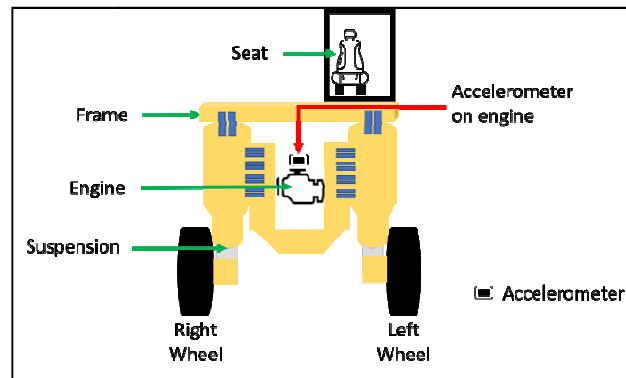


Figure 4: Schematic diagram for accelerometer position on dump truck

3.2. Data acquisition process

After installing accelerometer on the dump truck's engine block, the sensor is connected by BNC to the data acquisition module's chassis. Later, a mini-PC connected via a USB port that powers this chassis. Even when all connections have been made properly, the mini-PC still need an AC power source. The dump truck itself, which includes a battery power source, satisfies the need for electricity. Using inverter, this battery power source is transformed to AC. Now, Lab VIEW-developed data acquisition software is deployed in mini-PC to collect vibration data from a moving dump truck and store it on local storage of mini-PC, and then data are transferred to cloud storage using Wi-Fi network modem. Figure 5 depicts the data collecting method and system developed.

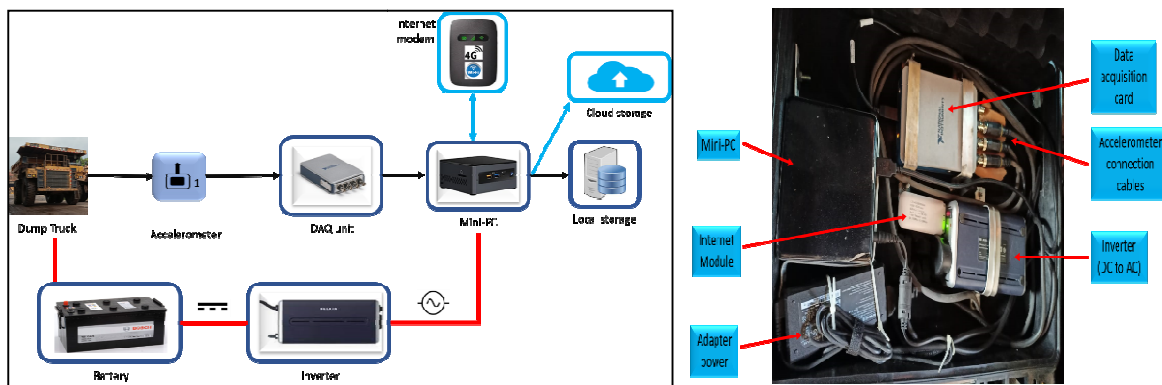


Figure 5: (a) Experimental setup for data acquisition, (b) Data acquisition system

3.3. Mining Site

Dump truck was operated as usual and performed its tasks. Truck was driven from Sonepur Bazari workshop to mine site on all shift of a day which needed 40 minutes of time for moving from workshop to site and performing its intended task of loading, haulage and dumping. And truck, which has to be remotely monitored, had been operated on same mine road for long period of time. In the path of mine road, there was down slopes, elevations and different grade of road roughness conditions that lies in low frequency region of 30 Hz [12], [13]. So, vibration data was recorded while movement of truck in mine sites.



Figure 6: Sonepur Bazari mines: experimental site

3.4. Signal Processing

Vibration data in the cloud is extracted then processed to get rms values set of data using moving window method. After finding rms values which is very noisy so Kalman filter is used to remove that noisy part and a smooth curve is obtained. Then this curve is studied to get the operation of dump truck. After that statistical evaluation such as standard deviation (sd), variance and mean of smooth curve are calculated. Here, rms has been calculated from eqn. (1) and mean, sd and variance of curve are calculated using eqs (2-3).

$$x_{rms} = \sqrt{\frac{1}{N} \sum_{i=1}^N x_i^2} \quad (1)$$

$$\bar{x} = \frac{1}{N} \sum_{i=1}^N |x_i| \quad (2)$$

$$\sigma = \sqrt{\frac{1}{N} \sum_{i=1}^N (x_i - \bar{x})^2} \quad (3)$$

$$\sigma^2 = \frac{1}{N} \sum_{i=1}^N (x_i - \bar{x})^2 \quad (4)$$

3.5. Kalman filter

As the measured signal is impacted by many types of noise, the Kalman filter is used here to smooth out the signal and remove noise. The state-space model of a dynamic system is often connected to the Kalman filter. In this investigation, the recorded vibration signal is originally represented as discrete 1D rms values. The state equations are as follows [14].

$$x_k = Fx_{k-1} + Bu_{k-1} + w_{k-1} \quad (5)$$

The state and measurement relationships at time step k are described by the process model and measurement model as follows:

$$z_k = Hx_k + v_k \quad (6)$$

Where, F is the state transition matrix, B is control-input matrix, H is measurement matrix, w is process noise that is $w_{k-1} \sim N(0, Q)$, v is measurement noise that is $v_k \sim N(0, R)$.

The two steps of the Kalman filter algorithm are prediction and update. The Kalman filter algorithms are as follows in eqns 7:

Prediction:

Predicted state estimate

$$\hat{x}_k^- = F\hat{x}_{k-1}^+ + Bu_{k-1}$$

Predicted error covariance

$$P_k^- = FP_{k-1}^+ F^T + Q$$

Update:

Measurement residual $\tilde{y}_k^- = z_k - H\hat{x}_k^-$

Kalman gain $K_k = P_k^- H^T (R + H P_k^- H^T)^{-1}$ (7)

Updated state estimate $\hat{x}_k^+ = \hat{x}_k^- + K_k \tilde{y}_k^-$

Updated error covariance $P_k^+ = (P_k^- - K_k H) P_k^-$

Where, \hat{x} is estimate of x , \tilde{y} is measurement residual, K is Kalman gain, P is covariance. The hat operator, $\hat{\cdot}$, in the eqns above denotes a variable estimate. In other words, \hat{x} is estimate of x . Prior and posterior estimations are indicated by the superscripts - and +. The parameters selected for the scenario in this study are given below. \hat{x} is final output from and z is input to Kalman filter.

$$F = \begin{bmatrix} 1. & 1. \\ 0. & 1. \end{bmatrix}, H = \begin{bmatrix} 1. & 10 \end{bmatrix}, P = 10000, Q = 1, R = 1, x(0) = z(0).$$

3.6. Frequency analysis

According to the Fourier theorem, a signal is made up of many sinusoidal signals. The frequency spectrum analysis of the signal is the process of analysing the amplitude, frequency, and phase of these sinusoidal signals. The signal is filtered, converted to digital form, and then Fourier transformed to the frequency domain to retrieve these properties. Here, a dump truck vibration signal is transformed to a frequency domain signal.

In the studied system, four stroke V8-diesel engine is used in dump truck. The crankshaft contains eight independent journals arranged in such a way as to produce a firing order with combustion events. Engine firing frequency (EFF) can be calculated from the engine speed (rpm), by dividing the rpm by 60 since there is 60 rpm = 1 revolution per second, or 1 Hz. Thus, the firing frequency changes proportionally as the engine speed changes and is detected in frequency spectrum. Formula for EFF is given in eqn (5).

$$EFF = \frac{RPM}{60} \times \frac{EC}{2} \quad (8)$$

Where, EFF=Engine firing frequency (Hz)

RPM=Rotational speed of engine

EC= No. of cylinders

4. Result and Discussion

4.1. Vibration data from truck

Recorded vibration from truck is completely random in nature. Raw vibration data is passed through high pass filter to remove effect of road. Raw vibration data acquired from engine of truck is shown below in Figure 6. From raw vibration rms is calculated. RMS values and Kalman filtered curve, using above discussed parameters in sect. 3.5, for one time of movement is shown in Figure 7.

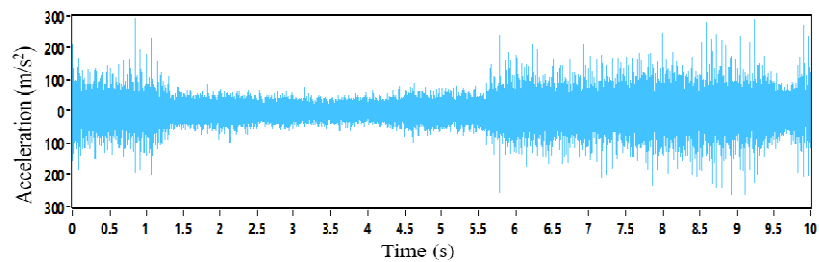


Figure 7: Raw vibration signal from engine block of dump truck

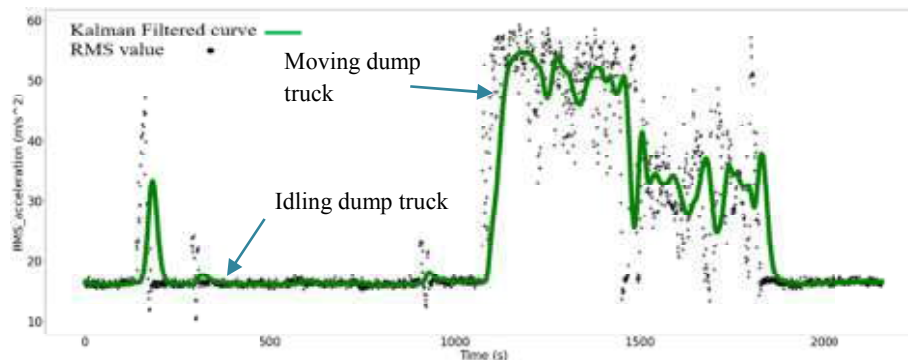


Figure 8: RMS value calculated from vibration data and Kalman filtered curve

4.2. Statistical evaluation for operation identification

Mean, sd and variance values are found from calculated rms values of vibration data for idling and moving truck. It is found that sd and variance are very less for idling dump truck compare to moving truck. In percentage difference, sd changes by 93.52 - 96.33 % and variance changes by 99.66 - 99.86 %. And also mean is coming out to be more by 26.4 - 67.33 % for moving truck. So, it is estimated that idling condition has lesser statistical values than moving operation. Statistical evaluation for operation identification is shown in Table 2.

Table 2: Feature calculation and comparison

	Mean	Standard deviation	Variance
Idling while engine running	15.6 - 15.81	0.33 - 0.50	0.11 - 0.25
Movement	21.2 - 47.75	5.76 - 9.01	33.20 - 81.25
%age difference	26.4 - 67.33	93.52 - 96.33	99.66 - 99.86

4.3. Frequency spectrum evaluation for operation identification

Vibration signal from dump truck is studied using Fourier transform and changed to frequency domain to get frequency spectrum during idling and moving conditions. It is found that engine rotational speed during idling condition is 700 RPM which comes out to be 46.67 Hz firing frequency of engine. While the same 46.67 Hz is not found in case of moving condition due to engine rotation at higher RPMs. Moreover, higher dB amplitude is found in low frequency region of 10 Hz in moving condition because of road roughness which is missing for idling condition. So, frequency spectrum clearly helps in operation identification as shown in figure 9.

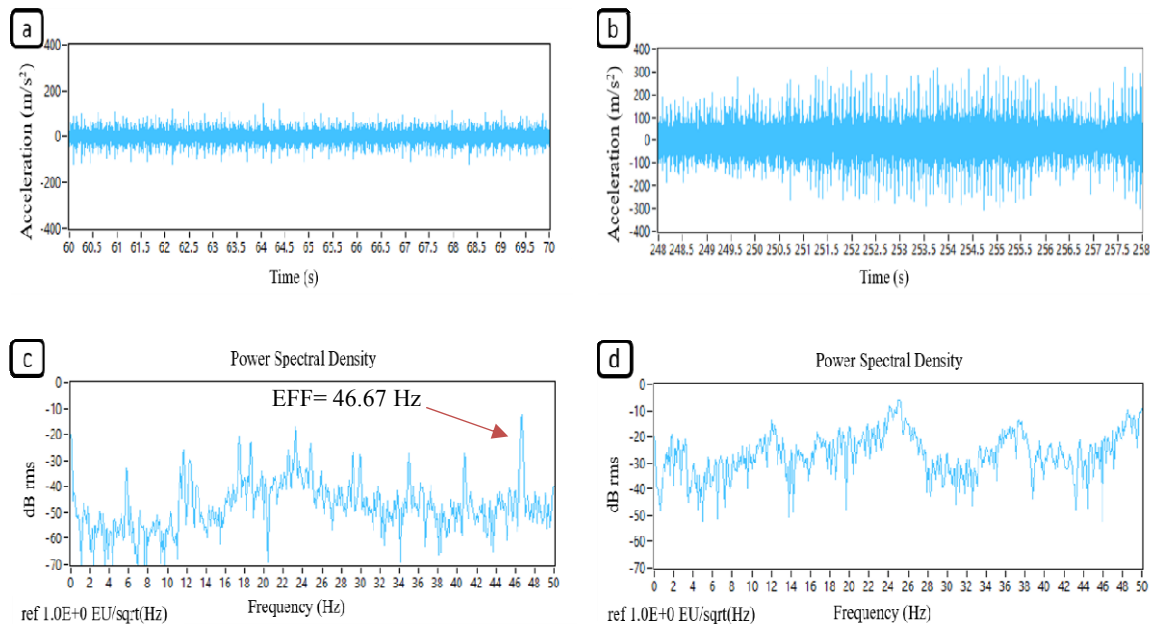


Figure 9: Truck vibration (a) Idling, (b) Moving; Power spectral density (c) Idling, (d) Moving

4.4. Fuel consumption

After identification of truck operation using vibration data, fuel consumed in time of idling are determined. As mention above, 36 litres/hours of fuel is consumed for low duty. Therefore, for single day of monitoring operation of 35 minutes as shown in Figure 8, dump truck was idling for 24 minutes and moved only for 11 minutes. So, idling while idling engine consume 14.4 litres of fuel whereas total monitoring time consumed 21 litres only. It is very clear that 69 % of fuel is consumed while truck is idling. Thus, it is very much required to reduce fuel consumption in dump truck and use this amount of fuel for production. Fuel consumption is shown in figure 10.

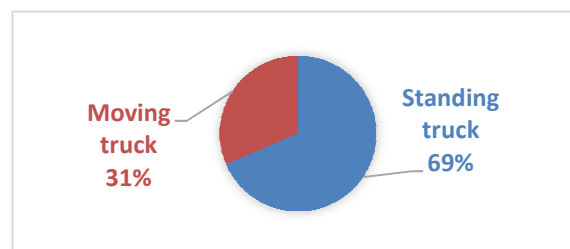


Figure 10: Fuel consumption in dump truck

5. Conclusions

This paper deal with monitoring mining dump truck operation remotely utilising system developed. Vibration data from dump truck have been acquired and processed using time-domain features, frequency domain analysis and Kalman filter. Statistical evaluation of processed data reveal operation of dump truck as idling or moving. Moreover, these operations are further clarified using frequency domain analysis of engine vibration. After identifying operations of dump truck, their fuel consumption for single day usage has been shown which reveal that two third portion of the fuel is consumed for idling of dump truck and only one third portion is used for moving operation. Thus, dump truck has been remotely monitored using engine block vibration and this need further investigation for efficiently reducing fuel consumption, reducing operational cost and increasing production.

Acknowledgments

The research work presented in this paper is supported under the REO project grant by ECL Asansol (Eastern Coalfield Limited), CMPDI Ranchi (Central Mine Planning and Design Institute) and CIMFR Dhanbad (Central Institute of Mining and Fuel Research). The authors are grateful to CIMFR Dhanbad for providing prompt assistance in field data collection and ECL Asansol for providing all necessary facilities to conduct the research work.

References

- [1] R. J. Franklin and Mohana, "Industry 4.0: Real time embedded system with integrated data acquisition," *Proc. 3rd Int. Conf. Smart Syst. Inven. Technol. ICSSIT 2020*, no. Icssit, pp. 637–642, 2020, doi: 10.1109/ICSSIT48917.2020.9214251.
- [2] B. Chen, J. Wan, L. Shu, P. Li, M. Mukherjee, and B. Yin, "Smart Factory of Industry 4.0: Key Technologies, Application Case, and Challenges," *IEEE Access*, vol. 6, pp. 6505–6519, 2017, doi: 10.1109/ACCESS.2017.2783682.
- [3] K. Umachandran, I. Jurcic, and D. Ferdinand-james, "Gearing up education towards Industry 4.0," *Int. J. Comput. Technol.*, vol. 17, no. 2, pp. 7305–7312, 2018, doi: 10.24297/ijct.v%vi%i.7754.
- [4] A. Telukdarie and M. Sishi, "Implementation of Industry 4.0 technologies in the mining industry - a case study," *Int. J. Min. Miner. Eng.*, vol. 11, no. 1, pp. 1–22, 2020, doi: 10.1504/ijmme.2020.10027477.
- [5] Bella Puspa Octaviana, Supriyadi, and A. Hartono, "Analysis of Fairness Limit on Fuel Oil Consumption of TwoTail Test Based Excavator and Dump Truck A Case Study in PT XYZ," *J. Innov. Technol.*, vol. 1, no. 1, pp. 6–12, 2020, doi: 10.31629/jit.v1i1.2128.
- [6] V. Kecojevic and D. Komljenovic, "Haul truck fuel consumption and CO2 emission under various engine load conditions," *Min. Eng.*, no. December, pp. 44–48, 2010, [Online]. Available: https://www.researchgate.net/publication/261214668_Haul_truck_fuel_consumption_and_CO2_emission_under_various_engine_load_conditions
- [7] N. Dewangan, A. K. Agrawal, M. A. H. Siddiqui, and S. Chattopadhyaya, "Degradation analysis of gear oil SAE 90 used in load haul dumper machine," *IOP Conf. Ser. Mater. Sci. Eng.*, vol. 624, no. 1, 2019, doi: 10.1088/1757-899X/624/1/012011.
- [8] K. Elisabeth, L. John, H. Lars, K. Magnus, and L. Jing, "Vibration-based condition monitoring of heavy duty machine driveline parts: Torque converter, gearbox, axles and bearings," *Int. J. Progn. Heal. Manag.*, vol. 10, no. 2, 2019.
- [9] A. R. Mohanty, *Machinery Monitoring Condition Principles and Practices*. CRC Press, 2014.

- [10] E. Jakobsson, E. Frisk, R. Pettersson, and M. Krysanter, "Data driven modeling and estimation of accumulated damage in mining vehicles using on-board sensors," *Proc. Annu. Conf. Progn. Heal. Manag. Soc. PHM*, pp. 98–107, 2017.
- [11] P. Aqueveque, L. Radrigan, F. Pastene, A. S. Morales, and E. Guerra, "Data-Driven Condition Monitoring of Mining Mobile Machinery in Non-Stationary Operations Using Wireless Accelerometer Sensor Modules," *IEEE Access*, vol. 9, no. Cm, pp. 17365–17381, 2021, doi: 10.1109/ACCESS.2021.3051583.
- [12] S. Madhusudhana, "Road profile estimation and classification," 2019.
- [13] H. M. Ngwangwa, P. S. Heyns, F. J. J. Labuschagne, and G. K. Kululanga, "Reconstruction of road defects and road roughness classification using vehicle responses with artificial neural networks simulation," *Journal of Terramechanics*, vol. 47, no. 2, pp. 97–111, 2010. doi: 10.1016/j.jterra.2009.08.007.
- [14] Y. Kim and H. Bang, "Introduction to Kalman Filter and Its Applications," *Introd. Implementations Kalman Filter*, pp. 1–19, 2019, doi: 10.5772/intechopen.80600.

Root Cause of High Vibration in a Vertical Circulating Water Pump and its Remedial Suggestion

**Biplab Swarnakar, Sourav Kansabanik, Swarup Kumar Laha
& Kamalkishor Uke**

CSIR-Central Mechanical Engineering Research Institute, Durgapur-713209

Abstract

Circulating Water (CW) pumps are the backbone of any water package system of a power plant. The power output of a plant may need to be de-rated if these pumps aren't operating efficiently. Various types of faults may cause the failure of CW pumps. The faults may be mechanical, electrical, structural or hydraulic. The natural frequency of a pump structure mainly depends on the mass and the effective stiffness of the pump structure. As the mass is almost fixed for a particular structure therefore the variation of the connections between the concrete, base plates, pump base and motor flange may change the effective stiffness. The change in stiffness may also change the natural frequency. If the operating speed of the pump is coincide with any of the natural frequencies of the system a condition of resonance has occurred. In this paper how resonance is contributing a major role to cause high vibration of a CW pump in a power plant is explained. A 3D model of the above pump structure was made and various modes were calculated. The results of these tests are used to identify the root cause of the problem and recommendations are made to resolve the same accordingly.

Keywords: *circulating water pump, vibration, natural frequency, resonance, stiffness.*

Introduction:

The central component of the water package system in a thermal power station is a vertical circulating water pump. A heavy motor is positioned above the pump in the vertical configuration. This heavy motor results the pump-motor configuration heavy on top which makes the system vibration prone (Karassik et al. [1]). In CW pump, the water is sucked through the strainer and suction bell mouth to the impeller from the cooling water sump. The Impeller forces the water to the condenser through the discharge elbow and discharge pipe. Nag [2] described that the water supplied by the CW pump is used in a condenser to cool the exhaust "steam" of the LP Turbine and create "condensate".

In this type of CW pump two concrete floors were used to support the pump. The discharge elbow mounted on the intermediate circular foundation ring. The ring anchored with intermediate floor by means of foundation bolts. Motor foundation ring used to support the motor stool and motor on operating floor. Motor stool bottom flange was anchored to the floor by foundation bolt through motor foundation ring. A distance piece top flange connected with the motor foundation ring by fasteners. Therefore the proper connectivity between the connecting flanges is very crucial for overall stiffness of the structure.

Rao [3] described the methodology of vibration measurement used in vibration analysis. An accelerometer is used to get a quality signal from a measurement point. The analog input is then transformed into a digital signal using an analog to digital converter. The measured time domain signal is then stored in a database and analyzed by various

signature analysis techniques. Spectrum analysis is used to ascertain the source of high vibrations by analyzing the frequency and amplitude. Fast Fourier Transform (FFT) is used to convert the signal from time to frequency domain.

Thompson [4] explained that mass and stiffness are the two controlling parameters for natural frequency of any dynamic system. To identify a vertical turbine pump's dynamic properties, such as its natural frequencies and associated mode shapes, Kumatkar et al [5] performed a modal analysis on the device. They conducted theoretical, numerical, and experimental analyses of the VT Pump rotor component. Corley et al. [6] predicted the resonant frequencies of a 3000 HP vertical pump which is close to the operating speeds. The research experimentally and analytically demonstrates the vibration modes. De souza [7] used operating deflection shape (ODS) by measuring the vibration amplitude and phase at pre-determined locations of a machine and structure to study the dynamic characteristics. Sinha et al. [8] performed a modal analysis on the entire assembly of pumps and piping arrangement and according to them, resonance was found to be one of the main factors contributing to pump failure. DeMatteo et al. [9] applied Modal techniques on a vertical pump to comprehend the sources of vibration. Smith et al. [10] conducted some experimental tests to shift the natural frequency of a vertical pump away from its running frequency and its merits and demerits. They applied stiffeners to increase and neoprene isolator pads as a soft base to reduce the natural frequency respectively. Tompkins et al. [11] calculated a pump / motor structure's natural frequency by using finite element analysis software, and then possible modifications are modeled to see how these might affect the presence of harmful resonance. El-Gazzar [12] described why a pump vibrated so much after replacing its original motor with one of a different design and weight. He used Finite Element Analysis (FEA) to model the motor structure and discovered that the third natural frequency of the system coincides with the working speed of the pump, resulting in resonance. His suggested structural modification methodology significantly reduces the pump vibration. Aladesaye et al. [13] applied a combination of four methods to determine the underlying cause of a pump with frequent bearing failures. They used vibration analysis, motion amplification camera, FEA and mathematical modeling to find out the root cause of the problem. They used FEA to determine the natural frequencies and mode shapes of the pipe support structure. To combat the resonance problems, previous square-section supports were replaced by a new set of I-section supports with greater stiffness.

In this paper, the root cause for the high vibration of a vertical CW pump was investigated by analyzing the vibration spectrum, impact response function, and theoretical Finite Element Analysis. Structural modification is also proposed by increasing the stiffness of the machine stool support structure in various combinations to increase the margin between natural frequency and operating frequency.

Methodology:

The CW pump of a power plant as shown in figure 1 had suffered a frequent motor bearing failure with high vibration. Each bearing failure required motor decoupling, motor removal from the top of the pump to the ground, replacement of bearings, and the motor to be reinstalled again and realignment before operation. This increases downtime and the non-availability of the pump. Therefore root cause analysis of high vibration is required for the smooth operation of the pump motor system.

The CW pump was running at 500 rpm (8.34Hz). Vibration data was collected from the pump at Motor Non Drive End (MNDE) and Motor Drive End (MDE) bearing points using a portable vibration analyzer and accelerometer with sensitivity of 100 mv/g. The sampling frequency of 8192 Hz was used to collect the vibration data at rated rpm. The overall vibration was then recorded and compared with relevant ISO standards to assess the condition of the pump. The overall vibration is shown in table 1. Spectrum analysis was carried out to identify the fault frequency and amplitude was used to identify the severity of the problem. A sampled spectrum of MNDE bearing is also shown in figure 2. A bump test is also carried out on the motor top perpendicular to the flow and parallel to the flow direction.

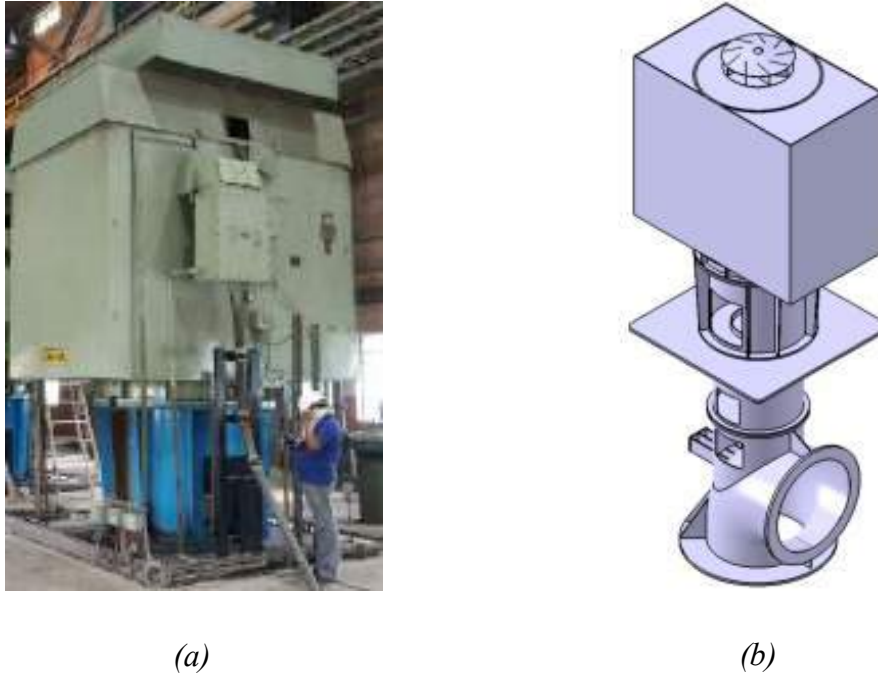


Figure 1. (a) actual CW Pump and (b) 3D CAD model

Table 1

5.1. Overall Radial Direction Vibration Levels at Motor Bearings of CW Pump in Coupled Condition (Speed = 500 rpm)

Measurement position	Displacement (pk-pk) in μm	Velocity (rms) in mm/sec
Motor NDE Perpendicular to flow direction	360~461	8.1~9.7
Motor NDE Parallel to flow direction	132~180	2.6~3.4
Motor DE Perpendicular to flow direction	186~242	3.6~4.3
Motor DE Parallel to flow direction	76~94	1.3~1.6

Results and discussion:

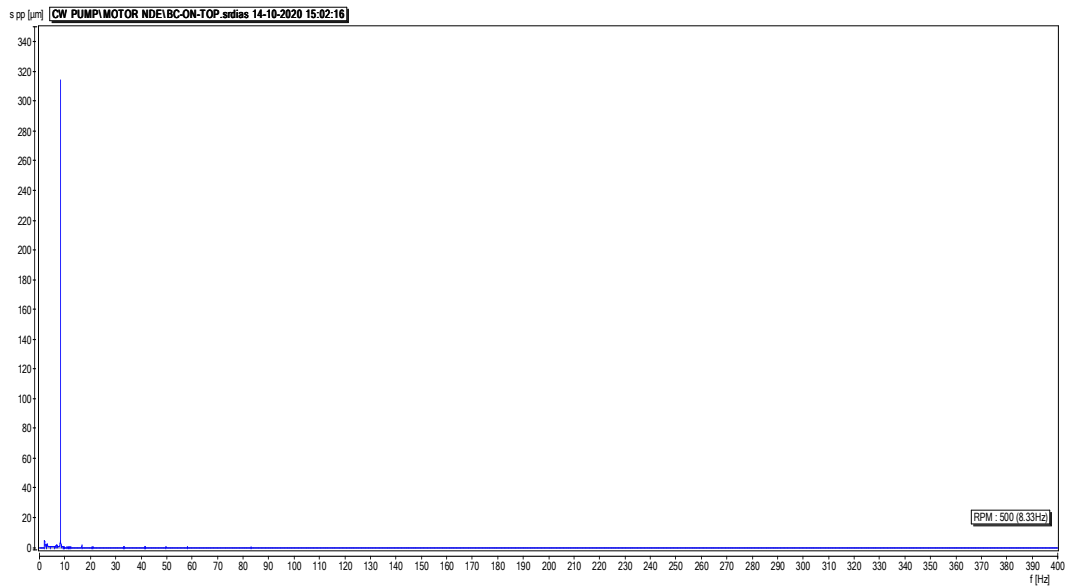


Figure 2. Frequency Spectrum of Pump

The spectrum analysis reveals the cause of high vibration is dominating 1X rpm peak. High directional vibration was observed in perpendicular direction as compare to the parallel direction of the flow at MNDE bearing. This directional vibration may be the first indication of resonance. Therefore to ascertain the natural frequency of the pump structure with the motor above the base, an impact test was carried out. Time waveform impulse response and impact test spectrums are shown in figure 3 and figure 4 respectively.

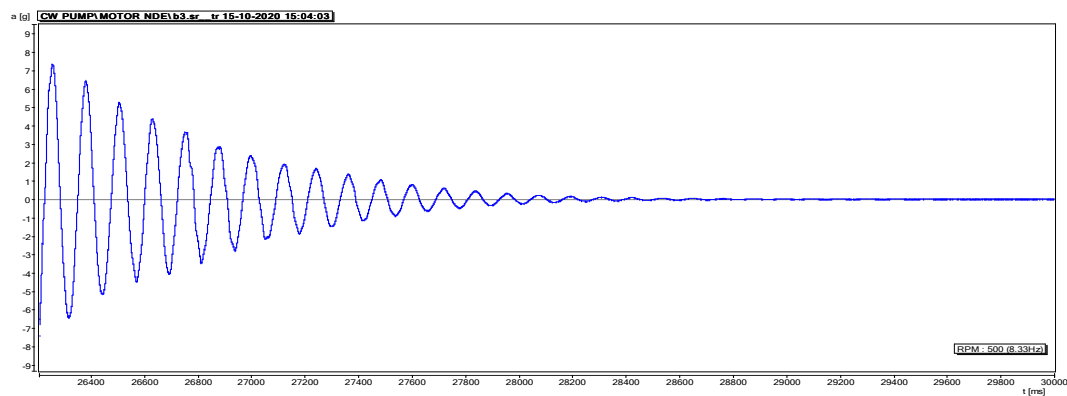


Figure 3. Impulse response of Pump structure

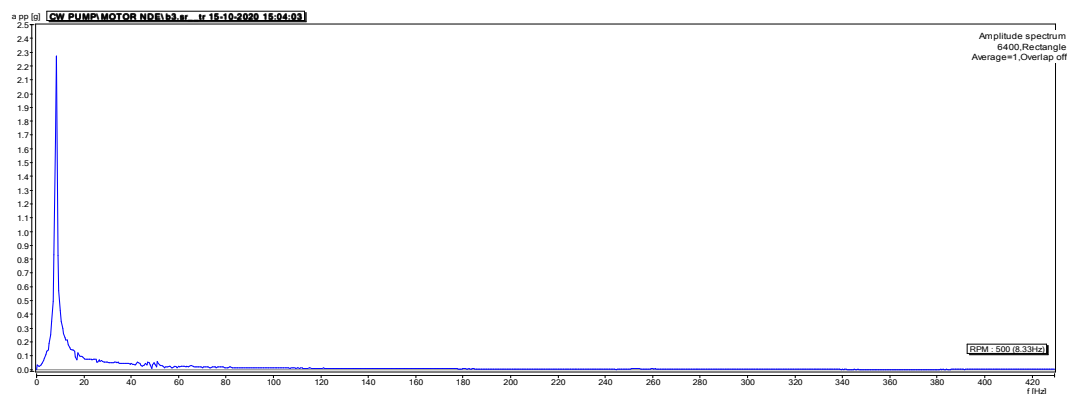


Figure 4. Impact test spectrum of pump structure

Based on the drawings of different parts of the pump-motor system, a CAD model of the pump structure above the operating floor was prepared using CATIA software. Finite Element (FE) modal analysis of the existing system was performed using CATIA generative structural analysis workbench in order to determine the natural frequencies and mode shapes of vibration. From the theoretical modal analysis it was found that the first mode is very close to the 1X rpm. The first ten mode corresponding frequencies of the present configuration are shown in the figure 5.

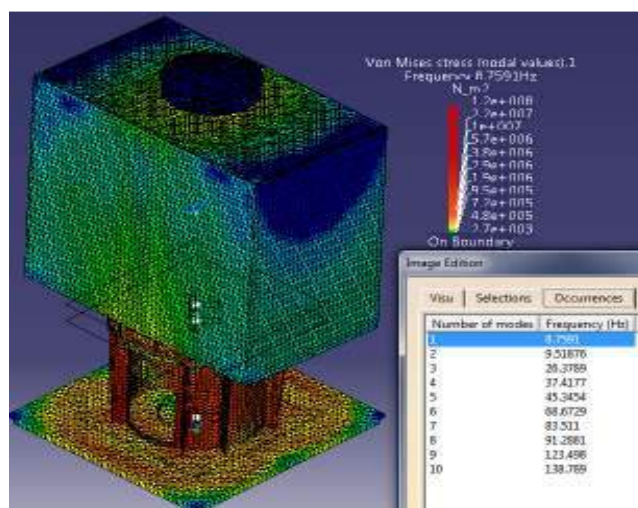


Figure 5. First ten modes and corresponding frequencies of CW pump structure with existing motor stool stiffener

The above FEA indicates the low stiffness portion of the structure. These low stiffness portion, mainly motor stool and motor stool joints has to be stiffened to increase the margin between natural frequency and operating frequency. Accordingly, various combination of motor stool stiffener was theoretically modeled and analyzed with the existing motor stool bottom flange. Initially, additional two stiffeners were fixed with the existing stool but the targeted improvement has not been achieved. The result is shown in figure 6. Therefore the motor stool was rotated 90° in the theoretical model such that the stool window portions are in the parallel direction to flow. No such improvement was observed. The result is shown in figure 7.

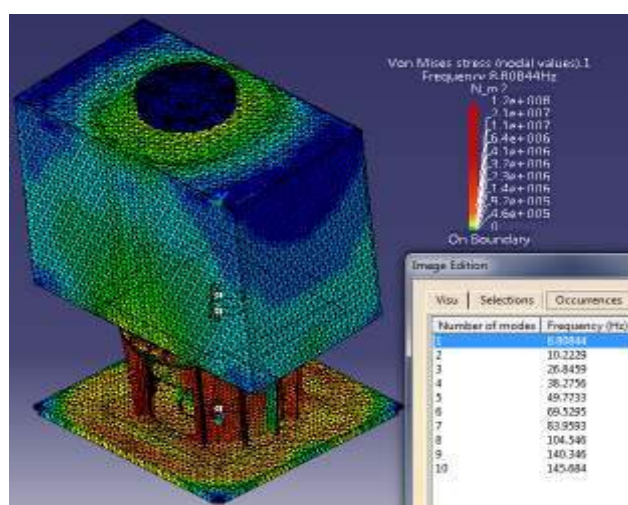


Figure 6. First ten modes and corresponding frequencies of CW pump structure with additional motor stool stiffener

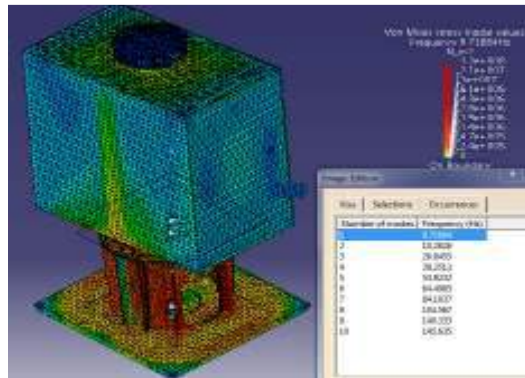


Figure 7. First ten modes and corresponding frequencies of CW pump structure after 90° rotation of the motor stool

Finally, motor stool bottom flange outside diameter was increased to 2100 mm from existing 1840 mm and accordingly the stiffeners width also modified from 145mm to 275 mm in the model as shown in figure 8.

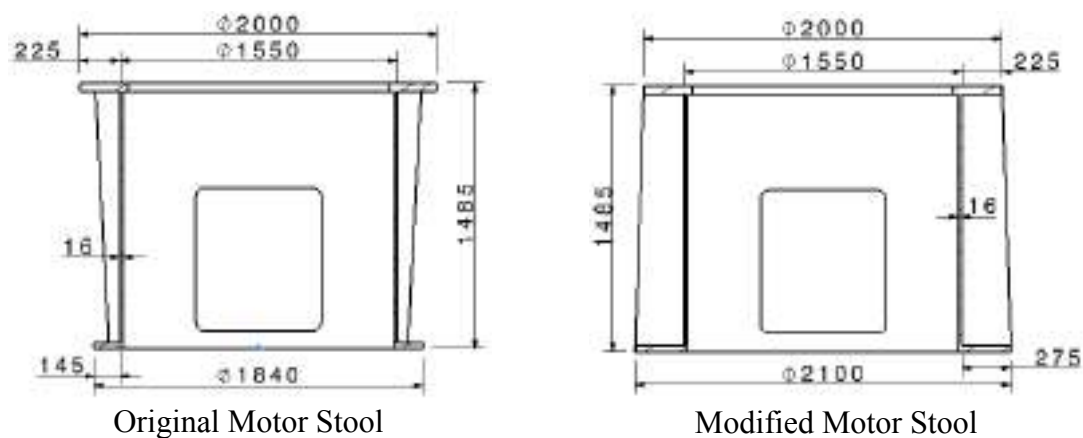


Figure 8. Existing and modified motor stool stiffener dimension

The isometric view of the motor stool (existing and modified) is shown in figure 9. Modal analysis of the pump assembly with modified stiffener and bottom flange has been carried out theoretically. The first ten modes of CW pump structure with modified stiffener are shown in figure 10.

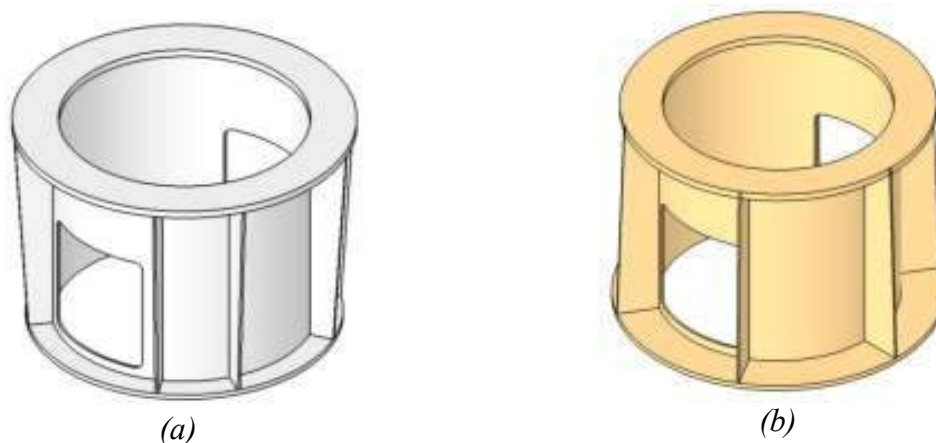


Figure 9. Isometric view of existing (a) and modified (b) motor stool with stiffener

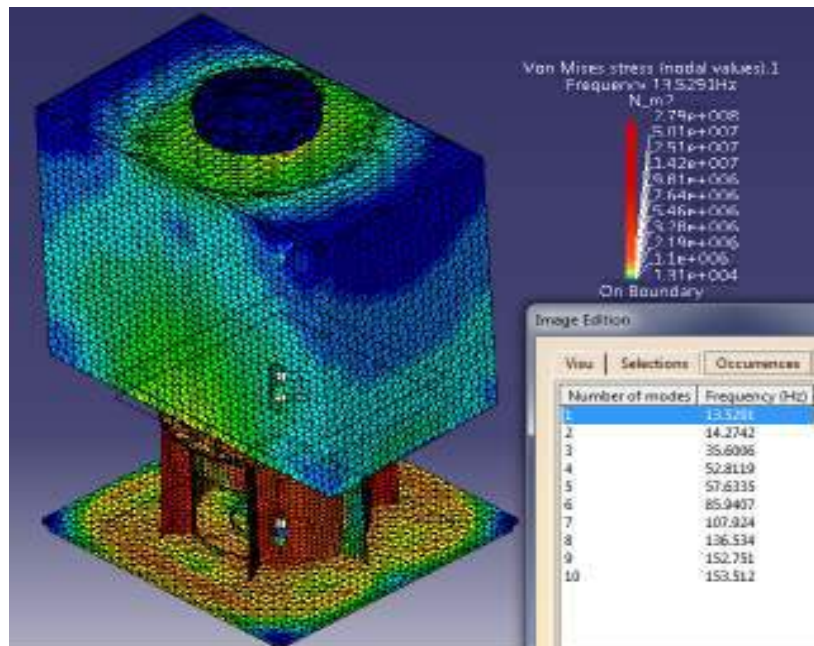


Figure 10. First ten modes and corresponding frequencies of CW pump structure with modified motor stool bottom flange and stiffener

A comparative frequency result for first six modes and corresponding separation margin after the proposed modification is shown in the table 2.

Table 2

5.2. First six modes of CW pump structure before and after proposed motor stool stiffener modification and corresponding separation margin:

Mode	Running Frequency and their harmonics in Hz	Before modification		After modification	
		Existing Frequency (Hz)	Separation margin in %	Modified Frequency (Hz)	Separation margin in %
1	8.34	8.759	5.0	13.529	61.0
2	16.68	9.518	-42.9	14.274	-14.4
3	25.02	26.378	5.4	35.600	42.2
4	33.36	37.417	12.1	52.811	58.3
5	41.70	45.345	8.7	57.633	38.2
6	50.04	68.672	37.2	85.940	71.7

Conclusion:

In this paper, the vibration spectrum, impact response function, and theoretical FE Analysis were used to examine the root cause of a vertical CW pump's high directional vibration and frequent motor bearing failure. From the table 2, it was concluded that the margin of separation between the running frequency and 1st natural frequency of the system before modification was very close which may cause the resonance. At resonating condition the system will generate high vibration, which leads to bearing failure of the system.

In the proposed modification, we have increased the stiffness of the motor stool and theoretically found that the first three modes of natural frequencies are shifted away from the operating frequency by a margin of 61.0 %, 14.4% and 42.2% respectively which may solve the resonance, existing high vibration problem and frequent bearing failure.

References:

- [1] Karassik, I. J., Messina, J. P., Cooper, P., & Heald, C. C. (2008). *Pump handbook*. McGraw-Hill Education.
- [2] Nag, P. K. (2008). *Power plant engineering*. New Delhi, India: Tata McGraw-Hill.
- [3] Singiresu, S. R. (1995). *Mechanical Vibrations*. Boston, MA: Addison Wesley.
- [4] Thomson, W. T. (2018). *Theory of vibration with applications*. CrC Press.
- [5] Kumatkar, R., and Panchwadkar, A., 2015, "Modal analysis of rotor assembly of vertical turbine pump," *International Engineering Research Journal*(Special Issue2) pp. 325-333.
- [6] Corley, J. E., "Vibration Problems of Large Vertical Pumps and Motors," *Proceedings of the Ninth Turbo machinery Symposium*, Turbo machinery Laboratories, Department of Mechanical Engineering, Texas A&M University, College Station, Texas (1980).
- [7] De Souza, K. (2014, July). Analysis of the dynamic stiffness of a centrifugal pump by ODS. In *Proc. 21st International Congress on Sound and Vibration*.
- [8] Sinha, J. K., and Rao, A. R., 2006, "Vibration Based Diagnosis of a Centrifugal Pump," *Structural Health Monitoring*, 5(4), pp. 325-332.
- [9] T. DeMatteo, *Operational Deflection Shape and Modal Analysis Testing to Solve Resonance Problems*, Consultant Emerson Process Management/CSI Division, CSI RBM University, 2001.
- [10] Smith, D. R., & Woodward, G. M. (1986). *Vibration Analysis Of Vertical Pumps*. In *Proceedings of the 15th Turbo machinery Symposium*. Texas A&M University. Turbo machinery Laboratories.
- [11] Tompkins, M., Stakenborghs, R., & Kramer, G. (2016, June). Use of FEA software in evaluating pump vibration and potential remedial actions to abate resonance in industrial vertical pump/motor combinations. In *International Conference on Nuclear Engineering* (Vol. 50015, p. V001T01A011). American Society of Mechanical Engineers.
- [12] El-Gazzar, D. M. (2017). Finite element analysis for structural modification and control resonance of a vertical pump. *Alexandria Engineering Journal*, 56(4), 695-707.
- [13] Aladesaye, M., Aladesaye, P., Stepien, L., & Elverd, M. (2022, January). Improving the Reliability of a Critical Pump by Reducing Resonance Using Four Methodologies. In *2022 Annual Reliability and Maintainability Symposium (RAMS)* (pp. 1-7). IEEE.

Vibration and Acoustic Signal Monitoring of High-Speed Bearings for Electrical Vehicles

Ajiket Patil, Madhav Bavu, Gautam Susarla, and B. Venkatesham

*Department of Mechanical and Aerospace Engineering,
Indian Institute of Technology, Hyderabad, India.*

Abstract

The increased demand for electric and hybrid vehicles necessitates the development of high-power density and compact drive trains. As torque is reduced and operating speeds are increased, the power density of an electric vehicle increases. However, as the speed increases, the centrifugal loads on the bearings increase significantly. Vibrations and acoustic signals from bearings at high speeds are key indicators of bearing performance. As a result, it is critical to examine bearing behaviour at high speeds. A high-speed (up to 18000 rpm) bearing test rig with radial (up to 3 kN) and axial (up to 2 kN) load capabilities has been developed. As test bearings, grease-lubricated 6309 deep groove ball bearings (DGBB) are used. The test bearing's vibration and acoustic signatures are recorded up to 7000 rpm. For the acquired vibration and acoustic signals, statistical parameters are calculated. Pearson correlations are established for vibrations and acoustic statistical parameters, while vibration and acoustic measurements are also correlated.

Keywords: High Speed Bearing Noise, Deep Groove Ball Bearings; Statistical Parameters, Pearson Correlations.

Introduction

Vibration and acoustic signatures are critical indicators for machinery health and condition monitoring. Several researchers have used vibration measurements for fault detection in rotating machines [1] [2]. However acoustic measurements at high speeds remains a relatively unexplored area [3]. The early diagnosis of defects and increased pre-warning time are the major advantages of condition monitoring for dynamic elements [4]. Correlating acoustic signatures with vibrations offers advantages in predicting the health of the rotating elements.

Ball bearings are important mechanical transmission element because their quality and reliability directly affect the lifespan and functionality of machines. Ball bearings are important noise and vibration generators in high-speed applications, and their failure can cause extreme damage to other machine components, prolonged downtime, heavy repair costs, and the potential for fatality. Even if the geometry of a ball bearing is perfect, it will still produce vibrations caused by the rotation of a finite number of loaded rolling contacts between the balls and the races. Because these contacts are elastic and change with time, the bearing stiffness becomes explicitly dependent on time. A time-varying stiffness causes vibrations even in the absence of external loads. Variable stiffness causes parametric excitations, which are a major source of vibration in ball bearings. These vibrations are responsible for generating structure-borne noise in bearings.

Deep-groove ball bearings (DGBB) are used in the majority of electric vehicles because they can withstand both large radial loads and relatively high axial loads. In this article, the

authors describe the process of developing a high-speed ball bearing test rig setup in order to measure the vibration and acoustic characteristics. The test rig is capable of both radial and axial loading and was designed to reach a maximum speed of 18000 rpm. The purpose of this paper is to report the vibration and acoustic signatures of deep groove ball bearings when operating at high speeds. The mechanical limiting speeds of the 6309 DGBB is 9500 rpm, and thus operating speeds are limited up to 7000 rpm to not exceed the limiting bearing stresses. In addition, linear correlation coefficients using Pearson's method are calculated to determine the relationship between vibrations and acoustic statistical parameters.

Experimental Setup and Instrumentation

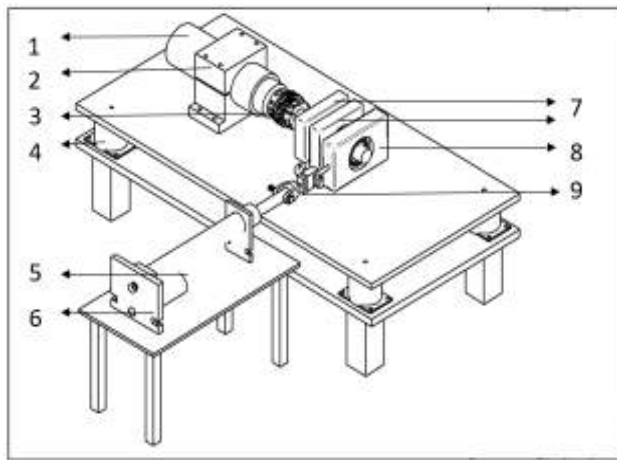


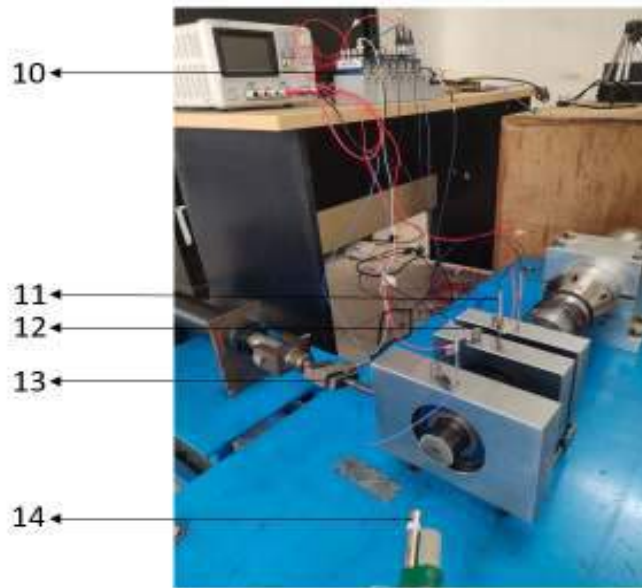
Figure 1: Schematic diagram of the High-speed Bearing test rig assembly

Figure 1 shows the schematic drawing of the high-speed bearing test rig assembly. The drive motor spindle and the two support bearings are fixed by bolting to the top plate of the vibration isolation table, whereas the test bearing is supported by roller supports in the vertical direction. As the test bearing block is located at the free end of the drive shaft, it is simple to replace the test bearing without disturbing the alignment of the support bearings and the drive shaft. The entire test rig setup is supported by a vibration isolation table. The maximum speed of the spindle is 18000 rpm and the vibrations transmitted are periodic in nature. The transmitted vibrations to the ground are reduced by adding suspension elements (helical springs) and damping elements (elastomer layers of neoprene) combined as vibration isolators. The isolators are selected with a fundamental natural frequency of 11 Hz and thus vibration isolation occurs at operating speeds of the drive spindle above 1000 rpm (16.67 Hz). Note that $f/f_n = 1.515 \geq 1.414$ is necessary and sufficient condition for vibration isolation and thus having transmissibility ratio less than one. Moreover, the vibration isolation table and the load actuator support table are fixed to the ground using concrete slurry.

The drive unit is a constant power high-speed spindle. It has a Power rating of 12 kW and is used for CNC engraving machines with a maximum spindle speed up to 18000 rpm. The spindle is cooled by circulating water around the spindle with a water chiller to prevent overheating of the windings of the high-speed spindle. The constant flow of water around

Sr no.	Nomenclature
1	CNC drive motor
2	Aluminium clamp
3	High-speed coupling
4	Vibration isolators
5	Linear actuator
6	Actuator support
7	Support Bearing blocks (2)
8	Test bearing block
9	Load cell, knuckle fork and loading assembly

the spindle takes away the excessive heat generated in the motor windings. Drive motor shaft and bearing shaft are connected with a high-speed flexible coupling. A stud-bolt threaded on both ends pulls the test bearing block thereby applying a radial load on the test bearing. The Knuckle fork is pulled with a linear electromechanical actuator (Dynamic Load capacity 5000 N, Stroke Length 300 mm), pulling the S - shaped load cell and the test bearing block. The back plate supporting the linear actuator is fixed by bolting it to the actuator table. The constrained motion of the actuator by the back plate applies a compressive radial load on the test bearing.



Sr no.	Nomenclature
10	NI DAQ
11	Thermocouples
12	Accelerometers
13	S - Shaped load cell
14	Microphone

Figure 2: High-speed Bearing noise and vibration test rig

Figure 2 shows the actual high-speed bearing test rig setup. A total of six sensors for measuring load, temperature, sound pressure level, vibrations, speed, and torque are used in the bearing test-rig to carry out respective measurements. The hardware used for data acquisition is a National Instruments 8-slot USB compact DAQ chassis (NI c-DAQ- 9178). J type thermocouples (range 20 °C to 200 °C with sensitivity of 50 $\mu\text{V}/^\circ\text{C}$) is used to measure the temperature of the test bearing. The vibration data is measured from a Dytran Uniaxial accelerometer (model no: 3055B1; Sensitivity = 10.437 mV/g. Sound Pressure level is measured from a PCB Prepolarized condenser microphone (Model:378B02; Sensitivity = 48.7266 mV/Pa). The vibration and sound pressure level results under no-load conditions are discussed here. The microphone was calibrated in a microphone calibrator which produces 94 dB at 1000 Hz whereas; the accelerometer was calibrated in a vibration shaker which produces 1 g acceleration at 159.2 Hz.

The measurements are taken up to 7000 rpm in the steps of 1000 rpm which is most relevant maximum bearing speed in electrical vehicles. All the sensors' data captured for test and support bearings as a function of speed. For brevity, only vibration and acoustic signals data at 7000 rpm of test bearing is given in the manuscript. Figure 3(a) shows the vibration signal of the test bearing at 7000 rpm. The corresponding sound level is represented in Figure 3(b) The signals are recorded for a duration of 1s with a sampling frequency of 25600 Hz. Acceleration spectrum is marked with the harmonics of the excitation frequency (i.e., 7000 rpm or 117 Hz in Figure 3(c) The third and the sixth modal

harmonic represent the highest magnitude in the acceleration frequency spectrum. The three characteristic frequencies i.e., Ball spin frequency (BSF), Ball pass frequency outer race (BPFO) and Ball pass frequency inner race (BPFI) respectively are clearly identified in the vibration spectrum for the test bearing.

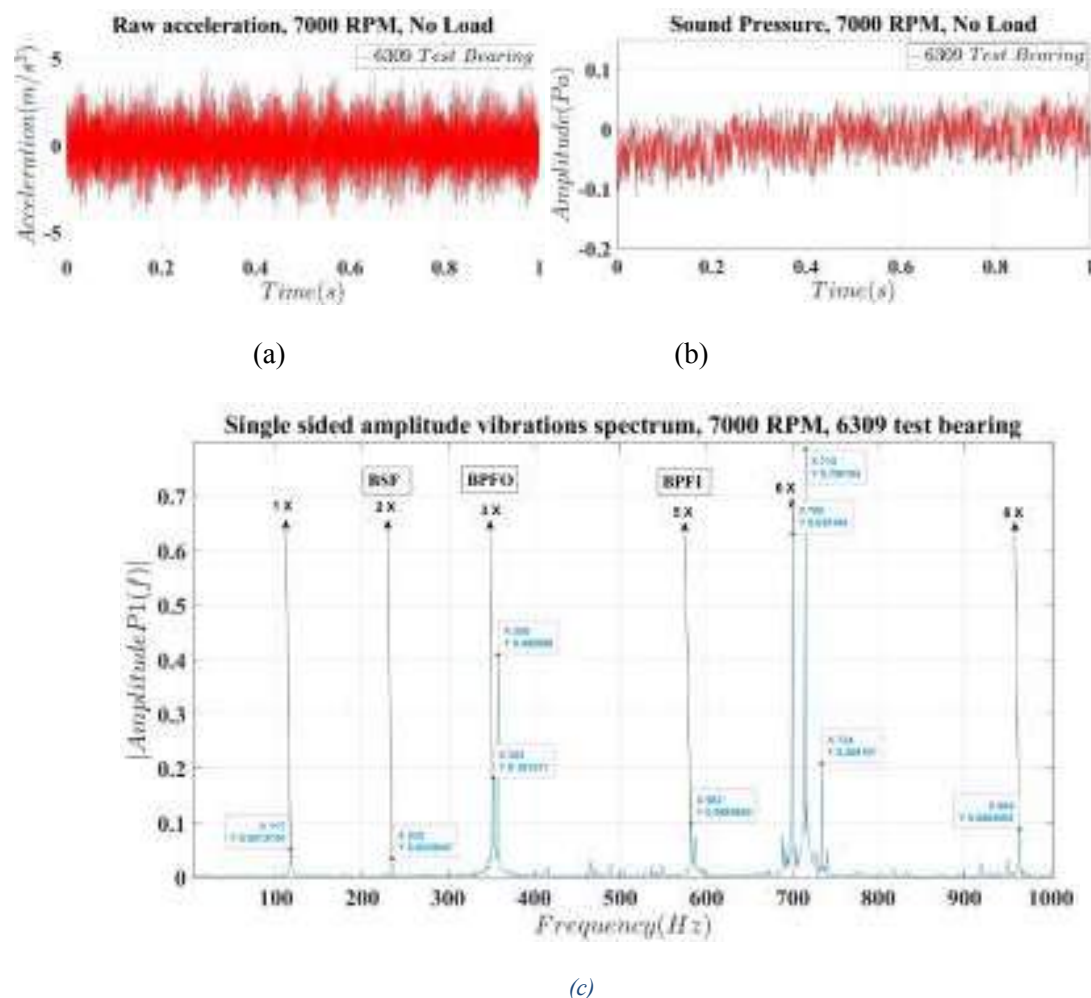


Figure 3: (a) Acceleration signal in time domain (b) Sound Pressure signal in time domain (c) Vibrations spectrum at 7000 RPM for Test bearing 6309 DGBB.

Statistical Parameters

Statistical parameters are computed for the acceleration and acoustic signals of the test bearing with rotational speeds (1000-7000 rpm in steps of 1000 rpm). The mathematical formulae used for calculating the statistical parameters are as in Parameters Table 1. A_i is the amplitude of the corresponding vibration and acoustic signal, respectively.

The vibration statistical values for operational speeds up to 7000 rpm are shown in Table 2. The mean of the vibration signal is small in magnitude and changes with speed. The root means square and peak value increase steadily as the operating speed increases. The crest factor provides early warning of ball bearing problems as they develop, and as operating speed increases, the crest factor decreases.

Table 3: Formulae for Statistical Parameters

Sr no.	Statistical Parameter	Formula	Sr no.	Statistical Parameter	Formula
1	Mean (μ)	$\frac{1}{N} \sum_{i=1}^N A_i$	7	Variance (σ^2)	$\frac{\sum_{i=1}^N (A_i - \mu)^2}{N}$
2	RMS	$\sqrt{\frac{1}{N} \sum_{i=1}^N A_i ^2}$	8	Standard deviation (σ)	$\sqrt{\frac{1}{N-1} \sum_{i=1}^N (A_i - \mu)^2}$
3	Peak Level (P_v)	$\frac{1}{N} [Max(A_i) - Min(A_i)]$	9	Clearance factor (CI)	$\frac{P_v}{(\frac{1}{N} \sum_{i=1}^N \sqrt{ A_i })^2}$
4	Crest factor (CF)	$\frac{P_v}{RMS}$	10	Impulse factor (I_f)	$\frac{P_v}{\frac{1}{N} \sum_{i=1}^N A_i }$
5	Skewness (S)	$\frac{\frac{1}{N} \sum_{i=1}^N (A_i - \mu)^3}{(RMS)^3}$	11	Shape factor (S_f)	$\frac{RMS}{\frac{1}{N} \sum_{i=1}^N A_i }$
6	Kurtosis (K)	$\frac{\frac{1}{N} \sum_{i=1}^N (A_i - \mu)^4}{(RMS)^4}$			

Skewness is a measure of data asymmetry around the sample mean. The skewness calculated is non-biased and thus refers to no systematic difference between the sample and the population. As the skewness of the vibration data is positive (except for 4000 rpm), the data spreads out more to the right. However, the low magnitude of the skewness indicates close conformity with the normal distribution of the data. Kurtosis is used to detect the presence of outliers in the data, with a greater value referring to a higher peak. As seen, the kurtosis of the deep groove ball bearings transitions from a positive kurtosis (≥ 3) to a negative kurtosis (≤ 3) value at higher speeds. The variance and standard deviation increase significantly at higher speeds, indicating wider spreads of the data from the mean. With the decrease in the clearance factor and the shape factor, it may be possible to expect a fault or instability signature from the bearings at higher operational speeds.

Table 3 shows the acoustic statistical parameters. The mean and rms acoustic signals are constant; however, the peak level and crest factor are small and decrease with speed. The acoustic signals' skewness is slightly negative, indicating that the data is spread to the right of the mean. The kurtosis is negative across the whole operating speed range, indicating a heavier tail and flatter peaks in the acoustic data. Unlike the variance and standard deviation in the case of vibrations, the signal data remains near the mean for acoustic signals. Significant changes are not observed with increase of speed for clearance factor, impulse factor, or shape factor in acoustic signals from the bearings up to 7000 rpm.

Table 2: Statistical Parameters for Bearing vibration signal as a function of speed (6309 Test Bearing)

Sr no.	Statistical Parameter for vibration response	1000 RPM	2000 RPM	3000 RPM	4000 RPM	5000 RPM	6000 RPM	7000 RPM
1	Mean	0.00028	0.00074	0.00046	0.00046	0.00080	0.00042	0.00105
2	RMS	0.09973	0.31142	0.37536	0.50722	0.64544	0.73447	1.27740
3	Peak Level	0.00004	0.00014	0.00012	0.00017	0.00021	0.00024	0.00036
4	Crest factor	0.00037	0.00046	0.00031	0.00034	0.00033	0.00033	0.00028
5	Skewness	0.02712	0.09034	0.01633	-0.01614	0.02071	0.07269	0.02124
6	Kurtosis	3.19696	4.08802	3.12702	2.97208	2.99447	3.02318	2.77957
7	Variance	0.00995	0.09698	0.14090	0.25727	0.41659	0.53945	1.63175
8	Standard Deviation	0.09973	0.31143	0.37537	0.50722	0.64545	0.73448	1.27743
9	Clearance factor	0.00054	0.00071	0.00047	0.00051	0.00049	0.00049	0.00041
10	Impulse factor	0.00046	0.00060	0.00040	0.00043	0.00041	0.00042	0.00035
11	Shape factor	1.25687	1.28718	1.26057	1.25102	1.25457	1.25250	1.24021

Table 3: Statistical Parameters for Bearing acoustic signal as a function of speed (6309 Test Bearing)

Sr no.	Acoustic Statistical Parameter	1000 RPM	2000 RPM	3000 RPM	4000 RPM	5000 RPM	6000 RPM	7000 RPM
1	Mean	-0.01709	-0.01618	-0.01686	-0.01630	-0.01690	-0.01656	-0.01658
2	RMS	0.03834	0.03807	0.03829	0.03765	0.03797	0.03810	0.03774
3	Peak Level	0.00001	0.00001	0.00001	0.00001	0.00001	0.00001	0.00001
4	Crest factor	0.00021	0.00019	0.00020	0.00018	0.00018	0.00019	0.00019
5	Skewness	-0.11678	-0.15809	-0.15817	-0.09912	-0.09326	-0.12793	-0.12791
6	Kurtosis	2.17941	2.23741	2.23160	2.15876	2.15490	2.21277	2.17341
7	Variance	0.00118	0.00119	0.00118	0.00115	0.00116	0.00118	0.00115
8	Standard Deviation	0.03432	0.03446	0.03438	0.03393	0.03400	0.03431	0.03390
9	Clearance factor	0.00030	0.00027	0.00029	0.00026	0.00025	0.00027	0.00027
10	Impulse factor	0.00026	0.00023	0.00025	0.00022	0.00021	0.00023	0.00023
11	Shape factor	1.22414	1.22738	1.22815	1.22162	1.22255	1.22585	1.22691

Correlating Acceleration and Acoustic Statistical Parameters

Pair wise Pearson correlation coefficients have been established between the vibration and acoustic statistical parameters. The Pearson correlation coefficient (ρ) is a descriptive statistical parameter

and the most common way of measuring a linear correlation. It measures the strength and direction between the two variables. The below formula is used for calculating the Pearson correlation coefficient $-1 \leq \rho \leq 1$ between the two variables x and y .

$$\rho = \frac{n\sum xy - (\sum x)(\sum y)}{\sqrt{[n\sum x^2 - (\sum x)^2][n\sum y^2 - (\sum y)^2]}} \quad (12)$$

Table 4: Strongly correlated statistical parameters between Acoustic and Vibration bearings signals.

Sr no.	Acoustic Statistic	Vibration Statistic	Correlation	95% CI for ρ	P-Value
1	Variance acoustic	Skewness vibration	0.749	(-0.010, 0.960)	0.053
2	Standard Deviation acoustic	Skewness vibration	0.705	(-0.103, 0.952)	0.077
3	Variance acoustic	Kurtosis vibration	0.726	(-0.060, 0.956)	0.065
4	Standard Deviation acoustic	Kurtosis vibration	0.738	(-0.034, 0.958)	0.058
5	Kurtosis acoustic	Shape factor vibration	0.715	(-0.083, 0.954)	0.071
6	Variance acoustic	Shape factor vibration	0.764	(0.025, 0.963)	0.046
7	Standard Deviation acoustic	Shape factor vibration	0.785	(0.078, 0.967)	0.037
8	Kurtosis acoustic	Kurtosis vibration	0.686	(-0.139, 0.949)	0.089

Table 5: Weakly correlated statistical parameters between Acoustic and Vibration bearing signals.

Sr no.	Acoustic Statistic	Vibration Statistic	Correlation	95% CI for ρ	P-Value
1	Mean acoustic	Mean vibration	0.289	(-0.593, 0.856)	0.529
2	Crest factor acoustic	Crest factor vibration	0.174	(-0.666, 0.820)	0.708
3	Clearance factor acoustic	Clearance factor vibration	0.174	(-0.666, 0.820)	0.709
4	Impulse factor acoustic	Impulse factor vibration	0.166	(-0.671, 0.817)	0.723
5	Shape factor acoustic	Shape factor vibration	0.222	(-0.638, 0.835)	0.632

Table 4 represents strong correlation coefficients between the acoustic and vibration statistical parameters. The shape factor is dependent on the signal shape while being independent of the signal dimensions and is observed to have a direct relationship with the acoustic parameters. It should be noted that kurtosis is the common correlation statistic parameter between the DGBB acoustic and vibration data. Causal relationship understanding between the parameters is the next critical step for the strong correlations.

Table 5 shows the common statistics that are not correlated for vibration and acoustic data. Thus, it would be inappropriate to predict the nature of one statistical parameter based on the other. Note that the data reported in Table 5 is for up to 7000 *rpm* only, and further investigations are planned to understand the nature of DGBB at higher operating speeds.

Conclusion

The present manuscript describes the development of a high-speed bearing test rig to measure the noise and vibration response of the bearings at various speeds and loads for electrical vehicle applications. Statistical data of the vibration and acoustic signal were calculated for the deep groove ball bearing for speeds up to 7000 *rpm*. Pearson linear correlation coefficients were utilized to assess the relationship between vibration and acoustic data, with the aim of better understanding the underlying physics. Additional research is planned to further elucidate and identify the causal relationships between the correlations. Knowledge of the vibro-acoustic behaviour of DGBB at high speeds is essential for evaluating performance and satisfying industry demands for quieter, and energy-efficient bearings.

Acknowledgements

Authors would like to thank Ministry of Heavy Industry, Government of India, NEI Pvt Ltd Jaipur for financial support to conduct current investigation and Indian Institute of Technology Hyderabad for providing the required resources.

References

- 1] Kankar, P. K., Sharma, S. C., & Harsha, S. P. (2013). Vibration signature analysis of a high-speed rotor supported on ball bearings due to localized defects. *Journal of Vibration and Control*, 19(12), 1833-1853.
- 2] Patil, M. S., Mathew, J., Rajendrakumar, P. K., & Desai, S. (2010). A theoretical model to predict the effect of localized defect on vibrations associated with ball bearing. *International Journal of Mechanical Sciences*, 52(9), 1193-1201.
- 3] Meserkhani, A., Jafari, S. M., & Rahi, A. (2021). Experimental comparison of acoustic emission sensors in the detection of outer race defect of angular contact ball bearings by artificial neural network. *Measurement*, 168, 108198.
- 4] Grebenik, J., Zhang, Y., Bingham, C., & Srivastava, S. (2016, December). Roller element bearing acoustic fault detection using smartphone and consumer microphones comparing with vibration techniques. In *2016 17th International Conference on Mechatronics-Mechatronika (ME)* (pp. 1-7). IEEE.

Case Study on Defect Rectification of an External Gear Pump through Vibration Monitoring

S Jagadeesh Kumar¹, MP Patmase²

¹Principal Scientific Officer, ²Sr. Scientific Assistant
Central Dockyard Laboratory, Naval Dockyard, Visakhapatnam (India)

ABSTRACT

Vibration Signature Analysis is an effective tool of a well-designed Condition Monitoring/Predictive Maintenance Program. It comprises of (a) Defect detection (b) Analysis of defect (c) Corrections needed in the system and (d) Verification of elimination of defect. It is also considered to be an effective tool for detecting the very onset of problems within machinery. It provides extensive diagnostic techniques required to analyse machine problems to determine both their cause and severity and thus make solid recommendations based on "fact" rather than "feeling" and allow the maintenance department to schedule such corrective measures at convenient times.

The multi gear lubricating oil booster pump selected for case study has significant importance at the site to circulate highly viscous lubricating oil from low atmospheric pressure zone to high pressure area by scavenging method involving huge torque for fluid circulation. This case study presents the data pertaining to vibration measurements and analysis as well as scope of improvement in the existing noise and vibration levels. Also the need of implementing remedial measures recommended post vibration signature analysis.

Indication of mechanical/structural looseness, eccentricity and gear mesh frequency associated with side bands in FFT spectrum analysis carried out on various similar type pumps during condition monitoring activities revealed that excessive clearance in the slots & the respective rubber bushings inside flexible coupling has been one of the factor for excessive vibrations. Also, provisioning of wire mesh at the connection between suction pipe and port of the pump was causing pressure pulses in the pump. Further, it was generating excessive noise & vibrations in the pump and frequently damaging other components of the pump like Main shaft keyway, Key, multiple gear teeth, drive shaft and coupling between pump/motor.

Recommended remedial measures: (i) Manufacturing & fitment of rubber bushings as per designed specifications (ii) Removal of wire mesh between pump suction port & suction pipe (iii) Provision of bellows on suction & discharge pipes to arrest hydraulic pressure pulses.

Results: Noise & Vibration Levels of the pump have been reduced.

Key words: Multiyear lubricating oil booster pump, FFT spectrum, Hydraulic pressure pulses, Flexible coupling.

Conclusion: Defect of excessive vibrations on an external gear pump has been effectively identified and rectified through condition monitoring tool i.e. vibration measurement and analysis.

Introduction

Rapid acceptance of technological advancements in worldwide engineering applications made us to think and apply it in our routine life. On majority occasions, vibrations associated with noise have strategic importance to make closer interpretations/assumptions about machinery defects.

Some of the exemplary procedures of condition monitoring to avoid excessive noise and vibrations of any type of engineering machines are elaborated as under [3].

- (a) Mount equipment/machines on rigid and solid foundations, which do not permit it to vibrate. Make certain that foundation bolts are kept tight.
- (b) If equipment/machine vibrates, determine whether its characteristics can be changed by use of such devices as dynamic dampers, rubber or plastic bumpers, flexible mountings and coupling or resilient flooring.
- (c) Make certain that the piping are firmly secured enough & flexible one to prevent pressure pulsing.
- (d) Locate noisy activities, such as individual noisy machines in sound absorbing enclosures, or provide barriers between such activities and other locations where personnel are present.

External Gear Pump

The External Gear Pump and its internal components (Fig. 1, 2, 3) has been commonly used for pumping lubricating oil or fluids with generally higher viscosity than that of water. The rigid design of the gears and housing allows for very high pressure and the ability to pump highly viscous fluids.



Fig. 1 Sectional View



Fig. 2 Gears inside pump



Fig. 3 Shaft inside gears

Working principle

This pump is simple in its operating principle, as the gears rotate, the fluid is transferred from inlet port to outlet port around the outside of gears, and the displacement of the fluid is accomplished by two meshing gears rotating against each other (see Fig. 4).



Fig. 4 Principle of operation

Gear teeth routinely carry the fluid at a periodic interval that causes the flow rate and pressure in the intake and discharge to vary periodically and these variations are referred to as flow and pressure ripples. When two gears meshing with each other, it will form a closed cavity which separates suction side and discharge side known as the trapped

volume. The trapped volume of fluid with rapid changes results in the generation of pressures above and below the inlet and discharge pressures.

Probable causes of excessive noise/vibrations in the pump

Two main sources of excessive noise are hydraulic pressure pulsation and inadequate gear meshing. These can lead to high loading of the gears and excessive mechanical losses cause huge vibrations/noise affecting the stationary and stresses in the pump. Therefore, meshing actions make a significant contribution to pressure and flow ripples that are critical dynamics affecting system's lifetime performance. Generally, gears can dig their relief grooves on the side plates or wear plates to reduce the localized pressure spikes and fluid cavitation in the meshing volumes [3].

Meanwhile, the periodic variation of gear meshing forces can produce pressure ripples. These pumps almost always have a strong vibration component at the tooth mesh frequency i.e. the number of teeth on the gear times the RPM. Generally, the amplitude of vibrations at higher orders of the gear mesh frequency normally starts to diminish if no gear impact is present. This will be highly dependent on the output pressure of the pump. If the tooth mesh frequency changes significantly (in comparison with any previous reading) – i.e. if there is a sudden appearance of harmonics or sidebands in the vibration spectrum– this could indicate a cracked or otherwise damaged tooth and flexible coupling. The high vibration in the gear pump, specifically at the gear mesh frequency with the presence of a side band, is normally an indication that the generated harmonic torque is greater than the mean torque. The amount of backlash - clearance between the meshing teeth – will have a high influence on the vibration level and its severity.



Fig. 5 Isolated soundproof compartment

General observations

As per the guidelines of ISO: 10816 Standards, Pump was mounted on rigid foundation [without use of anti-vibration mounts (AVMs)] inside an isolated soundproof compartment (Fig. 5). Metallic rigid pipings found connected to suction and discharge sides (Fig. 6). Suction & discharge pipings found without dampers to arrest hydraulic pressure ripples.



Fig. 6 Assembly on rigid test bed

Calculated Gear Mesh Frequencies (GMF) -1524 Hz, 382 Hz

RPM - 2900 to 2950

Power of attached motor - 50 to 55 Kw

Gears are hollow with an internal shaft (Fig. 4) provided with teeth

Initial investigation

Findings of noise & vibration measurements (Table 1) undertaken with identical conditions are appended below. Measurements at six locations on the pump (horizontal, vertical & axial direction of drive and non-drive side) and six locations on the motor (horizontal, vertical & axial direction of drive and non-drive side) have been undertaken. These measurements were carried out to establish vibration amplitude and determine dominant frequencies, pump general operating characteristics and current condition and its acceptability.

Locally made rubber bushings have been used inside the flexible coupling used between Motor & Pump. Wire mesh provided between suction port & suction pipe causing disturbance to the oil flow (being gravitational feed) resulted in variation of suction pressure. Suction & Discharge pipes have been rigidly attached with the pump without vibration dampers.



Damaged/broken gear teeth

Effect of excessive vibration

FFT Spectrum Analysis

- (i) All the gear mesh frequencies appearing in the FFT Spectrum are associated with side bands indicates backlash between meshing gear teeth which has been the effect of hydraulic pressure ripples generated due to absence of dampers to the suction and discharge pipes as well as wire mesh provided between suction port & pipe.
- (ii) FFT Spectrum pertaining to axial direction of pump drive end shows the pattern of structural looseness/looseness inside the coupling which has been caused due to excessive clearance generated between the slots and the surface of locally made rubber bushings provided inside flexible coupling.

Probable defects & recommended remedial measures post vibration signature analysis

S. No	Observed Defects	Recommended remedial measures
1.	Excessive Vibration on Pump due to Hydraulic Oil Pressure ripples/pulsations	Removal of wire mesh between pump suction port & suction pipe to maintain smooth gravitational feed
2.	Excessive wear & tear of gear teeth / coupling	Provision of accurately designed rubber bushings inside flexible coupling
3.	Abrupt changes in the geometry of suction & discharge pipings due to multiple welded joints	Suitable metallic dampers to be manufactured and provided to suction & discharge pipings to arrest pressure ripples/pulsations

Implementing recommended remedial measures

Provision of metallic spring bellows (dampers) on suction & discharge pipes to arrest hydraulic pressure pulses (Fig. 7). Manufacturing & fitment of new rubber bushings inside the coupling as per design (Fig. 8)



Fig. 7 Provision of suitable dampers

Removal of wire mesh between pump suction port & suction pipe (Fig. 9).

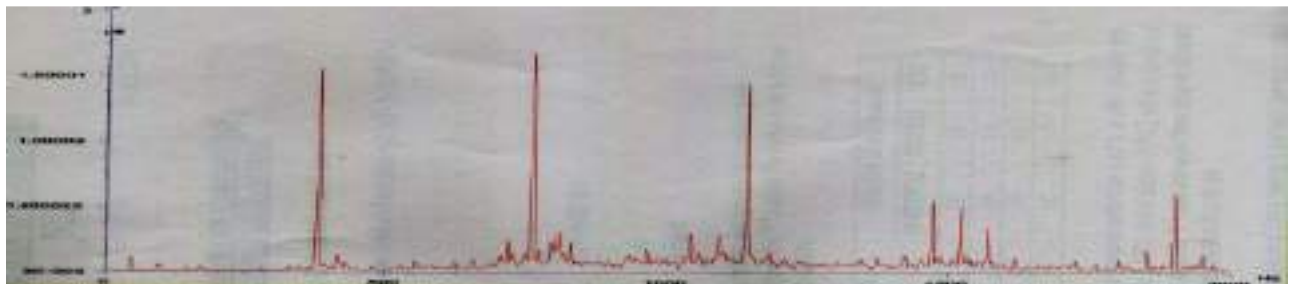


Fig. 8 Rubber bushings as per design Fig. 9 Wire mesh between suction port & pipe

Table 1: NOISE & VIBRATION MEASUREMENTS ON EXTERNAL GEAR PUMP

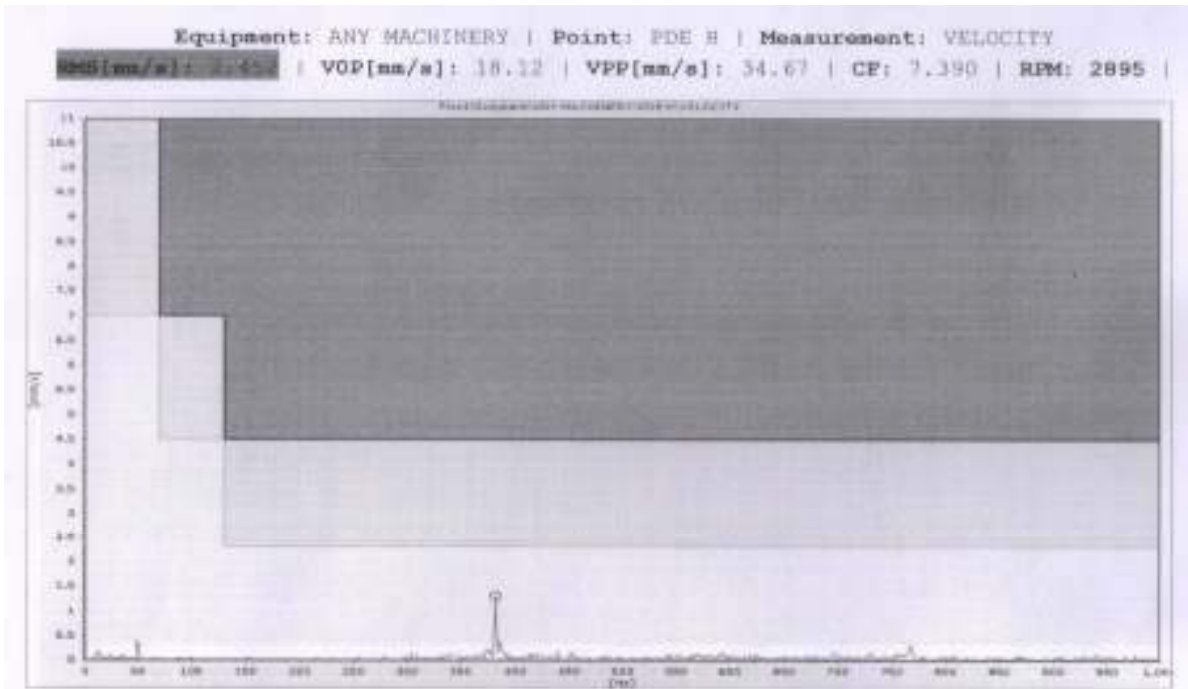
Date	Vibration velocity (RMS) in mm/s												Noise in dB (A)	Defects revealed post vibration analysis
	Motor NDE			Motor DE			Pump DE			Pump NDE				
	H	V	A	H	V	A	H	V	A	H	V	A		
DATA RECORDED WHILE MACHINE INSTALLED ON RIGID FOUNDATION														
07.04.16	5.35	6.63	3.52	5.30	4.41	6.95	22.1	12.7	12.6	10.3	8.12	5.43	106.6	Hydraulic pulsations, Excessive backlash, Loose coupling
28.04.16	2.42	2.62	2.12	3.22	3.21	3.12	23.4	14.1	5.91	11.7	7.67	5.56	109.0	Hydraulic pulsations, Excessive backlash, Loose coupling
03.01.17	3.29	6.62	5.24	7.56	5.12	6.75	26.6	13.4	7.14	13.0	11.5	10.9	106.0	Hydraulic pulsations, Excessive backlash, Loose coupling Wear/tear of gear teeth
23.01.17	4.12	2.95	2.91	5.06	3.51	3.20	31.2	6.49	7.99	26.1	12.1	5.46	110.5	Hydraulic pulsations, Excessive backlash, Loose coupling Wear/tear of gear teeth
07.03.18	6.92	4.51	2.75	3.71	4.73	2.35	23.8	13.6	8.93	27.5	14.6	9.61	109.8	Hydraulic pulsations, Excessive backlash, Loose coupling Wear/tear of gear teeth
10.04.18	2.31	4.73	4.85	2.93	2.64	4.24	17.0	18.2	14.6	22.9	18.8	6.24	109.8	Hydraulic pulsations, Excessive backlash, Loose coupling Wear/tear of gear teeth
RESULTS POST IMPLEMENTING RECOMMENDED REMEDIAL MEASURES														
03.10.20	1.82	1.39	1.39	1.37	1.88	1.40	2.45	1.88	2.61	7.29	2.77	1.82	100.2	--
03.10.20	2.24	1.60	1.80	2.03	1.33	1.15	6.13	3.42	1.94	6.79	4.42	0.96	103.9	--

FFT SPECTRUMS - PRIOR IMPLEMENTING REMEDIAL MEASURES

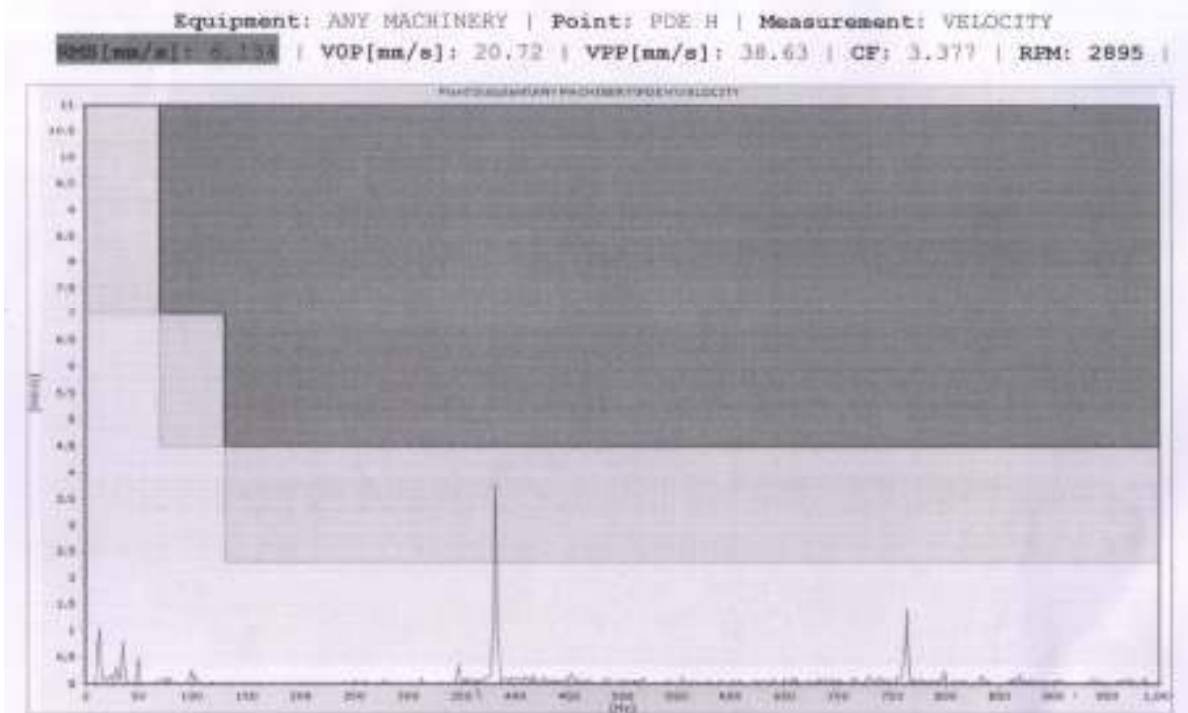


Horizontal direction of pump drive end

FFT SPECTRUMS - POST IMPLEMENTING REMEDIAL MEASURES



FFT SPECTRUM - HORIZONTAL DIRECTION OF DRIVE END OF PUMP NO. 3



FFT SPECTRUM - HORIZONTAL DIRECTION OF DRIVE END OF PUMP NO. 4

Conclusion

Through FFT spectrum analysis, it has been observed that Gear Mesh Frequencies with side bands which indicates the presence of defects has been completely disappeared post implementation of recommended remedial measures. Thus, it can be concluded that root cause of excessive vibrations on an external gear pump has been effectively identified and rectified through condition monitoring tool i.e. vibration measurements and analysis.

References

1. Text book on “Vibrations & noise for Engineers” by Kewal Pujara, Dhanpat Rai & Co.
2. Research article “Flow characteristics of external gear pumps considering trapped volume” by Xiaoru Hao, Xiaojun Zhou, Xiaoguang Liu and Xiaohu Sang published in the Journal “Advances in Mechanical Engineering 2016”.
3. “Safety Standing Orders” [Short title: NDVSSO (Rev.01)] of Naval Dockyard, Visakhapatnam.
4. IS 14817 (Part 1):2000 & ISO: 10816 (On rigid platform)
5. OHSAS Standards

Acknowledgements

1. Cdr MSN Murthy, Manager, Gas Turbines Dept., Naval Dockyard, Visakhapatnam
2. Lt Cdr M Chavan, Officer-in-Charge, Machine Test House, Naval Dockyard, Visakhapatnam
3. Lt Rohit Rawat, Officer-in-Charge, Gas Turbines Dept., Naval Dockyard, Visakhapatnam
4. Mr. Madan, Foreman (Z), Gas Turbines Dept., Naval Dockyard, Visakhapatnam
5. Mr. Sankar Raju, Foreman (Z), Machine Test House, Naval Dockyard, Visakhapatnam
6. Mr. Kalyan Chakravarthy, Chargeman, Machine Test House, Naval Dockyard, Visakhapatnam
7. Mr. Suraj Prabhas, Scientific Staff, Central Dockyard Laboratory, Naval Dockyard, Visakhapatnam

Condition Monitoring of Rigid Shaft Supported on Foil Bearings with Defects in Supporting Bump Foil

Balaji Sankar, Dr Sadanand SKulkarni

Propulsion division, CSIR, NAL, India.

Abstract

In this work, the performance of a rigid shaft supported on defective gas lubricated foil bearings is analyzed using an in-house developed mathematical model based on first-principles. A validated in house fluid film solver based on pseudo-spectral method is integrated with an improved finite element based structural model of the gas lubricated foil bearing. By selectively weakening the elements of the foil bearing in the high load region, the failure of the bump foil support structure is simulated. By concurrently solving the fluid film and the structural model, the increase in film thickness and the decrease in load capacity of the bearing is quantified. If the same load is applied on the bearing after failure of the bump foils, the shaft attains a new steady state at a higher eccentricity. This new eccentricity can be measured using air gap sensors and thus the failure of the bump foil of the gas lubricated bearing can be detected online using eccentricity measurements from air gap sensors.

Introduction

Gas foil bearings (shown in Figure 2) are simple in their construction and hence reduce rotor system complexity in small gas turbines. They help in reducing maintenance cost and increases efficiency of the shaft system of the engine [1]. These bearings are being used in air cycle machines and have shown high reliability in aircraft environmental control system applications[2]. Gas foil bearings are typically classified into 3 generations based on the variation of the stiffness. The first generation foil bearings have constant stiffness in the tangential and axial directions and are most mature.



Figure 2 Gas lubricated foil bearing of inner diameter 20 mm, developed in CSIR-NAL and commercialized.

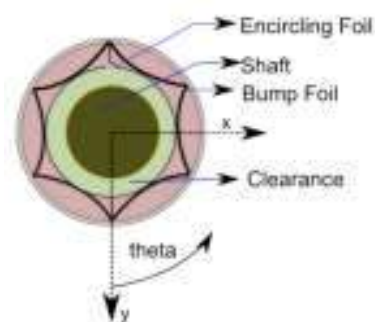


Figure 3 Schematic of the foil Bearing, showing concentric location of shaft with exaggerated clearance between shaft and encircling foil.

The front view of the first generation foil bearings is shown in Figure 3. The encircling foil (supported by the bump foil) surrounds the shaft. The corrugated bump foil

forms the flexible backing foundation to the encircling foil. In practice, the bearing diameter is often designed to have very small clearance or interference fit with the encircling foil. When the shaft rotates, due to viscous action, the shaft drags air into the converging space between encircling foil and the shaft. This leads to positive gauge pressure being developed in the converging portion. Upon reaching the ‘‘lift-off speed’’, pressure developed will be sufficient to form a continuous layer of air film between the journal and bearing inner surface and completely separates them apart. Though in Figure 3, the shaft is shown to be at the center of the sleeve, it's usually at an eccentric position as shown in Figure 4. The occurrence of this ‘‘lift-off speed’’ is indicated by the sharp reduction in the torque required to drive the rotor.

Several simulation approaches exist to model these first generation gas foil bearings. Simulation of the foil bearings involve simultaneous solving of the structural deformation of the encircling foil, bump foil and the pressure distribution of the gas film surrounding the shaft, inside the encircling foil. In this work, a validated simulation model([4] and [6]) for the compliant film gas lubricated foil bearing is used. The previously validated ([4] and [6]) simulation model uses a simplified structural model based on the compliance factor of the bump foil of the bearing. Only this structural model is replaced in this work with a finite element based structural model so that the bump foil can be artificially weakened at a particular angle to simulate the damaged bump. The effect of this damaged bump in the steady state location of the shaft is then studied using the combined structural and fluid film simulation model.

The paper is organized as follows: In the next section, a brief overview of the fluid film simulation model and the conventional structural model is given. The conventional structural model is based on the compliance factor of the foil bearing. Next, the finite element based structural model is presented in detail. The equivalent finite element based structural model is then used with the fluid film model to obtain the steady state location of the shaft. Then, the finite element model is modified to simulate a damaged bump foil and the effect of the damage in the bump foil on the steady state location of the shaft is then obtained from the combined structural and fluid film simulation model.

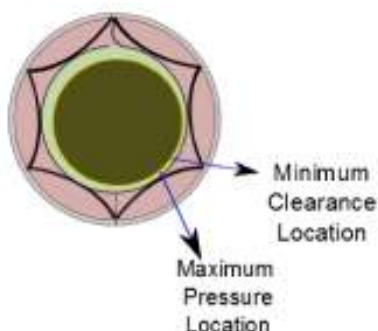


Figure 4 Schematic of the foil Bearing, showing eccentric location of shaft inside the encircling foil.

Simulation model of the gas foil bearing

The objective of the simulation model of the gas foil bearing is to provide the distribution of pressure and gap clearance around the rotating shaft. The simulation model simultaneously solves the flexible structural model and the fluid film equation to obtain the pressure distribution and the clearance distribution. By integrating the pressure distribution,

the net force on the shaft is found. This net force from the pressure distribution supports the shaft weight at the running condition using a purely vertical force at the correct attitude angle. The steady state location of the shaft is the attitude angle and eccentricity at which the integrated net force is equal to the shaft weight, without any horizontal component.

Fluid model of the gas foil bearing

The pressure distribution of the fluid between the encircling foil and shaft surface is solved for a given surface speed and clearance distribution using the compressible Reynolds equation. The compressible Reynolds equation contains mainly 4 terms: tangential pressure diffusion, axial pressure diffusion, pumping effect due to shaft oscillation and wedge effect due to surface speed of the shaft. The tangential diffusion term is given by $\frac{\partial}{\partial x} \left(ph^3 \frac{\partial p}{\partial x} \right)$, where p is the non-dimensional pressure in encircling film, x is the tangential co-ordinate along the bearing and h is distribution of clearance around the shaft.

Axial diffusion is given by $\frac{1}{(L/D)^2} \frac{\partial}{\partial y} \left(ph^3 \frac{\partial p}{\partial y} \right)$, in which y is the axial co-ordinate and L/D is length to diameter ratio of the bearing. The wedge effect of the bearing is given by $\frac{6UR\mu}{c^2 p_a} \frac{\partial}{\partial x} (ph)$. C is the distribution of clearance around the shaft, U is the surface speed of the shaft, R is the radius of shaft and μ denotes viscosity of air. The pumping term includes the time history of pressure and is given by $\frac{12\mu B^2}{c^2 p_a} \frac{\partial}{\partial t} (ph)$. The complete Reynolds equation is given by

$$\frac{\partial}{\partial x} \left(ph^3 \frac{\partial p}{\partial x} \right) + \frac{1}{(L/D)^2} \frac{\partial}{\partial y} \left(ph^3 \frac{\partial p}{\partial y} \right) = \frac{6UR\mu}{c^2 p_a} \frac{\partial}{\partial x} (ph) + \frac{12\mu B^2}{c^2 p_a} \frac{\partial}{\partial t} (ph).$$

This compressible Reynolds equation is solved using finite difference method, finite volume method or pseudo spectral methods over a rectangular grid. The rectangular grid is basically the unwrapped encircling foil, ignoring the curvature of the bearing. The curvature of the bearing is ignored as it is too small compared to the clearance of the bearing. This solution process using pseudo spectral methods, finite volume method and finite difference method and their validation are given in detail in references [4] and [6] and hence not repeated here for brevity.

Conventional structural model of the gas foil bearing

The simplified structural model (from [3]) gives the distribution of the clearance \bar{h} around the shaft in the bearing. The fluid of the gas foil bearing occupies this clearance space around the shaft. This clearance distribution depends on the eccentricity and attitude angle of the shaft (ϕ), initial clearance H and the deflection of the top foil and is given by

$$\bar{h} = H + \epsilon \cos(\theta - \phi) + k_1(\bar{p} - p_a)$$

In the above equation, p_a is the ambient pressure and \bar{p} is the local pressure at the grid point. k_1 denotes the structural compliance of the foil structure. This compliance is less for a stiff structure. For journal bearings with rigid structure, this k_1 becomes zero. The above clearance expression is non-dimensionalised using the initial clearance H using the relation $h = \frac{\bar{h}}{H}$ and $e = \frac{\epsilon}{H}$. This non dimensional clearance distribution is given by

$$h = 1 + e \cos(\theta - \phi) + \frac{k_1}{H} (\bar{p} - p_a)$$

The non-dimensional deflection of the top foil as a function of local non-dimensional pressure is then given in terms of its compliance factor (α) as

$$h = 1 + e \cos(\theta - \phi) + \alpha(p - 1)$$

where e is the eccentricity ratio of the shaft in the encircling foil, and $p = \frac{\bar{p}}{p_a}$. The compliance factor (α) is obtained from the geometry of the bump foil arch profile using Euler's beam equation as

$$\alpha = \frac{sp_a}{\left(H \left(\frac{Et^3}{12(1-\gamma^2)l_0^3} \right) \right)}$$

In the above expression, l_0 is the half length of the bump, s is the pitch of the bump, E is the Young's modulus of the material of the bump, γ is the Poisson's ratio and t is the thickness of the bump foil. These parameters are shown in the image Figure 5, which shows a single bump of the bump foil bearing. The numerical values of the parameters of the gas foil bearing used in this work are given in Table 4.

Using the parameters given in Table 4, the steady state eccentricity and attitude angle are computed for the shaft weight of 25N. The result of the simulation model is shown in Figure 6. In this figure, the non dimensional pressure distribution is shown as a red circle and the shaft is shown as the black filled circle. The unfilled black circle represents the ambient pressure in the bearing. When the red line is outside the black unfilled circle, it indicates a region of above ambient pressure. When the red line is inside the black unfilled circle, it indicates below ambient pressure, which may not occur in practice due to foil lift off condition.

The maximum non dimensional pressure seen in the converging portion of the wedge is 1.13, which gives a maximum absolute pressure of 1.144 bar. The red arrow shows the resultant direction of integrating the pressures over the encircling foil. The resultant force is pointing vertically upwards, showing that the pressure distribution supports the weight of 25N without any horizontal destabilizing component. The pressure distribution and clearance distribution as a function of the circumferential angle is shown in figures Figure 7 and Figure 8. This pressure distribution is used as loading functions for the next finite element based structural model.

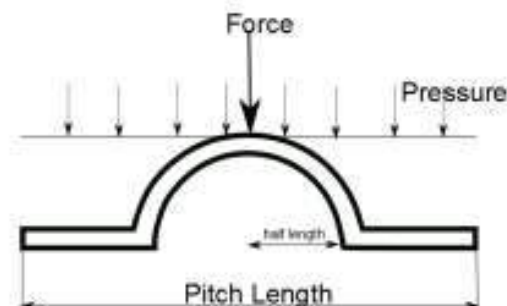


Figure 5 Parameter names of one bump of the bump foil bearing for the structural model

Table 4 Parameters of the gas foil bearing used for simulation model

Bearing length	38.1 mm
Radius of shaft	19.05 mm
Bump foil thickness	0.101 mm
Bump pitch	4.57 mm
Bump length	3.55 mm
Young's modulus	200 GPa
Poisson's ratio	0.31
Eccentricity ratio	0.79 (initial)
Compliance factor	0.4
Bearing number (Gamma)	0.483
Concentric clearance	50 microns
RPM	30000 RPM

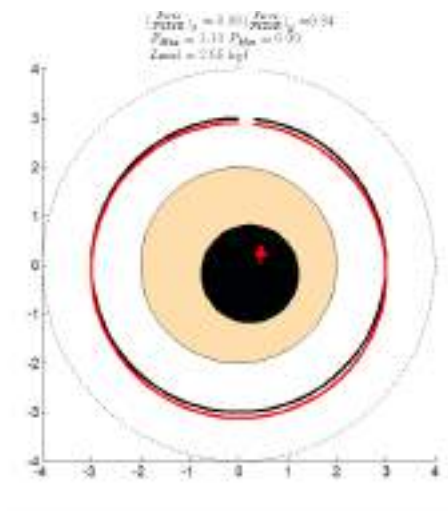


Figure 6 Results of simulation model for a shaft weight of 25N, showing attitude angle (ϕ) of 52.9 degrees and eccentricity ratio (e) of 0.289.

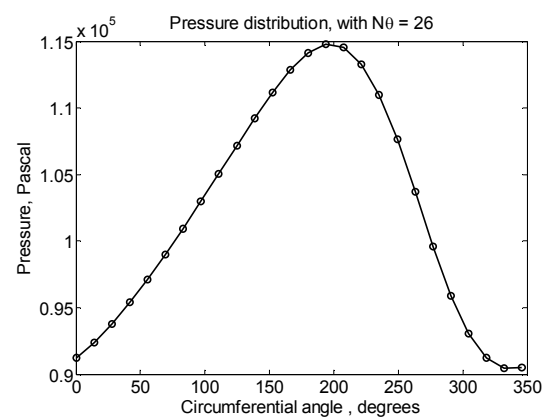


Figure 7 Resultant pressure distribution as a function of circumferential angle, used to apply load to the finite element model. Zero reference is from vertically upward direction.

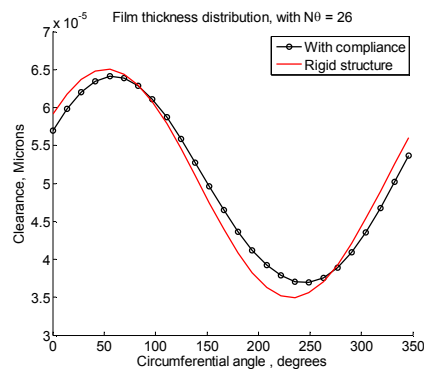


Figure 8 Resultant clearance distribution as a function of circumferential angle, used to obtain the equivalent “AE” value of the stiffness matrix of the finite element model. Zero reference is from vertically upward direction.

Finite element model of the structure of gas foil bearing

In this work, in addition to the above described simplified structural model approach, the deformation of the bump foil is also modeled using the finite element method. The FE model is given in detail as it is the novel contribution of this paper. It is to be noted that the combination of the pseudo-spectral method based fluid film solver and compliance factor based structural model has already been validated in references [4] and [6]. In this work, only the structural model is replaced with the FE model, ensuring that the resultant validated pressure distributions are unchanged.

This model made of truss members is required so that certain truss members *can be weakened to simulate the damaged bumps* whose contribution to the stiffness of the overall bump foil backup structure is reduced. In this method, the bump foil is treated as a network of inter connected truss members as shown in **Error! Reference source not found.**. In this figure, the red circle indicates the outer radius of the bump foil and the black circle indicates the encircling foil of the shaft. The element numbers are given in the **Error! Reference source not found.**, showing the location of the elements 42,16,43 and 17 in the high pressure region of the fluid film.

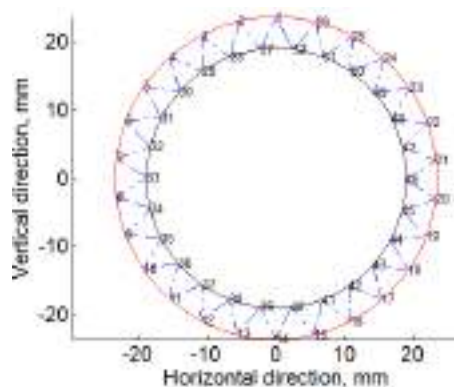


Figure 10 Finite element model of the bump foil structure with 26 inner surface nodes. The numbers indicate the node numbers on the inner and outer surface

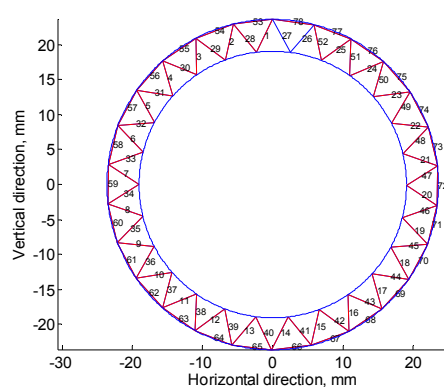


Figure 9 Finite element model of the bump foil structure showing the element numbers.

The load to be applied on the node points of the finite element model is calculated by assuming that the midplane pressure distribution extends to the full 38mm axial length of the bearing. The same pressure from the node is also assumed to be exerted over the 4.6mm circumferential arc length that each of the 26 nodes represents over the full circumference of 119mm. By applying the uniform nodal pressure to the area of the rectangle 38mm in length and 4.6mm in width, the exerted force on the node of the FE model is computed and plotted in Figure 11. The force applied on each node on the inner radius is plotted in Figure 12. The forces are then plotted on the inner surface node in Figure 13 to show the regions where the elements are under compression and the region where the truss elements are under tension. Load values in red show that the elements are in compression and the clearance increases due to pressure. The blue values show that the elements are in tension due to below ambient pressure and the clearance decreases due to encircling foil lift off. Upon application of the load, the exaggerated deformed shape is shown in Figure 14 on the nodes plot. The triangular trusses have been compressed in the regions where there is above ambient pressure and have hence dipped below the blue circle. In regions of below ambient

pressure, the truss vertices have come towards the centre, proud of the blue circle, showing the reduction in clearance clearly.

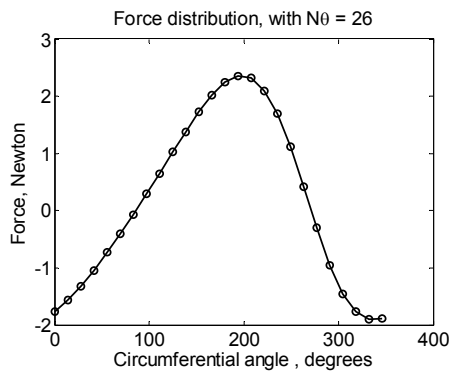


Figure 11 Force to be applied on the FE model as a function of angle, obtained from the midplane pressure distribution. Zero reference is from vertically upward direction.

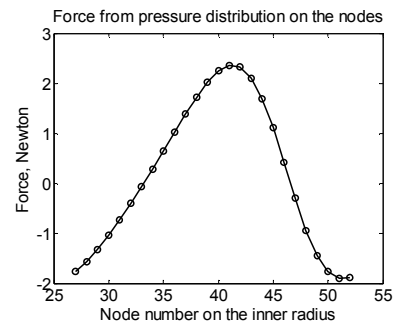


Figure 12 Force to be applied at the 26 inner nodes of the FE model, obtained from the midplane pressure distribution. Node numbers referenced from **Error! Reference source not found.**

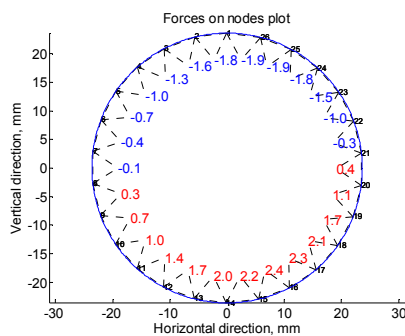


Figure 13 Force to be applied at the 26 inner nodes of the FE model, obtained from the midplane pressure distribution. Node numbers are not shown in the inner surface for clarity

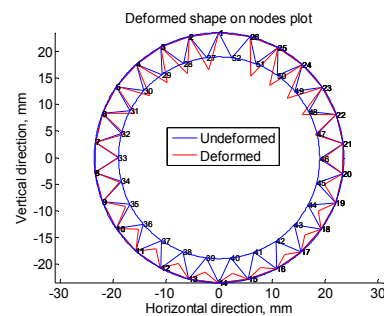


Figure 14 Deformed shape (exaggerated: red) shown superimposed on the un-deformed bump foil grid (blue) Node numbers are shown on inner and outer surfaces.

After getting the correct deflected shape for a given pressure distribution, the conventional compliance factor based film thickness estimation function is replaced with the FE based film thickness estimation function. This comparison is shown in Figure 15, where in the area of the truss elements in the FE model have been tuned to give close approximation of the compliance factor based film thickness estimation function. The pressure distribution computed using the FE based structural model agrees very well with the conventional structural model based pressure distribution. This close agreement is shown in Figure 16.

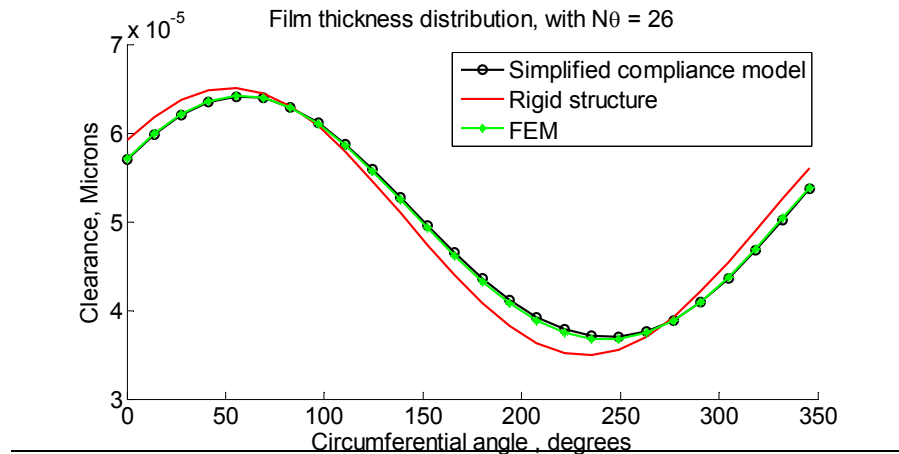


Figure 15 Comparison the compliance factor based film thickness estimation code output with the FE method based film thickness estimation.

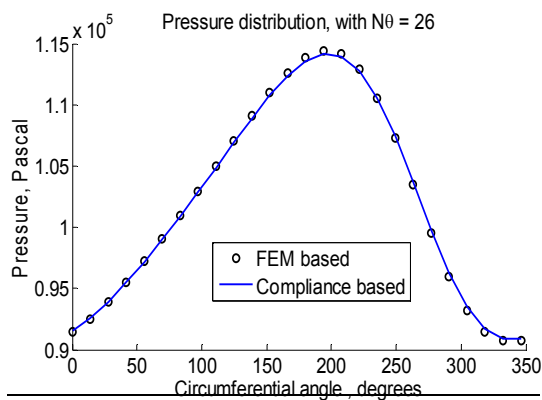


Figure 16 Comparison the pressure distribution from compliance factor based film thickness estimation code with the pressure distribution from FE method based film thickness estimation code.

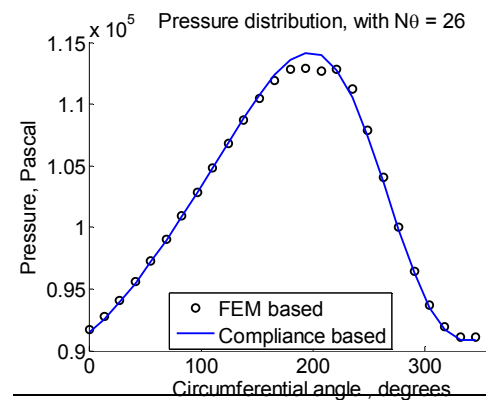


Figure 17 Pressure distribution from FE method based film thickness estimation code after weakening of elements 16,17,42 and 43 showing lower maximum pressure in the converging region.

Weakening of the elements to simulate failure

After tuning of the FE model (shown in Figure 15), some of the truss elements are weakened by reducing the AE/L value of the truss element to one fifth of their original value, thereby simulating the failure of one of the bumps in the high load region. This weakened truss element changes the film thickness distribution by deflecting more for a given pressure load. This higher film thickness affects the development of the above ambient pressure distribution, thereby reducing the net positive force exerted by the film. This in turn changes the eccentricity at which the shaft settles down in the foil bearing. The shaft is forced to go to a higher eccentricity in order to generate sufficient above ambient pressure with the weakened bump foil giving higher film thickness. Thus, by measuring the changed eccentricity of the steady state location of the shaft online using air gap sensors, it is thus possible to detect the failure of the bump foil bearing.

Results

The axial stiffness of the truss element numbers 16, 17, 42 and 43 are reduced to one fifth of their initial values. This simulates the failure of the bump foils in the high pressure high load region of the foil bearing. Due to this, the pressure distribution and the film thickness distribution changes in the high pressure region. Originally, the vertical non dimensional force coefficient from FE model when all elements were in ideal condition is $F_y=0.3318$. Multiplying by the ambient pressure and the projected area of the bearing, this gives us a vertical force of 24.4N, which is close to the load capacity (25N) of the bearing in this condition. After weakening of the elements 16,17,42 and 43, the vertical non dimensional force coefficient becomes 0.3155. Again, converting to force, we get 23.3N. This shows a 4.5% reduction in the load capacity of the bearing. This reduction in load capacity can also be seen in the pressure distribution shown in Figure 17. In this figure, the reduction in the peak pressure of the foil bearing is clearly seen due to the weakening of the bump foil in the high pressure region of the fluid film. In order to still support the original shaft weight of 24.4N, the shaft needs to go to a higher eccentricity of 0.31 compared to the original eccentricity of 0.289. This higher eccentricity is required so that sufficient above ambient pressure may be developed in spite of the weakened bumps increasing the foil deflection and film thickness.

Conclusion

In this work, the conventional compliance factor based bump foil model has been replaced with a FE based bump foil model thereby enabling us to simulate the weakening of the individual bumps in the high load region of the bump foil bearing. The weakening of the bump foil increases the foil deflection and gap clearance. This in turn decreases the peak positive gauge pressure, thereby reducing the load capacity of the bearing. If the same shaft load is applied on the bearing, the shaft settles at a higher eccentricity compared to the healthy bearing. This measurable change in shaft eccentricity enables us to monitor the health of the bump foil bearing.

Acknowledgment

The authors thank the management of CSIR-NAL for permission to carry out this work.

References

- (a) Agarwal G L, 1997, "Foil Air/Gas Bearing Technology – an Overview," ASME Paper No. 97-GT-347.
- (b) Emerson T P, 1978, "The Application of Foil Air Bearing Turbomachinery in Aircraft Environmental Control Systems," Paper No. 780-ENAS-18, ASME Proc. Intersociety Conference on Environmental System, San Diego, CA, July 10-13
- (c) Heshmat H, Walowit J A, and Pinkus O, 1983, "Analysis of Gas-Lubricated Foil Journal Bearings," J. Lubr. Tech., 105, pp. 647-655.
- (d) Balaji Sankar, 2012, "Numerical Simulation and Experimental Validation of Compliant Surface Gas Film Bearings", Masters Thesis, Academy of Scientific and Innovative Research, India.
- (e) Luis San Andres, Tae Ho Kim, 2006, "Computational Analysis Of Gas Foil Bearings Integrating 1D And 2D Finite Element Models For Top Foil", Research Progress Report, Texas A&M University.
- (f) Balaji Sankar, Sadanand S Kulkarni, 2015, "Modeling gas lubricated compliant foil bearings using Pseudo spectral scheme", Tribology online, 10,5(2015), pp 295-305.

A Comprehensive Case Study on Tripping of VFD Motor Driven AFC Fan & 3-Stage Centrifugal Air Compressor on High Vibration

Padmakar Jaiswal – Engineer, G.V.S.S.K Varma - Engineer

*Condition monitoring division, Rotary-Maintenance Department
HPCL Visakh refinery, Visakhapatnam*

Abstract

Variable frequency driven (VFD) Air Fin Cooler (AFC) fans are increasingly being used in refineries to control process temperatures by varying airflow. Because VFDs operate at different RPMs, some of the system's forcing frequencies may interfere with the natural frequency of the fan blade, resulting in resonance and increased vibrations.

The 3 stage centrifugal air compressors are critical rotary equipment which cater to entire requirement of refinery instrumentation air and plant air. Being critical equipment various parameters corresponding to compressors are monitored and these parameters have both alarm and trip values. Among those parameters are LVT (Low speed vibrations) and HVT (High speed vibrations) which indicate vibrations of the compressor during service. When equipment is stopped for maintenance, these compressor exhibit peculiar behaviour of increase in LVT & HVT Vibrations.

The various maintenance strategies used to address the aforementioned problems are discussed in this paper.

1.0 Introduction

The 3- stage centrifugal air compressors are critical rotary equipment which cater to entire requirement of refinery instrumentation air and plant air. The compressor which is considered in this case study is Elliot make PAP plus, Model DA3 compressor. The first and second stage impellers are mounted on the low speed pinion, the third stage impeller is mounted on the high speed pinion. The impellers are housed in scroll type casings. Both pinions are driven by one gear. The gear and pinions are helical design and are housed in a horizontally split gear case.

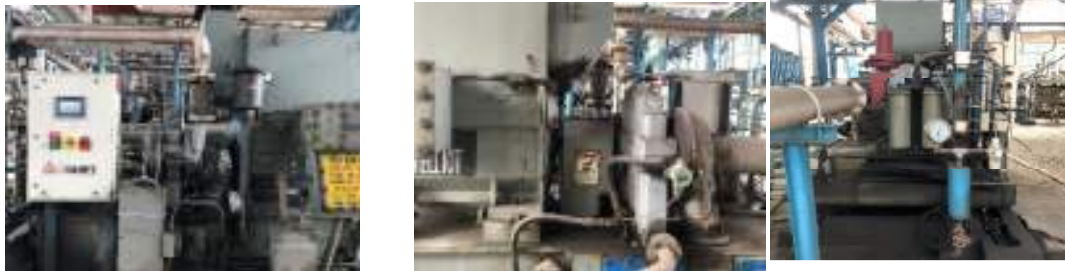


Fig 1: Elliot make air compressor

1.1 Principle of Compressor Operation

Filtered air controlled by an automatically operated inlet valve enters compressor's first stage, where it undergoes initial compression then it enters into 1st stage intercooler from there it enters compressor's second stage undergoes compression then it enters into 2nd stage intercooler and finally it enters into compressor's third stage there air is compressed to final discharge pressure before passing into plant air system.

1.2 Monitoring of Compressor parameters

Centrifugal compressors are critical rotary equipment and their outage reduces available plant and instrumentation air affecting entire refinery, so various parameters related to compressor are monitored so that it prevents unplanned outage and also catastrophic failure of the compressors.

Some of those parameters of the compressor that are monitored are:

1. Interstage Air Temperature (IAT)
2. Oil Temperature (IOT)
3. After Cooler Temperature (ACT)
4. Oil Pressure (OPT)
5. Low Speed Pinion Vibration (LVT)
6. High Speed Pinion Vibration (HVT)
7. Inboard side Temperature in Motor (IMT)
8. Outboard side Temperature in Motor (OMT)

All the monitored parameters have both alarm and trip values and when value of respective parameter reaches alarm value then alarm is displayed on the panel & in DCS and when that value reaches trip value and trip is enabled, compressor automatically trips protecting itself from catastrophic failure.

1.3 Vibrations in the compressor and it's causes

It is necessary to be interested in vibration in centrifugal compressors because it has a major effect on the performance. Generally, increasing vibration levels indicate some kind of failure. It is so because excessive vibrations are the outcome of some system malfunction. Below are some of the causes of Vibration:

- Unbalance
- Misalignment
- Looseness
- Bearing Issue
- Damaged Parts etc.

1.4 Unbalance

Most vibration problems in compressors are related to unbalance. A high vibration level may be directly related to a rotational force or a translational force that is caused by an unbalance condition. Unbalance may be caused due to several factors but most

predominant factor in case of centrifugal air compressors is dust accumulation on impeller vanes.

Generally centrifugal air compressors being rotating equipment are balanced and have certain vibration values but over a period of time dust enters inside and accumulates on vanes, being high speed machines even though there is small increase in mass it gets amplified causing large unbalanced forces and subsequently increase in the vibrations.

1.5 Maintenance Strategy

Whenever either LVT or HVT of the centrifugal air compressors reaches either alarm or trip value the maintenance strategy adopted in the refinery is to open respective stages (low speed or high speed) casings and carryout impeller cleaning so that dust gets cleaned and as a result unbalance due to additional mass of dust gets reduced and ultimately this leads to decrease in vibrations in the compressor.

1.6 Case Study

The 150KM2A (New Elliot) air compressor with design capacity of 6116 m³/hr was installed in MEROX unit in the year 1989. The alarm and trip values of the LVT for this compressor are 28.00µm and 30.48µm respectively, similarly the alarm and trip values of the HVT for this compressor are 22.86 µm and 30.48 µm respectively

The LVT value of this compressor was on increasing trend and the compressor tripped on high LVT at 30.48 µm on 23/01/2023, then the impeller cleaning job was taken up on 24/01/2023, first and second stage (low speed) were opened and impellers were cleaned, then the compressor was placed in service on 27/01/2023, it was observed that LVT values were reduced from 30.48µm to around 14.00µm and henceforth the LVT value of the compressor was in between 13.00µm to 15.00 µm till date.



Fig 2: Dust accumulated on Impeller and diffuser of 150KM2A compressor

1.7 Conclusion

Centrifugal air compressors being critical rotary equipment, various parameters associated with them are monitored to prevent catastrophic failure of compressors. The maintenance

strategy adopted i.e. Impeller cleaning was found to be useful in reducing vibrations in compressors not only in the above case but also in many other cases in the refinery.

2.0 Variable frequency driven (VFD) Air Fin Cooler (AFC) fans

Variable frequency driven (VFD) Air Fin Cooler (AFC) fans are seeing ever increasing usage in refineries as an efficient way to control process temperatures by varying the airflow. By progressively ramping up the motor's speed, variable frequency drives reduce power peaks. The drive allows the motor to run at maximum horsepower only when necessary by automatically regulating motor speed. As a result, energy costs are reduced, and operational efficiency is raised.

Since VFDs run at different RPM, there are chances that some of the forcing frequencies of the system might interfere with the natural frequency of fan blade and may result in resonance causing increased vibrations.

2.1 Troubleshooting of high vibration in Variable Frequency Drive AFC fan: A case study.

Recently during commissioning of one of the VFD AFC Fan (Tag no. 501-AM-111E1) in our new unit (CDU-IV), it was observed that the fan was tripping at high vibration. Multiple vibration diagnosis were carried out by the Condition Monitoring team to find out the root cause of high vibration. 'Coast Down Peak Hold' tool of AMS 2140 vibration analyzer was used to check for resonance during coast down of VFD motor and natural frequency of the fan blade was identified. It was observed that when 'Blade Pass Frequency' interferes with 'Blade Natural Frequency', vibrations in motor & fan observed to escalate. Same was verified by collecting motor and fan vibrations with handheld accelerometers.

Following observations were noted during troubleshooting of CDU-IV AFC Fan 501-AM-111E1:

- Motor Coast Down Peak Hold spectrum was taken. 1st Natural Frequency=15.3 Hz i.e. 918 rpm. (Refer Fig. 3)
- Also as per OEM data sheet, Fan Blade Natural Frequency= 849 RPM which is almost similar to our Coast down Peak Hold spectrum analysis result. However, the bolting and fixing of blades can cause changes in rigidity of material and thus natural frequency can also slightly differ from the ideal value.
- Fan blade pass frequency varies with Fan RPM and vibration found at higher side when blades pass frequency pass through blade natural frequency band.
- Fan blade pass frequency of 918 rpm corresponds to Motor RPM = 1227 rpm [$918 / (\text{Velocity ratio} * \text{No. of blades}) = 1227 \text{ RPM}$]. Here velocity ratio = 0.187 ($274/1460 = 0.187$); No. of blades = 4.
- Both motor and fan vibrations were collected with handheld accelerometers. It was observed that both motor and fan vibrations increased in the range of 1200-1300 RPM. Max motor vibration- 5 mm/s; Maximum fan vibration- 6.5 mm/s.
- Beyond 1200-1300 RPM range, vibrations are less than 2 mm/s.
- Trip limit of fan vibrations were 8 mm/s.

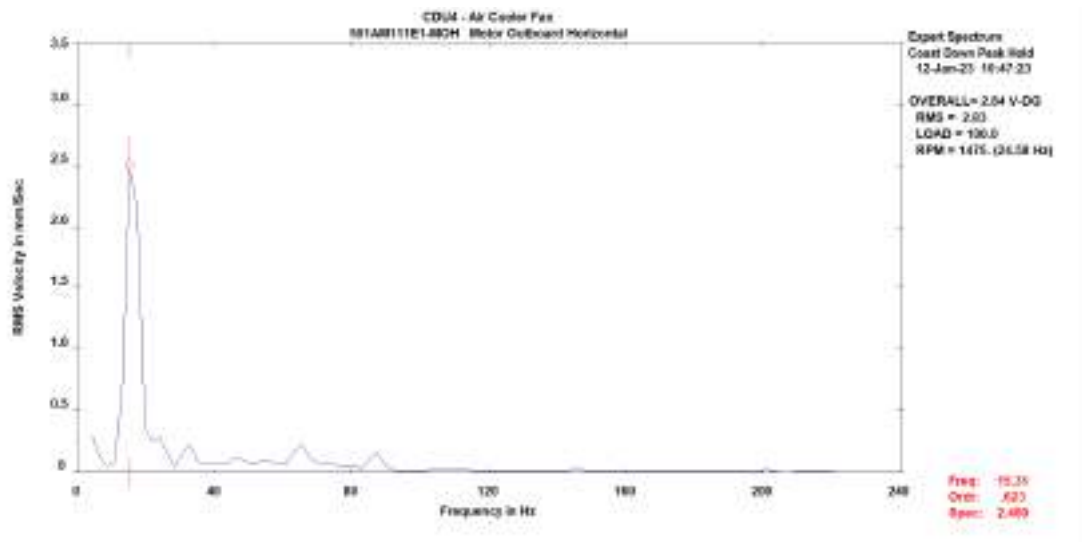


Fig 3: Coast Down Peak Hold Spectrum

Following were the recommendation released by Condition Monitoring as per the observation:

- Take up with OEM to make suitable modifications on Fan blade so that it's natural frequency shifts beyond blade pass frequency for entire motor RPM range i.e 0-1500 RPM.
- Make modification on VFD so that motor skips of 1200-1300 RPM range.

2.2 Conclusion

This aforementioned case study discusses how VFDs can excite resonant frequencies of Fan blade. If the fan operating on VFD has one or more resonances in the operating speed range, these speeds must be 'locked out' so as to keep the vibrations in motor and fan within permissible limits.

Acknowledgements

I would like to acknowledge the support from Mr. Marpina Naveen Kumar and Mr. V. V. Rajsekhar, Maintenance, HPCL Visakha Refinery

References

- [1] Klaus Brun and Rainer Kurz: Compression Machinery for Oil and Gas, 2019
- [2] G. Genta: Kinetic Energy Storage, 1985
- [3] Miroslav Chomat: New Applications of Electric drive

Eliminating the Problem of Frequent Tripping of Main Reversing Mill Motor of Cold Rolling Mill

Sudip Kumar Mukherjee, Saurav Ghosh, Malay Choudhury

Tata Steel Limited, Jamshedpur India.

The CRM Bara complex produces Cold Rolled Coils by rolling the Hot Rolled sheets. The facility has a 6Hi reversing cold rolling mill which is powered a reversing motor. The motor rotates a gearbox which in turn rotates the work rolls. In the last major shutdown, both the motor and the gear box were replaced. The motor bearings are spherical sleeve bearings, lubricated by hydrostatic and hydrodynamic lubrication. The oil pressure & flow parameters are being monitored by field instruments and the logics are in place for fail safe operation. The shaft vibration of the bearings is being monitored by proximity probes. After the startup of the plant, there were instances observed when the hydrostatic oil pressure of drive end bearing was found as fluctuating and sometimes it reaches below its set limit causing the tripping of motor and hence resulted loss of production. The vibrations were within the limits. A vibration multichannel analyzer connected to the buffer output of the proximity probes along with a data logger to measure hydrostatic oil pressure & flow. This paper describes the method adopted based on real experience to reach at the root cause and the problem. The shaft centerline plots at different operating condition of the motor helped to identify the rotor position causing the hydrostatic pressure fluctuation. Accordingly corrective action was taken to eliminate the problem.

Keywords: *Hydrostatic Lubrication, Proximity probe, Shaft Centerline plot, Alignment correction.*

Introduction:

The CRM Bara complex of Tata Steel Limited of Jamshedpur produces Cold Rolled Coils by rolling the Hot Rolled sheets. The facility has a 6Hi reversing cold rolling mill which is being powered by a reversing motor. The motor rotates a gearbox which in turn rotates the work rolls. Any outage /interruptions in this equipment leads to loss of production. The motor bearings are spherical sleeve bearings lubricated by hydrostatic and hydrodynamic lubrication system. The mill is the reversing mill and hence the motor changes its direction of rotation after each pass of rolling. As per the operational requirements, both hydrodynamic oil pumps and hydrostatic lubrication pumps runs continuously to maintain a constant lift of the journal inside the bearing. The oil pressure & flow parameters are being monitored by field instruments and the logics are in place for fail safe operation. The shaft vibration of the bearings in the motor are being monitored by proximity probes.

Problem Statement:

In the last major shutdown, both the motor and the gear box were replaced based on the Condition Based Maintenance. The gearbox and motor were installed as per the standard operating procedure.

After the startup of the plant, there were instances observed when the hydrostatic oil pressure of the motor drive end bearing (Figure 1) was found fluctuating and sometimes it

reaches below its set limit causing the tripping of motor and hence resulted loss of production. The vibrations were measured and found within the limits.

The lubrication system consists of three numbers of hydrostatic oil pumps, in which one pump supplies oil to each bearing and one is kept stand by. Similarly, there are three pumps for hydrodynamic lubrication with same operation philosophy.

Figure 1 shows the pressure & flow recorded in the motor drive end (DE) bearing and Figure 2 shows the pressure & flow recorded at Motor Non-Drive end (NDE) bearing, during the different pass of rolling.

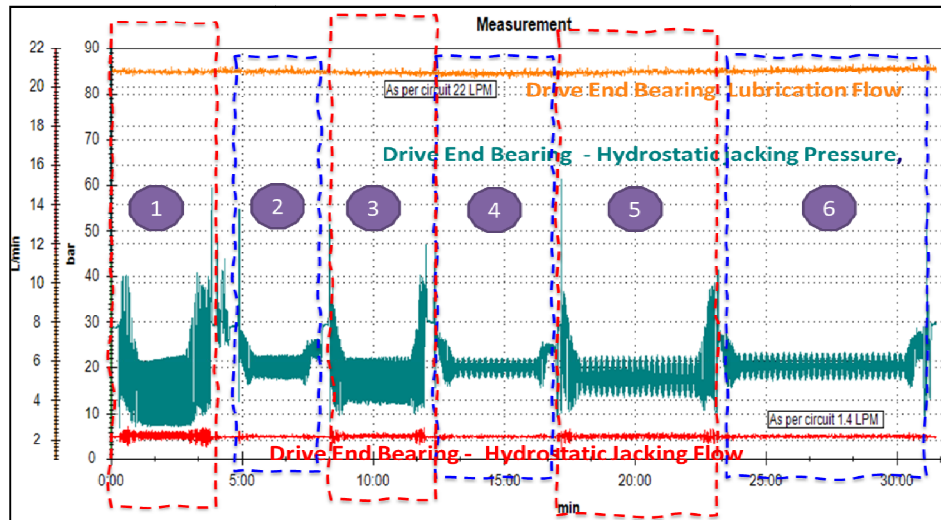


Figure 1 – Hydrostatic oil pressure and flow trend in Motor DE Bearing

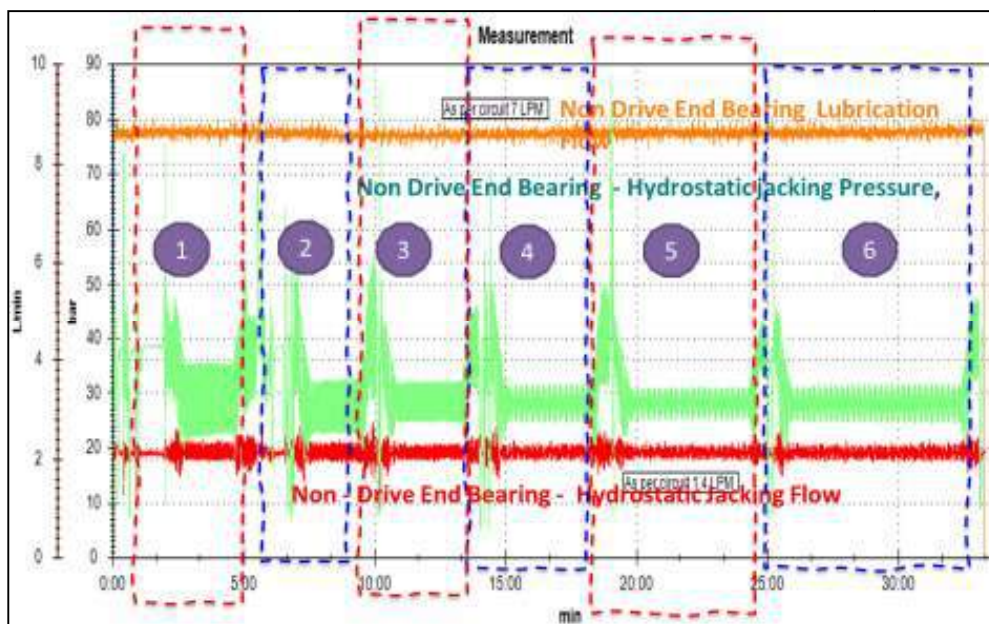


Figure 2 – Hydrostatic oil pressure and flow trend in Motor NDE Bearing

Measurement & Analysis:

For further analysis of the problem the construction of the bearing was studied. The OEM of the motor confirmed that the bearing is a plain cylindrical sleeve bearing and the hydrostatic oil port is located at the bottom centrally. It was then thought to monitor and analyze the shaft vibration (Figure 3) by a multichannel analyzer along with the hydrostatic oil pressure at different pass of the rolling.

Table 1: The comparative data of Hydrostatic oil pressure correspond to vibration at different pass of rolling

Pass No	DE_Min Oil Pressure	DE_Max Oil Pressure	NDE_Min Oil Pressure	NDE_Max Oil Pressure	ViB_DEX	ViB_DEY	ViB_NDEX	ViB_NDEY
UOM	Bar	Bar	Bar	Bar	Micron P-P	Micron P-P	Micron P-P	Micron P-P
Pass1	7.00	22.50	22.00	35.00	60.00	41.00	21.00	21.00
Pass2	18.00	22.50	22.00	33.00	21.00	35.00	10.00	21.00
Pass3	11.00	22.50	25.00	33.00	41.00	30.00	21.00	18.00
Pass4	18.00	22.50	25.00	32.00	21.00	30.00	18.00	21.00
Pass5	12.00	22.50	25.00	31.00	40.00	21.00	20.00	18.00
Pass6	17.50	22.50	25.00	32.00	20.00	25.00	18.00	21.00

OVERALL VIBRATION

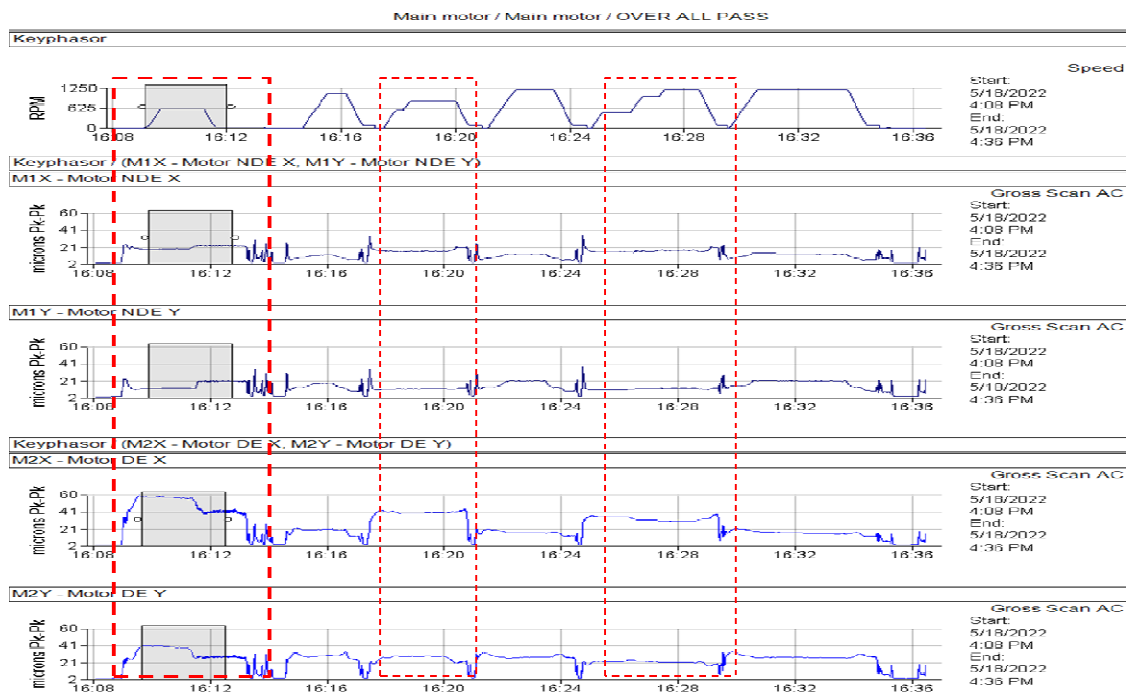


Figure 3: Shaft vibration of the motor DE & NDE bearing from the proximity probes X & Y

The data collected is statically correlated and found that the Low oil Pressure of the Motor bearing is highly correlated with the vibration and this phenomenon is predominant in

ODD pass only. Further the shaft centre line plot of Motor Drive end bearing has been studied along with the orbit plot during the even and odd pass of the rolling.

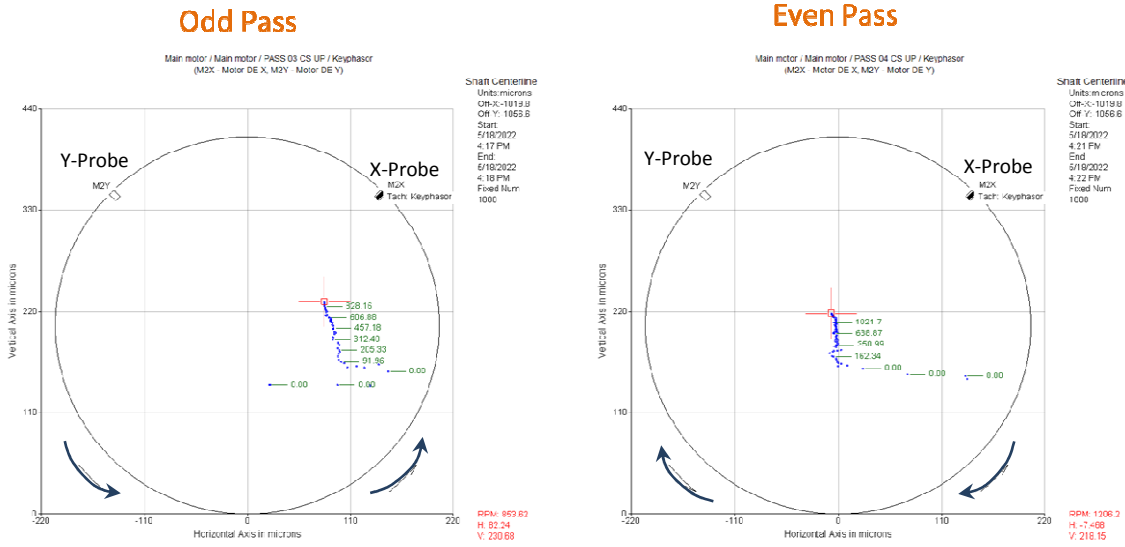


Figure 4: Shaft Centre line plot of drive end bearing a) During the odd pass and b) during the even pass.

The figure 4 shows the Shaft centre line plots and Figure 5 shows schematic position of the shaft inside the bearing and viewed along with the orbit plots (unfiltered) under odd and even pass of rolling.

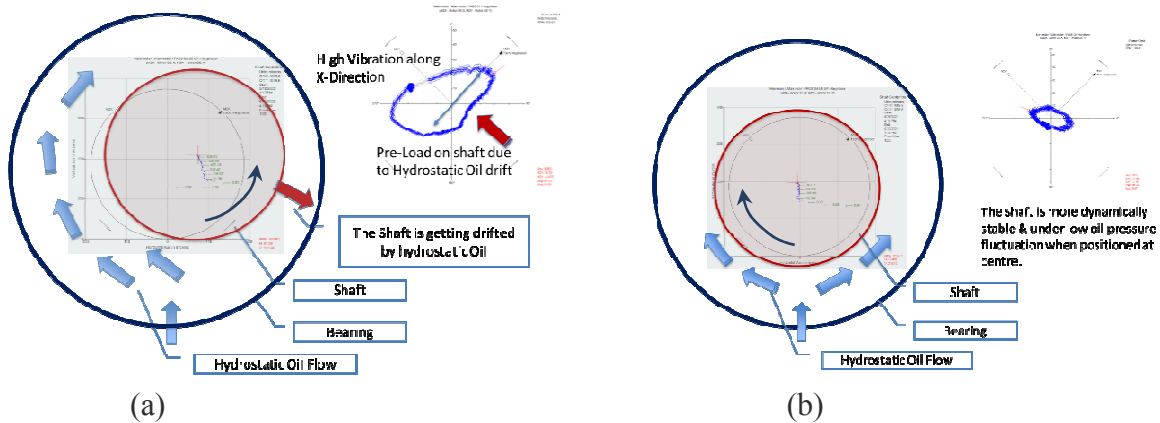


Figure 5: Shaft centre line plot along with the orbit plot a) during the odd pass and b) even pass of the rolling.

The observations are summarized by using the following why-why analysis. This shows that during the odd pass and due to direction of rotation, shaft is positioned off centre and the hydrostatic oil drifted the shaft towards one side and the shaft is getting preloaded in Y direction & increased vibration in X direction.

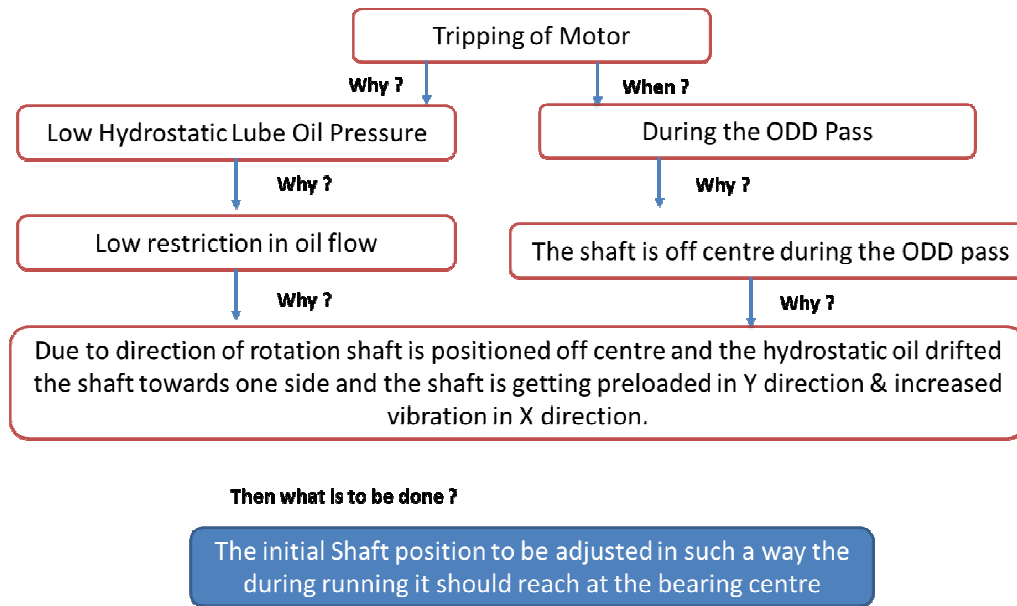


Figure 6: Root cause analysis of the problem

Corrective action & Confirmation of Effect:

To achieve the desired shaft position, it was decided to change the rotor position by re-alignment, such that, during running condition the rotor should reach at the center of the bearing to create enough restriction over hydrostatic oil port. This will in turn help to maintain the required pressure in the hydrostatic lubrication system.

Trial 1: During the first trial the initial alignment readings checked. The correction decided to lower the motor shaft compared to the gearbox, by the amount, as measured vertical lift due to hydrostatic oil pressure. In the vertical plane the initially the offset was measured as +0.02 mm which is adjusted to -0.12. However, in the horizontal plane the offset was measured as +0.17mm (+ indicate towards X – probe) which is adjusted to -0.10 mm (- indicate towards Y probe) and a trial taken.



Figure 7: Correction of alignment in Trial 1

Result of Trial 1: The result of trial 1 was not encouraging, the hydrostatic oil pressure came to the level that the standby lubrication oil pump started to maintain the pressure. Again, the shaft centre line data was taken for further analysis.

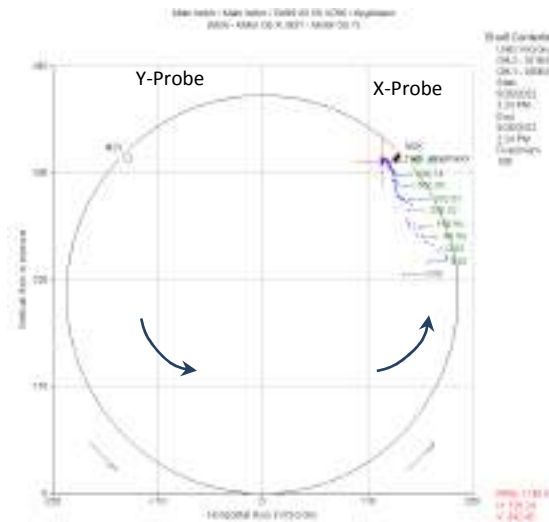


Figure 8: Shaft centre line plot of Motor Drive End bearing after Trial 1

Trial 2: The (-) horizontal movement resulted the shaft centre to reach at the extreme position of rotor, in the clearance circle. This condition is opposite of the desirable location. The motor to be moved in (+) direction within the tolerance limit so that the shaft position reaches to the optimum location. Again, the alignment of the motor was done and following correction was done.



Figure 9: Correction of alignment in Trial 2

Result of Trial 2:

The result of the trial 2 was encouraging and the hydrostatic oil pressure found improved (Figure 10). The shaft centre line plot data was captured and found the position of the journal inside the bearing. (Figure 11)

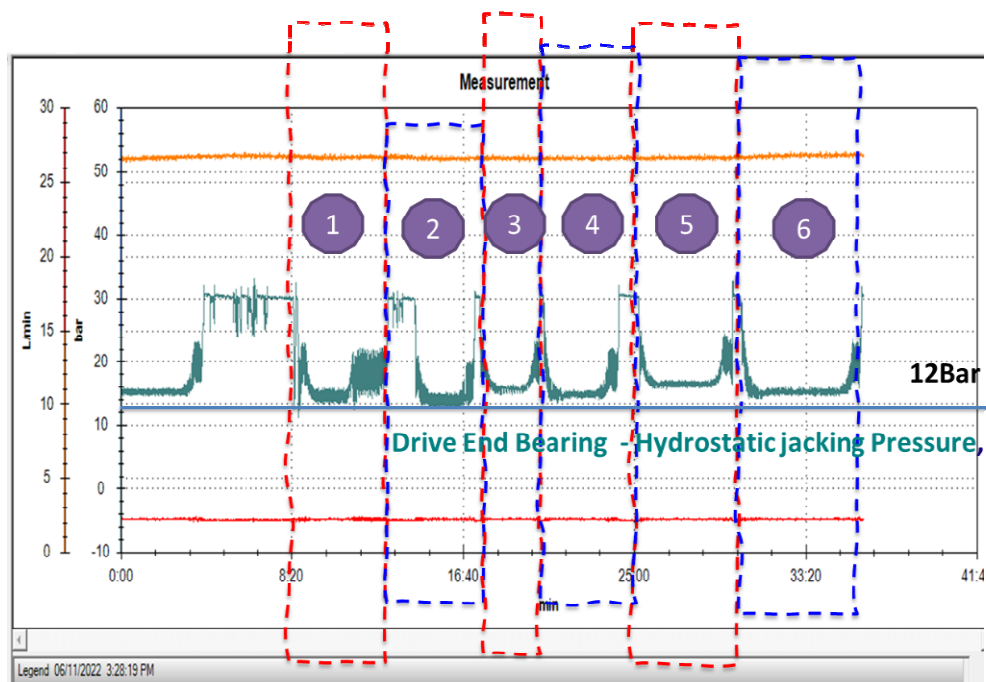


Figure 10: Hydrostatic oil pressure and flow trend in Motor DE Bearing

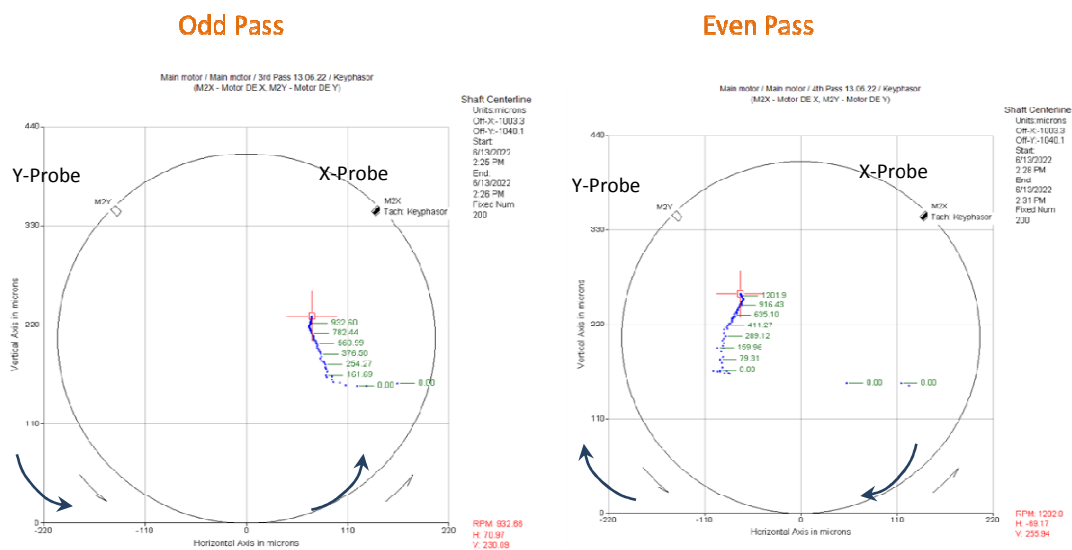


Figure 11: Shaft centre line plot at Motor Drive end bearing after Trial 2

The shaft centre line plot as per Figure 11 shows that the Shaft centre is being symmetrically placed across the centre line and one of hydrostatic pump sufficient to maintain the pressure. The data was kept under the observation and found the plant is operating smoothly without any interruption.

Conclusion:

The protocol for the alignment is made and standardized so that such problem should not be repeated further. The shaft centre line plots determine the position of the journal inside the bearing which helped to determine the desirable location of the journal and the alignment correction helped to achieve the position.

References:

- 1) Fundamentals of Rotating Machinery Diagnostics –Donald N Bentley, Charles T. Hatch Edited by Bob Grissom. Book ISBN 0-9714081-0-6
- 2) Importance of Monitoring Shaft Centreline Data – Mark A Jordan, Bently Nevada Corporation, Orbit Article, May 1992 Page 11-14.

Vibration Analysis – An ideal tool to detect early signs of Locomotive Wheel axle Bearing Deterioration.

Hemant Bari, Atul Deshpande, Suhas Patil

*#Department of Maintenance Planning, Condition Monitoring Cell,
Adani Electricity Mumbai Limited,
Adani Dahanu Thermal Power Station, 2x250 Mw, Dahanu, Mumbai, INDIA.*

Abstract

Adani Dahanu Thermal Power Station (ADTPS) is one of the best power generation plants in the country, which commenced its commercial operations in January 1996. Recognized with innumerable awards, this power plant is known for its distinctive features that set it apart from others in terms of technological innovation, international performance, and sustainability for a longer period.

This paper shares a success story out of the Implementation of Co-ordinated Condition Monitoring techniques at ADTPS, wherein imminent Wheel Axle bearing deterioration of Diesel Locomotive was diagnosed. The Condition Monitoring Techniques Noise, Vibration and Acceleration spectrum analysis helped in diagnosing the exact root cause of abnormality of knocking sound from Wheel axle & detected early deterioration of the bearings at notch 04 speed during no-load condition & thus avoided secondary damage to Loco wheels, Traction Motor & associated Gear drive and other major benefit includes prevention of downtime, avoidance of major repair or replacement costs and reliability of Unit.

Case study has clearly demonstrated the importance of Vibration Monitoring & FFT analysis that has saved the plant from huge losses in terms of demurrage risk and coal availability for electricity generation, unplanned breakdown time and associated maintenance & spares costs.

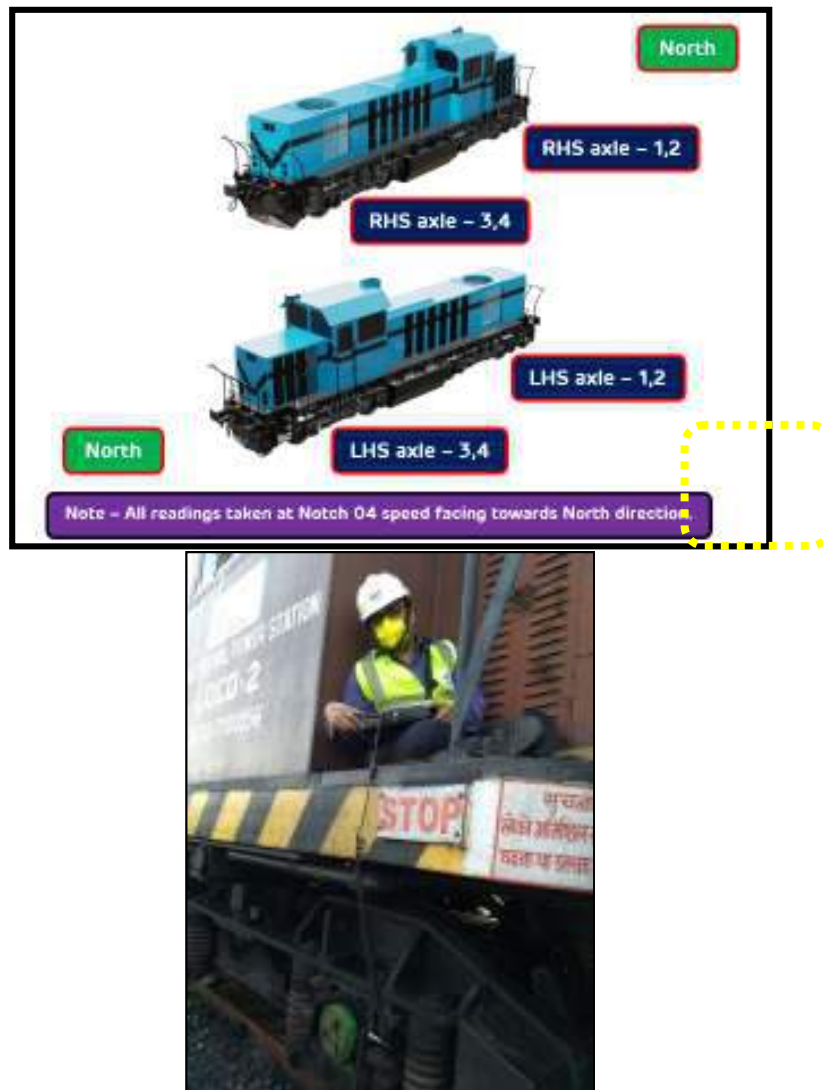
Key Words: *Vibration & Acceleration Monitoring, FFT Analysis.*

Case 1: Detection of Locomotive wheel axle bearing deterioration

Following is success story of the Implementation of Condition Monitoring techniques at ADTPS, wherein imminent Wheel Axle bearing deterioration of Diesel Locomotive was diagnosed.

1.1 Pre - Maintenance History:

1. On 10.10.2021, during routine operation, Loco Pilot reported to Auto base Maintenance team regarding abnormal sound from left bearing of first axle below driver cabin
2. After the initial checks, on 11.10.2021, Condition Monitoring team was consulted for the issue & checked feasibility for safe vibration data collection to pinpoint the defect
3. Then, offline data collected for all the wheel axle bearing at notch 04 speed & observed that while facing towards North direction, first axle left & right bearing (below operator cabin) Vibration & acceleration value was maintaining on higher side @ 15 mm/sec (RMS) & 6.3 g (Peak) respectively.(Refer figure 1)



4. High Acceleration spectrum analysis revealed that early bearing deterioration is in progress.
5. Other wheel axle bearing vibration found @ 5 to 6 mm/sec with stable acceleration value @ 1.5 to 2.0 g respectively and no deviations noticed for online vibration of Diesel Engine & Alternator.
6. All above points discussed in plant HOD meeting&observing high noise, vibration & acceleration value, decided to stop LOCO operations for replacement of wheel axle.
7. The detail diagnosis analysis was carried out as follows

1.2 Vibration Diagnosis:

Acceleration spectrum (Refer figure 2) analysis revealed that there is increase in higher frequencies and the contribution of Non- Synchronous Energy (Any vibration that is greater than the 1x frequency but is not a whole number multiple of it) is at higher side which confirms bearing defects

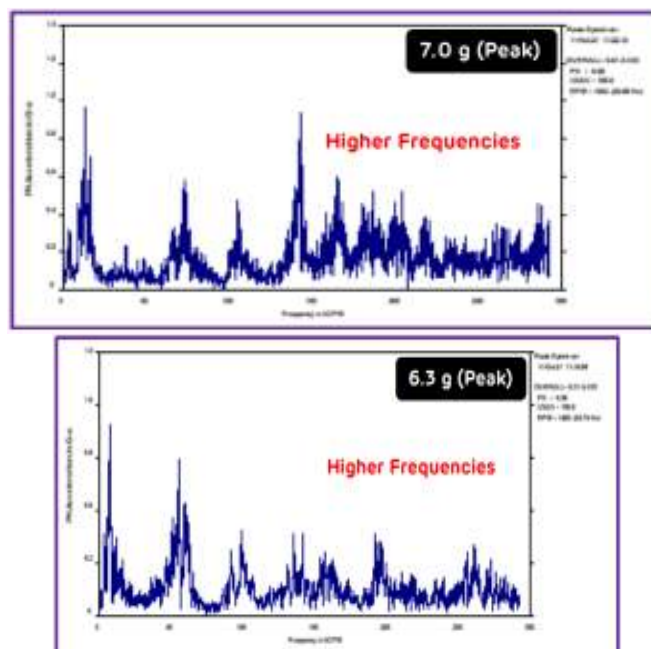


Figure 2: Acceleration Spectrum of Wheel Axle Bearing (LHS & RHS)

Acceleration spectrum (Refer figure 2) analysis revealed that there is increase in higher frequencies and the contribution of Non- Synchronous Energy (Any vibration that is greater than the 1x frequency but is not a whole number multiple of it) is at higher side which confirms bearing defects.

Table 1: Fault Identification chart

Synchronous	Non-Synchronous	Sub-Synchronous
<ul style="list-style-type: none"> • Mass imbalance • Looseness • Worn or damaged gears • Eccentric rotation • Misalignment • Reciprocating motion • Vane-pass 	<ul style="list-style-type: none"> • <u>Bearing defects</u> • Cavitation • Electrical faults • Nearby machines and components • System resonances 	<ul style="list-style-type: none"> • Nearby machines and components • Severe looseness • Rubbing of rotors or shafts • Belt vibrations

The high frequencies are got excited. These high frequencies happen to be the bearing defect frequencies. (Refer Table 1). Thus, it was confirmed that front wheel axle bearing deterioration is in progress.

Decided to go for replacement of all wheel axles (Total 04 nos.).

1.3 Maintenance work carried out:

1. Loco-02 was towed to the maintenance bay with the help of Loco-01.
2. Ensured locking all the wheels with wedges.
3. The upper carriage was lifted by EOT crane by following all safety norms .
4. Traction Motor connections and pneumatic connections removed.

5. Traction Motors and accessories removed, and bogies lifted.
6. Old wheel and axle assemblies removed.
7. Through inspection & testing of all Traction Motor, driver gear carried out & no abnormality noticed.
8. All Bearing carriers and shell bearing cleaning ensured, and inspection done. Found ok.
9. All New wheel installed, and axle assemblies cleaned, and bogies mounted back. (Refer figure 3)



Figure 3: Maintenance work execution

10. All Traction Motors mounted on respective axles, and accessories fitted.
11. Upper carriage fitted and Loco trial taken at notch 04 speed & all Vibration, Acceleration, Noise found within limit. (Refer figure 4).

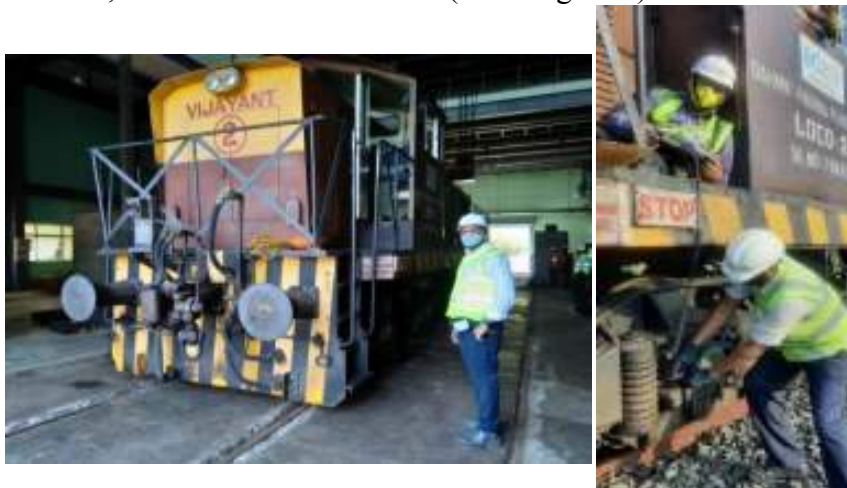


Figure 4: Post Maintenance data collection

12. Also, all online vibration of Diesel Engine & Alternator recorded normal.

1.4 Post Maintenance Vibration readings

Table2: Pre-post maintenance vibration & acceleration data

Initial Vibration & Acceleration readings – 11/10/2021				
Wheel Axle Bearing - H (Facing towards north)	Vibration (mm/sec)	Acceleration (g)	Vibration (mm/sec)	Acceleration (g)
	LHS		RHS	
01	15 to 30	7 to 18	15.2	6.3
02	5.9	2.0	5.5	1.7
03	5.7	1.8	5.9	1.5
04	6.0	1.7	6.1	1.9
Final Vibration & Acceleration readings – 20/10/2021				
Wheel Axle Bearing - H (Facing towards north)	Vibration (mm/sec)	Acceleration (g)	Vibration (mm/sec)	Acceleration (g)
	LHS		RHS	
01	5.7	1.4	5.5	0.9
02	5.9	1.3	5.4	1.0
03	5.6	1.0	5.7	1.2
04	5.8	1.2	5.3	1.0

2. Results and Discussion

This case study has clearly demonstrated that Noise Monitoring is a vital tool for detection of abnormality in rotating machinery at an early stage. Deviation in Vibration & Acceleration value played important supportive role to confirm the deterioration of Wheel axle bearing even before any noticeable changes to be reflected in any other process parameters (Refer table 2). Every vibration analyst should use this tool to improve vibration analysis accuracy as this can help maintenance organization to become more proactive and accurate.

3. Conclusion

- Co-ordinated Condition Monitoring helped in diagnosing the exact root cause of abnormality at a very early stage.
- It shows that early diagnosis has resulted in timely action and savings in cost and avoidance of unplanned shutdown.
- This has saved the plant from huge losses in terms of generation, unplanned breakdown of equipment and associated maintenance & spares costs.
- Also, other major benefits include reduction in downtime, avoidance of major wheel repair or replacement costs and reliability of Locomotive.

REFERENCES

- [1] Rao J S, 2000, *Vibratory Condition Monitoring of Machines*, Narosa Publishing House, New Delhi.

Analysis of Incorrect Condition Predictions Leads to Corrective Action for Understanding Monitoring Defects & Instrument Limitations - A Case Study

Rana Dutta, B. Koteswar Rao, Janaki Rajan

*Consultant, Electro steel Castings Limited, Srikalahasthi. Rachagunneri, AP
Manger &, Engineer CBM, Electro steel Castings Limited, AP*

Abstract

Condition Monitoring reports regarding the status of process machines at time tend to go wrong and equipment declared as 'normal' fails abruptly and vice-versa. As the occurrence of such prediction failures are minimal, condition monitoring engineers tend to overlook them as outliers and no root cause analysis of the failure in predictions are normally done. In this paper it has been shown that if root cause analyses for wrong predictions are done then it leads to take corrective actions for forthcoming monitoring. Analysis corrects the monitoring technique and also apprises about the instrument's limitations.

Key Words: *Shock pulse, monitoring, prediction, Instrument.*

1.0 Introduction

In one of the manufacturing process a head pulley is belt driven and is operating at an ambient temperature of about 40⁰-45⁰ centigrade. The head pulley bearing is water cooled and the operating condition is continuous except for mandatory stoppages for tool change. Lubrication is manual and done during stoppages for tool change.

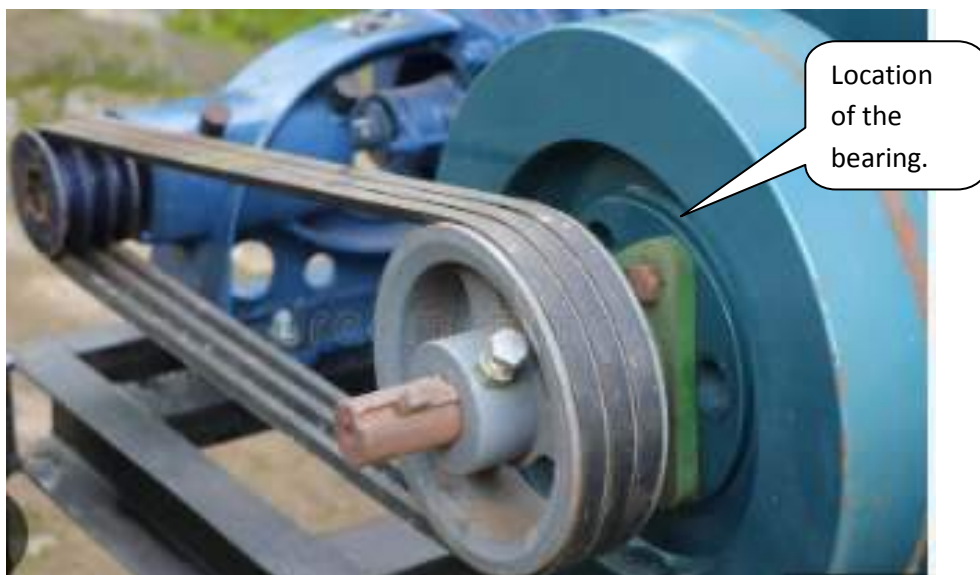


Figure : 1 Picture of the headstock showing the bearing location

The specification of the blower and the motor is given in Table : 1

Table: 1 Motor & Blower Specification:

Motor Rating	Full Load Current	Motor RPM	Motor Type	Motor Bearings	Head Pulley Bearings	Cooling Water Pressure	Number of belts	Belt Size
80kW	117 A	992	DC	Anti-friction Bearings	Anti-friction Bearings	0.0429 MPa	8	SPB 3800

The head pulley is attached to a rotary kiln which rotates on roller bearings as shown in the schematic sketch Figure: 2

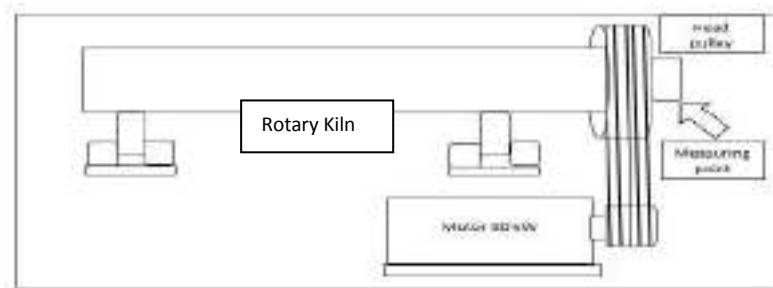


Figure : 2 Schematic layout of the head pulley of the rotary kiln

2.0 Earlier Condition Monitoring Program of the System

The equipment being critical in the process daily vibration readings were noted and monitored but the monitoring process was not effective as many failures were reported which were sporadic. Through vibration monitoring early warning signs of bearing condition deterioration were not being observed and as such timely corrective action were not being taken and failures were sudden. Root cause analysis of these prediction failures were carried and it revealed two interesting issues.

2.1 Measuring Point not Appropriate

Figure : 3 shows the schematic position of the bearing & the nearest available measuring point.

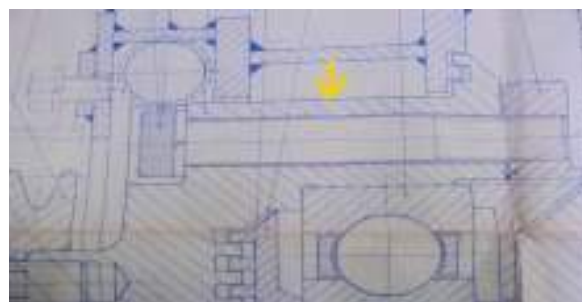


Figure: 3 Measuring Point (arrow) & location of the bearing.

From Figure :3 it is evident that the nearest point where the vibration probe could be held was quite a distance from the probe and correct signals were not being noted (figure:4) . More over due to location of the head pulley vibration monitoring could be done only in radial position. Signature analysis of axial position gave no real values (figure:5)

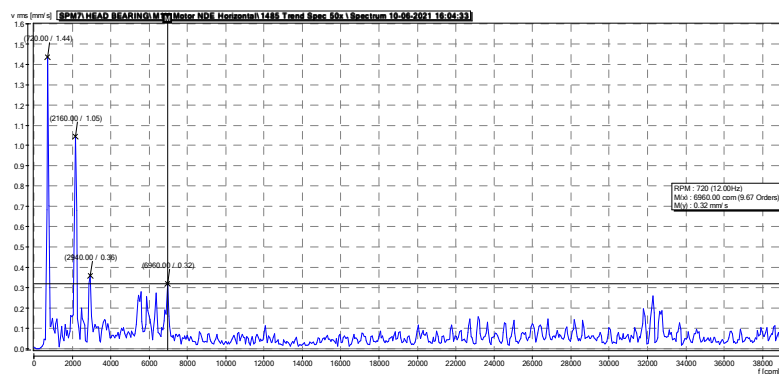


Figure: 4 Signature analysis no significant impact as probe is held away from bearing

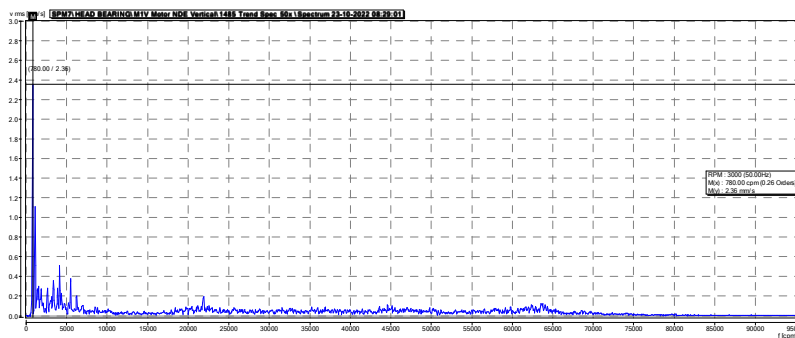


Figure: 5 Axial axis signature analysis shows no significant impact

2.2 Wash Out of the Lubricants for Seal failure.

The bearing and the rotary kiln are water cooled so there are many seals to protect the bearing from water ingress (figure: 6). At time seals do fail and there is water ingress in the bearing resulting in wash out of the lubricants. This water leakage is barely visible externally unless there is a gross failure of the seals then water pours out from the cover indicating seal failure and calls for machine stoppage for seal replacement. With even minor leakage bearing lubricants gets drained out subjecting the bearing for an early failure. With vibration monitoring this lubricant failure is difficult to predict from signature analysis and ultimately there is a sporadic failure.

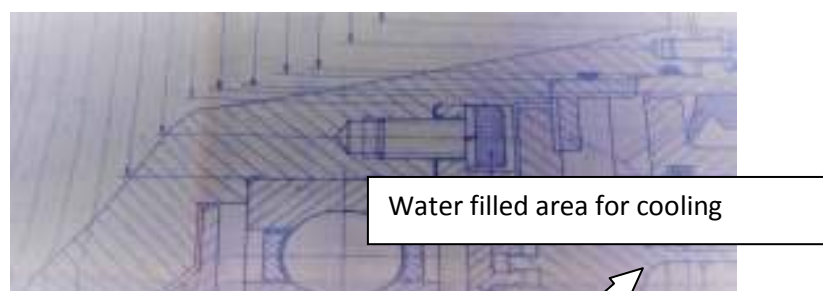


Figure: 6 Seal (arrow) & water filled area in respect to bearing location

2.3 Inconsistent RPM

The rpm of the kiln varies during the process and though all efforts are taken to monitor at fixed rpm but because of operational problem this is not always possible.

2.4 Analysis for vibration monitoring inadequacy & corrective action

From the three monitoring problems it was envisaged that to depend upon vibration monitoring alone will not give the correct condition of the bearings and correct prediction will frequently elude the reporting. The next preferable tool was the bearing checker which not only gives the condition of the bearing but also the lubricant condition and it is based on shock pulse and not bearing frequency. A similar tool was used earlier in one of our sister organization for checking of lube oil condition thus necessary expertise was available to operate instrument. The analyzer that was being used in the sister concern measured the lube condition in terms of High Rate of Occurrence (HR) & Low Rate of Occurrence (LR).

3.0 Brief description of the Shock Pulse Method and its function.

In the paper ‘Condition Monitoring of Anti-Friction Bearing Using Shock Pulse Method’ author V Vijayanand¹ has described the Shock Pulse Method ‘as development of a mechanical shock wave caused by the impact between the masses. At the instantaneous moment of impact, molecular contact occurs and a compression (shock) wave develops in each mass. ‘

‘These mechanical impacts cause shock pulse so the bearing is a "Shock Pulse Generator". The magnitude of these shock pulse is dependent upon the surface condition and peripheral velocity of the bearing (size & rpm) using the SPM technique. it is possible to measure the shock pulses caused by the above surface roughness and thus follow the progress of a bearing’s conditions from new installation through the various stages of deterioration, until ultimately, the bearing has to be replaced. Decibel scale (dB) is used. Thus, the intensity of the shock pulses generated by the bearing is measured and expressed in dBsv decibel shock value). Relationship between shock pulses’ A picture of the instrument is shown in Figure :7



Figure: 7 The bearing checker along with the headphone

4.0 Monitoring of the Head Pulley Bearings with Bearing Checker.

Monitoring started with the new checker after making a schedule as per Table:2 and the reports generated are shown in Table : 3

Table: 2 Schedule for Bearing Checker Monitoring

Bearing Checker SCHEDULE												
Schedule Planned Monitoring Date	DBT	Breakdown	SC	Not in Operation	DBT	Bear Cond. Wearing	OP	EDM Resource Pro.				
CBM Schedule Vibration Monitoring Plan	DBT	Shutdown	STA	Offical to Receive	ETE	Equip. StandBy	USC	En Safe Condition				
		ALERT	ALARM			NORMAL						
Sr.	Equipment	UNIT	POWER RATING (KW)	CURRENT RATING (A)	SPEED (RPM)	DD of Bg	DE BEAR	DE BEAR	NDE BEAR	DBT	Am-23	Feb-25
1	M-2 Head bearing	Kiln	380								*	*
2	M-3 Head bearing	Kiln	550								*	*
3	M-4 Head bearing	Kiln	550								*	*
4	M-5 Head bearing	Kiln	80								*	*
5	M-6 Head bearing	Kiln	80								*	*
6	M-7 Head bearing	Kiln	80								*	*
7	M-8 Head bearing	Kiln	550								*	*

Table 3: Reports generated after checking with the bearing checker.

ELECTROSTEEL CASTING SRIKALAHASTHI WORKS CBM CELL SPM 02-08 HEAD BEARING SPM (SHOCK PULSE METHOD) REPORT						
Area	DIP-HZ	Machine	SPM 02 to 08			REPORT DATE:02.01.2023
MACHINE NAME	Kiln rpm	DN	Head Bearing Drawing no	Head Bearing ID	STATUS	Remarks/Recommendation
M-02	324	400	NA	D3	ALERT	Lubricate the Head bearing and inspect for any remarks.
M-03	280	450	NA	D4	ALERT	Lubricate the Head bearing and inspect for any remarks.
M-04	550	200	401	B2	NORMAL	Operate with schedule inspection and maintenance.
M-05	440	300	421	C2	ALARM	Immediate Lubrication and Lube test to be Required.
M-06	480	300	421	C3	ALERT	Lubricate the Head bearing and inspect for any remarks.
M-07	760	150	381	A1	ALERT	Lubricate the Head bearing and inspect for any remarks.
M-08	1160	100	381	A4	NORMAL	Operate with schedule inspection and maintenance.

The CBM department internally plotted the trends of each machine with the dBC (carpet decibel) & dBM (maximum decibel) values to check the relation of the two trends. This learning was inherited from the earlier use of the lube oil analyzer where the widening difference of LR & HR indicated deterioration of the bearing (Figure:8)



Figure: 8 An earlier trend graph report of LR / HR showing difference between trends

Based on the learning from HR & LR trends (figure8) the same principle was followed for dBC & dBM plotting for each of the 7 head pulleys reading which was taken once daily (Figure: 9).

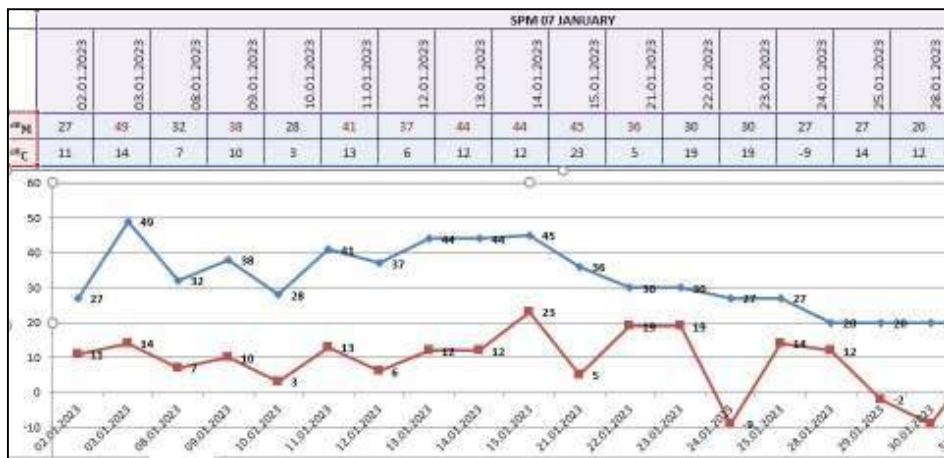


Figure 9: Trend Graphs of dBC & dBM of one of the machines

The bearing checker was commissioned in December 22 and the monitoring system from the CBM department continued on the trend graph basis till mid-January 2023 when a head pulley bearing of one of the machines failed though the trend graph showed no abnormality as per the trend (Figure:10).

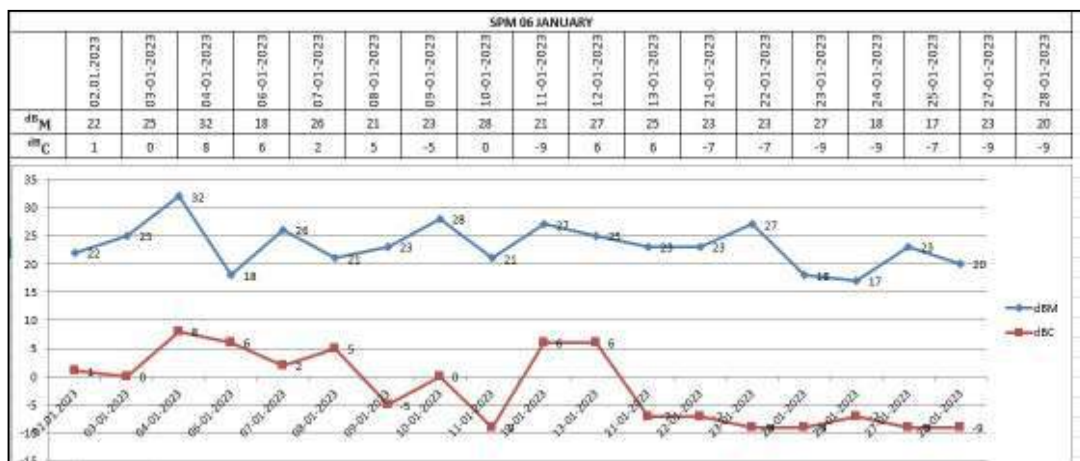


Figure 10: The trend graph showing no abnormality of bearing failure

The auto generated report of the instrument was however constantly on ‘ALARM’ mode for each reading near about the date of failure but since the engineers were trending only the trend graph of dBC & dBM which showed no signs of alarm so no forewarning was given to the department other than normal schedule of lubrication (Table:4)

Table 4: The auto generated report showing ‘alarm for the machine bearing that failed

 ELECTROSTEEL CASTING SRIKALAHASTHI WORKS CBM CELL SPM 02-08 HEAD BEARING SPM (SHOCK PULSE METHOD) REPORT						
Area	DIP-HZ	Machine	SPM 02 to 08		REPORT DATE:12.01.2022	
MACHINE NAME	Mould rpm	DN	Head Bearing Drawing no	Head Bearing ID	STATUS	Remarks/Recommendation
SPM-02	324	400		D3	NORMAL	Operate with schedule inspection and maintenance.
SPM-03	280	450		D4	NORMAL	Operate with schedule inspection and maintenance.
SPM-04	550	200	401		NORMAL	Operate with schedule inspection and maintenance.
SPM-05	440	300	421	C2	NORMAL	Operate with schedule inspection and maintenance.
SPM-06	480	300	421	C3	ALERT	Lubricate the Head bearing and inspect for any remarks.
SPM-07	700	150	381	A1	ALERT	Immediate Lubrication and inspect for any remarks.
SPM-08	1160	100	381	A4	NORMAL	Operate with schedule inspection and maintenance.

The bearing was dismantled and its was found broken and analysis showed the failure was due to improper lubrication (figure 11)



Figure:11 Broken cage of the failed bearing found after dismantling

4.1 Analysis for the Failure in Monitoring.

Initial investigation showed that the monitoring technique of one machine was adopted to another though both the machines worked on the same principle the reporting was on different aspects. The bearing analyzer that was used earlier worked on the principle of shock pulse method and the analysis was for lube oil condition for which LR (low rate of occurrence) & HR (high rate of occurrence) were used. To determine the effectiveness of shock pulse method detection of lubrication film thickness a research program was conducted by SPM instrument US Inc. the research team being headed by the President of Research Mr. Ervin School. (V. Vijayanand). What was evident that the User Guide² that was sent with the bearing checker was not read to understand the machine function.

In the User Guide² (pp11) it is mentioned that ‘lubrication condition is indicated by the delta value i.e. difference between dBm & dBc. High readings and small delta value indicate poor lubrication and dry running. Now this reading is being calculated and users being informed accordingly. Another reference to User Guide²(pp 10) it is mentioned ‘a condition indicator on the scale: green for dBn up to 20dBn =good condition ,yellow for 21-34 dBn=caution ,red for 35dBn and more = bad condition’ As these color codes are auto generated and if the same is trended bearing condition can be correctly ascertained .

5.0 Corrective Action:

- The trending of dBc & dBm was stopped and the auto generated color codes were trended and departed informed accordingly.
- A small program is being made so that automatically the delta value is generated when both the dBc & dBm values are noted in the report. This job is in progress and expected to be completed shortly.

6.0 Result & Conclusion:

Soon after implementation of trending of color code correct prediction was observed for another kiln and department was instructed to change the bearing.(figure 12)

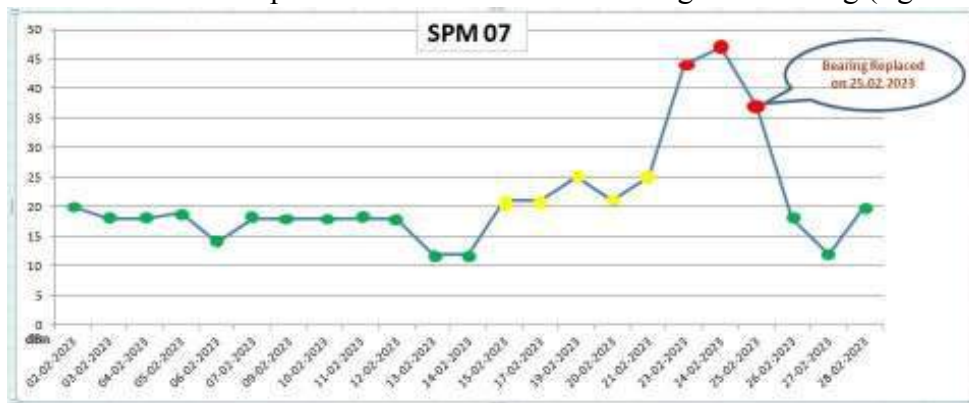


Figure: 12 Trend graphs based on the auto generated color code of the instrument.

Based on the report the user department took the bearing off the machine and after dismantling the inner race and the rolling elements were found damaged. From history card of failure, the root cause of failure was found due to long time in use. (Figure: 13)



Figure: 13 Damaged inner race and the rolling elements of the failed head pulley bearing

The learning from the failure analysis of the wrong condition-based monitoring prediction was:

- Not to accept any prediction failure as an outlier but with proper analysis some unknown aspects in monitoring can surface and with proper corrective actions condition based monitoring engineers can learn new and better techniques and of instrument's limitations.

7.0 References:

1. V Vijayanand. Condition Monitoring of Antifriction Bearings Using Shock Pulse Method. IPPTA J Volume 15, No: 3 (July 2003)
2. User Guide, Bearing Checker, spminstrument.com
Further reading:
- 3: Tim Sundstrom, An Introduction to the SPM HD Method ,R&D, SPM instrument AB,Oct:26 2010
- 4: Seyed-Hosseni et al, Relationship Between Reliability Centered Maintenance & Condition Monitoring (Case Study) ,Vol:6 Num.10:1 ,Pp. 122-136 , Enero Junio 2017
- 5: Jinboo Yaa et al. A Fault Feature Extraction Method for Rolling Bearing Based on Pulse Adaptive Time Frequency Transform .Vol-2016, Article ID:4135102,12pages Hindawi Publishing Corporation , Shock & Vibration.
- 6: B Hulluguppa et al. Condition Monitoring of Induction Motor Ball Bearing Using Monitoring Technique .IJSRP Vol:2 Issue 1 ,Nov-12 ISSN-2250-3153

Latest Trends in Condition Monitoring of Rotating Equipment

Padmakar Jaiswal - Engineer

*Condition Monitoring Division, Rotary-Maintenance department
HPCL Visakh refinery, Visakhapatnam, AP*

Abstract

Industry-wide efforts to boost throughput while lowering maintenance costs and downtime have increased the relevance of real-time, continuous, condition-based monitoring. In light of the aforementioned, HPCL Visakh Refinery has introduced two new cutting-edge technologies to our existing condition monitoring tools: "DIGITAL TWIN technology for reciprocating compressor" and "Ultrasound technology for bearing monitoring."

DIGITAL TWIN Technology uses 4G network to transmit recorded data to a server around-the-clock while operating independently of any client network or control systems. Currently, Digital TWIN Technology is being used in our refinery for monitoring of 2 Nos of Net Gas Compressor (NGC) which are 2 stage, 4 cylinder, double acting reciprocating compressor.

Ultrasonic Detector is another piece of technology. One of the most effective ways to identify issues like lack of lubrication and impending bearing failure. The ultrasonic warning appears prior to a rise in temperature or an increase in low frequency vibration levels. An ultrasound detector can be used to determine whether a bearing is healthy, inadequately lubricated, or defective.

This paper explains how contemporary technology, including the "DIGITAL TWIN and "Ultrasonic Detector" is employed in real time and enables one to perform predictive maintenance before any significant failure

1. Introduction

The purpose of a Digital Twin (DT) is to characterize the behaviour of physical entities by employing a virtual counterpart in real time. Physical space, virtual space, and their connectivity of data and models are the three main components of Digital twin. Digital twin is essentially a virtual representation of a physical system (twin), which is continuously updated with information about the operation, upkeep, and overall health of the original system. The digital twin may conduct real-time data/information interchange, dynamic modelling, and updates throughout its existence by creating a precise one-to-one mapping and feedback link between real physical space and digital space. The purpose of this study is to characterize the state-of-the-art of digital twin in developing Condition monitoring by providing a systematic overview of its theoretical and practical development.

Ultrasonic technology for bearing monitoring is another recent advancement. Ultrasonic bearing inspection and monitoring is one of the most reliable methods for detecting early bearing failure and circumstances such as lubrication deficiency. Ultrasonic detector technology detects faulty bearings even before vibration or heat arise. Equipment faults are detected earlier than with other technologies such as vibration analysis or oil/grease

analysis. Ultrasonic technology determines whether a bearing is normal, under lubricated, suspect, or questionable. This is proven in this study through one of the case study.

2.1 Digital Twin

Digital twin (DT) mainly consists of physical space, virtual space, and the bidirectional connection. Here in our HPCL Visakh Refinery, 'UpTime' a DT based tool is used for monitoring of reciprocating compressors.

'UpTime' is a crank-angle referenced condition and performance monitoring system. The UpTime system is working stand-alone without any communication with a client network or control systems and uses a 4G network to transmit recorded data to a server. The complete system, including 4G antenna, is certified to operate in an ATEX Zone I or equally classified hazardous area.

Currently, UpTime is being used in our refinery for monitoring of 2 No's of Net Gas Compressor (NGC) which are 2 stage, 4 cylinder, double acting reciprocating compressor. The probes/sensors that are being used here are: 4 No's cylinder acceleration probe, 4 No's crank case acceleration probes, 4 No's rod drop probe, 8 No's pressure sensors, 1 No's key phasor sensor. All the sensors are connected to one common Single Enclosure Module (SEM) which uses a 4G network to transmit recorded data to a server.

The UpTime tool provides vital information like suction pressure, discharge pressure, valve leakages at suction and discharge valves, Crosshead Vibration, Cylinder vibration, Piston Rings condition, P-V Diagram, P-A diagram etc. These parameters are being recorded 24x7.

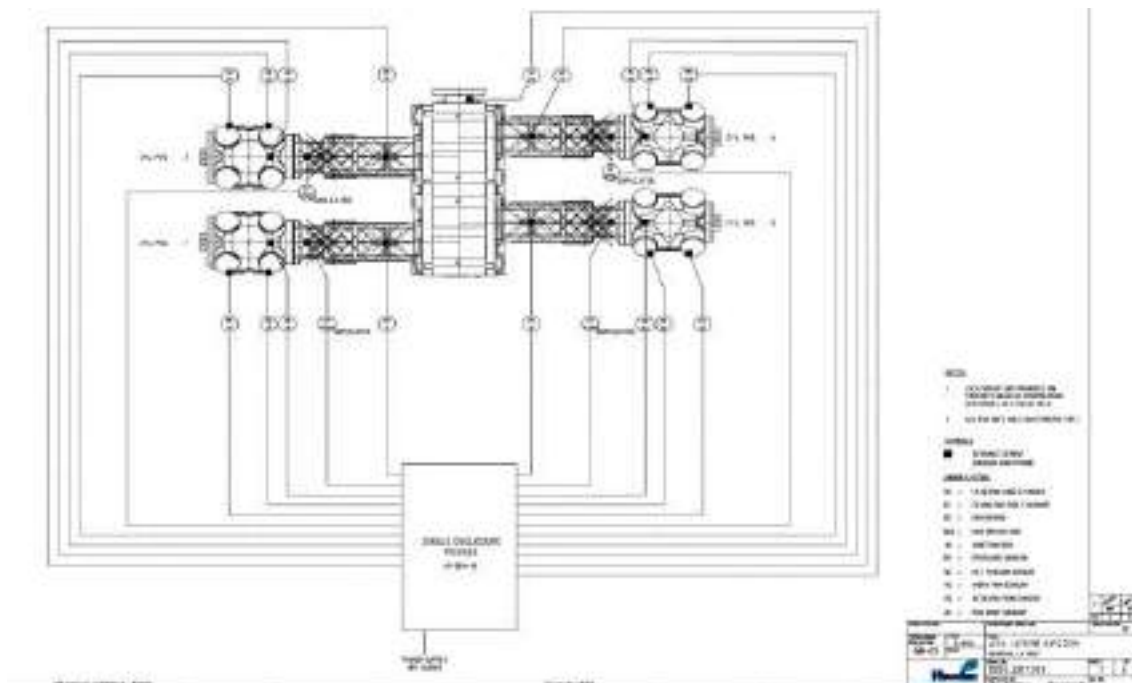


Figure 1. UpTime system general layout

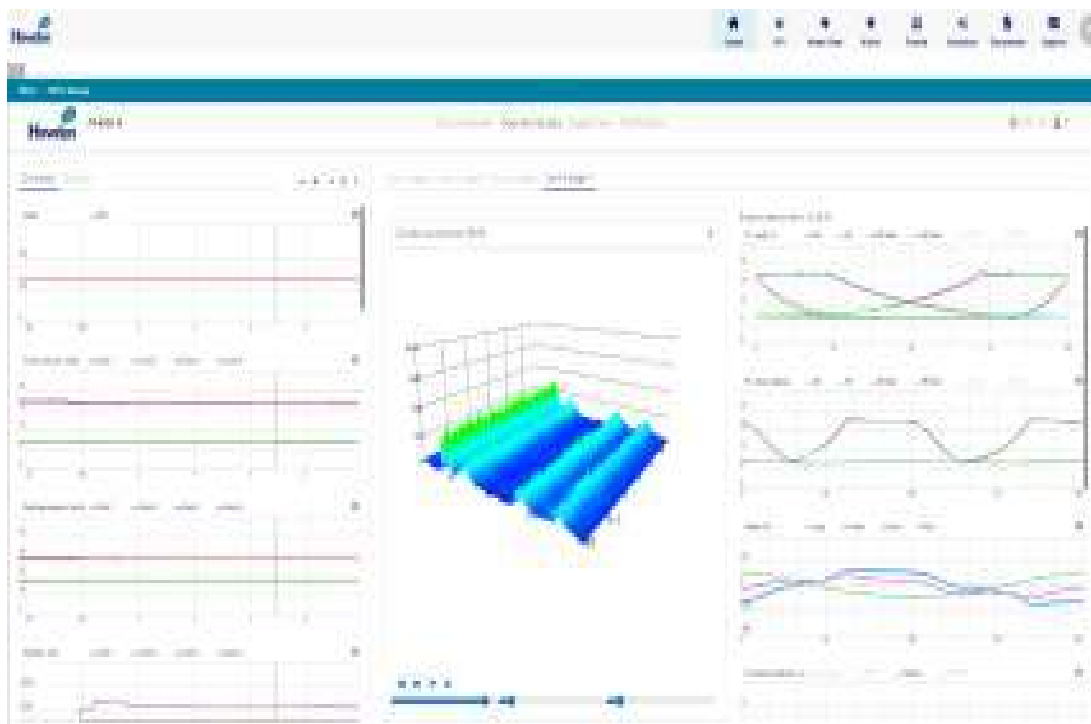


Figure 2. Reciprocating compressors Process parameters monitoring

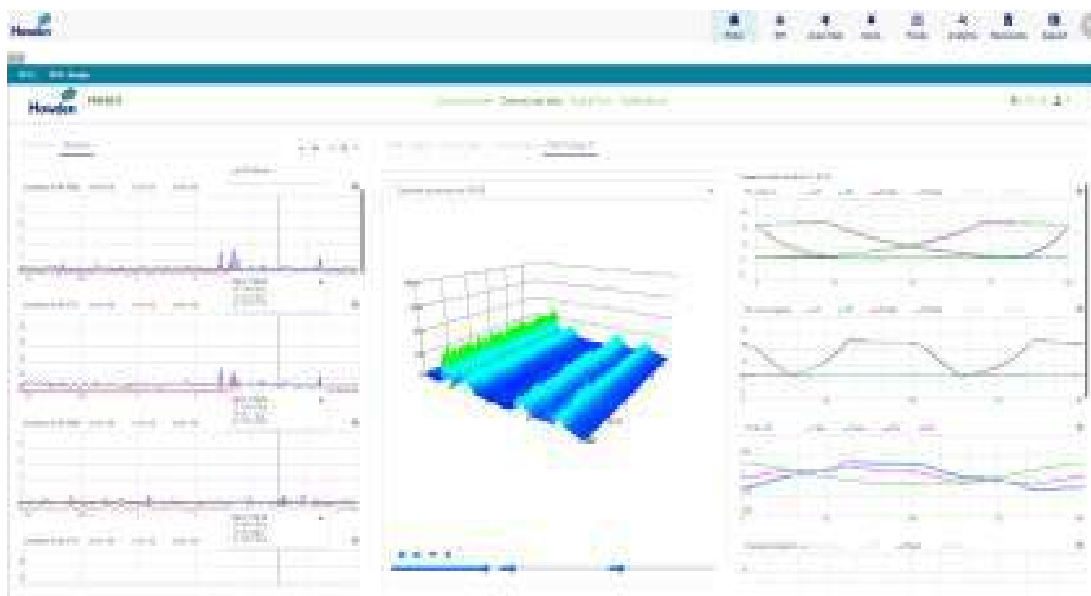


Figure 3. Reciprocating compressors Vibration monitoring

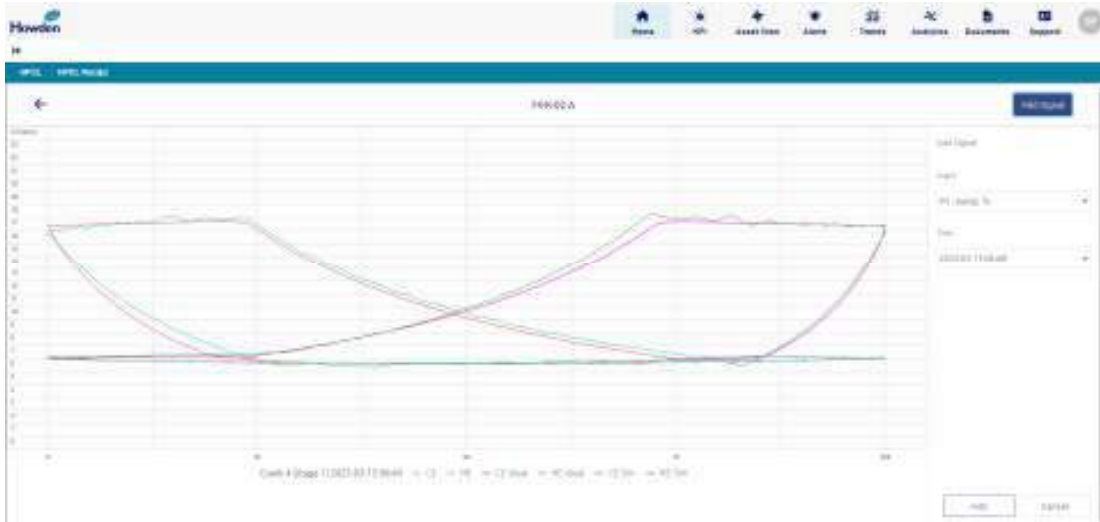


Figure 4. Reciprocating compressors PV diagram monitoring

2.2 Case study on Net Gas Compressor (74-K-02 A) CE Valve Leakage

Crank 2 CE discharge valve leakage	
Crank	2
Stage	1
Time	October 20 th 2022
Analysis	<p>Uptime pV diagrams shows relatively large leakage over the crank 2 CE discharge valve. Refer to Figure 5 and Figure 7.</p> <p>During the October 20th - 27th period, higher valve leakages were observed. HPCL Rotary section, during inspection in the period October 27th to November 4th, replaced a number of crank 2 discharge valves. Figure 5 shows an example of a pV measurement prior to valve replacement. Figure 6 shows an example of a pV measurement after valve replacement. After this, valve leakage reduced considerably (Refer Figure 7).</p>

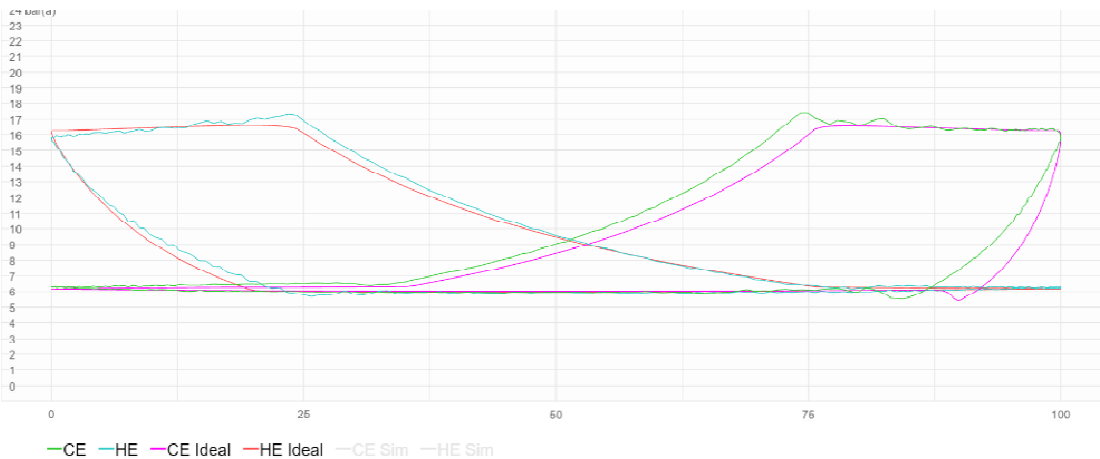


Figure 5. Crank 2 CE discharge valve leakage prior to valve replacement [Oct. 25th 2022, 20:08]

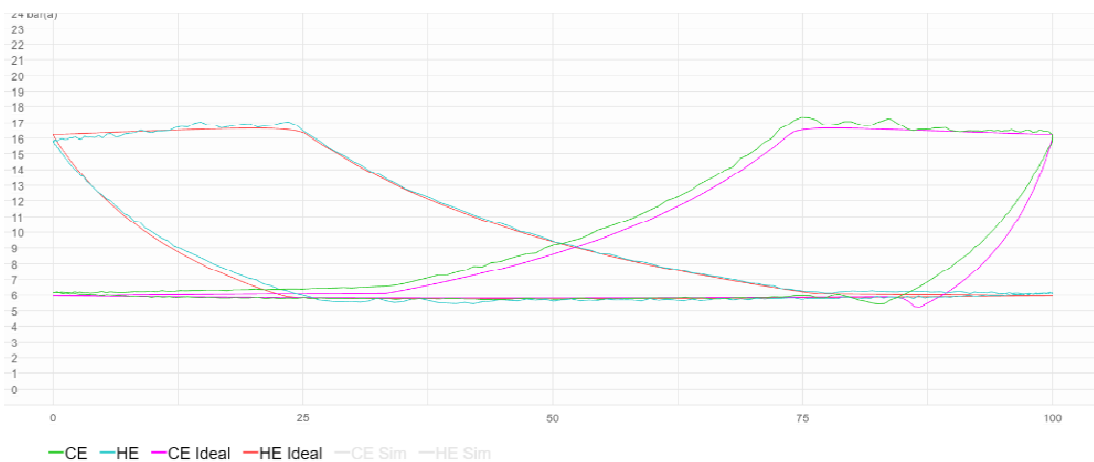


Figure 6. Crank 2 CE discharge valve leakage – after valve replacement [Nov. 13th 2022, 21:02]



Figure 7. Crank 2 CE discharge valve leakage trend line

2.3 Conclusion

UpTime which is a Digital Twin based Condition monitoring tool is highly versatile and proven technology for condition monitoring and fault analysis for reciprocating compressors online. The advantage of using this technology is that it can detect these problems at an early stage and thus avoid secondary damage and catastrophic failure of reciprocating compressors. The major benefits include the prevention of lost downtime, avoidance of major compressor repair, or replacement costs. DT ensures the reliable data, appreciating the operational condition of the compressor and correct interpretation of the data.

3.1 Ultrasound technology for bearing monitoring

Ultrasonic inspection and monitoring of bearings is one of the most reliable method for detecting incipient bearing failure and conditions such as lack of lubrication. The ultrasonic warning appears prior to a rise in temperature or an increase in low frequency vibration levels. In antifriction bearings, as the metal in the raceway, roller or ball elements begins to

fatigue, a subtle deformation begins to occur. This deforming of the metal will produce irregular surfaces, which will cause an increase in the emission of ultrasonic sound waves. The ultrasonic detector is used to trend dB values of different equipment. It can listen to bearing sound, record sound, generates FFT (spectrum) & Time waveform. By using the bearing fault calculator, it is possible to match the spectrum peaks with bearing fault frequencies. It is possible to know when to lubricate & how much to Lubricate, compare & record dB levels & sound before lubrication & after lubrication & generate report. It is suitable for low RPM bearings also unlike vibration.

3.2 Bearing inspection

The audible signature can reveal conditions within the bearing itself while checking bearings. 30 kHz is the suggested frequency for inspecting bearings. A failed bearing can be identified by an increase in loudness and a change in the sound quality. For ultrasound assisted lubrication, as per “ISO – 29821-18” creating a baseline for every bearing is mandatory to implement this program.

For setting baseline, following can be followed:

- Take the first reading and consider it the baseline.
- Use the lowest decibel value on identical equipment as the baseline.
- Take the minimum value observed during lubrication.
- Use a brand new, properly installed bearing as the baseline.

As per ISO 29821 -18 LIMITS, Set up the alarm limits:

- Low Alarm: 8 dB above baseline
- High Alarm: 16 dB above the baseline
- Bearing replacement: 35+ dB above the baseline

Apply grease to those bearings only which are currently in low alarm levels until the baseline readings reached. Figure 8 and Figure 9 shows typical Db trend values for a good and defective bearing. Figure 8 shows the right time for doing greasing. Figure 9 shows the right time for undergoing bearing replacement.



Figure 8: Db trend values for Good bearing

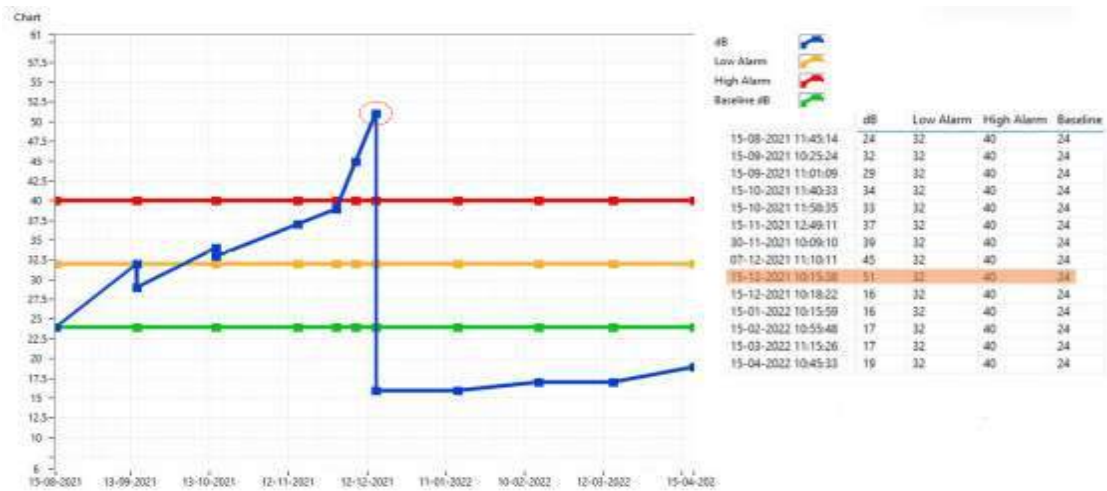
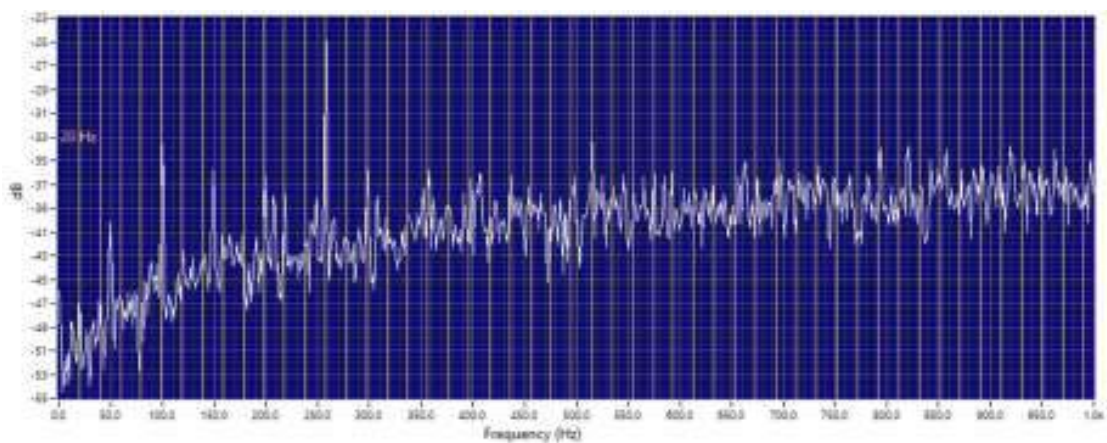


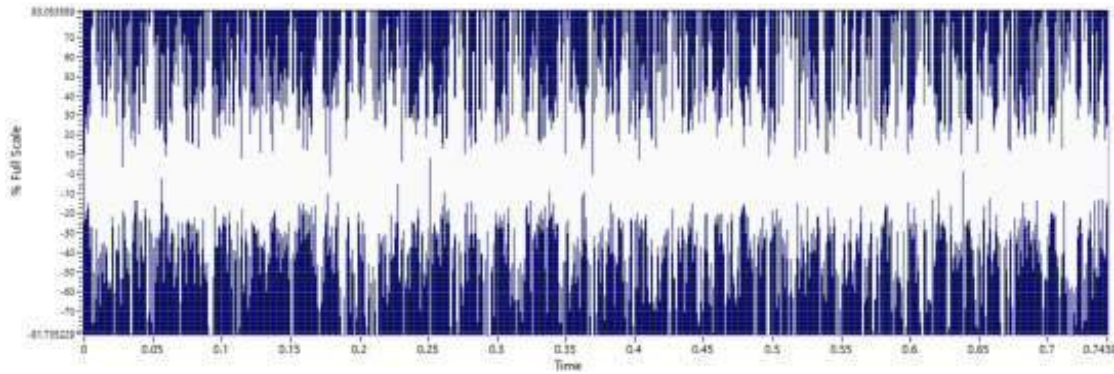
Figure 9: Db trend values for Defective bearing

3.3 Case study on 11M8C motor (Drive end side)

Readings were taken on 11M8C Motor DE side because of abnormal noise and following were our readings and observations from the ultrasound detector:

Plant Name	Group Application Type	Location Name	Point Name	Date	dB	Frequency	Sensitivity
CDU-II	Bearing	11P8C	DE	09-12-2022 11:45:22	51	30	34





Ultrasound observed metal hitting sound and as per the rpm & number of balls the bearing fault calculator indicates the dB peaks matching at 19.8Hz frequency which is indicating cage defect. Even after greasing dB values did not reduce. Hence, decision was taken to replace motor bearings.

3.4 Conclusion

Ultrasound bearing inspection is definitely an add on tool to strengthen the condition monitoring capabilities. It helps in increasing uptime and avoid downtime, helps to know bearing health condition, plan for lubrication and inventory and hence reduce maintenance and production loss.

Acknowledgements

I would like to acknowledge the constant support from Mr. Marpina Naveen Kumar and Mr. V. V. Rajsekhar, Maintenance, HPCL Visakh Refinery for this work.

References

- [1] He Liu , Min Xia , Darren Williams, Jianzhong Sun and Hongsheng Yan : Digital Twin-Driven Machine Condition Monitoring: A Literature Review
- [2] E. Glaessgen and D. Stargel, “The digital twin paradigm for future NASA and U.S,” Air Force Vehicles, 2012.

Experimental Evaluation of Modal Damping to Assess Onset of Flutter in Aero-Engine Blades

Manish Kumar*, Giridhar RK*, Sanjay Barad G*

*Gas Turbine Research Establishment, Bangalore-93

Abstract

Successful operation of aero engine depends mainly upon the structural integrity of its rotating component which in turn depends on its ability to withstand the dynamic and steady stresses without any failure. Of all the rotating components in a jet engine, compressor and turbine blades are highly susceptible to failure because of adverse operating condition viz high rotational speed, high pressure and temperature which demand special attention during monitoring as well as in the design phase. Vibratory failure in blades can occur in any stage of developmental program of engine like rig level testing, final testing phase etc. In worse cases blade failures have happened in past when engine was in production stage. Many a times' blades have failed in middle of flight which leads to major catastrophe. There are many reasons for failure in blades, but of these resonance and flutter are the most common blade vibration problem occurring in the jet engines that concern the designer. Failure due to flutter is the most serious because it is an aero-elastic instability and once initiated is difficult to control and the extent of damage is very high. One of the important features of flutter is that it is a non-synchronous vibration and the overall damping become zero at the onset of flutter and negative during flutter.

Structural dynamic analysis of blades helps to mitigate these vibration issues by improving the design but major problem is difficulty in predicting non uniform gas load and calculating overall damping in the system. The overall damping in the gas turbine depends on material, aerodynamic and friction damping which can change with respect to operating and loading conditions, therefore it become necessary to estimate the damping of the bladed disk system in operating condition. In this paper an attempt is made to estimate the total damping of bladed disc assembly during resonance and onset of flutter using various time domain and subspace techniques. Further, estimated damping from various technique are compared and satisfactory results were found. The damping values can be used as an input in design phase and can also act as an indicator for monitoring the blade vibration during resonance or onset of flutter.

Keywords: *Blades, Flutter, Modal Damping, Operational Modal Analysis, Vibration.*

Introduction:

Flutter is one of the most perplexing problems in the development of gas turbine engines. The inability to accurately predict flutter in the blades during design stage or even at bench test is the big concern for design engineers. It is an aerodynamic instability occurring due to aero-elastic interaction of unsteady aerodynamic gas forces with the complex blade profiles. Hence, it becomes difficult to predict flutter in advance without

testing because as it depends on following factors and thorough understanding is required on how these influence the dynamics of the complex profile blades. [1]

1. Unsteady aerodynamics of series of stator and rotor under wide range of flow condition expected in the operating range.
2. Structural vibration frequencies and modes of vibration over operating range
3. Quantification of damping in the system due to non-aerodynamic as well as aerodynamic sources.
4. Aerodynamic parameters of blade like chord length, stagger, flow incidence angle and structural parameters like frequencies, mode shapes and damping etc.
5. Arrangement and dissimilarities in aerodynamics and structural parameters in assembled bladed disk.
6. Accurate estimation of material properties like fatigue strength, modulus of elasticity in the operating range of temperature.

Of these, calculation of aerodynamic forces and aerodynamic damping is most tedious complex and computationally expensive even for normal flat plate. Additional complexities arise when actual blade profile is considered. [1]

As aforementioned, the actual operating condition and arrangement of blades in the assembly of bladed disk have huge influence on instability of the blades. The conventional experimental modal analysis of individual blades using impulse as a source of excitation is not sufficient in understanding the aero-elastic interaction of blades which is the cause of instability.

Hence this paper discusses few methods used to identify the structural dynamic characteristics of the blades using the only available response data from the blades instrumented with strain gauge. This process of identifying the modal parameters in actual running condition is known as Operational Modal Analysis (OMA). [9] Here few auto and cross correlation driven algorithms like Least Square Complex Exponential and Stochastic Subspace Identification are discussed and implemented as a case study on raw time domain response data to estimate the modal damping in the blades at the onset of flutter and the results from all the algorithms are compared and discussed. Though flutter is a non-linear phenomenon, the system is assumed to be linear throughout the analysis as here attempt is made to assess the damping just before the onset of flutter.

Another advantage of the availability of in-operation modal characteristics is that it helps in in-situ diagnosis, prediction, and monitoring of any vibratory phenomenon. [5] [12].

Least Squares Complex Exponential (LSCE) Method:

Least-squares complex exponential method is the time domain modal analysis technique used for extraction of modal parameters like natural frequency, damping factor and mode shapes for dynamical system. However, only damping ratio of blades is calculated here to assess the onset of flutter in the engine as damping ratio tend to zero at onset of flutter.

LSCE uses the relationship between Impulse Response Function of an MDoF system and its complex roots, modal constant through a complex exponential to construct an auto-regressive (AR) model. The solution of this model results in a polynomial whose roots are

the complex root of the system which contains information about the natural frequency and damping ratio of the dynamic system. [2]

Consider a receptance (α_{jk}) FRF of a general MDOF system with viscous damping, which may be written as [3]

$$\alpha_{jk}(\omega) = \sum_{r=1}^N \frac{r^{A_{jk}}}{\omega_r \xi_r + i(\omega - \omega_r \sqrt{1 - \xi_r^2})} + \frac{r^{A_{jk}^*}}{\omega_r \xi_r + i(\omega + \omega_r \sqrt{1 - \xi_r^2})} \quad \dots (1)$$

Or

$$\alpha_{jk}(\omega) = \sum_{r=1}^{2N} \frac{r^{A_{jk}}}{\omega_r \xi_r + i(\omega - \omega_r')} ; \quad \omega_r' = \omega_r \sqrt{1 - \xi_r^2}, \omega_{r+N}' = -\omega_r', (r+N)^{A_{jk}} = r^{A_{jk}^*} \quad \dots (2)$$

From classical theory, we can obtain the corresponding Impulse Response Function (IRF) by taking the Inverse Fourier Transform of receptance:

$$h_{jk}(t) = \sum_{r=1}^{2N} r^{A_{jk}} e^{s_r t}; \quad s_r = -\omega_r \xi_r + i\omega_r' \quad \dots (3)$$

If the original FRF has been measured in discrete form at number of equally spaced frequency IRF will similarly be described at corresponding number of equally spaced time intervals ($\Delta t = 1/\Delta f$) as given below:

$$h_0, h_1, h_2, \dots, h_q = h(0), h(\Delta t), h(2\Delta t), \dots, h(q\Delta t)$$

Substituting, $r^{A_{jk}} = A_r$; $e^{s_r \Delta t} = V_r$

Omitting the subscript jk and extending the full data set of q samples with above substitution gives

$$\begin{aligned} h_0 &= A_1 + A_2 + \dots + A_{2N} \\ h_1 &= V_1^q A_1 + V_2^q A_2 + \dots + V_{2N}^q A_{2N} \\ h_2 &= V_1^{2q} A_1 + V_2^{2q} A_2 + \dots + V_{2N}^{2q} A_{2N} \\ &\dots \\ h_q &= V_1^{q^2} A_1 + V_2^{q^2} A_2 + \dots + V_{2N}^{q^2} A_{2N} \end{aligned} \quad \dots (4)$$

If the number of sample points, q exceeds $4N$, equation (4) can be used to setup Eigen value problem, the solution to which yields the complex natural frequencies contained in parameters V_1, V_2 , etc. from solution using Prony method.

Multiplying each equation with coefficient β_i to form the following set of equation:

$$\begin{aligned} \beta_0 h_0 &= \beta_0 A_1 + \beta_0 A_2 + \dots + \beta_0 A_{2N} \\ \beta_1 h_1 &= \beta_1 V_1^q A_1 + \beta_1 V_2^q A_2 + \dots + \beta_1 V_{2N}^q A_{2N} \end{aligned}$$

$$\beta_2 h_2 = \beta_2 V_1^q A_1 + \beta_2 V_2^q A_2 + \cdots + \beta_2 V_{2N}^q A_{2N}$$

$$\begin{array}{cccc} \cdot & \cdot & \cdot & \cdot \\ \cdot & \cdot & \cdot & \cdot \end{array}$$

$$\beta_q h_q = \beta_q V_1^q A_1 + \beta_q V_2^q A_2 + \cdots + \beta_q V_{2N}^q A_{2N}$$

Adding all these equations gives

$$\sum_{i=0}^q \beta_i h_i = \sum_{j=1}^{2N} (A_j \sum_{i=0}^q \beta_i V_i^j) \dots \quad (5)$$

These coefficients β_i are taken such that

$$\beta_0 + \beta_1 V + \beta_2 V^2 + \cdots + \beta_q V^q = 0 \dots \quad (6)$$

Hence the roots are V_1, V_2, \dots, V_q .

Since q is the number of data points and N is the number of degrees of freedom of the system's model (constituting N conjugate pairs of modes) it is now convenient to set these parameters to the same value i.e., to let $q = 2N$.

Then,

$$\sum_{i=0}^{2N} \beta_i V_i^r = 0$$

For $r = 1 \dots 2N$

As every term on right side of equation (5) is zero, thus

$$\sum_{i=0}^{2N} \beta_i h_i = 0$$

Rearranging the above equation by setting $\beta_{2N} = 1$ we get,

$$\sum_{i=0}^{2N-1} \beta_i h_i = -h_{2N}$$

Successive application of this procedure lead to a full set of $2N$ equations:

$$\begin{bmatrix} h_0 & h_1 & h_2 & \cdots & h_{2N-1} \\ h_1 & h_2 & h_3 & \cdots & h_{2N} \\ \vdots & \vdots & \vdots & \cdots & \vdots \\ \vdots & \vdots & \vdots & \cdots & \vdots \\ h_{2N-1} & h_{2N} & h_{2N+1} & \cdots & h_{4N-2} \end{bmatrix} \begin{Bmatrix} \beta_0 \\ \beta_1 \\ \vdots \\ \beta_{2N-1} \end{Bmatrix} = - \begin{Bmatrix} h_{2N} \\ h_{2N+1} \\ \vdots \\ h_{4N-1} \end{Bmatrix}$$

We can obtain the unknown coefficients using below equation

$$\{\beta\} = -[h]^{-1}\{h\}$$

With these coefficients, equation (6) is used to determine the values of V_1, V_2, \dots, V_{2N} from which we can obtain the complex natural frequency and hence the un damped natural frequency and modal damping value using below equations

$$\omega_r = \frac{1}{\Delta t} \sqrt{\ln V_r \ln V_r^*}$$

$$\zeta_r = \frac{-\ln (V_r V_r^*)}{2\omega_r \Delta t}$$

The procedure described above to extract the modal parameter is for impulse response function, however if we assume that system is excited by stationary white noise, it has been shown that correlation function between the response signals can be expressed as a sum of decaying sinusoids. Each decaying sinusoid has a damped natural frequency (ω_r) and damping factor (ζ_r) corresponding to a particular mode. [4] Consequently, the correlation function of response signal will be of the same form as impulse response function hence, the classical modal parameter identification techniques LSCE is used in the case study to extract modal parameter from response data only.

Stochastic Subspace Identification technique:

Stochastic Subspace Identification (SSI), technique is considered as one of the most powerful data driven technique used for the identification of modal parameters when system is in operating condition and only response data is available i.e., input excitation force is either random or difficult to measure, like aerodynamic and traffic loads on bridges, aerodynamic loading on gas turbine engines and wind turbine blades etc. [7] [10].

Stochastic Subspace Identification (SSI) modal identification is being used from a decade but the real break-through happened in 1996 when a book was published by Overschee and De Moor [8], the book contains a set of MATLAB which helped in realizing the effectiveness of the algorithm and acted as a strong and efficient tool for modal parameter estimation in-situ also known as Operational Modal Analysis (OMA).

This technique involves several mathematical steps and concepts from linear algebra, a crisp explanation about its algorithm is given. [6] [11].

Consider a stochastic response from a system as a function of time for M measurement channels

$$y = \begin{Bmatrix} y_1(t) \\ y_2(t) \\ \vdots \\ y_M(t) \end{Bmatrix}$$

Considering the system a typical MDoF structural system,

$$M\ddot{y}(t) + D\dot{y}(t) + Ky(t) = f(t) \quad (7)$$

Where M, D, K is the mass, damping and stiffness matrix and f is the forcing function.

Converting the second order differential equation (7) to first order differential equation using state space formulation

$$x(t) = \begin{Bmatrix} y(t) \\ \dot{y}(t) \end{Bmatrix}$$

The original 2nd order differential equation simplifies to a first order equation

$$\begin{aligned} \dot{x}(t) &= A_c x(t) + B f(t) \\ y(t) &= C x(t) \dots \end{aligned} \quad (8)$$

Where A_c the system matrix and B is the load matrix.

$$\begin{aligned} A_c &= \begin{bmatrix} 0 & I \\ -M^{-1}K & -M^{-1}D \end{bmatrix} \\ B &= \begin{bmatrix} 0 \\ M^{-1} \end{bmatrix} \end{aligned}$$

General solution of first order differential equations (8) in discrete time domain is given by,

$$\begin{aligned} x_k &= e^{A_c k \Delta t} x_0 = A_d^k x_0 \\ y_k &= C A_d^k x_0 \dots \end{aligned} \quad (9)$$

Where $A_d = e^{A_c t}$

For exponential function of matrix, exponential function of the Eigen value of matrix is taken.

For N data points in discrete time, system response is represented in matrix form

$$Y = [y_1 y_2 \dots y_N]$$

If $Y_{(1:N-k)}$ denotes a data matrix after removing the last k data points and $Y_{(k:N)}$ denotes data matrix after removing first k points then

$$R_k = \frac{1}{N-k} Y_{(1:N-k)} Y_{(k:N)}^T$$

is known as unbiased estimation of the correlation matrix at time lag k .

$$Y_h = \begin{bmatrix} Y_{(1:N-2s)} \\ Y_{(2:N-2s)} \\ \cdot \\ \cdot \\ \cdot \\ Y_{(2s:N)} \end{bmatrix} = \begin{bmatrix} Y_{hp} \\ Y_{hf} \end{bmatrix}$$

Y_h is known as Block Hankel matrix, defined as gathering of family of matrices created by shifting the data matrix.

Here, the number of rows in Block Hankel matrix is $2sM$ and number of columns is $N-2s$. Y_{hp} denotes the upper half part of the matrix known as “the past” while Y_{hf} denotes the lower half part known as “the future”. The number of block rows $2s$ in upper or lower half matrix denotes the total data shift.

The orthogonal projection of the future part of Block Hankel matrix is carried out on past one. This projection is defined as conditional mean in stochastic responses, represented by matrix O

$$O = E(Y_{hf}|Y_{hp})$$

A conditional mean like this can for Gaussian processes totally be described by its covariances. Since the shifted data matrices also defines covariances, therefore projection can also be calculated directly by

$$O = Y_{hf}Y_{hp}^T(Y_{hp}Y_{hp}^T)^{-1}Y_{hp} \dots \quad (10)$$

The last matrix Y_{hp} defines the conditions while the first four matrices in the product define covariances between channels at different time lags. The conditional mean like given by above equation simply consist of free decays of the system given by different initial conditions specified by Y_{hp} . The matrix O is $sM \times sM$ and any column in the matrix O is a stacked free decay of the system to a set of initial conditions. Using equation (9) any column in O can be expressed by

$$o_{col} = \Gamma_s x_o$$

$$\Gamma_s = \begin{bmatrix} C \\ CA_d \\ \cdot \\ \cdot \\ CA_d^{s-1} \end{bmatrix}$$

Since neither Γ_s , (observability matrix) nor initial conditions are known, SVD is performed on matrix O .

$$O = USV^T$$

And then Γ_s and X_0 is estimated as given below:

$$\Gamma = US^{1/2} \quad X_o = S^{1/2}V^T$$

Now system matrix A_d is estimated from the matrix Γ by removing one block from the top and a block from the bottom yielding

$$\Gamma_{(2:s)}A_d = \Gamma_{(1:s-1)}$$

The observation matrix C is given by

$$C = \Gamma_{(1:1)}$$

Now, performing Eigen Value Decomposition (EVD) on system matrix A_d :

$$A_d = \Psi[\mu_i]\Psi^{-1}$$

Since, $\mu_i = e^{\lambda_i}$

$$f_i = \frac{|\ln(\mu_i)|}{2\pi\Delta T}$$

$$\zeta_i = \frac{Re(\lambda_i)}{|\lambda_i|}$$

ζ_i Represent, modal damping factor.

Depending upon the choice of reference response, Stochastic Subspace Identification technique can be subdivided into different method. Two of them used in the case study are Balanced Reduction (BR) and Canonical Variate Analysis (CVA). In BR the subset of response signal is taken as reference while in case of CVA whole response data is taken as reference. Balanced Reduction method is useful in identifying the most dominant modes excited whereas Canonical Variate Analysis is useful for identifying the less excited mode in better way.

Case Study, Results and Discussion:

An attempt is made to assess the modal damping of the blades during resonance and flutter condition, using OMA techniques. Figure 1 shows the layout of an aero engine (core engine) which is single spool having six stage compressor and turbine. During early developmental testing flutter is observed in 1st stage compressor rotor blade. As a part of root cause analysis and better understanding, modal damping is estimated using strain data. The 1st stage rotor blades are strain gauged and the data is measured and stored using LMS data acquisition system. Further, OMA is carried out on measured strain data using LSCE and SSI.

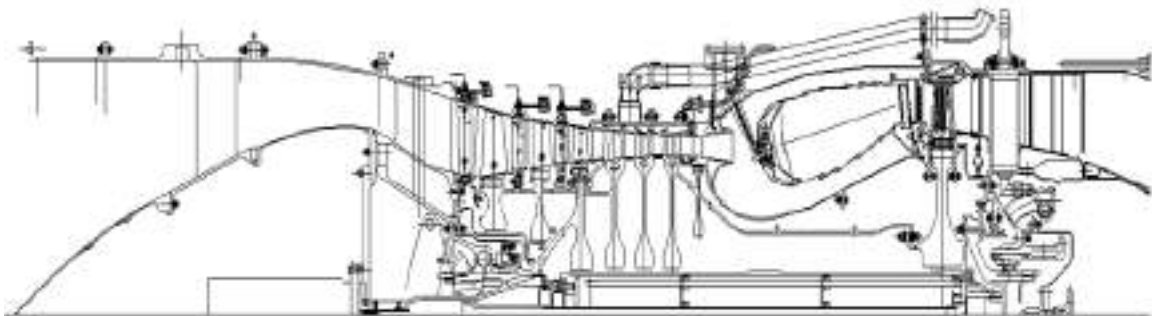


Fig 1: Layout of Core Engine

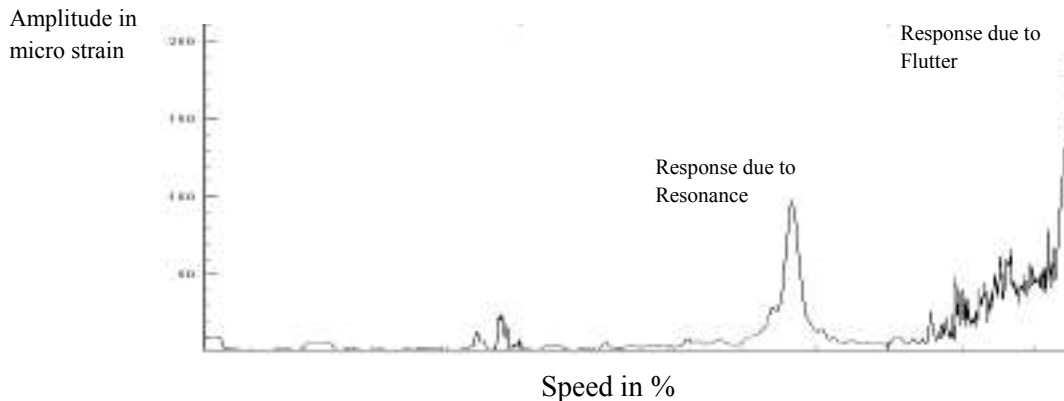


Fig 2: Natural frequency track indicating both resonance and flutter condition

Fig 2 shows a natural frequency track of a first flexure mode during the test of a core engine, indicating resonance and flutter condition. Some small peaks at low speed corresponds to excitation from the higher order harmonics and the peak around 72% is due to resonance from second order excitation. At max speed, sudden increase in the strain amplitude is due to blade flutter.

In addition to strain response data, another way which was used to identify the blade flutter is the Inter Phase Blade Angle (IBPA). The inter blade phase angle is a phase relationship that represents the motion of a blade with respect to other blades.

In a well-defined travelling wave mode, the motion of a blade can be shown to be identical to the motion of its neighbour except for a phase angle between them. During flutter condition there will be a fixed phase relationship between all the blades in that particular mode, associated with either forward travelling wave or backward travelling wave. The Fig 3 is a cross spectrum measured between various strain gauge signals mounted on the first stage rotor blades. The inter blade phase angle between blades corresponding to flutter frequency is identified. The mode identified in this case is a 2D bladed disc mode with a backward travelling wave. The coherence values throughout the frequency range were estimated and it was found to be one at flutter frequency. Operational Modal Analysis technique is used to extract the modal parameters from the response only measurements. Here, damping extraction is carried out at different speeds using three different techniques discussed above. The results obtained are in good correlation with published literature: The damping estimated under normal running condition (at resonance) is around 0.58% corresponding to first flexure mode. This has been confirmed by various techniques. Figure 4 shows stability plot and corresponding damping value form one of the technique.

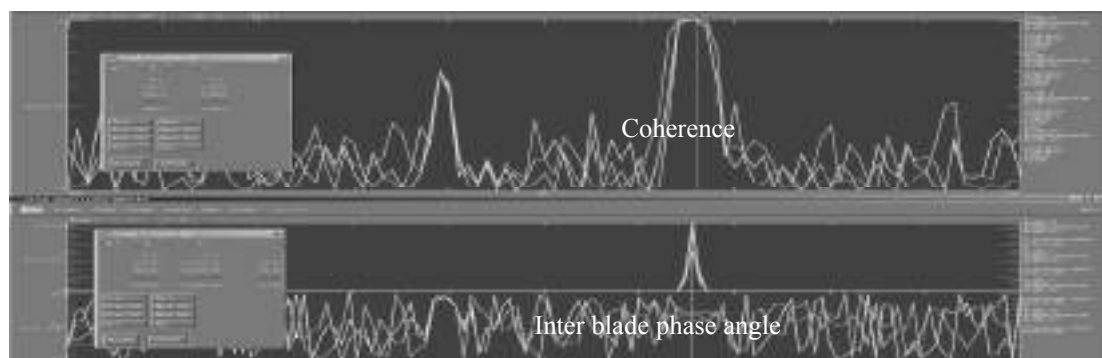


Fig 3: Inter blade phase angle and coherence of rotor strain gauges

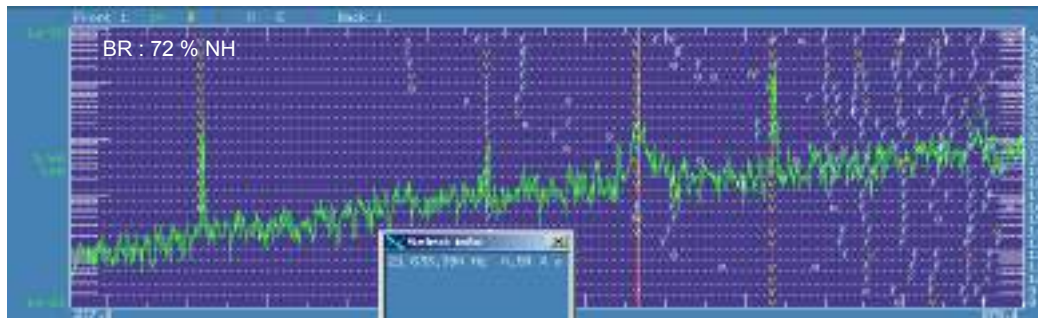


Fig 4: Estimated total modal damping using OMA at Resonance

At the onset of flutter a sudden drop in damping is noticed. The damping at this point is around 0.01 %. Fig 5 is a typical stability diagram at the initiation of the flutter. In short the following observations made during flutter condition. The advantage of using this at the onset point is because of the fact that during flutter all the blades lock to the same frequency and the blades have a fixed phase relationship. The damping drops sharply to a negative value and the onset condition can be fixed accordingly.



Fig 5: Estimated total modal damping using various OMA techniques during flutter

Table 1 indicates the damping values at resonance condition, i.e., 72% NH and Table 2 at onset of flutter i.e., 83 % of NH.

NH Speed %	Technique Used	Frequency (Hz)	Damping %
No Flutter			
72	SSI (BR)	633.39	0.59
72	SSI (CVA)	633.91	0.58
72	LSCE	633.12	0.59

Table 5

NH Speed %	Technique Used	Frequency (Hz)	Damping %
Flutter			
83	SSI (BR)	665.58	0.05
83	SSI (CVA)	665.58	0.01
83	LSCE	666.58	0.01

Table 6

Conclusion:

The operational modal analysis technique used to estimate damping corroborates with the experimental modal analysis result.

There is a sudden drop in the overall damping, tending to zero at the onset of flutter as the negative aerodynamic damping nullifies the frictional and material damping present in the system.

All the operational modal analysis techniques used viz Stochastic Subspace Identification (SSI), Least Square Complex Exponential (LSCE) gives almost the same damping estimate so any one of them can be used for damping estimation during flutter.

The damping values can be estimated real time during the running of an aero-engine and hence can be used as monitoring parameter for predicting and avoiding blade flutter during operation.

References

1. A.V. Srinivasan: Flutter and Resonant Vibration Characteristics of Engine Blades. *The 1997 IGTI Scholar Paper*
2. Jimin He, Zhi-Fang Fu: Modal Analysis method-time domain. *Modal Analysis (pp. 180-197)*.
3. D.J. Ewins: Modal Testing: Theory, Practice and Application. *Research Studies Press Ltd. 2000*.
4. G. H. James III, T. G. Carne and J. P. Laufer: The Natural Excitation Technique (NExT) for modal parameter extraction from operating structures. *The International Journal of Analytical and Experimental Modal Analysis 10(4),260-277 1995*.
5. L. Hermans, H. Van Der Auweraer: Modal Testing and analysis of structures under operational conditions: Industrial Applications. *Mechanical Systems and Signal Processing (1999), 193-216*.
6. Rune Brincker: Understanding Stochastic Subspace Identification. *IMAC-XXIV: A Conference & Exposition on Structural Dynamics*
7. Le Thai Hoa, Yukio Tamura, Akihito Yoshida and Nguyen Dong Anh: Frequency Domain versus Time Domain Modal Identifications for Ambient Excited Structures, *International Conference on Engineering Mechanics and Automation (ICEMA 2010)*.
8. Peter van Overschee and Bart de Moor: Subspace Identification for Linear Systems. *Kluwer Academic Publishers, 1996*.
9. Zhang, Lingmi, Brincker, Rune, An Overview of Operational Modal Analysis Major Development and Issues, *Proceedings of the 1st International Operational Modal Analysis Conference, April 26-27, 2005, Copenhagen, Denmark*.
10. Bart Peeters and Guido De Roeck, Stochastic Subspace Identification for Operational Modal Analysis: A Review, *Journal of Dynamic Systems, Measurement and Controls, ASME 2001*
11. Reynders, E. System Identification Method for Operational) Modal Analysis: Review and Comparison, *Arch Computat Method Eng 19 51-124 (2012)*
12. Fahad Bin Zahid, Zhi Chao Ong, Shin Yee Khoo, A review of operational modal analysis techniques for in-service modal identification, *Journal of Brazilian society of Mechanical Sciences and Engineering, 2020*

A Case Study on Condition Monitoring and Accuracy Assessment of Coordinate Measuring Machine

Ravi George¹, Suneel Kumar¹, B Chiranjeevi²

¹. Gas Turbine Research Establishment, DRDO, Bengaluru, India

². QUEST, Bengaluru, India

Abstract

Industry 4.0 or the fourth industrial revolution conceptualises new requirements for smart industry. The concept formulates improving Machine-to-Machine (M2M), Machine-to-Tool (M2T) communication and Condition Monitoring of Measuring Systems. Geometry and GD&T parameters of machined parts are properly verified by measuring systems which in turn assures the machine capabilities in the manufacturing. So, the condition and accuracy of the measuring system is very crucial in order to take the decision for acceptance of the parts. This paper presents the condition monitoring methodology of an Articulated arm Coordinate Measuring Machine (ACMM) and bring out the influence of condition monitoring and Accuracy assessment of the Metrology System as part of Measuring System Analysis.

Key words: Condition Monitoring, Measuring System, ACMM, Accuracy

1. Introduction

Quality Inspection, Quality Control and Quality Assurance are part of continuous improvement processes and are very much crucial in manufacturing aspects in R&D organisations. In order to provide the reliable inspection and meeting the demands of GD&T accuracy, it is necessary to keep the measuring systems under continuous condition monitoring to enable its accuracy. Coordinate Measuring Machines (cmms) are placed top in the field of Metrology and GD&T due to their reliable accuracy and repeatability. They are reliable inspection resources in manufacturing process monitoring, achieving product specification and also to measure the continual quality improvement. It is so important that the cmms are required to be monitored for its condition and accuracy for every usage.

Monitoring the condition and performance of CMM at regular intervals is very much essential in order to control the quality and provide the confidence. Condition of the CMM can be monitored by the systematic measuring process with the defined standard gauges and then, comparison analysis of obtained measurements with the nominal calibrated values of the gauges.

Condition monitoring of the cmms and the accuracy assessment may be checked by the application of various calibrated artifacts such as “standard step gauges, standard gauge blocks, standard end bars, hole plates and ball plates etc.”

2. Condition and Accuracy of the CMM

Condition and accuracy of the CMM can be assessed by verifying the sources of errors affect the CMM measurements. These errors can be Spatial or Computational [6]. Errors in

the position of points taken on the surface of measured work piece are called as Spatial errors. Sources that determine the spatial errors are:

- Components of CMM such as “Scales, Qualification Sphere, Probe system and Guide ways.
- Environmental conditions such as “Temperature, Humidity, Dust and Vibration.
- Strategy of probing such as “Probing force, Probing Speed, Probing Direction and Type of Stylus and Probe used”.
- Characteristics of the measured work piece such as “Cleanliness, Surface finish, Elasticity etc.”.

Errors in the dimensions estimated while inspection and work piece form deviations are called as Computational errors. Sources that determine these errors are:

- Software used in the CMM to capture the geometry of the work piece.
- Number of points taken and its relative position.
- Datum specifications and computing the geometry.

3. CMM Performance Verification Guidelines and Tests

The set of guidelines and procedures are provided for Verification of CMM in the standards such as [6]

- ISO 10360-1: 2000 GPS (Geometrical Product Specifications) covers “Acceptance and reverification tests for Coordinate Measuring Machines” – (Part 1 – Vocabulary)
- ISO 10360-2: 2009 (GPS) Geometrical product specifications cover “Acceptance and reverification tests for Coordinate Measuring Machines used for measuring linear dimensions”.
- ISO 10360-12 Geometrical product specifications cover “Acceptance and reverification tests for Articulated arm Coordinate Measuring Machines” [1].

The best practice to determine the performance of the CMM or any instrument is, to carry out the tests such as “reverification and interim tests”. Some standard sampling lengths to be checked with the CMM and the readings will be compared with the maximum permitted error stated by the manufacturer.

The reverification test and the related checks helps to understand the cmms and its probing system on periodic basis [6]. Interim tests help to understand the CMM and its probing system between regular reverification tests. The conditions stated in para 2 will affect the measurements taken and the errors obtained if any.

The material standard used to carry out these tests must be any of them mentioned below as recommended.

- Standard Step Gauge
- Standard End Bars
- Standard Gauge Blocks

The material standard that are considered for the verification test must have 2 or more nominal parallel planes, with a specified the distance between them.

4. Condition Monitoring – Experimental Set up

4.1. Articulated arm Coordinate Measuring Machine

Condition Monitoring and Accuracy assessment carried out for an Articulated arm Coordinate Measuring Machine (shown in Figure-1) used in a Metrology Lab of an R&D Organisation.

- CMM model - Romer Absolute Arm-RA7312
- Make - Hexagon, USA
- Software used - PC-DMIS CAD ++ VERSION 2017 R1
- Uncertainty - $U=5+L/40 \mu\text{m}$
Where, L is the length of the measured range in mm



Figure-1 Articulated arm CMM

4.2. Material Standard of Sizes

The Material standard of sizes which were used for the test are shown in Figure 2. Details of the standard sizes are presented in Table 1.

Sl. No	Description	Make	Calibration standard	Material
1	Standard Sphere \varnothing 25.4mm	STL	ASME B89-4.22	Tungsten Carbide Grade 10
2	End Bar 550 mm	Mitutoyo	IS2984	Steel Grade 0
3	End Bar 350 mm	Mitutoyo	IS2984	Steel Grade 0
4	End Bar 250 mm	Mitutoyo	IS2984	Steel Grade 0
5	End Bar 200 mm	Mitutoyo	IS2984	Steel Grade 0
6	Gauge Block 100 mm	Mitutoyo	IS2984	Steel Grade 0

Table-1 Details of the standard sizes

The condition monitoring test is carried out as per the procedure provided by the part 12 of ISO 10360 in a systematic way as mentioned below.

- Measurement of reference ball to verify the performance of the probing system.
- Measurement of Standard sizes of five different lengths to verify the Maximum Permissible Error of the lengths.
- Each standard size is measured in seven positions such as “one vertical position, three horizontal positions and three inclined positions of 45⁰ with reference to the base.
- Five different lengths at seven different positions and measured each three times such that captured 105 measurements.

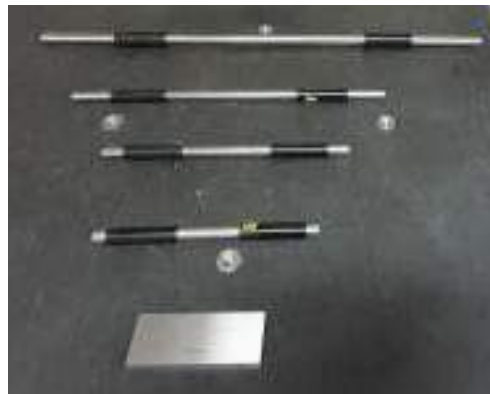


Figure-2 End Bars and Gauge Block

4.3.Preliminary Precautions Taken

The following precautions are taken during the experiment.

- Machine start up as stated in the CMM instruction manual.
- Cleaning Procedure (Machine, Probe, Stylus, Sphere)
- Qualification of Probe
- Reference Sphere
- Dust and Vibrations
- Room Temperature: 20⁰C
- Humidity: 55-60 %

4.4.Coefficient of Thermal Expansion (CTE)

The difference in the size of the part material for a change in the given temperature is called as Coefficient of Thermal Expansion (CTE) and is denoted by α .

The following equation is used to correct the measured length to a Standard Temperature ST °C

$$L_{ST} = L_{AT} + (20 - AT) \cdot \alpha \cdot L_{AT}$$

L_{ST} is length at the standard temperature

L_{AT} is length at the actual temperature

α is the coefficient of thermal expansion. (for Steel $\alpha = 11.6 \times 10^{-6}$)

5. Results and Discussions

5.1. Measurement of Standard Sizes

Data obtained from the inspection of standard sizes using Articulated arm CMM are tabulated in Table 2 - 6.

Sl. No.	Orientation	Actual values			Error		
		1	2	3	1	2	3
1	XYg+Z	550.010	550.008	550.011	000.010	000.008	000.011
2	XYg+X	550.009	550.009	550.011	000.009	000.009	000.011
3	XYg-X	550.009	550.009	550.010	000.009	000.009	000.010
4	XYg+Y	550.011	550.009	550.010	000.011	000.009	000.010
5	XZ g+45 ⁰	550.012	550.010	550.012	000.012	000.010	000.012
6	XZ g-45 ⁰	550.011	550.012	550.011	000.011	000.012	000.011
7	YZ g+45 ⁰	550.012	550.012	550.011	000.012	000.012	000.011

Table-2 Measurements of 550 mm End Bar

$$E_{L, MPE} = 0.01875$$

Sl. No.	Orientation	Actual values			Error		
		1	2	3	1	2	3
1	XYg+Z	350.009	350.009	350.009	000.009	000.009	000.009
2	XYg+X	350.010	350.009	350.009	000.010	000.009	000.009
3	XYg-X	350.009	350.009	350.009	000.009	000.009	000.009
4	XYg+Y	350.009	350.009	350.008	000.009	000.009	000.010
5	XZ g+45 ⁰	350.009	350.010	350.009	000.009	000.010	000.009
6	XZ g-45 ⁰	350.010	350.010	350.010	000.010	000.010	000.010
7	YZ g+45 ⁰	350.010	350.009	350.009	000.010	000.009	000.009

Table-3 Measurements of 350 mm End Bar

$$E_{L, MPE} = 0.01375$$

Sl. No.	Orientation	Actual values			Error		
		1	2	3	1	2	3
1	XYg+Z	250.009	250.008	250.008	000.009	000.008	000.008
2	XYg+X	250.008	250.009	250.008	000.008	000.009	000.008
3	XYg-X	250.008	250.009	250.008	000.008	000.009	000.008
4	XYg+Y	250.008	250.009	250.008	000.008	000.009	000.008
5	XZ g+45 ⁰	250.009	250.009	250.010	000.009	000.009	000.010
6	XZ g-45 ⁰	250.009	250.010	250.009	000.009	000.010	000.009
7	YZ g+45 ⁰	250.010	250.009	250.010	000.010	000.009	000.010

Table-4 Measurements of 250 mm End Bar

$$E_{L, MPE} = 0.01125$$

Sl. No.	Orientation	Actual values			Error		
		1	2	3	1	2	3
1	XYg+Z	200.008	200.006	200.006	000.008	000.006	000.006
2	XYg+X	200.006	200.005	200.008	000.006	200.005	000.008
3	XYg-X	200.006	200.005	200.005	000.006	200.005	200.005
4	XYg+Y	200.006	200.008	200.006	000.006	000.008	000.006
5	XZ g+45 ⁰	200.007	200.008	200.007	200.007	000.008	200.007
6	XZ g-45 ⁰	200.007	200.007	200.007	200.007	200.007	200.007
7	YZ g+45 ⁰	200.007	200.008	200.008	200.007	000.008	000.008

Table-5 Measurements of 200 mm End Bar

$$E_{L, MPE} = 0.010$$

Sl. No.	Orientation	Actual values			Error		
		1	2	3	1	2	3
1	XYg+Z	200.002	200.003	200.002	000.002	000.003	000.002
2	XYg+X	200.004	200.003	200.003	000.004	200.003	000.003
3	XYg-X	200.003	200.004	200.003	000.003	200.004	200.003
4	XYg+Y	200.004	200.005	200.004	000.004	000.005	000.004
5	XZ g+45 ⁰	200.006	200.006	200.005	200.006	000.006	200.005
6	XZ g-45 ⁰	200.007	200.006	200.007	200.007	200.006	200.007
7	YZ g+45 ⁰	200.006	200.006	200.007	200.006	000.006	000.007

Table-6 Measurements of 100 mm Gauge Block

$$E_{L, MPE} = 0.0075$$

5.2. Maximum permissible error and Length Measuring Accuracy of a CMM for a size Measurement

The term $E_{L, MPE}$ specifies the Maximum Permissible error and Length Measuring Accuracy of any CMM. It is also defined as the maximum error obtained by for a given size measurement when measured utilising all the axis within the measuring volume of the CMM as per the regulations and specifications and it is stated as [6]

- $E_{L, MPE} = \pm (A + L/K) \mu m$ where,

A is a positive constant in μm .

K is a dimensionless positive constant given by the manufacturer.

L is the measured size in mm.

In the experiment, the manufacturer's constant for the Articulated arm CMM that is being tested, A is given as 5 and K is given as 40. Hence,

- $E_{L, MPE} = \pm (5 + L/40) \mu m$

Then Maximum Permissible Error $E_{L, MPE}$ for the Standard sizes that are used for the experiment are calculated as,

for 550 mm, $E_{L, MPE} = \pm (5 + 550/40) = 18.75 \mu m = 0.01875$

for 350 mm, $E_{L, MPE} = \pm (5 + 350/40) = 13.75 \mu m = 0.01375$

for 250 mm, $E_{L, MPE} = \pm (5 + 250/40) = 11.25 \mu m = 0.01125$

for 200 mm, $E_{L, MPE} = \pm (5 + 200/40) = 10.00 \mu m = 0.01000$

for 100 mm, $E_{L, MPE} = \pm (5 + 100/40) = 07.50 \mu m = 0.00750$

5.3. Analysis of Data

The measurements taken from the five different standard sizes are tabulated and the maximum errors obtained are compared with the maximum permissible error for the related sizes. The comparison and the acceptance test result are shown in table-7.

Sl.No.	Standard Size (mm)	Max Error Measured (mm)	Max Permissible Error (mm)	Acceptance Test Result
1	550	0.012	0.01875	Within Limits
2	350	0.010	0.01375	Within Limits
3	250	0.010	0.01125	Within Limits
4	200	0.008	0.01000	Within Limits
5	100	0.007	0.00750	Within Limits

Table-7 Acceptance Test Results

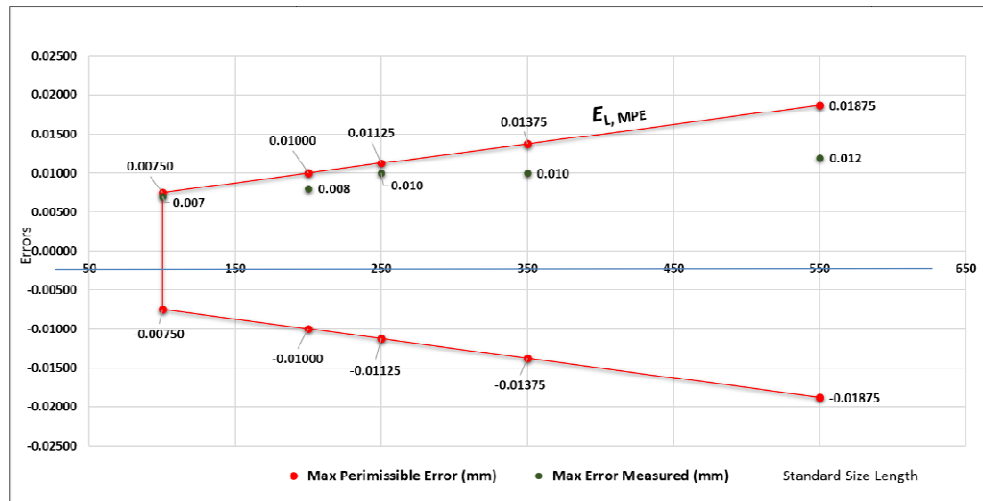


Figure-3 Acceptance Test Results

From the table-7, the maximum errors obtained are found to be within the acceptable or permissible range when compared to their respective maximum permissible errors. Acceptance test results are shown in Figure-3. It is also observed from table 2-6, that the repeatability of measurements might have little variation but the errors are again within the permissible range. The results clearly show that the Articulated arm CMM is maintained in good working condition and can be used for the inspection. The accuracy test and condition monitoring can be further continued by measuring and computing the GD&T parameters in depth.

6. Conclusion

In metrology, each and every precision instrument that are being used for the inspection of parts to be placed and maintained in the recommended environmental and operational conditions. Condition of the measuring systems are to be monitored and accuracy checks to be carried out at regular intervals to avoid any unidentified errors and to obtain reliable measurements.

Acknowledgements

Authors gratefully acknowledge the Director-GTRE for the permission and support. Also sincerely acknowledge “Sreelal Sreedhar - Associate Director (R&QA)” and “Ramaraja Bhat - Technical Director (QA)” for their guidance and knowledge sharing.

References

- [1] ISO 10360-12 Geometrical Product Specifications (GPS) — Acceptance and Reverification Tests for Coordinate Measuring Systems (CMS) — Part 12: Articulated Arm Coordinate Measurement Machines (CMM)
- [2] ISO 10360-2 2001 GPS – Acceptance test and re-verification test for coordinate measuring machines (CMM) - Part 2: CMMs used for measuring size, 2001

- [3] International standard ISO 10360-2:2009, Geometrical product specifications (GPS) - Acceptance and reverification tests for coordinate measuring machines (CMM) - Part 2: CMMs used for measuring linear dimensions;
- [4] S. El Asmai, F. Hennebelle, T. Coorevits, R. Vincent, J.J. Fontaine; Proposition of a periodic verification test for Articulated Arm Coordinate Measuring Machines using a small 3D artefact Measurement, 154 (2020)
- [5] VDI/VDE 2617-9 Accuracy of Coordinate Measuring Machines. Characteristics and Their Reverification. Acceptance and Reverification Tests for Articulated Arm Coordinate Measuring Machines
- [6] David Flack, Engineering Measurement Division National Physical Laboratory, Measurement Good Practice Guide No. 42, CMM Verification, ISSN 1368-6550, issue 2 (2011)
- [7] Ravi George, Murugesan R, and Dillibabu V “Comparative Measurement Variation Analysis on Coordinate Measuring Machine and White Light Scan Systems”. International Journal of Mechanical Engineering and Technology (IJMET) Volume 8, Issue 8 (2017), 607-614, ISSN: 0976-6340.

Health Monitoring of Gear Box by Wear Debris Analysis-Practices and Case Study from Strip Processing Line Tata Bluescope Steel, Jamshedpur, India

**Naval Kishor Prasad (DGM Mech. Maintenance) &
Premangshu Saha (Manager Mech. Maintenance)**

Abstract

Plant maintenance fraternity will ever remain thankful to Mr. Vernon C. Wescott, who invented Ferro graph. Mating machine components are always subjected to wear and tear – which if not monitored and controlled - leads to suboptimal life/unplanned failures, high maintenance costs, loss of business and so on.

Every mating part in a simple or complex machine is wears out. But Size, shape and quantity of wear out particles tell about the source of wearing, reason of wearing and health condition of machine. Through diagnosis of wear debris analysis, machine condition can be precisely predicted thus helping in timely corrections to maintain machine health at its best. Trending of wear debris analysis from new equipment to first time oil change and checking of components health timely, by oil analysis gives us information for replacement of oil and machine components.

At the Coated Steel Plant of Tata BlueScope Steel, Jamshedpur – oil condition monitoring is being practiced since last 10 years [i.e., since inception of the plant] and it helped immensely to maintain highest levels of optimized and sustained equipment reliability. Besides this, a plethora of condition monitoring activities enabled us for cost effective maintenance too.

Presently, we are into offline oil condition monitoring, and exploring to bring in latest & cost-effective “online oil condition monitoring”.

Benefits of regular condition monitoring

- *Get early warnings of wear*
- *Control contaminant levels*
- *Detect lubricant degradation*

Key Words: *Wear Debris Analysis, Behaviour of strip processing line gear boxes.*

Introduction

Tata BlueScope Steel coated steel plant operating since 2011. Zinc-Al coated coil manufactured in metal coating line from cold rolled full hard coil and pre-painted colour coated coil manufactured in coil paint line from Zn-Al coated coil for better life and aesthetic look. Finally coil go to coil packaging line or if require it goes to sitting and recoiling line based on variable strip width requirement from customer. As layout of coil paint line mentioned below.

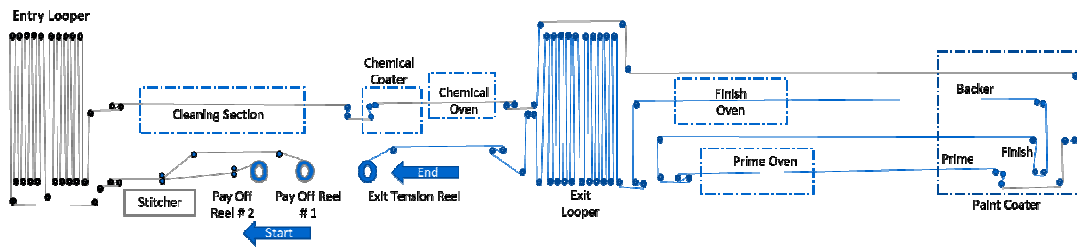


Figure 1- Layout of coil paint line

In metal strip process line variable speed drive gear boxes used in coil pay off reel or un-coiler by which fresh input coil moves to process section. And after processing of sheet rewind in tension reel or recoiler. Speed to be varied to maintain optimum production for different thickness of sheet and during joining of sheet or parting out final coated sheet. Each line having two un-coiler or pay off reel and one re-coiler or tension reel. Apart from these to maintains process speed one strip or sheet accumulator or looper in entry (supply sheet to process during sheet joining) and one strip accumulator or looper in exit (to accumulate sheet from process, during oil cutting at exit).

Details of gear boxes and Lubrication System Mentioned Below-

- Critical Gear Boxes = 11 no's
- Lubricant used = Gear oil viscosity 320
- Lubrication System = Through gear pump oil spray

Line	Equipment	Gear Ratio	Oil Capacity
Metal Coating Line	Pay Off Reel#01	13.287	300 Liters
	Pay Off Reel#02	13.287	300 Liters
	Tension Reel	11.235	300 Liters
	Exit Accumulator	273.22	520 liters
Colour Coating Line	Pay Off Reel#01	15.401	300 Liters
	Pay Off Reel#02	15.401	300 Liters
	Tension Reel	15.401	300 Liters
	Entry Accumulator	140	520 liters
	Exit Accumulator	140	520 liters
Slitting & Recoiling Line	Uncoiler	11.11	141 Liters
	Re-coiler	11.11	141 Liters

Table 1- Details of Critical Gear Boxes

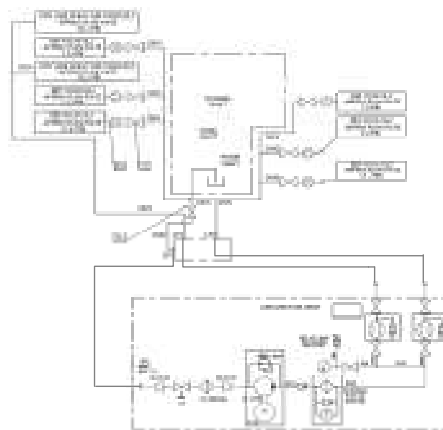


Figure 2 -Oil circulation system

Speed of the gear box changes rapidly during accumulator filling operation to maintain process speed. These gear boxes are critical due to high cost, high replacement time and maintaining main process parameters like speed and strip tension. To maintain health of these gear boxes, we are doing oil analysis, periodic vibration analysis and gear box inspection. Viscosity 320 grade oil is being used as lubricant for all these critical gear boxes by pressurised spray lubrication system.

Case Study

We monitor health of all these gear boxes, through oil analysis, periodic vibration analysis and inspection gear box internals. Sampling and oil analysis is outsourced.

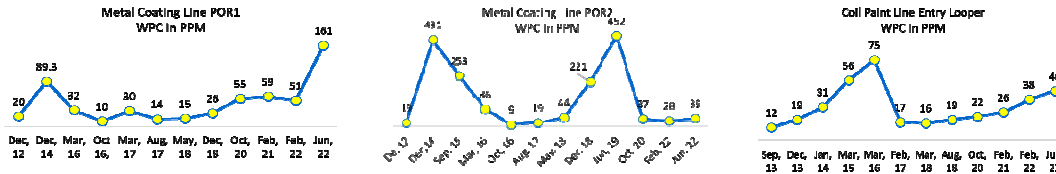


Figure 3-Wear Particle Concentration (WPC) Trend(in PPM)

Oil analysis done by external third party. From the oil analysis Ferrography quantitative and qualitative result for different gear boxes, it is being observed wear particle concentration is having strong correlation with service life of lubricant, speed of the gear box, rate of speed changes and torque transmitted by individual gear.

Metal coating line Pay off reel (POR) 1 gear box oil condition trend resembles to typical bathtub curve.

Metal coating line POR 2 gear box oil condition trend indicates sudden increase in Wear particle concentration (WPC) concentration, during initial run in 2011-12 and thereafter during Q2 and Q3 of 2018-19. It needed immediate correction for alarming oil condition.

Coil paint line entry looper gear box (used for intermediate operation) graph showing gradual increase in wear particle concentration. We also observed varied health behaviour for different make of gearboxes.

Our strategy is to do oil analysis of gear box as per yearly schedule which help us to understand condition of the gear box without disassembly. If any abnormality of oil is reported, oil condition monitoring and gear box internal inspection is intensified. Depending upon severity, oil replacement is done at earliest opportunity.

Qualitative result and action are mentioned below for one gear box Metal coating line POR 2

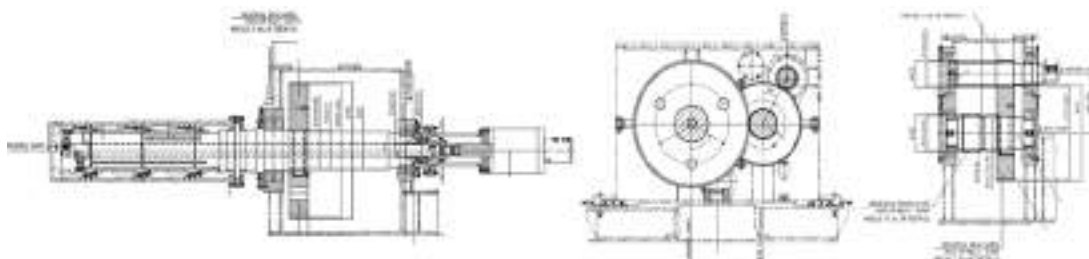
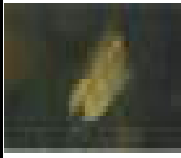
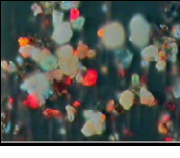


Figure 4- Cross Section of Pay Off Reel Gear Box

Date	Bearing wear particle Image	Gear wear particle Image	Image Non-Metallic items	Gear Box Inspection	Action
17 th Dec 2014					Gear box oil replacement done on 22nd Jan 2015
Discussion of result	Wear particle concentration (WPC) is 431. Normal rubbing wear particles are observed in small quantities. Gear wear particles of size ranging up to 24 microns are observed in small quantities. Bearing wear particles of size ranging up to 72 microns are observed in small quantities. Medium alloy steel bearing particles of size ranging up to 110 microns are observed in small quantities and Sand/dirt particles are observed in small quantities.			Gear box oil inspection done on 22nd Jan 2015	

Date	Bearing wear particle Image	Gear wear particle Image	Image Non Metallic items	Gear Box Inspection	Gear Box Inspection
29 th Sep 2015					Gear box oil replacement done on 22nd Dec 2015 and bearing clearance checking done.
Discussion of result	Wear particle concentration (WPC) is 253. Normal rubbing wear particles are observed in small quantities. Gear wear particles of size ranging up to 20 microns are observed in small quantities. Bearing wear particles of size ranging up to 30 microns are observed in small quantities. Red oxides and Sand/dirt particles are observed in small quantities.			Gear box oil inspection done on 22nd Dec 2015. Found rusting on gear teeth	

Date	Bearing wear particle Image	Gear wear particle Image	Gear wear particle Image	Gear Box Inspection	Action
17th June 2019					Input pinion replaced with bearing
Discussion of result	Wear particle concentration (WPC) is 452. Rubbing wear particles observed was rated moderate. Spherical particles are observed in various sizes and rated in few concentrations. Fatigue wear particles are measured up to 48 microns in size and concentration found Few. Laminar bearing wear particles are measured up to 68 microns in size as the particles was rated few to moderate. Cutting wear particles are found in traces measured to 16 microns in size and particles was rated few. Non-metallic crystal (sand/dirt) particles are observed was rated Few. Black oxides are observed was rated none to Few.			One sided fretting mark observed on gear teeth, possible reason alignment problem, pinion was replaced 23 rd Sept 2017. Noise and vibration level were also high during accumulator filling.	Intermediate gear replaced with bearing Gear box oil replacement done on 25 th Sept 2019



Figure 5- Replacement of POR 2 gear & bearing set and Alignment of gear set

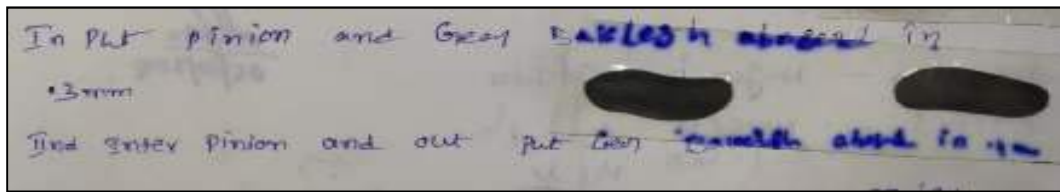


Figure 6- Gear Backlash Checking done after installing new

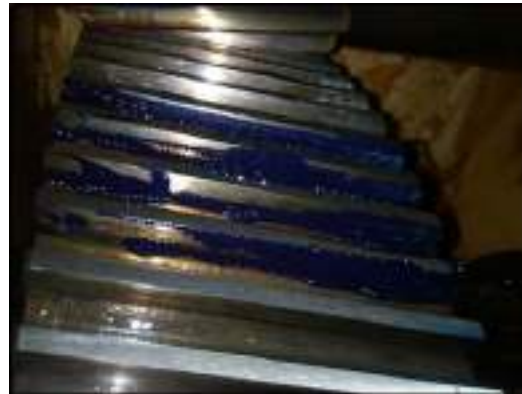


Figure 7- Checking Teeth contact by Prussian Blue Paint

Conclusion

We have observed initially wear pattern is high and falls down with time and again rises. Wear pattern and gear box inspection also reveals different problem like **lubrication starvation, gear misalignment, corrosion, seal damage, trapping of debris between tooth, spinning of bearings**. Our objective is to do timely oil analysis and increase the frequency of oil testing and replacement of oil. This practice helped us to do timely replacement of components.

For increasing oil replacement frequency, we planned to do replace gear box oil yearly instead of 4 years replacement plan. Collected oil to be filtered and tested and after maintaining oil quality by adding some amount fresh oil same oil to be reused.

Life enhancement of oil recycling and reuse-

Reason of gear oil replacement: --

- 1) Oil properties degraded.
- 2) High moisture content
- 3) Contents high wear particle generated inside gear box.
- 4) Contents high non-metallic particles like sand.

Undesirable effect of gear oil replacement: --

- 1) Huge cost (replacement of oil after every 4 years or before)
- 2) Health and Environmental Issue.

Solution

Offline filtration of gear oil.

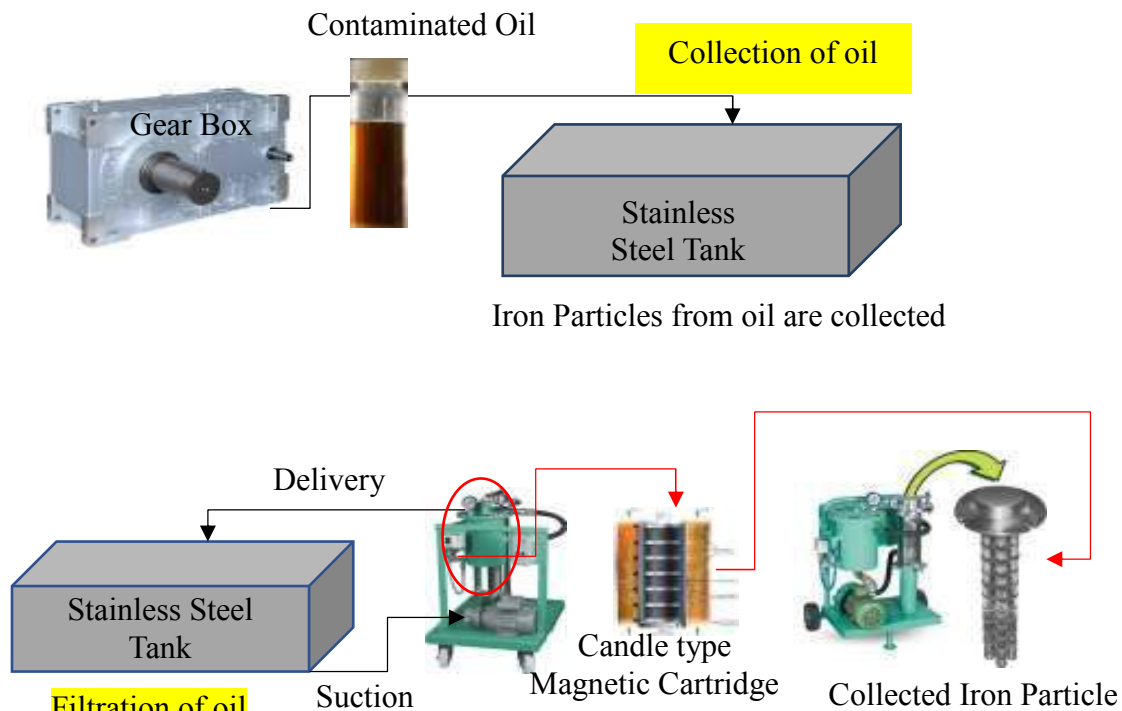


Figure 8- Schematic Arrangement Ferrous Particle Separation



Figure 9- Off line filtration of gear oil

Off line oil filtration serves dual purpose-

- 1) Reduction in overall cost of maintenance.
- 2) Reducing harmful impact on environment.

First 300 litres of oil filter on Dec -2022, which was collected from Slitting and recoiling line coiler and re-coiler gear boxes. After filtration for seven days, sample oil was sent for oil analysis. Result shown, ferrous debris concentration reduced from 57ppm to 3 ppm, and can be used further.

Way Forward

Because of time lag between “oil sample collection, analysis and monitoring” & “corrective action” we allow forced deterioration unknowingly.

Various online oil condition monitoring & analysis are evolved to reduce this time lag. We have started working on to adopt feasible online oil monitoring & analysis solution.

Acknowledgement

Authors would like to thanks Noria Publication for sharing different case studies, new technology development, bench mark data across industries and strategies on lubrication management.

Reference

- 1) A Tribute to Vernon C. Westcott, Inventor of the Ferrograph, By Teresa Hansen, Noria Corporation.
- 2) Reducing Wear Particle Generation-By Ted Naman, ConocoPhillips Ken Nicholas, Schroeder Industries Richard Winslow, Pacificorp - Naughton Plant
- 3) On-line and In-line Wear Debris Detectors: What's Out There? By SabrinGebarin

Intelligent Approach for Compound Fault Detection in Rolling Element Bearing using Sound Signals

Mohd Atif Jamil, Sidra Khanam, Md Asif Ali Khan

Department of Mechanical Engineering

Aligarh Muslim University

Aligarh-202002, India

Abstract

Failure of Rolling Element Bearing (REB) may result in shutting down of rotating machinery, which could have an impact on the final cost and product quality. The vibration and sound signals of a rotating machine carry active information about its performance. Several publications in the literature discuss the appropriateness of vibration signals for defect diagnosis applications, however, the transducer/accelerometer utilized is expensive. This hinders small-scale businesses and inexpensive equipment from employing diagnostic tools due to cost. On the other hand, sound signal acquisition transducers/microphone can be found at a reasonable price. Hence, research into the application of sound signals for fault diagnosis applications is quite significant. Artificial Neural Networks (ANN) are increasingly used, redefining the state-of-the-art in fault diagnosis and classification as Machine Learning (ML) enters the field of health monitoring of mechanical systems. A real-time fault detection approach for REBs based on the ANN algorithm utilizing sound signals is presented in this paper. The experimental sound data of several fault categories including healthy bearing, inner race defect, outer race defect and coexisting defects is captured using a microphone on a laboratory bearing test rig. In the quest of a combination of these parameters that yield the maximum performance in defect diagnosis, hidden layer count, layer size, and activation function of the ANN model are all tuned. It was possible to achieve a fault classification accuracy of maximum 86.5% using a single hidden layer with a size of 10 and the Tanh activation function, demonstrating the usefulness of sound signals.

Keywords – bearing defect, sound signal, feature extraction, ANN, fault detection

Introduction

Rolling element bearings (REBs) are essential components of rotary machinery in various production sectors. While permitting relative positioning and rotational motion, the bearings often transfer a load between shaft and its housing. Because bearings are necessary for the majority of rotating machinery and are a crucial part of them, the standards for them are growing more stringent every day. The bearing defects, if identified promptly can help avoid accidents. To prevent malfunctions and breakdowns while these bearings are in operation, appropriate methods for their condition monitoring and fault identification must be developed. The progress of ML in the last several years has increased the effectiveness of an intelligent approach of finding the REBs defect using vibration [1], thermal imaging, motor current and acoustic data [2]. A study has conducted out to examine the effect of surface defects in sliding and rolling contacts on noise generation [3]. The results exhibited that the overall noise level of a system increases along with system roughness. Measuring the discrete frequency patterns and overall noise level can provide information about the surface quality of the contacting pair because the noise level increases with the ageing of fine surfaces and decreases with the ageing of rough

surfaces. The statistical information from sound waves was employed in an experimental investigation to determine the best machining settings [4]. The machining process features of flank wear, surface roughness, chip morphology, and built-up edge development, highlighting the impact of sound signal, were explored. The statistical parameter estimation approach was used in a study on the use of sound pressure and vibration data to detect faults in rolling element bearings [5]. In their analysis, the authors used well-known statistical metrics including the crest factor, the distribution of moments, which includes kurtosis and skewness, and also other factors derived from the beta distribution functions. The results showed the kurtosis and crest factors of sound and vibration signals to be providing more helpful diagnostic information than the beta function parameters, and this study recommends the use of sound signals. The reference [6] provided the results of a summary dot pattern (SDP) method for failure diagnostics of fan bearings using sound signals. The SDP approach envisioned turning sound signals into diagrams that could be used to visually identify between healthy and defective bearings.

An experimental study showed that acoustic and vibration signals work well together to identify a variety of defects in two-stage gearboxes [7]. When the outcomes of acoustic signal analysis and vibration signal analysis were examined, it was discovered that acoustic signals are particularly effective for the early detection of faults in rotating machine elements. For the purpose of defect diagnosis employing a machine learning approach, a study was presented employing sound data obtained from the near field region of bearings in both healthy and the simulated faulty conditions [8]. Sound signals were used to extract descriptive statistical features, thereby employing decision tree for classification of healthy and faulty bearings. A review study is presented on utilizing sound and acoustic emissions for the condition monitoring and fault diagnosis of bearings, highlights the benefits and limitations of the technique [9]. The authors of [10] proposed an approach for identifying bearing defects by employing sound quality metrics that were extracted from the recorded signals and provided a descriptive analysis for five bearing conditions. The proposed method was experimentally validated using a variety of microphones and background conditions. Despite of a drawback of being its sensitivity to outside noise, the simplicity of sound signal, low-cost system, easy installation and flexibility in the placement of the microphones to put anywhere near the target component are some benefits of this technology [11]. Nevertheless, the described efforts employed traditional methods, intelligent automated fault diagnostic systems are required.

In this paper, an effort is made to use sound signals for bearing defect diagnostics in an effort to lower the cost of the transducer. Statistical features like mean, RMS, peak frequency, and kurtosis, were employed to extract some significant traits. Classification of fault categories was carried out using ANN classifier by training it with chosen statistical features, and the outcomes and related discussions are presented.

ANN classifier

A neural network made of artificial neurons is among the most suitable machine learning models. A neural network, which takes its inspiration from the human brain, comprises of densely connected neural networks of neurons that link inputs to desired outputs. A neuron is the simplest type of processing unit that may be joined to other neurons to form a neural network that processes data in a similar manner that of a human brain. As depicted in Fig. 1, neural networks feature input and output layers as well as a hidden layer that, in many circumstances, comprises of units that transform the input into something the output layer may employ.

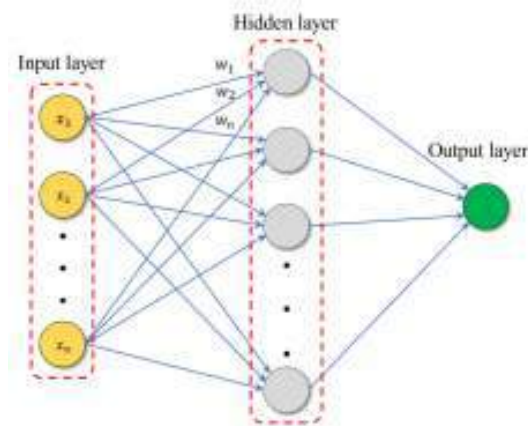


Fig. 1. Architecture of an Artificial Neural Network.

The input set is sent via a nonlinear filter called an activation function or transfer function, which releases the output, making it an ideal machine learning technique for discovering patterns that are either too complex or arduous for a human to identify.

$$I = w_1x_1 + w_2x_2 + \dots + w_nx_n = \sum_{i=1}^n w_ix_i$$

Where, I is the total input received by the summation unit, w_i , the weights, and x_i are the inputs to ANN.

In an ANN, input vectors and their corresponding target vectors are utilized to train the network until it can estimate a function and accurately link input vectors to certain output vectors.

Experimental setup and methodology

Fig. 2 shows the rolling element bearing test rig used for acquiring the experimental data in this work. Testing is done on four sets of deep groove ball bearings (FAG 808326). The shaft rotates at a speed of 2880 RPM. Healthy bearings, inner race faults, and outer race faults and coexisting faults are the fault conditions examined.

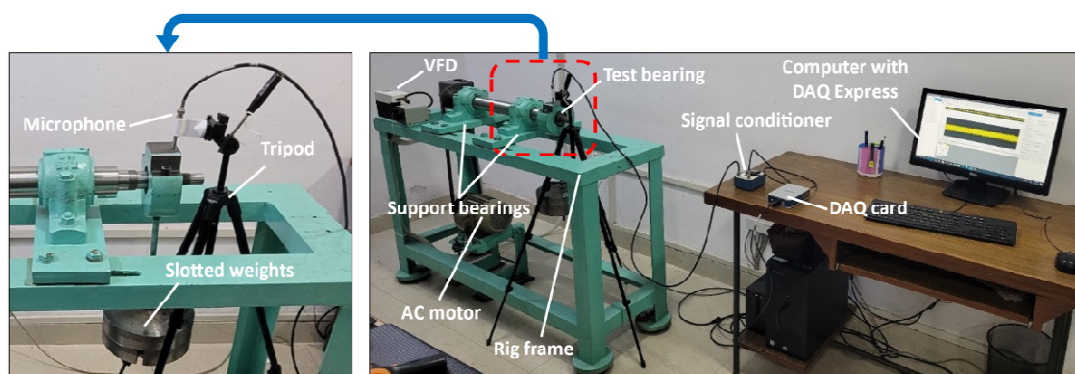


Fig. 2. Rolling element bearing test rig used to capture sound signals.

A PCB Piezotronics 130F20 microphone installed close to the test bearing housing was used to record sound signals, sampled at a rate of 51.2 kHz. The signals were recorded independently for each case, while operating under the identical conditions, after the

healthy bearing was swapped out for the faulty bearings. A healthy bearing was initially installed on the test rig. Single and multiple circular defects (pits) in the inner raceway and outer raceway of the bearing are created using Electro Discharge Machining (EDM). These are shown in Fig. 3. The diameter of the defects is about 1.8 mm.



Fig. 3. Single and multiple defects on bearing races (a) single defect on OR (b) two defects on OR (c) three defects on OR (d) single defect on IR (e) two defects on IR (f) three defects on IR.

The steps of the methodology are illustrated by Fig. 4. First, the experimental setup is used to collect the sound signals of healthy and defective bearings. These are then integrated in the MATLAB as a data ensemble of fault classes. Thereafter, a number of time-domain and frequency domain features, including Root Mean Square (RMS), Kurtosis, Skewness, and Peak frequency are extracted from the data ensemble.

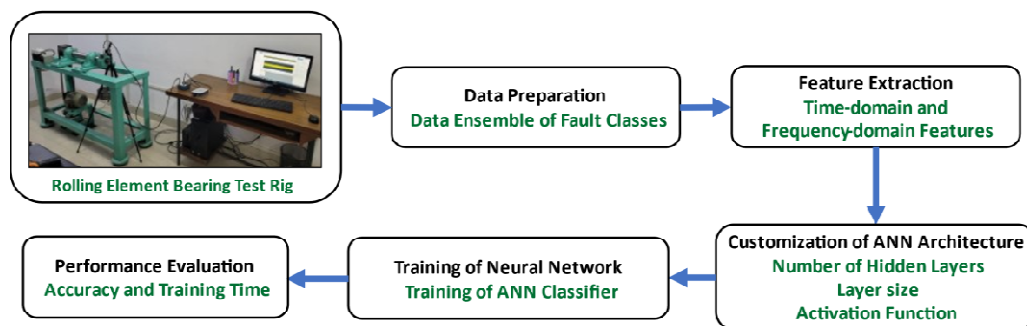


Fig. 4. Steps involved in the methodology used for bearing fault detection using ANN classifier.

The ANN architecture is then adjusted in terms of activation function, the number of hidden layers, and their size. After that, the classifier is trained with the time and frequency-domain features that were extracted. Next, the fault classification accuracy along with other associated ML metrics are used to assess the model performance. The following is a detailed description of the method employed in this work.

Preparation of data

The sound signals are required for the training of ANN classifier in order to monitor the condition of rolling bearing. Data can be gathered from any industrial machine that is in operation or may be produced in a lab using test rigs for several fault conditions. In the

current study, the experimental setup, which includes a bearing test rig and a provision for mounting a microphone, is used to collect sound data of healthy and defective bearings. The arrangement is depicted in Fig. 2. It contains data on both good bearing and faulty bearings with defects of various types and their combinations. Using MATLAB, several faults are selected and integrated into a data ensemble. Table 1 provides the specifics of these defect categories.

Table 1. Description of data taken for bearing fault classification.

Shaft Speed (RPM)	Radial Load (N)	Fault designation	Fault description	Fault code	Fault class
2880	210 (Inclusive of hanger mass)	H_0	Healthy	1	NA
		IR_1	Single IR defect	2	Single defect
		IR_2	Two IR defects	3	Multiple defects
		IR_3	Three IR defects	4	
		OR_1	Single OR defect	5	Single defect
		OR_2	Two OR defects	6	Multiple defects
		OR_3	Three OR defects	7	
		IR1 + OR1	OR & IR defect	8	Coexisting defects
		IR1 + OR2	OR & IR defect	9	
		IR2 + OR2	OR & IR defect	10	
		IR3 + OR3	OR & IR defect	11	

In the present bearing fault data, the fault class is regarded as single when either of the inner and outer races has a single defect. The category of multiple defects is the condition when inner race or outer race these two or three defects. However, the faults are considered to be coexisting in nature when different single or multiple defects occur on both the inner race and the outer race.

Extraction of fault features

Time as well as frequency-domain fault features are extracted after the data ensemble has been prepared. Mean, standard deviation, shape factor, kurtosis, crest factor, impulse factor, signal-to-noise ratio (SNR), and peak amplitude are a few of these features. In order to train the ML classifier with relevant features, the features are ranked by their relative importance using ANOVA technique.

Customization of the classifier

This step involves the tuning of ANN classifier with its activation function, hidden layer count and their size. Different instances by changing these variables are taken into account while assessing the effectiveness of the ANN model in classifying fault types. Tanh, ReLU, and Sigmoid are the three activation functions employed. With layer sizes of 10, 25, and 100, single-layered, bi-layered, and tri-layered ANNs are used.

Model training

Once the model is customized, the k-fold cross-validation method is used to train using the extracted fault features. The dataset is divided into k equal-sized folds (subsets) at random using this method. The model is trained using the remaining k-1 folds following the selection of one subset as the holdout (test) set. The process is repeated k times with a different holdout set every time. The 550 total data samples are divided into five equal-sized folds for the purpose of the current analysis, each of which contains 110 random sub-datasets. This is accomplished by using 5-fold cross-validation.

Results and discussion

According to methodology outlined in Fig. 4, the fault classification performance outcomes of the ANN classifier, attained with different combinations of activation function, hidden layer count, and layer size, are provided in Table 2. The highest level of accuracy obtained is 86.5%. Figs. 5, 6, and 7 illustrate the related confusion matrices for cases 1, 4, and 6, respectively, displaying the actual as well as predicted fault classes. Depending on the training time of the model, the cases producing the same accuracy might be further evaluated.

Table 2. Performance of ANN classifier in classifying bearing compound faults with different blends of activation function, hidden layer count, and the size of hidden layers.

Case	Activation function – ReLU, Hidden layer count – 1			
I	Size of layer	Accuracy	Training time	Prediction speed
	10	83.3 %	10.540 s	11000 Observations/s
	25	84.5 %	26.619 s	7300 Observations/s
	100	86.2 %	21.881 s	13000 Observations/s
II	Activation function – Sigmoid, Hidden layer count – 1			
	Size of layer	Accuracy	Training time	Prediction speed
	10	80.2 %	50.308 s	9500 Observations/s
	25	79.8 %	48.100 s	6900 Observations/s
	100	80.0 %	44.553 s	7800 Observations/s
III	Activation function – Tanh, Hidden layer count – 1			
	Size of layer	Accuracy	Training time	Prediction speed
	10	79.8 %	40.271 s	6700 Observations/s
	25	82.0 %	37.216 s	13000 Observations/s
	100	86.0 %	49.938 s	4800 Observations/s
IV	Activation function – ReLU, Size of layer – 10			
	Hidden layer count	Accuracy	Training time	Prediction speed
	1	86.5 %	66.001 s	9900 Observations/s
	2	83.3 %	10.540 s	11000 Observations/s
	3	82.5 %	28.803 s	7300 Observations/s

V	Activation function – ReLU, Size of layer – 100			
	Hidden layer count	Accuracy	Training time	Prediction speed
	1	83.1 %	16.579 s	7500 Observations/s
	2	85.8 %	22.079 s	4500 Observations/s
	3	84.4 %	39.224 s	11000 Observations/s
VI	Hidden layer count – 2, Size of layer – 25			
	Activation Function	Accuracy	Training time	Prediction speed
	ReLU	81.1 %	31.804 s	14000 Observations/s
	Sigmoid	76.0 %	36.311 s	10000 Observations/s
	Tanh	81.5 %	36.605 s	13000 Observations/s

The confusion matrices for Case I are displayed in Fig. 5 which correspond to a single hidden layer, a ReLU activation function, and a layer size of (a) 10, (b) 25, and (c) 100, respectively. The equivalent accuracies are 83.3%, 84.5%, and 86.2%. The confusion matrices with the ReLU activation function, (a) 1, (b) 2, and (c) 3 hidden layers of size 10 each are shown in Fig. 6 (Case IV), The respective accuracy values are 86.5 %, 83.3 %, and 82.5 %. The confusion matrices shown in Fig. 7 for case VI, corresponds to bi-layered ANN (two hidden layers), each of the size 25, and (a) ReLU, (b) Sigmoid, and (c) Tanh, the activation functions. The related accuracies are 81.1%, 76.0%, and 81.5%.

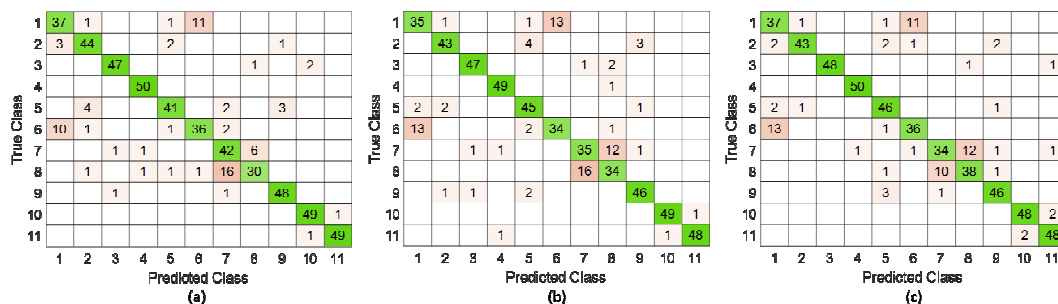


Fig. 5. Confusion matrices for One fully connected layer, ReLU activation function, and layer size (a) 10 (b) 25 (c) 100.

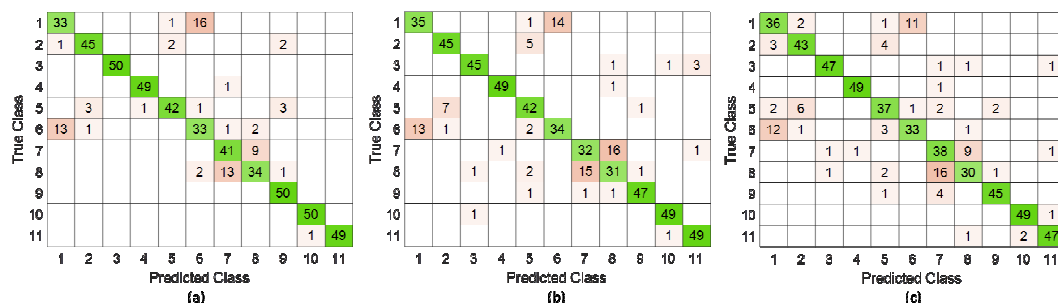


Fig. 6. Confusion matrices for Tanh activation function and (a) 1 (b) 2 (c) 3 fully connected layers of layer size 10 each.

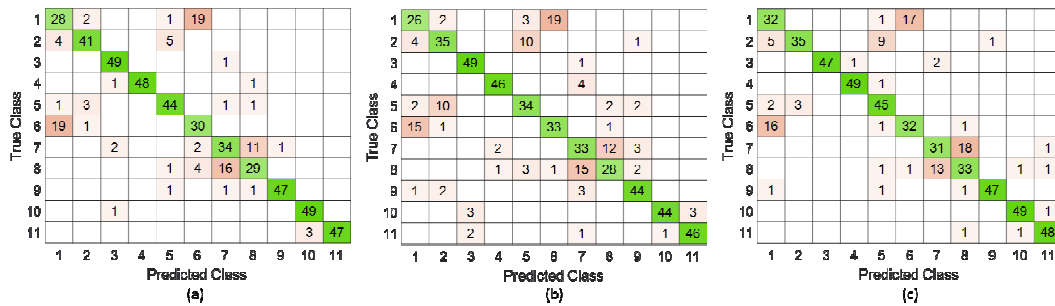


Fig. 7. Confusion matrices for Two fully connected layers of size 25 each, for (a) ReLU (b) Sigmoid (c) Tanh activation functions.

It is noteworthy that two sub cases of cases II and III (shown by the yellow cells in Table 2) have the same classification accuracy of 79.8%. In order to choose which of the two scenarios is better, there must be another performance criterion. As an illustration, the training time of 40.271 seconds for the second cell is shorter, as opposed to 48.100 seconds for the sub case of the first cell. As a result, for the dataset taken into consideration in the current study, Tanh activation function with one hidden layer of size 10 would result in the classifier learning the fastest.

Conclusion

The classification of rolling element bearing faults using an ANN classifier is examined while taking into account multiple defect categories. Time-domain and frequency-domain features are retrieved from the ensemble of bearing sound signals in order to train the ANN model with different blends of activation functions, number of hidden layers, and their size. The major variables used to assess the performance of the ANN model are classification accuracy, training time, and the prediction speed. In instance, the accuracy for a few cases is the same, the training time aids in identifying the better model. The current analysis found that when the ANN model is customized with one fully connected layer of size 10 and the ReLU activation function, it performs the best in classifying the bearing defects with a classification accuracy of 86.5%. It is anticipated that the proposed approach would find widespread use in actual industrial equipment for the precise identification of bearing faults. To enhance the fault diagnosis performance, other sound signal-based features will be examined in the near future, and defects in other rotating machine components will be investigated by conducting experiments in various background noise situations.

References

- [1] Sheng, H., Chen, Z., Xia, Y., and He, J., 2020, "Review of Artificial Intelligence-Based Bearing Vibration Monitoring," *2020 11th International Conference on Prognostics and System Health Management (PHM-2020 Jinan)*, pp. 58–67.
- [2] Hecke, B. Van, Qu, Y., and He, D., 2015, "Bearing Fault Diagnosis Based on a New Acoustic Emission Sensor Technique," *Proc. Inst. Mech. Eng. Part O J. Risk Reliab.*, **229**(2), pp. 105–118.
- [3] Ananthapadmanaban, T., and Radhakrishnan, V., 1982, "An Investigation of the Role of Surface Irregularities in the Noise Spectrum of Rolling and Sliding Contacts," *Wear*, **83**(2), pp. 399–409.

- [4] Tekner, Z., and Yeşilyurt, S., 2004, “Investigation of the Cutting Parameters Depending on Process Sound during Turning of AISI 304 Austenitic Stainless Steel,” *Mater. Des.*, **25**(6), pp. 507–513.
- [5] Heng, R. B. W., and Nor, M. J. M., 1998, “Statistical Analysis of Sound and Vibration Signals for Monitoring Rolling Element Bearing Condition,” *Appl. Acoust.*, **53**(1), pp. 211–226.
- [6] Shibata, K., Takahashi, A., and Shirai, T., 2000, “Fault Diagnosis of Rotating Machinery Through Visualisation of Sound Signals,” *Mech. Syst. Signal Process.*, **14**(2), pp. 229–241.
- [7] Baydar, N., and Ball, A., 2003, “Detection of Gear Failures Via Vibration and Acoustic Signals Using Wavelet Transform,” *Mech. Syst. Signal Process.*, **17**(4), pp. 787–804.
- [8] Amarnath, M., Sugumaran, V., and Kumar, H., 2013, “Exploiting Sound Signals for Fault Diagnosis of Bearings Using Decision Tree,” *Meas. J. Int. Meas. Confed.*, **46**(3), pp. 1250–1256.
- [9] AlShorman, O., Alkhatni, F., Masadeh, M., Irfan, M., Glowacz, A., Althobiani, F., Kozik, J., and Glowacz, W., 2021, “Sounds and Acoustic Emission-Based Early Fault Diagnosis of Induction Motor: A Review Study,” *Adv. Mech. Eng.*, **13**(2), pp. 1–19.
- [10] Mian, T., Choudhary, A., and Fatima, S., 2022, “An Efficient Diagnosis Approach for Bearing Faults Using Sound Quality Metrics,” *Appl. Acoust.*, **195**, p. 108839.
- [11] Grebenik, J., Zhang, Y., Bingham, C., and Srivastava, S., 2016, “Roller Element Bearing Acoustic Fault Detection Using Smartphone and Consumer Microphones Comparing with Vibration Techniques,” *2016 17th International Conference on Mechatronics - Mechatronika (ME)*, pp. 1–7.

Reliability Improvement of Exciter Gearbox at Sinter Plant

Aditya Jain (Technologist, One SSTG, aditya.jain@tatasteel.com)

T. Thirumurugan (Principal Technologist, One SSTG)

G. R. P. Singh (Head – Quality Assurance Group, One SSTG)

N. Rajesh Kumar (Chief- One SSTG)

Himangshu S. Mandal (Principal Technologist, One SSTG)

Tata Steel Limited, Jamshedpur – 831001, India

Abstract

In integrated steel plant, Sinter Plant plays an important role in providing sinter as raw material to the Blast Furnaces. Any unplanned outage of Sinter Plant leads to loss of hot metal production rate and impacts the quality of hot metal. In sintering process, after sinter machine, hot sinter is screens as per process requirement. Further, over size material goes to Blast Furnace and under size material returns to silo and finally reused for sinter making process.

Vibratory screens are used for this purpose and the exciter gearbox generates the excitation force in the screen due to unbalanced masses. The reliability of the exciter gearbox is very important for screen availability. The exciter gearbox is mounted on the screen console beam at 45 - 55 degrees in inclined/decline orientation which varies as per screen design. Because of this, oil level cannot be checked in running condition. The failure of bearing of exciter gearbox was the chronic issue at Sinter plant. Therefore, detailed Root Cause Failure Analysis has been carried out and recommendations implemented. The study has been done in followings aspect which has been addressed in this paper. Inadequate lubrication system & dust contamination were the main root cause of this case.

- *Calculation for correct size of Exciter gearbox*
- *Exciter gearbox Unbalanced mass tuning*
- *Gearbox lubricant type, grade, filling quantity, refilling frequency, & filling standard procedure*
- *Gearbox lubricant & Ferrography analysis*
- *Importance of presence of sinter dust contamination in gearbox oil*

Keywords: *Vibratory screen, Exciter gearbox condition monitoring , Oil analysis*

Introduction

Exciter gearbox:

These comprises of two shafts fitted with segments, rotated in opposite direction through a set of gears and generates linear motion. These exciters are used particularly for very heavy duty applications & fitted with special vibration duty bearings.

Operating principle:

The centrifugal force components F_1 and F_2 acting in the direction a-a add up to the resultant force F_{res} . The components occurring in direction b-b eliminate one another.

Static moment:

An important characteristic of the exciter is the so called static moment. In place of the static moment, the “working moment” is frequently indicated. The working moment is double the static moment. Static moment is the weight of the segments multiplied by its center of gravity radius. Normally, it is indicated in kgcm. The static moment and the centrifugal force generated by the exciter can be adjusted in the shutdown state by removing or adding unbalance masses.

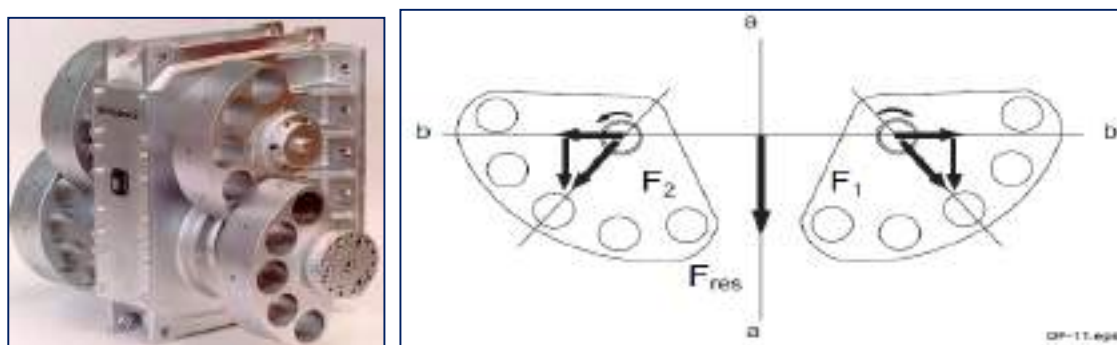


Fig.-1 Exciter gearbox working principle

The general arrangement of drive components of Vibratory screen (Fig.-2) and location of failed exciter gearbox (Fig.-3) are shown in the below figure-

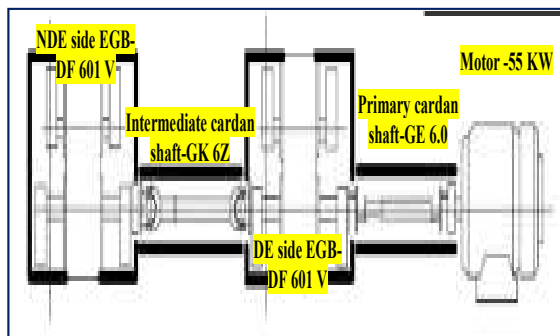


Fig.-2 GA of drive components of Screen



Fig.-3 Location of failed gearbox

Internal arrangement of Exciter gearbox (DF 601 V) is shown in figure 4.

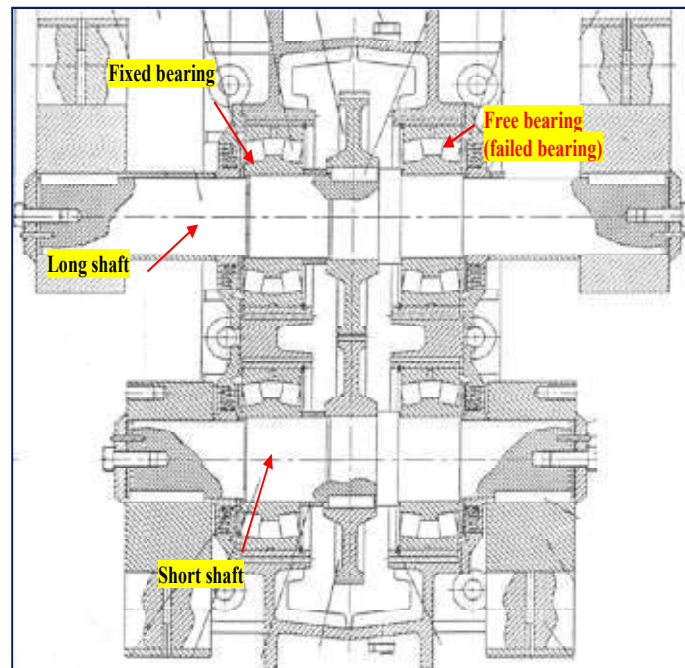


Fig.-4 Exciter gearbox internal arrangement

Key observation:

Both gears (long & short shaft gear, helical gear type) were checked, and 5 -6 teeth of drive gear (long shaft gear) were found to be in broken condition. Spalling and pitting marks were also observed on the same zone (Fig.-5). Physical condition of the pinion gear teeth (short shaft gear, Fig.-6) and rest teeth of drive gear was ok.

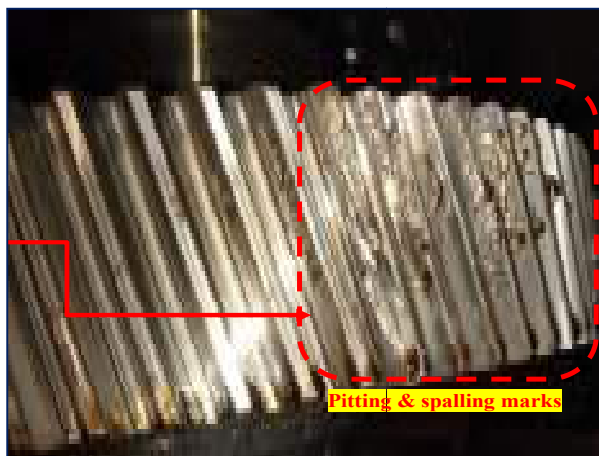


Fig.-5 deep spalling & pitting marks

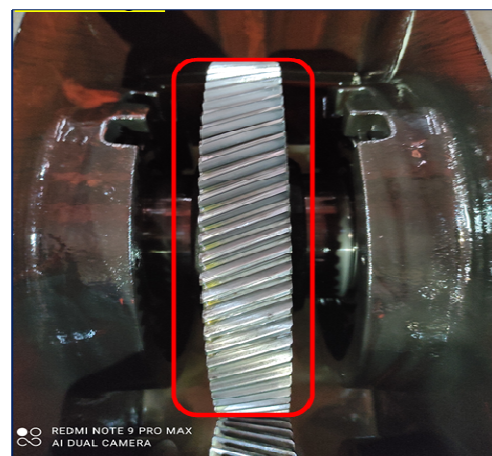


Fig.-6 Short shaft gear

Observation on bearing & housing assembly (failed, long shaft free bearing)

- Heating (blackish colour)/burning (bluish colour) marks were observed on the outer surface of the bearing outer ring (Fig.-7 (A)).

- Heavy dust deposition was observed (Fig.-7 (A) & (B)).
- Spalling marks observed on the rolling elements (spherical rollers) (Fig.-7 (C) & (D)).
- Carbon deposition (oil & felt ring burning deposition) was observed on the inside of dynamic labyrinth seal & oil splash ring (Fig.-7 (E)).
- Felt ring got ignited completely, only the residual was found in end cover (Fig.-7 (F)).



Fig.-7 Failed bearing

Analysis:

1.1 Calculation for Correct Size of Exciter Gearbox

As per GA drawing of vibratory screen

Weight of screen assembly (with screen deck) in Kg = 18800

Total weight of exciter gearbox in Kg = Weight X No. of exciter gearbox

Total weight to be vibrated = Weight of screen assembly + Total weight of exciter gearbox

Amplitude = 2 X stroke, Stroke = Amplitude/2 in mm

Required static moment = Total vibrating mass in Kg X Stroke in cm

= 22000 in Kg X 0.6 cm

= 13200 Kg-cm

Static moment for each exciter = Total required static moment/ no. of exciter gearbox

= 13200 Kg-cm / 2

= 6600 Kg-cm

Selection of exciter gearbox can be done as per chart 1.

For this case, size checked and found DF 601V which is okay for this application.

Chart 1: Directional Force Exciter Static Moments in Kgcm

Directional Force Exciter			Unbalance Arrangement							
Type	Design	Equipped With:	○	●	○	●	○	●	○	●
DF 100	S	Steel unbalance weights	208	238	264	294	300	330	356	386
		Lead unbalance weights	208	250	286	328	332	374	410	452
DF 200	S	Steel unbalance weights	312	362	406	456	460	510	554	604
		Lead unbalance weights	312	379	436	503	510	577	634	701
DF 300	S	Steel unbalance weights	484	546	618	680	694	756	828	890
		Lead unbalance weights	484	568	666	750	770	854	952	1036
DF 401	S	Steel unbalance weights	840	1060	1052	1264	1204	1420	1412	1624
		Lead unbalance weights	1200	1506	1496	1804	1716	2024	2012	2316
DF 404	S	Steel unbalance weights	1016	1283	1273	1529	1457	1716	1709	1965
		Lead unbalance weights	1016	1400	1386	1755	1650	2027	2013	2382
DF 501	S	Steel unbalance weights	1408	1736	1800	2128	2068	2396	2460	2800
		Lead unbalance weights	1160	-	2004	-	2264	-	3108	-
DF 504	V	Steel unbalance weights	1160	-	2320	-	2680	-	3840	-
		Lead unbalance weights	1792	2209	2291	2708	2632	3049	3131	3564
DF 601	S	Steel unbalance weights	1792	2393	2510	3111	3001	3602	3719	4342
		Lead unbalance weights	2296	2916	2872	3492	3304	3924	3880	4500
DF 604	S	Steel unbalance weights	3552	4528	4740	5676	5516	6452	6664	7600
		Lead unbalance weights	3916	4936	5167	6188	6013	7034	7265	8285
DF 604	V	Steel unbalance weights	3916	5346	5669	7099	6855	8285	8608	10038
		Lead unbalance weights								

1.2 Exciter Gearbox Unbalanced Mass Tuning:

Mass tuning (mounting sequence, installed quantity and Material of Construction) of all additional cylindrical masses was checked and found identical for all four segments of failed Exciter Gearbox (Fig.- 8 (A) & (B)).

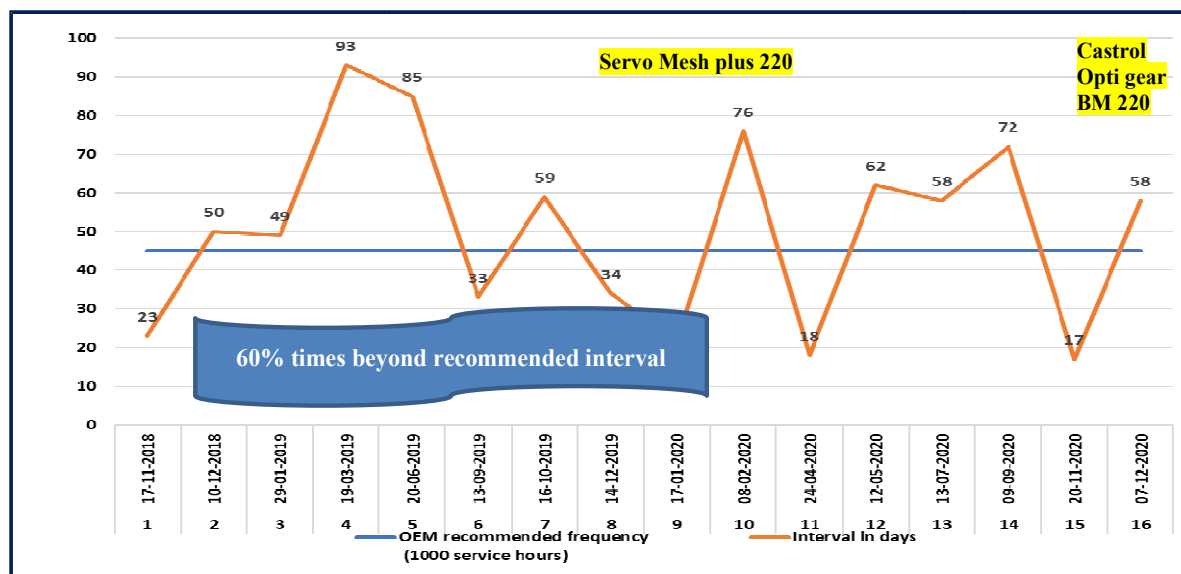


8 (A) Fixed side

8 (B) Free side

1.3 Lubrication interval

As per drawing, exciter gearbox oil should be changed every 1000 operating hours / 40-45 days or on the abnormality of oil/ ferrography analysis report, but in this case, oil replacement history of last two years was checked in department record and it was found that oil was changed several times (10 out of 16 times) after OEM recommended frequency.



Graph-1 Line graph of oil replacement history

In this failure, the last oil replacement was done on 07.12.2020. After that, oil was not changed until failure (03.02.2021). It means that the EGB oil had already crossed 58 days. Therefore, oil should have been changed which was not done. It is also observed that oil samples of EGB were not sent to lab for oil analysis for the past one year.

1.4 Selection of lubricant:

Type of lubricant was checked and found as per OEM recommended oil (Castrol Opti Gear BM 220). However, same oil is being used since Nov'20. Earlier, Servo Mesh Plus 220 oil was being used as lubricant which was an old generation oil (less oxidation stability and EP additives compared to new generation oil).

It means that the failed EGB was run over more than 90% of service days (734 out of 809 days) with Servo Mesh Plus 220 oil, which would have also adversely affected the gearbox (breakage of Elastic hydrodynamic lubrication (EHL) film).

1.5 Lubrication starvation:

Oil level of the exciter gearbox is maintained 225-230 mm (dip stick reading). It is obtained by filling 9 to 9.5 litres of oil in the gearbox which is found as per drawing.

1.6 Contaminants ingress:

After the failure, the oil sample was taken from the failed exciter gearbox and oil & ferrography analysis was done at lab. Contaminants were observed in the oil sample.

Failed EGB was dismantled at assembly shop and heavy dirt contaminants were observed in the failed bearing. However, it was also seen in small quantities in the other three bearings.



Fig.-9 Presence of contaminants

Lubricating holes of the failed bearing housing were also checked and 4 out of 6 were found to be in clogged condition. Same was checked of remaining three housings and found okay.

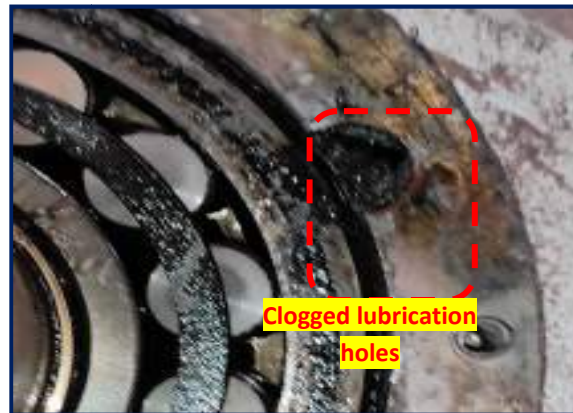


Fig.-10 Clogged oil lubrication holes

After failure, bearing RIC of all four bearings was measured and found to be 0.55 mm for failed bearing, while 0.15 mm for the other three bearings. Deep spalling marks were also noticed on the same failed bearing.

Marking no.	Bearing side	Before mounting RIC (as per OEM catalogue)	After mounting RIC (as per OEM catalogue)	After mounting RIC (actual measured at site)
Marking-1	Short shaft-fixed bearing	0.19 - 0.24	0.14 - 0.20	0.15
Marking-2	Long shaft-fixed bearing			0.15
Marking-3	Long shaft-free bearing			0.55
Marking-4	Short shaft-free bearing			0.15

It reveals that due to heavy dust ingress (highly abrasive sinter dust), spalling marks were initiated resulting in increased bearing RIC.

However, Since Feb'20, the oil sample was not sent to lab for oil/ ferrography analysis, as result of which the presence of contaminants could not be revealed at that time.

Further, oil was also not changed in time which would have increased bearing RIC (breakage of Elasto hydrodynamic lubrication (EHL) film as Servo oil having less oxidation stability and EP additives compared to new generation oil).

There are two possibility of contaminants ingress:-

1.6.1 Ineffective sealing:

Felt ring (asbestos type) is provided between static & dynamic labyrinth seal to prevent oil leakage/dust ingress.

After failure, all four segments were inspected. Heavy abrasive wear marks & step formation were observed on the end points of the both swing segments of long shaft (Fig.-10). While both segments of short shaft were found in good condition.



Fig-11 Abrasive wear marks

It indicates that both segments of long shaft were merged into sinter dust (highly abrasive), resulting in friction was happening in between contact area of segments and dust accumulation, during rotation. Due to this, long shaft was facing additional load resulting in the felt ring being suppressed and the radial gap between the two labyrinth seals increased.

Dust was entered into housing from this space. However, after failure, felt ring was found in burnt condition. Felt ring of other side of long shaft was also inspected and found to be in little suppressed condition. Dust contaminants were also noticed in small quantity.

1.6.2 Dust ingress during oil filling:

As per OEM, during oil filling, funnel should be used with fine-meshed filter cloth which was not found in this case.

The EGB oil is replaced at every shutdown and at that time, the equipment cleaning is also done by pressurized air blowing, resulting in increased possibility of dust entering the bearing housing.

Same was happened in this case. Contaminants/dust might have entered during the filling of the oil as fine-meshed filter cloth was not being used.

Conclusions:

Based on the above analysis, it can be concluded that Exciter gearbox oil was not changed as per OEM recommended frequency (10 out of 16 times). Further, sinter dust ingress which was entered from the suppressed felt ring of labyrinth seal that would have aggravated the failure. In order to avoid such premature failure followings guideline has been deployed-

- a) Exciter gearbox oil to be replaced as per OEM recommended frequency (1000 service hours / 40 - 45 service days / based on oil & ferrography analysis report).
- b) Exciter gearbox bearing end covers & segment cleaning to be done in every shutdown by using cotton cloth.
- c) In every oil replacement, sample of the oil to be sent to lab for oil & ferrography analysis to detect oil & equipment condition.
- d) During oil changing, funnel to be used with fine-meshed filter cloth to avoid dust ingress.
- e) Before oil draining, oil level to be measured and recorded.
- f) Oil replacement history to be recorded.

Acknowledgement:

The authors convey their sincere gratitude to the personnel of Sinter Plant team for their timely support and help for the successful completion of this case study. Also, thankful to the management of Tata Steel for providing us this opportunity to present this paper.

References:

- [1] M/s. Schenck process screen O & M manual
- [2] M/s. TVV screen O & M manual
- [3] M/s. Bivitec screen O & M manual
- [4] M/s. SKF bearing manual
- [5] GA drawing of Vibratory screen & feeder

Data driven based solution for condition monitoring of continuous Galvanizing line motors using time series data

**Gaurav Lal, Namrata, D.N Sharma, Priya Ranjan Mahaptra,
Arghya Deb, Sanjeev Kumar**

Automation Division, Tata Steel Limited, Jamshedpur -831001, India

Abstract

The objective of this paper is to present a data-driven-based solution for condition monitoring of motors driving the rolls of the continuous galvanizing line (CGL) at Tata Steel Ltd. (TSL). An intelligent system has been developed to continuously monitor and diagnose time-series data of motor drive parameters (speed-load) with coil parameters (primary data input (PDI)) and process line parameters (tensiometer) and send alerts if a significant abnormal deviation in motor loads found from their historical trend for the same PDI. The process line processes five different grades of coils, resulting in a motor with a wide operating range. K-mean clustering is used, and two working states are defined for each motor for each coil grade. A lookup table (centroids of each cluster) is created to test the functionality of new data points. After clustering, multivariate outlier detection using Mahalanobis distance (MD) is performed to remove outliers from each cluster data set. The cleaned data set is then trained on a regression-type supervised learning to predict theoretical load in order to monitor the progression of severity, especially in the case of abnormal or outlier data points. The XG Boost was chosen as the final model because it was found to perform relatively well on both large and small datasets. This application was extremely useful to the plant's electrical maintenance team. The proposed study could help similar industries transition from conventional to smart process lines with Industry 4.0.

Keywords: *Condition monitoring (CM), Data-driven, K-mean clustering, Multivariate, Mahalanobis distance (MD), Industry 4.0.*

1. Introduction

Industry 4.0 has the potential to significantly increase productivity, work efficiency, and supply information for production management by automating, robotizing, and digitising human tasks to ensure increased production speed and efficiency [1]. Tata Steel, being a top leader in the steel industry, has embarked on the journey of Industry 4.0 as a business goal to improve product quality, productivity, cost and process safety, which remains the foremost goal of the company. The applications of industry 4.0 in manufacturing industries include cyber security, augmented reality, big data, autonomous robots, additive manufacturing, simulation, system integration, and cloud computing [2]. With the advent of sensor technology, various machine parameters are captured on a real-time basis, resulting in a massive data lake. These data lake can be further formulated in an intelligent system to make an automatic decision on the health of the equipment. In the recent past, smart condition monitoring has gained popularity in which smart sensors are used to predict machine health status, asset utilization and failures in advance [3]. While various literature is available that discusses the scope or theoretical aspects of smart maintenance in industry, we aim to fill some gaps by presenting a complete solution to the real-life industrial problem of condition monitoring of CGL motors.

Condition monitoring of the induction motor is necessary for process safety and is directly linked to the productivity and uptime of the system [4]. The motors driving the CGL rolls at TSL are induction motors. Their failure results in 10 to 20 hours of down time or productivity loss, depending upon the location of the motor in the CGL process line. Speaking more specifically, bearing failure is the most common in motors, accounting for around 45% of all motor failures [5]. One of the reasons is that it is continuously subjected to mechanical stress and high vibration during operation [4]. Vibration-based condition monitoring using an accelerometer is the conventional approach for condition monitoring of rotating machines. In this approach, piezo-electric sensors are mounted on motor bearing casings and vibration is measured [6]. The time-series vibration value (accelerations) is converted into a frequency spectrum using the Fourier transform technique, and several fault frequencies like shaft rotational frequency, ball pass inner raceway, and outer raceway frequencies are calculated [7]. However, accelerometer sensors are very expensive, prone to faults, and their installation on machines is also specific; they are sensitive to corrosion and dusty environments [4]. Such failures can be categorised as failures from an internal source of the motor, caused by manufacturing error or degradation of material constituting the machine. Failure of a motor due to variations in load or power supply can be classified as an "external source failure" [5]. In the present work as well, the target is to detect the abnormal increase in motor load for a given PDI by comparing the load value with its historical trend. An incident involving a motor failure in the exit section of CGL has led to the trigger of this project. On further analysis, it was found that before failure, motor load had increased in the same PDI, and it continued to run and resulted in its failure. Additionally, the project does not have access to the specialised vibration sensors. This encourages us to use a machine learning strategy.

The paper aims to contribute in two ways:

1. This paper presents a methodology for diagnosing the health of CGL motors by condition monitoring in real time, motor-load value w.r.t coil grade (PDI information), and tensiometer readings in the time series domain.
2. It will serve as a case study to strengthen the literature on the theoretical idea and application of Industry 4.0 in the manufacturing industry. Elements of Industry 4.0 such as digitization, data acquisition, data analytics, etc. are also covered.

2. Background and CGL process line

A condition monitoring system's objective is to detect faults or anomalies. A defect can occur when an observed variable or calculated parameter deviates from a valid range. [8]. It is uncommon for a faulty dataset to be available in a condition monitoring context. Data sets of healthy duration are gathered to address this, and significant deviation from this healthy zone is viewed as a signature of abnormal behaviour. In the present study as well, the collected dataset is unlabelled. However, we can manually make some labelling of the datasets collected over time because of the fact that mechanical devices operating under load or stress deteriorate over time. The author in [9] has explained a multi-state deterioration mechanism where machine may perform at an intermediate working state between healthy and failure working states. The data collected from multiple sensors can be used to create a virtual simulator for that machine to make future decisions by using data-driven machine learning techniques as it has information about machines in several operating states. In a data-driven approach, decision making solely depends on quantitative data. Hence, the data is of primary importance. But the operating states are not labelled or

visible to us directly, so they need to be defined manually. For this situation, an unsupervised learning algorithm tends to be the best fit. Data-driven statistical parameters like mean, standard deviation, maximum, root mean square, skewness, kurtosis, and many more can be used as feature extraction or condition monitoring indicators, and the same is described by the author in [10] for condition monitoring of rotary machines.

Aside from that galvanizing is the process of applying a protective zinc coating to steel or iron to prevent it from rusting. The hot-dip method is used to coat zinc on steel. One way is to pass steel strip continuously through a molten zinc bath at high speed. This method is known as "continuous galvanizing." To make the process continuous, the steel strip ends are welded together [11]. The general schematic representation of the continuous galvanizing line is shown in Fig 1. It can be grouped into 4 sections: entry, process, furnace-galvanizing, and exit. In the entry section, there are two entry pay off reels (E1, E2), which allow continuous supply of a steel strip to the process line by welding their ends together. It is rotated by motors. The process section starts with cleaning and degreasing, soaking, and cooling of the coil. And then it passes to the furnace galvanizing, where preheating and heating of the coil is done to increase the steel temperature to around 450°C before it passes to a molten zinc pot. After this section, it passes through a skin pass mill to the exit section, where the coil is wrapped in the exit looper pay off reel (X1). The coil strip moves from entry to exit over rollers which are run by AC motors. For this project, 27 critical motors have been selected for condition monitoring. The design and implementation approach have been shown only for the KA motor of the exit section in this paper. The same is applied to the remaining 27 motors. Motor feedback speed (rpm), load (%), tensiometer (kg/m²), and coil details are available as input features. There are a total of nine tension set point throughout the CGLprocess line to measure tension in the coil strip.

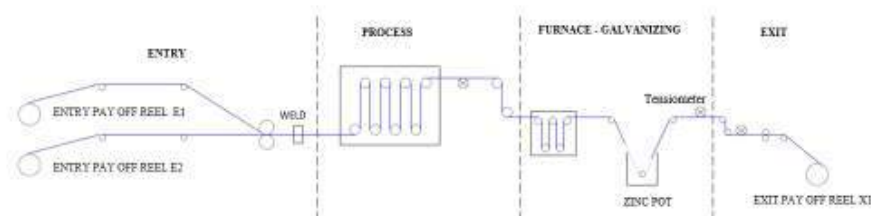


Fig 1. General schematic layout of CGL

There are mainly five grades of coils (EIF, DQ, CQ, HSQ, and HIF) that get zinc coated through the galvanizing process line. Coil parameters like width, thickness, and weight vary in each grade, and so does the motor load-speed, shown in Fig 2.1 and 2.2, respectively. From Fig 2.1, coil thickness varies from 0.6 to 1.8 mm in EIF grade and motor (KA) speed varies from 200 to 1400 rpm.

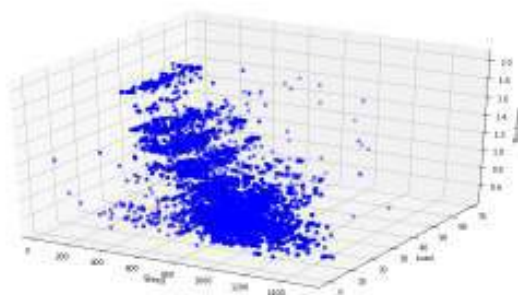


Fig 2.1. 3D scatter plot of KA motor (speed, load), w.r.t EIF coil thickness

The motor operating condition varies with thickness; for thicker coils, mostly galvanizing is done at a lower speed relative to thinner coils. For condition monitoring of the motor, the maintenance team suggested defining safe operating conditions for each motor and for each grade. Unfortunately, an unhealthy data set for the motors is not available. This leads to heading towards unsupervised machine learning techniques to explore historical data and define operating condition zones and safe operating limits.

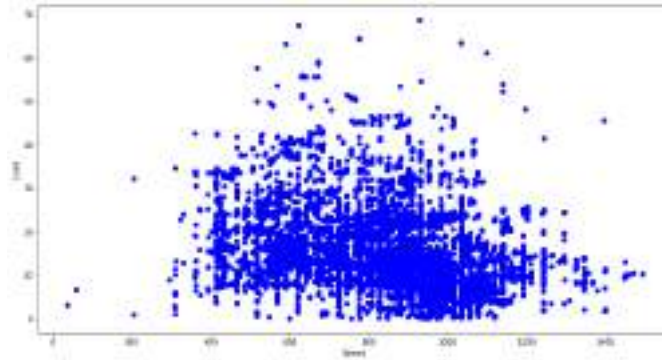


Fig 2.2. Scatter plot of load vs. speed of KA motor w.r.t EIF grade coil

3. Methodology

The fundamental infrastructure, including PLCs and an OPC server(iba PADU), was available at the start of this project. Any PLC can exchange data with OPC servers using the standard protocol known as OPC (Open Platform Communication). A server and client pair is used to implement OPC. Tensiometer set points maintain tension on the coil strip to allow it to move forward in the process line. Sometimes the wrong tensiometer set point value (high tension value creates more tension force on the coil strip) results in abnormal motor load.

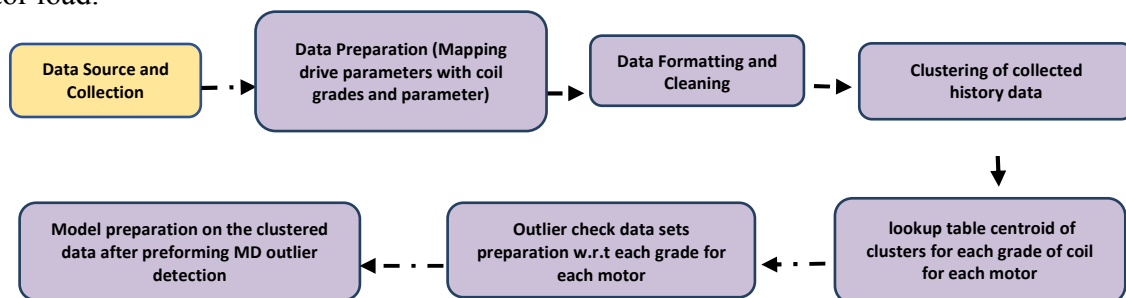


Fig 3: Flow diagram of methodology

This section of the paper describes the methodology followed to create the intelligent system using a data-driven approach. The collection of time series data of speed, load, and tensiometer values with coil PDI (Primary Data Input) is the initial stage because historical data is crucial in this situation. After data collection, it needs some formatting and cleaning to produce only the useful data in the appropriate structure. Because the solution employs an unsupervised learning approach, historical data is clustered to label motor operating ranges based on speed load value. Following clustering, a lookup table was created using the centroid of the clusters to determine which future input points belong to which motor operating group. Finally, after performing multivariate outlier detection (MD), a regression model is trained on the clustered data.

3.1 Data Source and Collection

The drive parameters and coil parameters are the two data sources. Drive parameters such as speed, load, and tensiometer (process line parameters) values are saved in an Oracle database (named "drive database") by the OPC server. As shown in Fig 4, PLCs receive data from sensors in registers, which are defined as tags in OPC servers (in our case, iba), and each tag is read in an OPC client application and saved in an Oracle database. Although the OPC server can read data from PLCs at a sample rate of 50 milliseconds, it was decided to save records in drive DB at a sample rate of 5 minutes as a trial. It was assumed that if load tends to increase, it will persist for a longer period of time.

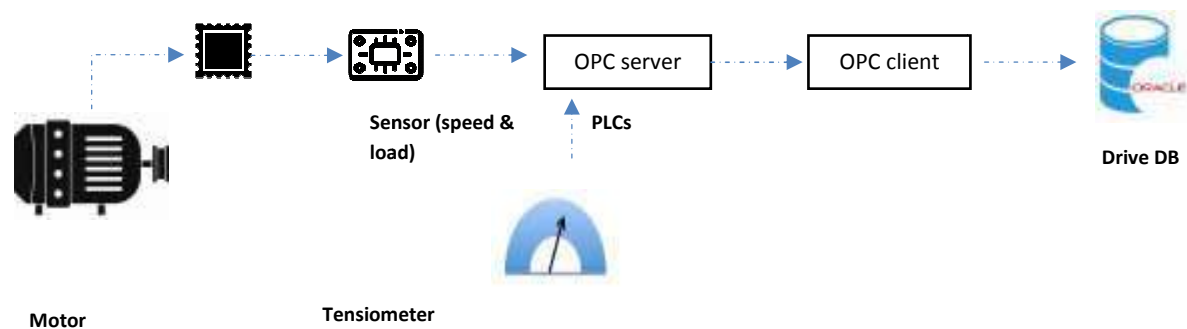


Fig 4: Drive parameter data collection flow

In our plant from level 1, PDI information is routed to the level 2 system. PDI records the coil's ID as well as its properties such as weight, thickness, width, and grade.

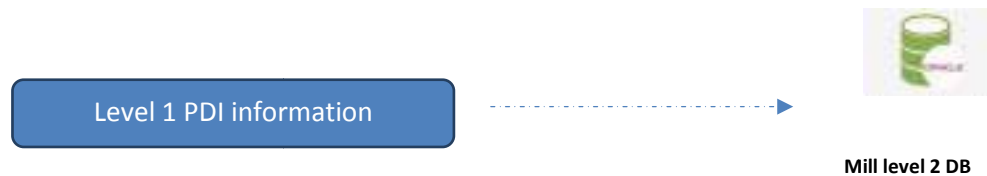


Fig 5: PDI information to Mill level 2 database

3.2 Data preparation (feature mapping, cleaning, and formatting)

In the above section, the data collection flow has been demonstrated. Both drive parameters (rpm), load (%), and tensiometer feedback (kg/m²), as well as coil parameters (grade, coil id, thickness (mm), and width (mm)) are saved in separate Oracle databases. It needs to be mapped together. For developing this project, data from September 2021 to December 2021 (24 k instances) was taken. To perform exploratory data analysis (EDA), data points pertaining to the idle condition of the motor were removed. There are five grades of coils being processed in the CGL line (EIF, CQ, DQ, HSQ, and HIF), and coil parameters vary for each grade. For demonstration, 18 coils of EIF grades of different thicknesses while processing through the KA motor have been shown below in Fig 6. The speed-load plot is shown with two different colours as we grouped the motor operating range into two clusters, as shown in the next section. An adjacent tensiometer has been considered for

predicting load through a developed regression model. T6 and T7 are the adjacent tensiometers to the KA motor.

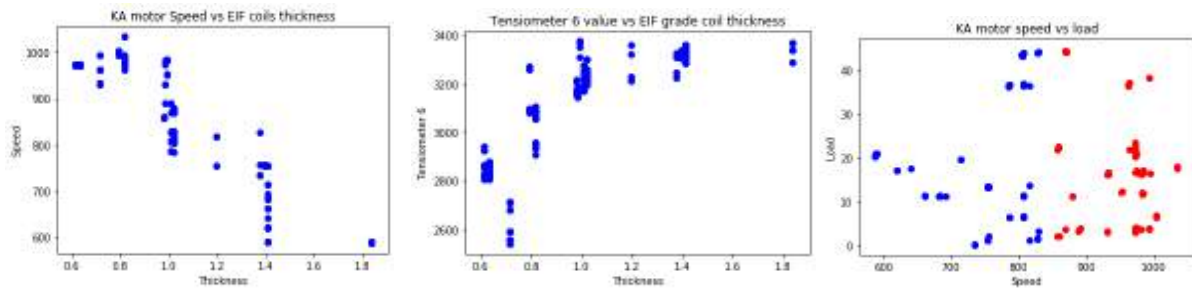


Fig 6: Scatter plot of drive parameter and coil parameters (features available for this project)

3.3 Clustering of history data

K-mean clustering was implemented on the historical data of motor speed and load to define some intermediate operating stages and to make the data labelled. It requires the number of clusters to be defined in the dataset as an input. Its algorithm randomly assigns a centre value to these clusters from the dataset. And the Euclidean distance (ED) of each point w.r.t each cluster is calculated. And the point is assigned to the cluster with the minimum ED. These steps are repeated till the last two iterations remain unchanged. The author of [12] has explained K-mean clustering in detail. A couple of methods are available to choose the appropriate number of clusters, like the elbow method and silhouette coefficient. In the elbow method, with in the sum of squares (WSS) is calculated. As the name suggests, it is the sum of the squared distance between the data points of the cluster and its centroid. The silhouette value indicates how well data is in the cluster. Its value varies from +1 to -1. The +1 value indicates that the number of clusters is very appropriate, and all points present in the cluster are well organised. If the value is less than 0, it indicates that the data points do not belong to that cluster [13]. However, the results of clustering are shown in result and discussion sections of this paper.

3.4 Outlier detection

Outlier detection is the process of finding data points that do not fit into the given dataset. In a production application, this process is deployed in automated mode to detect whether a new data point is an outlier or normal. Condition monitoring systems generally aim to detect such outlier points and generate alerts for the same. We have taken 3-month data (Sept to Dec 2021), which equates to around 24K data points for developing the models. Each clustered set is subjected to outlier detection after clustering in order to identify any unusual points within the group. Outlier detection can be divided into two categories: univariate outlier detection and multivariate outlier detection. As the name implies, in univariate, only one feature is available for outlier detection, which is typically done using a graphical tool like scatter, box plot, and so on [14]. In a multivariate case, two or more features are available. In such a case, a graphical tool may be ineffective. An outlier may have an unusual value in one or more dimensions. In our case, we have multiple variables: speed, load, and tensiometer values for outlier testing. In order to automate these processes, it requires some mathematical approach. Authors in [10] [14] have discussed Mahalanobis Distance (MD) for calculating outliers in multivariate datasets. MD calculates the distance between a point and the distribution. Six-sigma and critical chi square value is used to

determine threshold or UCL of MD. Above this threshold, the points can be considered as outlier.

3.5 Modelling

In this section of the paper, machine learning regression algorithms like XG Boost, Random Forest, and Partial Least Squares are discussed briefly. The idea behind selecting these algorithms is to do a comparison between ensemble and solitary machine learning techniques. XG Boost and RF belong to an ensemble group, whereas PLS is from a solitary machine learning group. The root mean square error (RMSE) and R square of the algorithms have been compared to select final model. However, it has been found that all three models performed well and were nearly similar. But ensemble machine learning algorithms show an upper edge over solitary machine learning algorithms.

3.5.1 Random Forest

In this algorithm, sub datasets are created by random sampling (known as bootstrapping) and they are trained and tested across multiple weak learners (known as aggregation). And the results of multiple models are combined to provide final predictions [15]. Thus, Random Forest (RF) is a bagging algorithm that trains weak learners in parallel. RF is a combination of large decorrelated decision trees (Classification and Regression Trees (CART)). These trees (weak learners) are trained with random sampling of datasets and variables, to select the best dependent variable (root node) [16]. The author [17] has used random forest for condition monitoring of a machine and has explained the key factors of decision tree like entropy, Gini index, and information gain. Both the entropy and the Gini index help to decide the root node. Lower entropy in datasets implies lower randomness in the dataset, i.e., the dataset is less heterogeneous. Such a dataset is best to start as a root node.

3.5.2 XG Boost

Extreme gradient boost (eXG Boost) is a tree-based ensemble learning uses boosting algorithm to boost model accuracy. Bagging and Boosting are used widely to perform ensemble learning [15]. However, in boosting, weights are assigned to the datasets and trained on weak learners. More weight is assigned to dataset which got incorrect by previous or earlier weak learners and then passed to next weak learners or model. This process of modifying weights from passing one to next weak learners makes it sequential process of training [15]. Bagging tends to reduce only variance by aggregating multiple model output, while boosting tends to reduce both bias and variance [18]. It is desirable to work with low bias and variance for accurate prediction. The silent features of XG boost includes regularization, parallel computing, cache awareness etc. The major advantage of using XG Boost is execution speed and model performance [19]. Author [19,20] has demonstrated mathematics of XG Boost and loss function.

3.5.3 Partial Least Square (PLS)

One of the major concerns in machine learning is multi co linearity in datasets. These features do not contribute to uniqueness and may lead to over fitting. Multi co linearity is available in our case too. The adjacent tensiometer readings are highly

correlated, as shown in Fig 11. It can be seen that T1 to T5 tension meters are highly correlated, and T6, T7, and T8 are the least correlated. One of the ways to overcome multi co linearity is to convert datasets into M linear combinations (principal components) and then fit a regression model using the least square error approach. It only takes input features into consideration to generate principal components [21]. Unlike this, PLS considers both input and output features to calculate M linear combinations (PLS components or latent variables) and uses least square error to fit the model. In PLS, the dataset is standardised in the first step, to bring all the features onto the same scale between 0 and 1. And to find the optimal number of M, k-fold cross validation is generally used [21]. However, in our case, the number of features is not very high. We have generally 3 input features: speed, and adjacent tensiometer value. Out of these, tension meters are highly correlated. So, we kept the generic value of M as 2.

4. Result and discussion

Data points from September to December 2021 were used to develop the model. Motor (speed, load) and tensiometer values are taken from the drive parameter database, and PDI information is taken from the mill level 2 database. The Mill level 2 database has the in and out time and processing duration details of coils processed in the CGL process line. It has been found that EIF grade is in the majority shown in Fig 7, i.e., EIF has been selected for demonstrating results of data exploration.

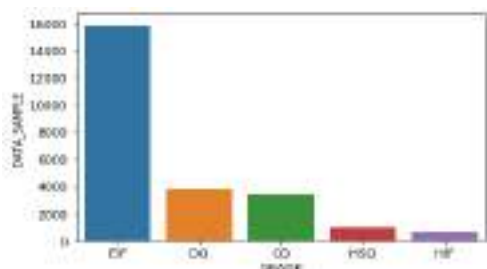


Fig 7: Bar plot of data sample w.r.t coil

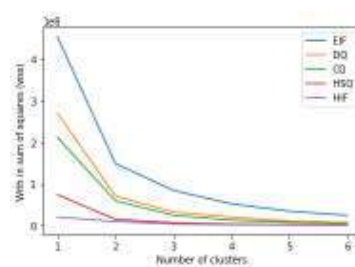


Fig 8: WSS vs number of clusters to grades determine optimal cluster size (KA motor w.r.t all grades)

After mapping the database, datasets for individual grades have been separated out. Data points (for KA motor) corresponding to idle or shut down condition is having speed-load value as zero has been removed. Now k-mean clustering has been performed on these datasets to define an intermediate working operating stage. The number of clusters has been concluded from the cross-elbow method and silhouette score. From Fig 8 and Table 1, it can be seen that at $k = 2$, there is a sharp decrease in the gradient of WSS and the silhouette score (0.652) is the maximum. Hence, the number of clusters 'k' is kept general for all the other motors. However, clustering is done only on speed and load value; coil parameters and tensiometer values are not considered for clustering. The idea behind doing this was to keep the model less dependent on coil parameters. Variations in the tensiometer and coil parameters (width and thickness) have an effect on the motor's speed-load.

Table 1: Silhouette score w.r.t number of clusters (EIF grade KA motor)

No. of clusters	Silhouette score
2	0.652
3	0.612

The clustered dataset (speed-load) for the KA motor is shown in Fig 9. Two operating stages are defined for each motor. The centroids of the clusters of each motor for individual grades have been saved to create a lookup table, shown in table 2. The centroid corresponding to low speed is named as C0 and the other one is named as C1. With the help of a lookup table, the very first step is to identify new datato which cluster it belongs.

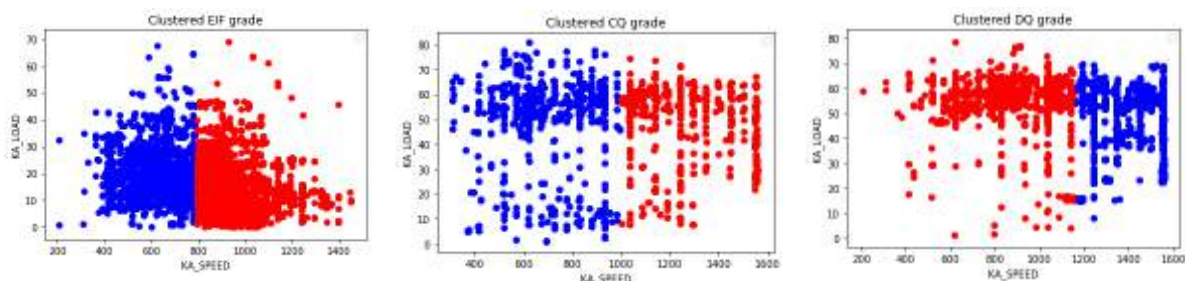


Fig 9: Clustered dataset of motor KA for different grades of coil

Table 2: Lookup table for clusters centroid in relation to motors and grades

Motor	Grade	C0_SPEED (rpm)	C0_LOAD (%)	C1_SPEED (rpm)	C1_LOAD (%)
KA	EIF	628.45	19.66	954.37	13.09
KA	DQ	705.63	48.57	1293.20	45.55
KA	CQ	896.55	54.45	1409.32	47.26
KA	HSQ	671.21	56.57	1323.58	35.28
EP	EIF	613.44	24.29	1244.33	19.15
EP	DQ	651.02	27.83	1217.93	18.39

Following clustering, the clustered data set is saved in a separate individual file with a generic unique name in a specific system folder. This is done to use it as a reference to check whether the new datapoint within that cluster is a normal or outlier. The Mahalanobis function receives the data point and clustered dataset files. However, an outlier check is performed on the clustered dataset, as shown in Fig 10 below for the EIF grade of motor KA. The red colour threshold line in Fig 10 is calculated using the critical chi square value (with four degrees of freedom and alpha equals 0.001) and six-sigma (UCL: mean + 3* standard deviation). Four degrees of freedom correspond to the number of variables. In our case, it is generally four. They are speed, load, and the adjacent tensiometer. The value of critical chi square is 18.47 and six sigma UCL is 16.31. We decided to keep a generic value of 18.

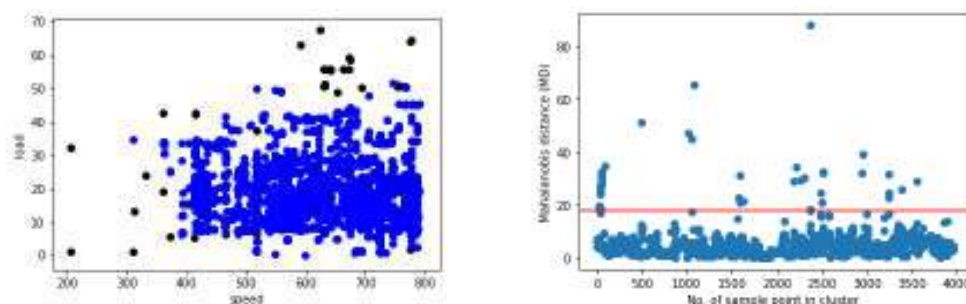


Fig 10: Outlier detection for EIF grade clustered dataset of KA motor.

A best-fit supervised machine learning model is now prepared from these cleaned datasets. These models take speed and adjacent tensiometer values as input and give predicted load as an output. In order to find the best fit model, the datasets trained and tested over various machine learning models and their RMSE and R2 have been compared together.

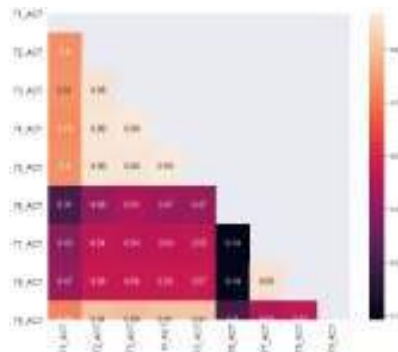


Fig 11: Correlation matrix plot of tensiometers with coefficients

A sample of the predicted value of load from various machine learning models is shown in Fig 12. A total of 270 (5 grades*2clusters for each grade* 27 no. of motors) models are prepared for this system. These models are saved in pickle files with specific generic names and get reloaded corresponding to grade and cluster.

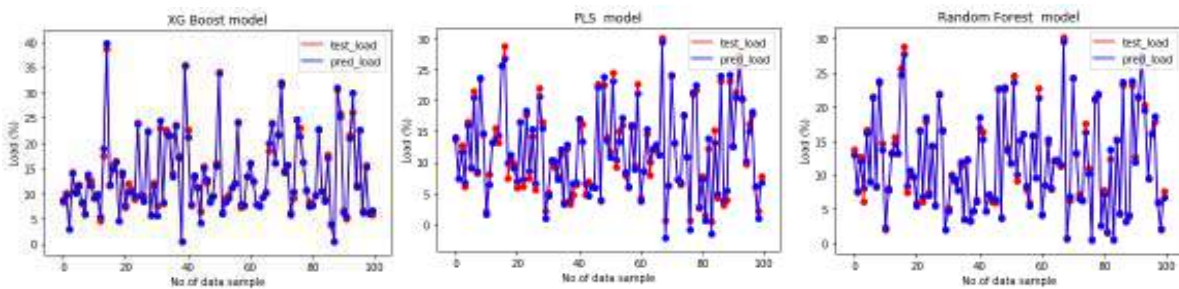


Fig 12: Actual vs prediction plot of KA motor for EIF grade and C0 cluster

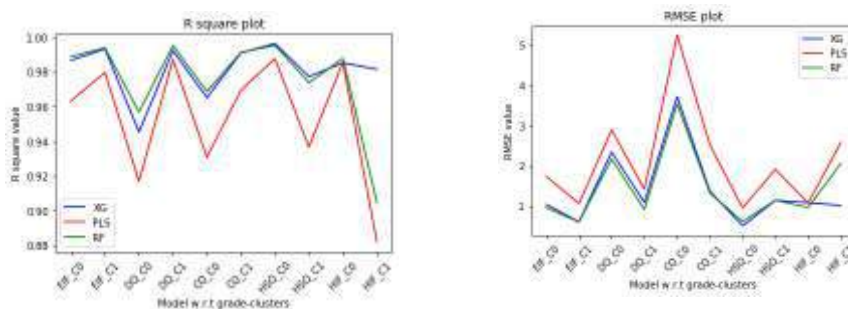


Fig 13: R square and RMSE comparison plot for KA motors model for all grade-cluster.

The difference between actual and predicted load is used to update the health status of the motor in the UI (user interface). Also, in the case of outlier detection, the severity of the progression is decided through this difference. From Fig 13, it can be seen that all the three machine learning models (XG Boost, RF, and PLS) performed well on the datasets. The coefficient of determination (R^2) is above 0.95 for all the algorithms. But among the three, it can be seen that XG Boost, and RF (ensemble machine learning) are relatively better than PLS (solitary machine learning). However, the final conclusion was taken from HIF grade, whose data sample (690 instances) was relatively low at the time of developing the system

(Fig 7). XG Boost was found to perform better on low datasets of HIF C1 model. Hence, the XG Boost was selected as the final model.

5. Implementation

In this section, implementation steps, UI, and an incident report from May 27th, 2022, are discussed. The backend development is done in the Python language, but the UI (web application) is developed in HTML5. History data files of clustering are saved with a specific generic unique name in csv format, and XG Boost files w.r.t each cluster are also saved with a specific generic unique name in pickle format. A python class has been created which takes speed, load, and adjacent tensiometer tags as input parameters. The following tags are passed to the drive parameter DB and, at the same time, PDI information (coil grade) is taken from mill level 2 DB. The deployment steps are shown schematically in Fig 14. And also, the final UI is shown which gives the health status of all 27 motors on a single HTML page. This page is refreshed every 5 minutes. A separate Python script is made to send the health status of these motors through the mail to the concerned people of electrical maintenance team. On May 27, 2022, the mail informed of very high alerts for the motors of EP, EQ, and ER rolls. These are bridle rolls of the entry section of CGL and they behave similarly. Responding to alert messages, the operation team checked iba and confirmed that the wrong (high) tension value was given to set point, which resulted in more load consumption for these motors. According to Fig 15(EP motor), load has reached around 60%, but the load centroid C0 cluster is only 24.29% (Table 2).



Fig 14: Deployment steps and UI screenshot.

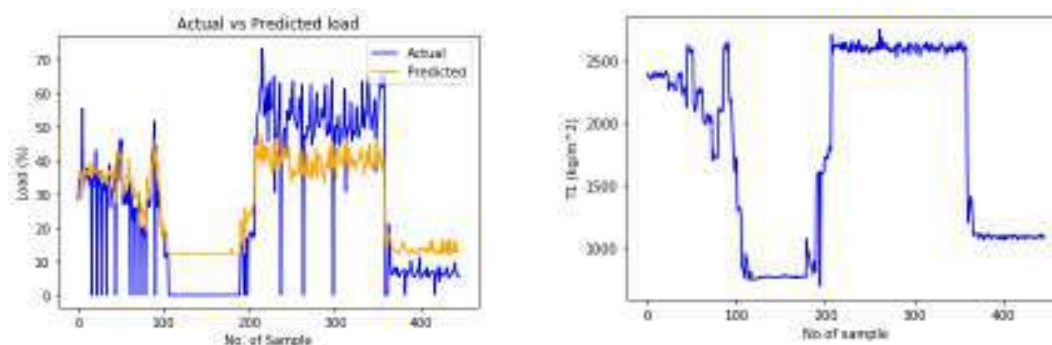


Fig 15: Line plot of load, predicted load and tensiometer (T1) during that incident (EP Motor).

A similar incident happened again on July 29th, in which it was found the line operator had set the tensiometer (T1) value in manual mode. And it remains at high value even after PDI changes. This results in a mismatch between the actual set point and the predefined tensiometer value and ultimately motor load shoot up. Alarm trend for EP motor is shown in Figure.

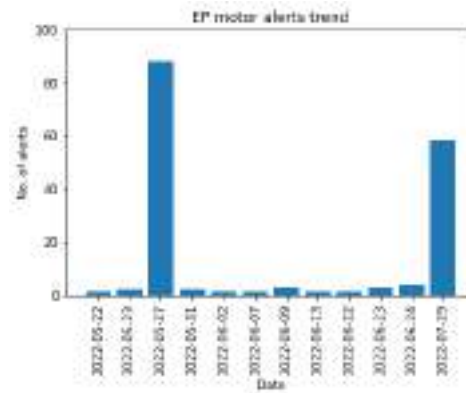


Fig 16: Alerts trend for EP motor

6. Conclusion

The intelligent system developed using a data-driven approach for condition monitoring of CGL motors has successfully diagnosed and informed the electrical maintenance team about an increase in the load of bridle roll 1 (BR1) motors (entry section of CGL) twice on May 27th and July 29th, 2022, through an e-mail alert. It was found that the adjacent tensiometer (T1) had been set with very high tension by the operator in manual mode, i.e., the operator had manually entered the (high) tension value in the tension set point for processing some previous coils, which was correct for that PDI. However, when the PDI changed, the operator did not reduce the tension value, and the coil was processed at the same previous tension value, which was incorrect. This event led to a change in the standard operating procedure for CGL processing, which now allows the operator to enter only +20% of the automatic mode tension value in T1 if a coil needs to be processed manually. Earlier, there was no such limitation. This improvement step is made after the deployment of this project.

Following conclusions can be drawn based on the present work:

1. The method suggested in this paper to diagnose the CGL motors health using a data-driven approach on time series data is feasible.
2. The five-minute sample rate has been found to be effective and is used in the live programme.
3. The outlier detection methods and XG Boost models have performed accurately and produced stable results.

The future challenge with respect to this work is to automate the retuning of models and lookup tables on a larger historical data set and also make the system adaptable if new grades of coil are added to the plant.

Acknowledgements:

We thank our colleagues from the automation department and plant operation team for their support during this project.

6. References:

1. Mouček, J. (2019). Digitalization in Industry 4.0, Knowledge Management. *Proceedings of the International Conference on Industrial Engineering and Operations Management Pilsen, Czech Republic, July 23-26, 2019*, Pages 870-874. [235.pdf \(ieomsociety.org\)](#)
2. Zadjali, S. A., & Ullah, D. (2021). Impact of Industry 4.0 in Manufacturing Sector. *International Journal of Management Science and Business Administration, Volume 7, Issue 6, September 2021*, Pages 25-33. <https://doi.org/10.18775/ijmsba.1849-5664-5419.2014.76.1003>
3. G, S. (2021). INDUSTRY 4.0 IN MANUFACTURING SECTOR. ITC Infotech India Private Limited, 1–4. Retrieved from <https://www.itcinfotech.com/wp-content/uploads/2021/05/industry-4.0-inmanufacturing-sector-whitepaper-ds1.pdf>.
4. Cipollini, F., Oneto, L., Coraddu, A., Savio, S., & Anguita, D. (2018). Unintrusive monitoring of induction motors bearings via deep learning on stator currents. *Procedia computer science, 144*, 42-51. <https://doi.org/10.1016/j.procs.2018.10.503>
5. Bazaruto, A. J., Quispe, E. C., & Mendoza, R. C. (2016, October). Causes and failures classification of industrial electric motor. In *2016 IEEE ANDESCON* (pp. 1-4). IEEE. <https://doi.org/10.1109/ANDESCON.2016.7836190>
6. Chaulya, S. K., & Prasad, G. M. (2016). Formation of digital mine using the Internet of Things. In *Sensing and Monitoring Technologies for Mines and Hazardous Areas* (pp. 279-350). Elsevier. <http://dx.doi.org/10.1016/B978-0-12-803194-0.00006-4>
7. Li, B., Chow, M. Y., Tipsuwan, Y., & Hung, J. C. (2000). Neural-network-based motor rolling bearing fault diagnosis. *IEEE transactions on industrial electronics, 47*(5), 1060-1069. http://www4.ncsu.edu/~chow/Publication_folder/Journal_paper_folder/2000_IE_IFDIM_Li_Bo.pdf
8. Mallick, Md Raihan, and Syed A. Imtiaz. "A hybrid method for process fault detection and diagnosis." *IFAC Proceedings Volumes* 46, no. 32 (2013): 827-832. <https://doi.org/10.3182/20131218-3-IN-2045.00099>
9. Moghaddass, R., & Zuo, M. J. (2012). A parameter estimation method for a condition-monitored device under multi-state deterioration. *Reliability Engineering & System Safety, 106*, 94-103. <https://doi.org/10.1016/j.ress.2012.05.004>
10. Pantula, S. R. (2014). *Automated fault diagnosis in rotating machinery* (Master's thesis, University of Waterloo). https://uwspace.uwaterloo.ca/bitstream/handle/10012/8743/Pantula_Shilpa_Reddy.pdf;sequence=1
11. Continuous hot-dip galvanizing versus general (batch) galvanizing. [G_Note9.PDF \(steelmillsoftheworld.com\)](#)
12. Pham, D. T., & Afify, A. A. (2007). Clustering techniques and their applications in engineering. *Proceedings of the Institution of Mechanical Engineers, Part C: Journal of Mechanical Engineering Science, 221*(11), 1445-1459. [0.1243/09544062JMES](https://doi.org/10.1243/09544062JMES)
13. Wang, F., Franco-Penya, H. H., Kelleher, J. D., Pugh, J., & Ross, R. (2017, July). An analysis of the application of simplified silhouette to the evaluation of k-means clustering validity. In *International Conference on Machine Learning and Data Mining in Pattern Recognition* (pp. 291-305). Springer, Cham. [An-Analysis-of-the-Application-of-Simplified-Silhouette-to-the-Evaluation-of-k-means-Clustering-Validity.pdf \(researchgate.net\)](#)

14. Ghorbani, H. (2019). Mahalanobis distance and its application for detecting multivariate outliers. *Facta Univ Ser Math Inform*, 34(3), 583-95. <https://doi.org/10.22190/FUMI1903583G>
15. Kesarwani, Rishabh. "XGBoost: A BOOSTING Ensemble. Does It Really Work as the Name... | by Rishabh Kesarwani | AlmaBetter | Medium." *Medium*, medium.com, 6 June 2021, <https://medium.com/almabetter/xgboost-a-boosting-ensemble-b273a71de7a8>.
16. Dalipi, F., Yildirim Yayilgan, S., & Gebremedhin, A. (2016). Data-driven machine-learning model in district heating system for heat load prediction: A comparison study. *Applied Computational Intelligence and Soft Computing*, 2016. DOI: [10.1201/B18565-44](https://doi.org/10.1201/B18565-44)
17. Vamsi, I. V., Abhinav, N., Verma, A. K., & Radhika, S. (2018, December). Random forest based real time fault monitoring system for industries. In *2018 4th International Conference on Computing Communication and Automation (ICCCA)* (pp. 1-6). IEEE. <https://doi.org/10.1109/CCAA.2018.8777673>
18. Kotsiantis, S., & Pintelas, P. (2004). Combining bagging and boosting. *International Journal of Computational Intelligence*, 1(4), 324-333. [.PDF\) Combining Bagging and Boosting \(researchgate.net\)](https://www.researchgate.net/publication/220211113)
19. Zhang, R., Li, B., & Jiao, B. (2019, April). Application of XGboost algorithm in bearing fault diagnosis. In *IOP Conference Series: Materials Science and Engineering* (Vol. 490, No. 7, p. 072062). IOP Publishing. <https://doi.org/10.1088/1757-899X/490/7/072062>
20. Bentéjac, C., Csörgő, A., & Martínez-Muñoz, G. (2021). A comparative analysis of gradient boosting algorithms. *Artificial Intelligence Review*, 54(3), 1937-1967. <https://doi.org/10.1007/s10462-020-09896-5>
21. Zach, and View all posts by Zach. "An Introduction to Partial Least Squares - Statology." *Statology*, www.statology.org, 17 Nov. 2020, <https://www.statology.org/partial-least-squares/>.

Hydraulic System Failure Prediction through Data Science Models

**Prashant Kumar, Sanjeev Kumar, Digvijay Narayan Sharma,
Hari Darshan Singh, Gyan Prakash**

Automation Division, Tata Steel Limited, Jamshedpur -831001, India

Abstract

There was a need at Tata Steel Europe (Shotton plant) to develop a site standard for hydraulic pack to predict failures or deteriorating performance of hydraulic systems. As part of synergy, in asset performance, the project of predicting hydraulic failure was completed in collaboration between Tata Steel Europe (TSE) and Tata Steel India (TSI). Pumps are the major equipment of hydraulic system. A machine learning (ML) model was developed for detecting anomalies in pumps in closed circuit hydraulic system. Pump data of critical parameters were analysed for development of data based analytical models. Case drain flow of the hydraulic pump was considered as the research object after exhaustive study. Increase in Case drain flow rate is directly correlated with asymptotic start in mechanical failure. The algorithm finalized for the modelling was XG-Boost which was trained with one-minute average data. The model has been deployed in the Google Cloud Platform. This paper investigates a predictive maintenance approach for hydraulic pump via an early warning system and transferring data through cloud computing system.

Key words: *Predictive Maintenance, Machine Learning, Cloud Computing, Hydraulic System, Pump, Tata Steel Ltd.*

Introduction

Hydraulic system play an important role in the manufacturing industry. Hydraulic pump is the main component of Hydraulic System. It is the combined pumping and driving motor unit. As the ‘heart’ of the hydraulic system, the stable operation of pump is an important requirement for its normal operation.

Condition monitoring of hydraulic pumps helps in improving productivity, maintenance cost reduction and prevents from further deterioration. Besides, it improves the reliability and safety of the equipment [1]. In the competitive world today, identifying a failure beforehand reduces the operational cost of the plant. Monitoring the critical equipment decreases the machine downtime and maintenance cost subsequently. A small fault in the equipment if not found and repaired in time may affect the performance of a mechanical equipment during operation, and the performance degradation process is frequently irreversible. The performance degradation of mechanical equipment makes their continuous operation impossible. Timely early warning of machinery equipment failure can be provided using appropriate methods to monitor the working state of machinery and equipment in real time. This will not only help equipment users to establish an appropriate maintenance and repair plan to prevent unexpected shutdowns of the mechanical equipment during use but also effectively prolong its normal operation time and avoid the economic losses caused by unexpected equipment failures. Therefore, conducting appropriate monitoring and maintenance and providing early warning of pump failure is highly significant [2]. At present, the methods for signal analysis, monitoring and fault diagnosis

of mechanical equipment are becoming increasingly mature, practical and specialized. This include continuous monitoring of different parameters and alarm generation for any anomaly detection. Monitoring health of the equipment mainly relies on the sensor data used in process monitoring [3]. In recent years, there has been a rise in the increased usage of artificial intelligence integrated with computer and information technologies [4]. Machine Learning algorithms are commonly used now a days for fault detection and prediction. The most major feature of data-driven prediction is that it does not require establishing a complex mathematical model for the prediction and evaluation of mechanical equipment. It only needs collection of a large amount of data generated in the industrial field, based on which a model is built. The establishment of a data-driven model can utilize the real-time measurement data sampled by sensors.

In this study, A machine learning model has been developed for predicting future failure of hydraulic system. Case Drain Flow was selected as the target variable. When mechanical failure starts to occur, the flow through the drain increases to enable the pump increases to continue operating to its standard. Increase in Case Drain flow is the failure signifier. Alarm is triggered for any anomalies detected in prediction. The followed approach is based on testing different situations and combinations, finding the best set up for the model.

Literature Review

Many studies on fault diagnosis of the hydraulic pumps have been conducted by theoretical approaches and test measurements, and certain research results have been obtained. Zhaomin He [7] presented a hybrid prediction method based on EMD (Empirical Mode Decomposition) and SVM (Support Vector Machine), in which EMD is used to get the pump's health state and PSO (Particle Swarm Optimization)-SVM is used to make a prediction for the pump's remaining useful lifetime. P. Casoli [8] proposed a solution to detect the health state of a variable displacement axial-piston pump based on vibration signals. J. Sun [9] approaches the pump as a key component for better improving the hydraulic system reliability. J. G. M. Lázaro [10] discusses about the advantages to implement Condition-based Maintenance (CBM) and the use of techniques of fault diagnosis in axial variable displacement piston pumps (VDAP). X. Wang [11] developed a prediction model based on contaminant sensitivity of hydraulic oil for the aviation hydraulic piston pump. He suggested condition-based maintenance of aircraft by determining remaining useful life (RUL) of the pump. A systematic approach [12] is developed and evaluated for the automated training of condition monitoring systems for complex hydraulic systems, with important suggestions about the dimensionality reduction and the cycle-based approach. N. Helwig [13] debates about condition monitoring, proposing a statistical condition monitoring system, and the determination of typical faults related to the hydraulic system as well as the sensors, too.

The machine learning algorithm selected for this project was eXtreme Gradient Boosting (XGBoost). XGBoost was first proposed by Dr. Chen Tianqi in 2014, can automatically utilize the central processing unit (CPU) multi-threaded parallel computing and has the advantages of low computational complexity, fast running speed, and high accuracy, no matter whether the data scale is large or small [5,6]. Since its introduction, this algorithm has been credited for being the driving force for several cutting-edge industry applications. This method has been successfully applied in many fields, such as fault diagnosis, environmental prediction, and medical detection.

The aim of this paper, due to the relevance of the degradation states' prediction for the predictive maintenance, is to develop, test and deploy a predictive model for the degradation state of hydraulic pumps.

Concept and Methods

The main objective of the project was to develop a smart hydraulic pack standard for Tata Shotton. Measurement data are sourced from real sensors installed in hydraulic system. Sensors have been installed for measuring real time values of process parameters (Fig 1).

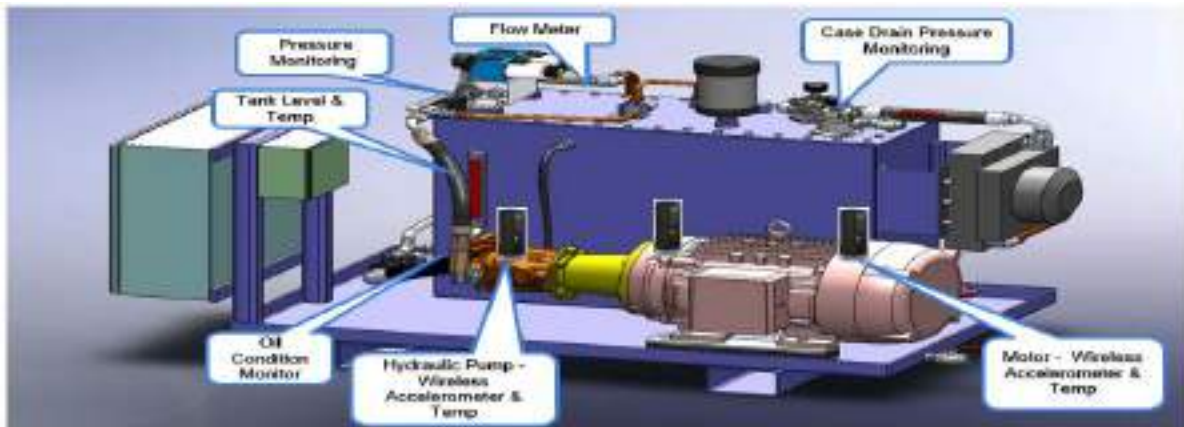


Fig. 1 Smart hydraulic system

Raw data of various parameters of pump are measured through sensors. Sensors have been installed for measuring tank level, temperature, pressure, flow, line speed, full load current and other important signals. Signal from sensor is recorded by IBA software. The IBA system is used for acquiring, recording, analysing and processing measurement data. Tags are extracted from the IBA generated output file and inserted into database for further analysis. Data flow from sensor to database has been demonstrated in Fig 2.

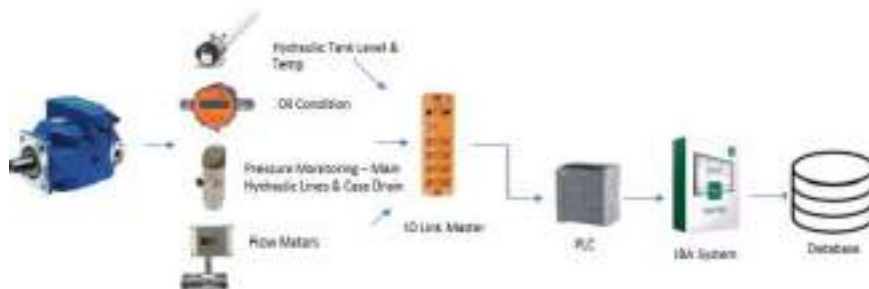


Fig. 2 An overview of data flow from sensor to database

The project required different stages to complete. It started with defining problem statement which was anomaly detection in entry hydraulic pump in this case. Thorough process understanding was done to build business case and to identify target variable.

One-minute average data of a month was collected for important parameters. It was followed with data sanctity of the collected data. Input parameters were chosen based on user's discussion and modelling techniques. For getting a better understanding of the variables and to find the relationship between them, exploratory data analysis was done

thereafter. Different modelling techniques were tried and XG Boost algorithm was finally selected based on performance matrix. The model deployed in Google Cloud fetches the data from TSE database at a regular interval and sends back the output over cloud computing. Model results were circulated for initial trials which were very encouraging. The approach for completing the project from beginning to end has been briefly shown in Fig 3.



Fig.3 Methodological framework of the project

Case Study

As a part of digital transformation, TSE team have deployed multiple SKF units at Shotton plant. These units are connected to both the SKF Observer platform and IBA system. This enables the vibration analysis to consider things like rotational speed, line tensions and the removal of events such as strip tension take up which may cause a short spike in recorded vibration. This information is analysed and normalised by plant engineers and alarm levels set in both IBA and the Observer platform and displayed on the digital dashboards. The data exchange between IBA and the SKF system is important to get accurate data from online systems. Some of the delay trend at Shotton plant were increasing which was related to both poor reliability and an increase in operational hours. To handle the situation, a machine learning model was needed for predicting failures or deteriorating performance of hydraulic systems. This paper explains the different stages of model development.

During abnormal behaviour of hydraulic system, pump also behaves differently. Case drain flow, Suction inlet pressure and Overall system flow are three critical parameters of hydraulic pump used for fault detection.

- Case Drain Flow

With variable displacement pumps a working hydraulic leakage flow is produced over the seal surfaces to lubricate the pump mechanism and to create the necessary seals needed for the pump to function. When mechanical failure starts to occur within a variable displacement pump, the flow through the drain increases to enable the pump to continue operating to its needed standard. By monitoring this flow one

can pick up the early signs of failure using it as a tool to monitor failure and to make a judgement call on when a possible catastrophic failure will occur.

- **Suction Inlet Pressure**
Suction inlet pressure is monitored to also look for step changes which would signify pump starvation such as filter blocked, Fluid density change etc. If the inlet pressure of a pump changes this could also signify a loss of efficiency. Comparing this against normal working conditions will tell if the pump is having to work harder to produce the same overall output pressure and flow.
- **Overall System Flow**
This is being monitored to ensure that the correct system flow is achieved as needed to operate hydraulic equipment on the line. With entry system, there is a main Pump and top up pump which kicks in if the flow or pressure demand is higher than the main pumps output. By monitoring this and how common the up pump is having to kick in to assist the main pump would also indicate a loss in pump efficiency.

Model Development

This study presents machine learning based algorithms for the anomaly detection in entry hydraulic pump. The analytical journey of hydraulic pump model has been explained in detail in the following section.

Data Engineering

Data collection is the first step for developing a machine learning model [14]. The collected chunks of data should be relevant to the business problem to be solved. In this study, we collected pump and motor one-minute average data for a month. The dataset had 43,204 data points and 286 variables. In the dataset, 18,152 data points were removed because of missing or wrong field values. A total of nine variables were selected for the modelling purpose as shown in Fig. 4.

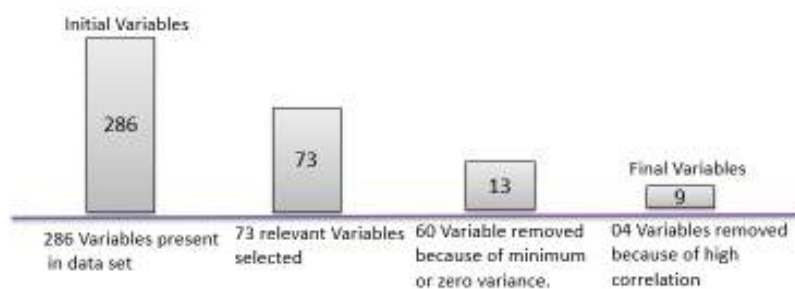


Fig. 4 Parameter selection steps for modelling

List of parameters finalised were system pressure, full load current, tank level, tension leveller roll position, motor drive end temperature, tank temperature, system flow, line speed and case drain flow.

Based on process understanding and literature review, few more variables (velocity vibration, enveloped vibration and acceleration vibration) could have been selected for

modelling. However, these parameters were not available because of sensor issue. They may be added in the next version of model.

Exploratory Data Analysis

Once the data set was ready, exploratory data analysis was done to get a better understanding of the variables and to find the relationship between them. It helped in developing initial insights and validating the traditional understanding of process. In previous section, it has been discussed that case drain flow and suction inlet pressure were commonly used parameters for failure detection. During analysis, it was found that case drain flow was highly correlated with suction inlet pressure. Correlation coefficient between them was 0.99. Subsequently, suction inlet pressure was dropped. Highly correlated features need to be avoided while building a machine learning model [15]. The correlation coefficient procedure is used to determine how strong a relationship is between the data. It yields a value between 1 and -1. In which, -1 indicates a strong negative and +1 indicates strong positive relationships. And an outcome of zero implies no connection at all.

Correlation plots help us to visualize the relation between continuous variables. In Fig 5, MP Case Flow (case drain flow of main pump) is the target variable and the rest are input variables.

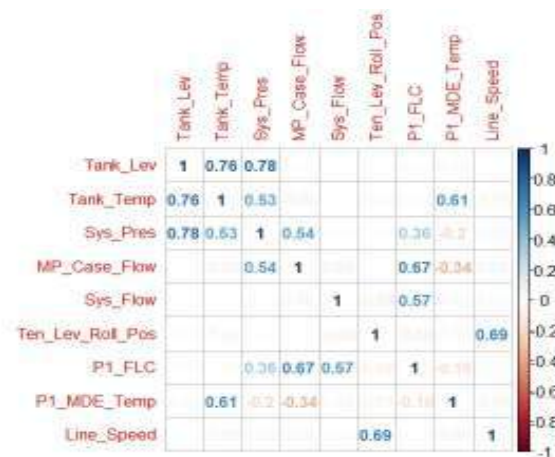


Fig. 5 Correlation Plot of Selected Features

In order to determine the importance of features, the permutation feature importance method is used. This method calculates the increase in the prediction error (MSE) after permuting the feature values. If the permuting wouldn't change the model error, the related feature is considered unimportant. It explains which features have more impact than others in predicting the target variable [16]. For e.g., by generating the variable importance plot (Fig. 6) of input variables, it was observed that system pressure and pump current turns out to be very important for predicting case drain flow. The var Imp Plot function of Random Forest algorithm was used to plot the variable importance diagram.

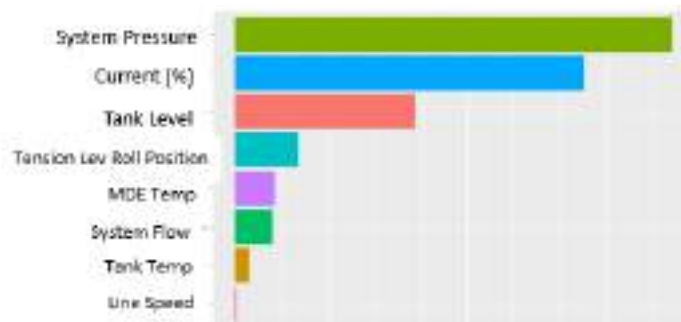


Fig. 6 Variable Importance Plot of Input Features

Modelling Techniques

The next important step was to explore the world of machine learning algorithms. The process involved segmenting the data into two types of samples: Train data and Test data. Data was split into 70:30 ratio. Training sets are used to fit and tune the models. The test data represents data that has not been used for training and provides a good measure for how well the algorithm generalizes on unseen data. Both train and test data contain an output variable and a list of input variables. Different algorithms like Linear Regression, Random forest, Extreme Gradient Boosting (XGB) and MARS were tried. The algorithm performing comparatively better on data sets was chosen. Root mean square error (RMSE) and mean absolute percentage error (MAPE) were the performance metrics in this case. The algorithm was chosen for the lowest RMSE and MAPE value.

The algorithms performances have been shown in Table I. Both, Random Forest and XG Boost performed equally well based on MAPE metric. However, XG Boost was slightly better considering RMSE metric. Hence, XG Boost algorithm was finalised for model development

TABLE I. Algorithm Performance on Test Data

Algorithm	RMSE	MAPE
Linear Regression	0.84	12
Multivariate Adaptive Regression Splines (MARS)	0.15	3.1
Random Forest	0.10	1.3
XG Boost	0.09	1.3

Model validation was done for a one-week of one-minute average data. A box plot has been prepared (Fig. 7) for getting an indication of how the residual (difference of actual and predicted) values are spread out. It was observed that most of the residual distribution is around zero which shows a good model performance.

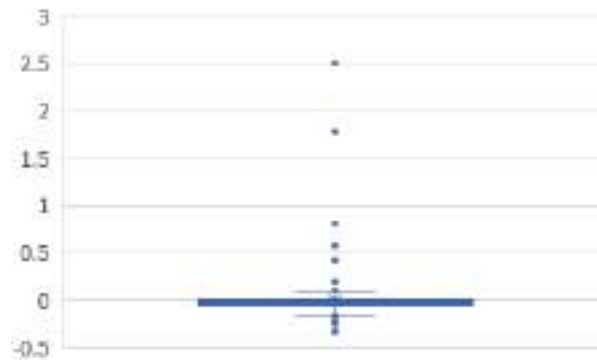


Fig.7 Model residual box plot for validation data

The same data distribution has also been represented by a line graph (Fig. 8) for better understanding of model performance. Except a few outliers predicted values matches closely with actual case drain flow values.

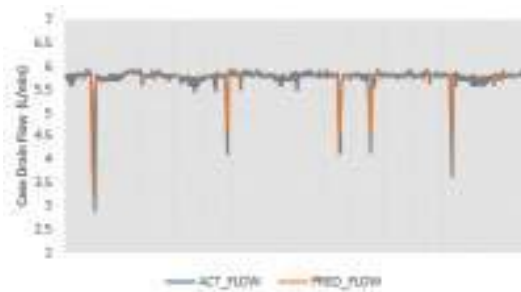


Fig. 8 Comparison of actual and predicted values

Once the model was validated successfully, the next step was productionization for reaping the benefits out of it.

Model Deployment

The implementation of model was a challenging task since it required to automate and securely transfer the data between environments of TSI and TSE. TSE UK had data that was required for running model. The model output had to be transferred back to TSE. Initial hurdles in data transfer were:

- Getting an access of TSE system or database outside Tata Steel Europe network was incredibly difficult because of IT Security policy.
- TSE team works mainly with Microsoft Azure environment; we did not have access to TSE azure environment.
- TSI team had account with Google Cloud. So, data exchange had to be between Azure and Google Cloud.
- Data transfer had to be secure and periodically at every few minutes.
- TSE security policy would not allow any general API, if it does not use TSE cloud application firewall which protect the TSE managed API platform when it connects to the public Internet.

To overcome the mentioned challenges, TSE team had arranged Shotton IBA data to be automatically fed to their cloud series database. A set of queries was developed to allow a generic request for any tag Id, timescale and resolution direct from their database

along with the ability to store results such as levels or alerts back into the database. The queries were wrapped into a set of REST APIs, tested and put live on production web server. The public replica was created through the necessary networks/firewalls etc. An authentication mechanism was developed to securely access the Web API from outside the TSE network via the public interface. This includes generation of Subscription key to grant access to the external Azure interface and a Bearer token to allow writing to specific REST endpoints.

A python application was developed to read REST API of TSE and store data in csv on Google Cloud Storage (GCS). Cloud scheduler was used to transfer data periodically to Google Big Query.

This data serves as an input to model. Another python application for running model deployed on Google Cloud scheduled periodically and write model output data back to Big Query. The output data is transferred back to TSE using the similar route as followed for input data. Data transfer strategy has been shown in Fig. 9.

Model output consists of predicted case drain flow and alert. Alert from model is typically generated when signal reading or measurement exceeds its acceptable tolerances or predicted acceptable values.

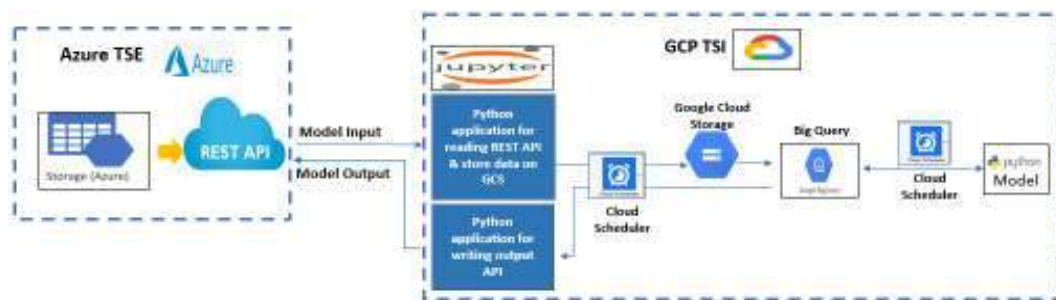


Fig. 9 Data transfer strategy between TSE and TSI

Conclusion

An analytical model was developed for Tata Shotton hydraulic pump. Based on the data of hydraulic motor and pump, the XG Boost algorithm was chosen to construct the model. The approach was based on existing process sensors but can also make use of additional sensors and can thus be easily adapted to different systems due to the fully automated signal processing scheme. The model has been deployed at google cloud to generate the predicted values of case drain flow at regular interval based on input conditions. It is imperative to note that the model is being used by the maintenance crew of Shotton plant for condition monitoring of hydraulic pump.

Acknowledgment

We are immensely grateful to TSE team for providing their valuable assistance. We thank Tom Yehya and Steve Smith from Shotton Works who provided insight and expertise that greatly assisted the project. We also thank Matthew Roberts for helping us with the data and business understanding for building model. We also appreciate Paul S Davies and David Jones from Process Control & Automation department for finalising the strategy in

automated data transfer. We would also like to thank Kevin White from IT & Digital team for providing immense support in project completion. At the end, we'd like to express since reappreciation to everyone with whom we have had the pleasure to work during this project.

REFERENCES

- [1] Y. Lei, W. Jiang, A. Jiang, Y. Zhu, H. Niu, and S. Zhang, "Fault Diagnosis Method for Hydraulic Directional Valves Integrating PCA and XGBoost," *Processes*, vol. 7, no. 9, p. 589, 2019.
- [2] Zhou, R.; Jiao, Z.; Wang, S. Current research and developing trends on fault diagnosis of hydraulic systems. *J. Mech. Eng.* 2006, 42, 6–14.
- [3] K. Liu, N. Z. Gebraeel, and J. Shi, "A Data-level fusion model for developing composite health indices for degradation modeling and prognostic analysis," *IEEE Trans.*
- [4] Wang, M.; Zhang, Z.; Li, K.; Si, C.; Li, L. Survey on Advanced Equipment Fault Diagnosis and Warning Based on Big Data Technique. *J. Stat. Mech. Theory Exp.* 2020, 1549, 042134.
- [5]. Chen, T.; Guestrin, C. Xgboost: A scalable tree boosting system. In Proceedings of the 22nd AcmSigkdd International Conference on Knowledge Discovery and Data Mining ACM, San Francisco, CA, USA, 13–17 August 2016; pp. 785–794.
- [6]. Nielsen, D. Tree Boosting with XGBoost-Why Does XGBoost Win "Every" Machine Learning Competition' Master's Thesis, Norwegian University of Science and Technology, Trondheim, Noreg, 2016.
- [7] Z. He, S. Wang, K. Wang, and K. Li, "Prognostic analysis based on hybrid prediction method for axial piston pump," *IEEE Int. Conf. Ind. Informatics*, pp. 688–692, 2012.
- [8] P. Casoli, M. Pastori, F. Scolari, and M. Rundo, "A vibration signal-based method for fault identification and classification in hydraulic axial piston pumps," *Energies*, vol. 12, no. 5, 2019.
- [9] J. Sun, H. Li, and B. Xu, "Prognostic for hydraulic pump based upon DCT-composite spectrum and the modified echo state network," *Springerplus*, vol. 5, no. 1, 2016.
- [10] J. G. M. Lázaro, C. B. Pinilla, and S. R. Prada, "A survey of approaches for fault diagnosis in axial piston pumps," in *ASME International Mechanical Engineering Congress and Exposition, Proceedings (IMECE)*, 2016, vol. 4A-2016.
- [11] X. Wang, S. Lin, and S. Wang, "Remaining useful life prediction model based on contaminant sensitivity for aviation hydraulic piston pump," in *AUS 2016 - 2016 IEEE/CSAA International Conference on Aircraft Utility Systems*, 2016, pp. 266–272.
- [12] N. Helwig, E. Pignanelli, and A. Schütze, "Condition monitoring of a complex hydraulic system using multivariate statistics," *Conf. Rec. - IEEE Instrum. Meas. Technol. Conf.*, vol. 2015-July, pp. 210–215, 2015.
- [13] N. Helwig, E. Pignanelli, and A. Schütze, "Detecting and Compensating Sensor Faults in a Hydraulic Condition Monitoring System," in *SENSOR 2015 - 17th International Conference on Sensors and Measurement Technology*, 2015, pp. 641–646.
- [14] C. V. Ramamoorthy, "Knowledge and Data Engineering", *IEEE Transactions on Knowledge and Data Engineering*, Volume 1, Issue 1, March 1989 pp 9–16
- [15] Jamal I. Daoud, "Multicollinearity and Regression Analysis", *Phys.: Conf. Ser.* 949 012009, 2017
- [16] B. Gregorutti, "Correlation and variable importance in random forests", *Statistics and Computing*, 27(3), 2016, pp.659–678

Dynamic Behaviours of a Functionally Graded Rotating Shaft-Bearing System with Nonlinear Supports

Bala Murugan S¹, Dr. R.K. Behera²

¹Research Scholar, ²Professor, Dept. of Mechanical Engineering
NIT Rourkela, Odisha, India

Abstract

To obtain accurate results, rotor-bearing-disk system evaluations must necessarily be substantial. According to the evolution in the modern industries, functionally graded (FG) rotating shafts are widely employed depending on the unique applications. It was found that very few studies on stability difficulties for FG rotor-bearing-disk systems were published. A TG rotor comprising two disk and supported by two fluid ring bearings (FRBs). A rotating FG rotor-disk-bearing system's stability is analyzed in the current study, which employs a finite element (FE) dynamic modelling approach. By taking into account gyroscopic effects, rotary and translational inertia, shear deformation, bending, and material (viscous and hysteretic) damping, the FG rotor shaft model is taken into consideration based on Timoshenko beam theory. Hamilton's principle is used to generate the governing equations. Zirconia (ZrO₂) and stainless steel (SUS304) are commonly treated as the main components of the FG shaft in this study. By accounting for a total of four freedom degrees per node, five-noded beam elements are taken into consideration. The findings of the Campbell diagram, the stability threshold, the time histories, and the damping ratio for the FG shaft are analyzed with those of the conventional standard steel shaft. As can be seen, the components of the radially classified FG shaft play a significant role in controlling the outcomes for FG rotating shaft. As a result, FG-shafts are preferred over regular steel shafts.

Keywords: Hamilton principle, internal damping coefficients, functionally graded shaft, Stability threshold speed, Campbell diagram, Time histories.

1. Introduction

The composite shafts have several uses in contemporary fields of industry. For the past fifty years, there has been a lot of interest in the safe design and dynamic analysis of spinning structures. Rotating machinery designs rely heavily on accurate predictions of the rotor-shaft-bearing system, dynamic parameters, and material qualities. The high stiffness to weight ratio, high specific stiffness, and high specific strength are some limits of the advanced composite materials. These composite materials produced impressive outcomes in the automotive, medicinal, and aerospace fields. Thus, the common occurrence of delamination, which results from a weak interface between neighbouring layers, is seen as the main drawback of employing a rotor shaft made of composite materials. The rotor dynamicists use functionally graded material (FGM) as proof against these claims.

FGMs are strong materials with multiple uses that are diverse and multifunctional. The property gradations in these materials are smooth and continuous. These characteristics are

produced in certain ways to provide the necessary performance, primarily when higher temperatures are applied. The benefits of FGMs include their enhanced thermal characteristics, durability, and decreased inter-laminar stresses. For the past ten years, researchers have concentrated their efforts on analysing the rotor-bearing system using FG materials. In order to increase the efficiency of energy conversion, M. Koizumi [1,2], was the first to conceptualise FGM. He also carried out the initial development of FGM materials that were functionally graded for structural technology. Argeso and Eraslan [3] has studied the simulated model that is partially elastic, plastic, and residual stress in the dynamic FG shafts. Nelson [4] proposed the dynamic simulation of a rotating rotor-disc-bearing system, taking into account the gyroscopic moment, rotational inertia, and shear deformation effects. The development of FGMs in the analysis of structural components, including the addition of crack and safety elements for the damaged structures, was critically examined by Gayan et al. [5]. Birman and Byrd [6] address the theory and many facets of key advances and their implications in FGMs with mathematical model, manufacturing, and design. The study examined numerous gradient composite types and took into account some of Bever and Duwez [7] findings regarding their characteristics. According to Wettergren and Olsson [8], the shaft's asymmetric stiffness and dampings work in concert with the bearing's anisotropic stiffnesses to prevent instability. The model was used by Piovan and Sampaio [9] to analyse various abbreviated isotropic material-based models. Kamil Aydin [10] have carried the comprehensive parametric analysis of the damaged FGM. Gayan et al. [11] have carried the detailed discussions on the effects of the crack relative location, temperature gradient, shaft's slenderness, shaft internal damping and gradient index of the FG fractured shaft system, and coefficients on the dynamic responses. An analytical research was done by Jahangiri and Bagheri [12] to determine how FGMs affect the resonances.

In the current study, we analyse the dynamic stability of a FG rotor-disk bearing model. The FG rotor system comprised material dampings and disc mass imbalances. The implicit Houbolt's time integration approach is used in MATLAB® to solve the equations in dynamic form. Phase-plane graphs, the Campbell plot, and the frequency response were used to study the system stability assessments.

2. System Modelling

The cross section of the shaft is divided into ' n ' layers for the sake of the current investigation. As a result, the cross section's inner and outer radii of the k^{th} layer are designated as r_{in} and r_{ou} , respectively. The shaft's material characteristics (P) in the radial direction are as follows:

$$P = P_{ou} V_{ou} + P_{in} V_{in} \quad (1)$$

The total volume fraction is stated as follows:

$$V_{ou} + V_{in} = 1 \quad (2)$$

The properties of the FG shaft material according to the law of gradation:

$$\begin{aligned}
E(r) &= \{E_{ou} - E_{in}\} \left(\frac{r - r_{in}}{r_{ou} - r_{in}} \right)^k + E_{in}; \\
v(r) &= \{v_{ou} - v_{in}\} \left(\frac{r - r_{in}}{r_{ou} - r_{in}} \right)^k + v_{in}; \\
\rho(r) &= \{\rho_{ou} - \rho_{in}\} \left(\frac{r - r_{in}}{r_{ou} - r_{in}} \right)^k + \rho_{in}
\end{aligned} \tag{3}$$

2.1. Equation of motion and dynamic equations

The Timoshenko beam theory is used to simulate a simplified rotor element. The shaft components are represented with five nodes. At each node of the shaft element, four degrees of freedom (DOF) are taken into account, including translational (v , w) and rotational displacements (θ_y , θ_z). The potential and kinetic energy of rotating shaft elements have been given as follows in order to take into account the effects of shearing and bending:

$$T_{shaft} = \frac{1}{2} \int_0^\ell \rho \left\{ A(\dot{v}^2 + \dot{w}^2) + I_D (\dot{\theta}_y^2 + \dot{\theta}_z^2) + I_P \left[\Omega^2 + \Omega(\dot{\theta}_z \theta_y - \dot{\theta}_y \theta_z) \right] \right\} ds \tag{4}$$

$$U_{shaft} = \frac{1}{2} \int_0^\ell \left\{ EI(\theta_y'^2 + \theta_z'^2) + kGA \left[(\theta_y - w')^2 + (\theta_z + v')^2 \right] \right\} ds \tag{5}$$

The following expression gives the stated disc kinetic energy:

$$T_{disk} = \frac{1}{2} m_{disk} (\dot{v}^2 + \dot{w}^2) + \frac{1}{2} J_{disk} (\dot{\theta}_y^2 + \dot{\theta}_z^2) + \frac{1}{2} J_p \left[\Omega^2 + \Omega(\dot{\theta}_z \theta_y - \dot{\theta}_y \theta_z) \right] \tag{6}$$

The disk's mass eccentricity is given as:

$$W_{disk} = m_{disk} r_{disk} \Omega^2 (w \cos \Omega t + v \sin \Omega t) \tag{7}$$

The EOM of the shaft and disk portion is obtained as follows:

$$[M_{shaft}] \{\ddot{\mathbf{u}}_{shaft}\} + \Omega [G_{shaft}] \{\dot{\mathbf{u}}_{shaft}\} + [K_{shaft}] \{\mathbf{u}_{shaft}\} = \{\mathbf{f}_{shaft}\} \tag{8}$$

$$[M_{disk}] \{\ddot{\mathbf{u}}_{disk}\} + \Omega [G_{disk}] \{\dot{\mathbf{u}}_{disk}\} = \{\mathbf{f}_{disk}\} \tag{9}$$

2.2. Bearing Forces representation

The true nonlinear fluid film force can be stated by Adiletta et al. [14] using the short bearing theory assumption as follows:

$$\begin{Bmatrix} F_{ix} \\ F_{iy} \end{Bmatrix} = (\Omega_j + \Omega_r) \mu_i L_i R_j \left(\frac{L_i}{2R_j} \right)^2 \left(\frac{R_j}{C_i} \right)^2 \begin{Bmatrix} f_{ix} \\ f_{iy} \end{Bmatrix} \quad (10)$$

$$\text{and} \quad \begin{Bmatrix} F_{ox} \\ F_{oy} \end{Bmatrix} = \Omega_r \mu_o L_i R_{ro} \left(\frac{L_i}{2R_{ro}} \right)^2 \left(\frac{R_{ro}}{C_o} \right)^2 \begin{Bmatrix} f_{ox} \\ f_{oy} \end{Bmatrix} \quad (11)$$

The external force components of Eq. (10) in x and y directions of inner fluid films are given by, F_{ix} and F_{iy} . Similarly, the force components of Eq. (11) in x and y directions of outer fluid films are given by F_{ox} and F_{oy} . The bearing parameters μ , R , L and C represents the viscosity of the fluid, bore radius, length of the films, and radial clearance of the films respectively. Where, (f_{ix}, f_{iy}) and (f_{ox}, f_{oy}) denotes the vector components of inner, and outer fluid film forces.

Hence, by using the both damping η_V (viscous) and η_H (hysteretic), the damped system equation of motion can be given as [13],

$$\left([M_{shaft}] + [M_{disk}] \right) \{ \ddot{u}_{shaft} \} + \left(\eta_V [K_{shaft}^b] - \Omega \left([G_{shaft}] + [G_{disk}] \right) \right) \{ \dot{u}_{shaft} \} + \left(\eta_a [K_{shaft}^b] - \eta_b [K_{shaft}^c] \right) \{ u_{shaft} \} = \{ f_{shaft} + f_{disk} + f_{FRB} \} \quad (12)$$

$$\text{where,} \quad \eta_a = \frac{1 + \eta_H}{\sqrt{1 + \eta_H^2}}; \quad \eta_b = \frac{\eta_H}{\sqrt{1 + \eta_H^2}} + \Omega \eta_V$$

3. Numerical Simulation

The stability of the FG rotor-disk-bearing system shown in Fig. 1 is achieved by solving the FE equations interactively in MATLAB[®]. The research of a metal ceramic material with radially functionally graded material made of Zirconia (ZrO₂) and stainless steel (SUS304) is taken into account for the design of the rotor element; k is in the range of $0 < k < \infty$. Fig. 2 depicts the variation in material properties along the radial direction.

Table 1: Shaft and disk physical and mechanical characteristics

Properties	Values
Density of shaft (kg/m ³)	7810
Young's modulus, E(GPa)	197
Shear modulus, G (GPa)	80
Radius of shaft (m)	0.012
Length of shaft (m)	0.600
Radius of disc, (m)	0.15
Thickness of disc, (m)	20
Viscous damping, η_V (s)	0.0002
MOI of disc, (kg-mm ²)	41750 & 168100 ($I_{yy} = I_{zz}$) 83500 & 336200 (I_{xx})

Timoshenko beam theory is used to model the FG rotor system using four elements. For simple simulation, the traditional static condensation technique is employed. Tables 1, 2, and 3 include the dynamic data that are utilised to analyse the rotor-disk-bearing system.

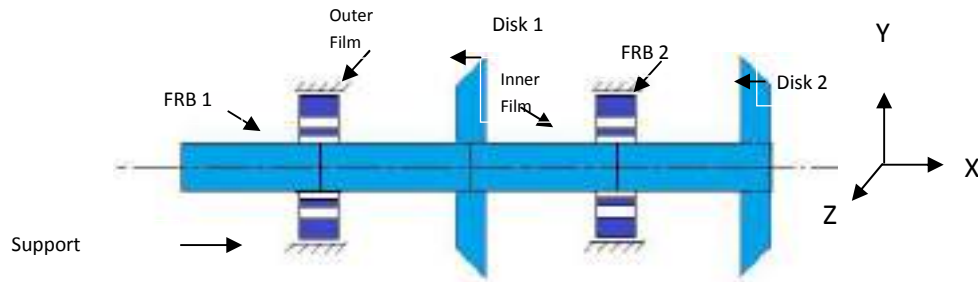


Fig.18 Rotor-disk-FRB bearing system

Table 2: FGM shaft material properties considered

Material properties	Stainless steel (SUS304)	Zirconia (ZrO ₂)
Young's modulus (GPa)	197	200
Density (kg/m ³)	7800	5000

Table 3: Bearing physical characteristics [15]

Parameters	FRB 1 & FRB 2	
	Inner film	Outer film
Viscosity, μ (10^{-3} Pa S)	6.4	6.4
Radial clearances, C_{film} (10^{-5} m)	3.4	7.4
Radius of bore, R_{bore} (10^{-3} m)	8.534	11
Length, L_{film} (10^{-3} m)	9.5	12
Ring mass, m_{rg} (g)	7.2	
Polar MOI of ring, I_{rg} (10^{-4} kg m ²)	48.0	

4. RESULTS AND DISCUSSIONS

The calculated system frequencies using prompt code are given in Table 4. The simulated results are further carried with the convergence study by considering the effect of rotary inertia, which are given in Table 3.

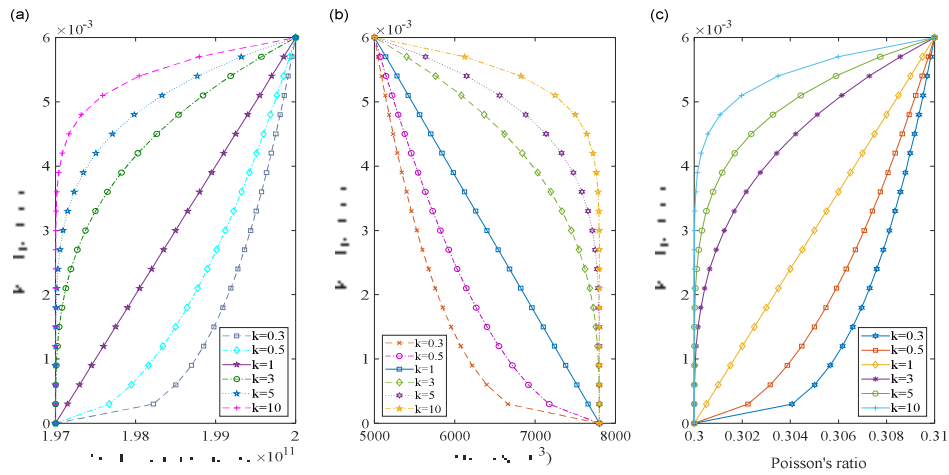


Fig. 19 Radially varying material characteristics with power law index (k) of FG shaft (a) Young's modulus, (b) Density, and (c) Poisson's ratio

Table 4. Study of convergence in numerical solution.

Frequency	Whirl modes(Hz)	Number of elements		
		4	8	12
1st	Forward	11.781	11.778	11.778
	Backward	11.013	11.010	11.010
2nd	Forward	41.528	41.523	41.523
	Backward	39.075	39.047	39.047
3rd	Forward	128.438	128.427	128.427
	Backward	94.385	94.369	94.369

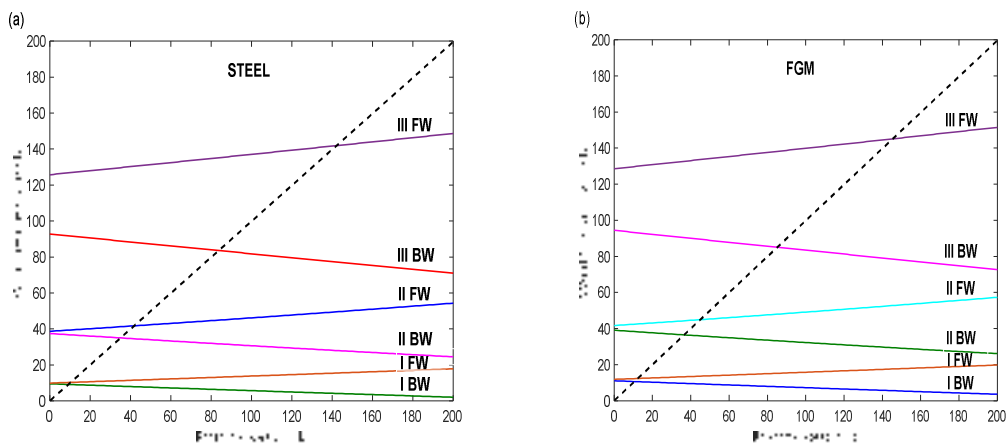


Fig. 20 Campbell plots of rotating shafts: (a) Steel, and (b) functionally graded material(FGM)

The results of the convergence investigation for several sets of elements are summarized in Table 3. According to the analysis, the frequencies are converging. A comparison between the FG shaft and traditional steel shafts has been done. As shown in Figs. 3(a) and 3(b), respectively, the natural whirl frequencies can be decreased by incorporating the viscous and hysteretic damping.

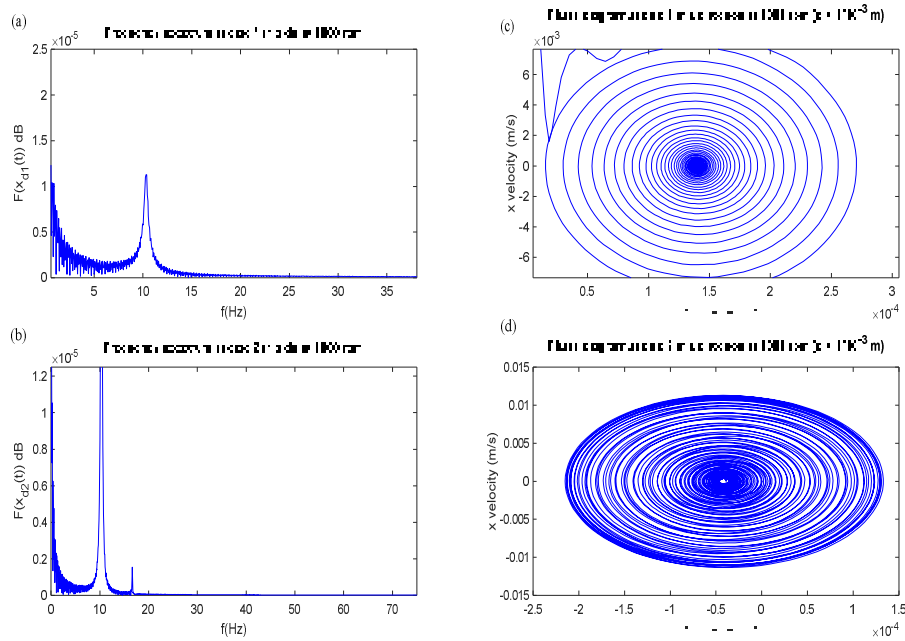


Fig. 4. Phase-plane orbits at disk 1 and 2 for $\Omega=1000$ rpm with eccentricity of 1mm.

Figure 4(a)-(d) illustrates the vibrational responses for the rotor-bearing system at discs 1 and 2. The analysis is performed using a disc eccentricity of 0.001 m and spin speeds of 1000. The observed amplitude for disc 1 is 1.10×10^{-5} dB, while the amplitude for disc 2 is found to be 1.65×10^{-5} dB under the identical conditions.

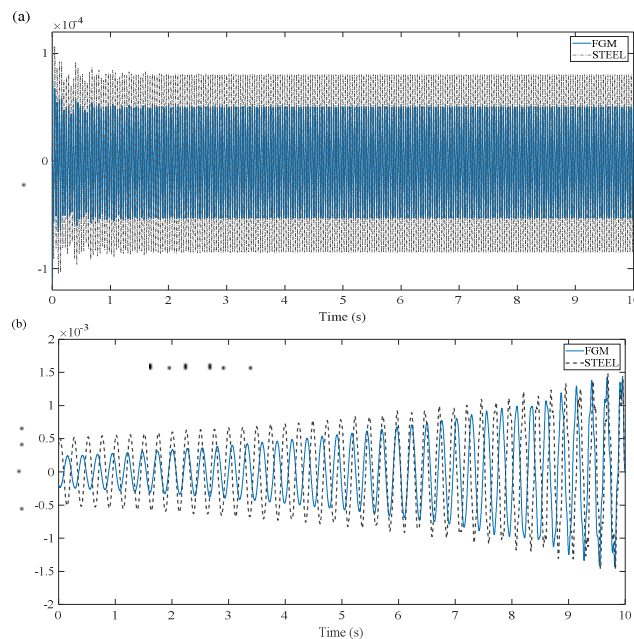


Fig. 5. Transverse responses of FG and Steel shaft for two speeds: (a) 6000 r/min, (b) 10000 r/min

It's to be noted that the traditional steel shaft's first critical speed is 3855 r/min, but the FG shaft's first critical speed is found at 4493 r/min. The effects of subcritical speeds are stabilized by viscous and hysteretic dampings, while the effects of the rotating system's lowest critical speed are destabilized by these dampings. At 4634 r/min, the first mode becomes stable. The comparisons of the displacement histories of the FG shaft-disk-bearing system to the traditional steel shaft for various sets of speeds in the transverse directions with the time period of 10 seconds are shown in Figures 5(a) and 5(b). The displacement curve in Figure 5(b) demonstrates that the unstable response occurs as the amplitude increases while the angular velocity increases.

5. Conclusions

Timoshenko beam theory and a four element FE model are used to model the FG rotor system. The radial direction is where the FG shaft material qualities change. The system contains forces resulting from mass imbalance, nonlinear bearing forces, gyroscopic forces, and the impact of internal dampings. The vibration and stability study of the rotating FG rotor system is the main focus of the numerical investigation. As part of the validation of the numerical codes, a convergence analysis was carried out. The FG shaft's radial grading is uniformly carried out using the power-law index, k . The FG shaft provides a good indication of stability limits, as shown by the comparison between the steel and FG shafts. In the FG system, a minimum value of k indicates good reaction, and dampings are crucial to stabilities.

Acknowledgments

This paper and the research behind it would not have been possible without the exceptional support of my FRIEND MEGHNA DAS CHAUDHURY.

References

- [1] Koizumi M. The concept of FGM. *Ceram Trans* 1993;34:3–10.
- [2] Koizumi M. FGM activities in Japan 1997;8368:1–4.
- [3] Argeso H, Eraslan AN. A Computational Study on Functionally Graded Rotating Solid Shafts 2007;2287. <https://doi.org/10.1080/15502280701577842>.
- [4] Nelson HD. A Finite Rotating Shaft Element Using Timoshenko Beam Theory. *J Mech Des* 1980;102:793–803. <https://doi.org/10.1115/1.3254824>.
- [5] Gayen D, Tiwari R, Chakraborty D. Static and dynamic analyses of cracked functionally graded structural components : A review. *Compos Part B* 2019;173:106982. <https://doi.org/10.1016/j.compositesb.2019.106982>.
- [6] Birman V, Byrd LW. Modeling and Analysis of Functionally Graded Materials 2019;60:195–216. <https://doi.org/10.1115/1.2777164>.
- [7] Bever MB, Duwez PE. Invited Review: Gradients in Composite Materials. *Mater Science Eng* 1972;10:1–8.
- [8] Wettergren HL, Olsson KO. Dynamic instability of a rotating asymmetric shaft with internal viscous damping supported in anisotropic bearings 1996;195:75–84.
- [9] Piovan MT, Sampaio R. A study on the dynamics of rotating beams with functionally graded properties 2009;327:134–43. <https://doi.org/10.1016/j.jsv.2009.06.015>.

- [10] Aydin K. Free vibration of functionally graded beams with arbitrary number of surface cracks. *Eur J Mech A/Solids* 2013;42:112–24.
<https://doi.org/10.1016/j.euromechsol.2013.05.002>.
- [11] Gayen D, Chakraborty D, Tiwari R. Stability behavior of two-crack functionally graded shaft in a rotor-disc system: Finite element approach. *Mater Today Proc* 2020;24:432–41. <https://doi.org/10.1016/j.matpr.2020.04.295>.
- [12] Jahangiri M, Bagheri E. Effect of radially functionally graded materials on the primary resonances of large amplitude flexural vibration of in-extensional rotating shafts. *Eng Struct* 2021;226:111362.
<https://doi.org/10.1016/j.engstruct.2020.111362>.
- [13] Zorzi ES, Nelson HD. Finite Element Simulation of Rotor-Bearing Systems With Internal Damping. *J Eng Power* 2010;99:71. <https://doi.org/10.1115/1.3446254>.
- [14] Adiletta G, Guido AR, Rossi C. Chaotic motions of a rigid rotor in short journal bearings. *Nonlinear Dyn* 1996 103 1996;10:251–69.
<https://doi.org/10.1007/BF00045106>.
- [15] Bonello P. Transient modal analysis of the non-linear dynamics of a turbocharger on floating ring bearings: [Http://DxDoiOrg/101243/13506501JET436](http://dx.doi.org/10.1243/13506501JET436) 2009;223:79–93.
<https://doi.org/10.1243/13506501JET436>.

Crack Localization in Composite Plates by Intersection of First Three Normalized Mode Shape Curves from Experimental Modal Analysis

V. Deepak Raj Kumar, S. Ramakrishna and M. Tarun

Gayatri Vidya Parishad College of Engineering, Visakhapatnam, Andhra Pradesh, India

Abstract

Crack in any structure is a destructive occurrence. Any structure or component could prematurely fail as a result of it. It may cause terrible mishaps and hurt people as well. In order to prevent failure or accidents, it is crucial to detect these cracks effectively and take the necessary precautions. Hence crack detection and localization techniques are used to avoid sudden failures of structures while in operation. To determine the change in natural frequencies and mode shapes, an impact hammer test is conducted on composite plates with and without cracks. Impact hammer, uni-axial accelerometer, and four-channel vibration analyzer are used to execute the impact hammer test. The crack in the composite plates is located using a change in natural frequencies. The normalized mode shapes algorithm is trained using test data of the first three natural frequencies collected from impact hammer tests on different cracked composite plates, and the mode shapes of the first three natural frequencies are plotted. The crack location is estimated with extremely high precision using the intersection of the first three normalized mode shapes.

Keywords: Composite beams, crack localization, composite plate, natural frequencies, mode shapes, normalized mode shapes algorithm.

1. Introduction

The structural integrity of diverse engineering constructions has been more and more in demand throughout time. All structures are susceptible to damage, whether it comes from an accident, extreme operational stress, or harsh weather. The component's in-service cracks have the ability to grow until they reach a critical size, at which point they will fail. A helpful tactic for preventing this early failure is structural health monitoring (SHM). The use of vibration-based condition monitoring is one of many SHM strategies that can help prevent structures from failing before they should.

It is preferable to examine the damage that has already occurred as soon as practical to prevent any catastrophic collapses from happening. Meruane et al. [1] has presented a mathematical framework for damage identification utilizing an impact hammer-based modal testing approach in a steel-concrete composite structure. The mathematical formulation makes it possible to pinpoint areas where stiffness differs from a starting virgin. Chen et al. [2] has used modal feature extraction and linear weight sum to build a multi-objective identification approach for detecting structural damage. To update the damage vector factor and produce reliable structural damage detection findings, a hybrid particle swarm optimization (HPSO) solver was chosen. Kaushar et al. [3] has provided a method for utilizing natural frequency to detect the presence of cracks on the surface of beam-type structural elements. The two obtained natural frequencies will be utilized to determine the size and location of the crack. Janeliukstis et al. [4] has presented an experimental validation of the use of the Mode Shape Curvature Squares (MSCS) approach

and the Mode Shape Based Spatial Continuous Wavelet Transform (CWT) technique for locating damage in beam constructions. Dancygier et al. [5] has reported an experimental verification and quantification of the localized cracking phenomenon in steel-fiber-reinforced concrete (RC) tension prismatic bars. Gillich et al. [6] has devised an algorithm based on natural frequency shifts caused by damage to evaluate transversal cracks in composite constructions. The strain energy contained in the beam is used to determine the crack location. Chin et al. [7] has proposed a method for crack-severity estimate that takes use of the various speeds and loads frequently experienced by gearboxes. This method includes an automated method for identifying the fractured tooth and a method for estimating the crack's depth based on comparison with a theoretical tooth stiffness model. Ortega et al. [8] has provided a non-destructive method to forecast the residual life of reinforced concrete beams with varying amounts of cracking caused by corrosion of the steel reinforcement while considering variations in dynamic behavior caused by changes in the initial natural frequency. Lyu et al. [9] has provided a universal prediction framework that consists of two deep learning models that are applied to data fusion and residual useful life (RUL) prediction, respectively, to complete the prognosis with multisensor data. Dhiraj et al. [10] has developed a novel composite deep Convolutional neural network (CNN) architecture for damage localization and quantification, which is followed by multivariate linear regressors. Melville et al. [11] has employed deep learning to understand ultrasonic guided waves to diagnose structural deterioration quickly, precisely, and automatically.

1. Materials and Methods

An E-Glass Composite plate with dimensions of 200 mm x 200 mm x 5 mm is used in the current work. Fig. 1 shows the picture of E-glass composite beam with grid points used for experimental modal analysis using OROS analyzer and experimental modal analysis software. Table 1 represents the material properties of E-glass composite plate.

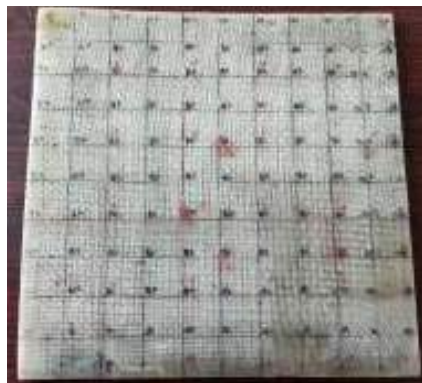


Fig. 1 E-Glass Composite plate with grid points

Table 1 Mechanical properties of E-Glass composite plate

Physical properties	Value	Physical properties	Value
Elastic Modulus (E_x), MPa	30,900	Rigidity Modulus (G_{xz}), MPa	2800
Elastic Modulus (E_y), MPa	8300	Poisson coefficient (ν_{xy})	0.22
Elastic Modulus (E_z), MPa	8300	Poisson coefficient (ν_{yz})	0.0866
Rigidity Modulus (G_{xy}), MPa	2800	Poisson coefficient (ν_{xz})	0.22
Rigidity Modulus (G_{yz}), MPa	3000		

2.1 Experimental modal analysis

The Experimental Modal Analysis (EMA) has been carried out using NV Gate software and Data Acquisition System (DAQ) by OROS on the E-Glass Composite plate. The plate has been first divided into various segments so as to obtain averaging of the signals. In general, there are two methods commonly used for the EMA, namely roving sensor method and roving hammer method. For the present experimental analysis, roving hammer method has been considered. In this method the accelerometer sensor will be positioned at a fixed location and the hitting will be done at different locations (which are divided earlier) using the impact hammer. The sensitivity of impact hammer is 2.248 mv/N and that of accelerometer sensor is 9.68 mv/g. First of all, the DAQ is connected to the personal computer and then the NV Gate software is launched. Then the Modal analysis module of NV Gate is used to create the geometry of the structure. The geometry of the plate is created with the specified dimensions and is divided to segments similar to that which has been done on the composite plate. The sensitivity of the accelerometer and that of the impact hammer have been entered. Then the sequence of the experiment and the other settings have been defined. Now the experiment has been done by attaching the accelerometer sensor at a fixed location, and then hitting at different segments divided on the plate using the impact hammer. The signals have been collected and the averaging of the signals have been done and the frequency response function and coherence function will be generated. Then the modes will be selected by using either broadband or narrowband in the software and the respective mode shapes will be generated. Fig. 2 shows the EMA setup used for experimental modal analysis using OROS analyzer and EMA software.



Fig. 2 Image of experimental modal analysis setup

2.2 Numerical Modal Analysis

Numerical modal analysis (NMA) has been carried out using ANSYS and Modal analysis module. First of all, the properties of the composite plate to be modelled are defined in the Engineering data section. Later the geometry of the plate has been modelled as per specified dimensions. The plate has been modelled layer wise with orientation of $[0/90]$ until the required thickness has been achieved. Then the model has been meshed into fine elements so as to obtain optimum results. Then the boundary conditions have been defined and the modal analysis has been carried out so as to obtain natural frequencies and mode shapes. For the present scenario, fixed-free condition of the plate has been considered. Fig.

3 and Fig. 4 shows the orientations of stack up plies and meshed plate healthy composite plate.

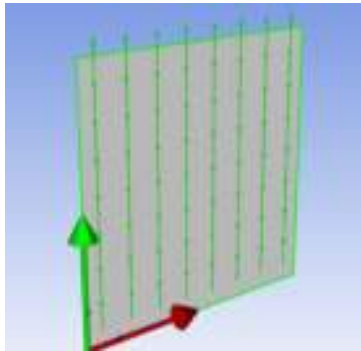


Fig. 3 Orientations of stack up plies

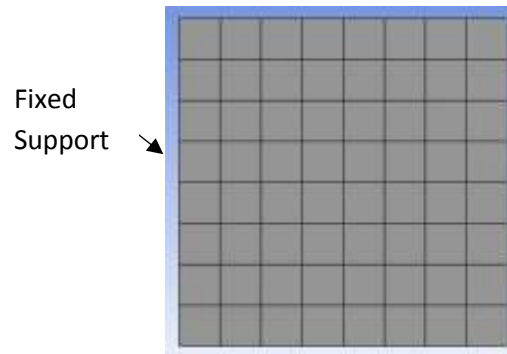


Fig. 4 Meshed plate structure

3 Results and Discussion

In this section, EMA and NMA of the composite plate along with crack detection and crack localization techniques have been discussed.

3.1 Experimental modal analysis

The EMA of composite plate is carried out using the NV Gate software applying the roving hammer method. The plate is fixed at one end and is free at other ends and the analysis has been carried out. From the analysis, a Modal Indication Function (MIF) as shown in Fig. 5 is obtained. From this MIF, we have obtained the first three natural frequencies as shown in Fig. 6, and the respective mode shapes against the natural frequencies have been generated. A MIF represents the natural frequencies obtained from EMA. Table 2 indicates the natural frequencies obtained from EMA.

Table 2 Natural frequencies from EMA

Mode	Natural frequency in Hz
1	60.93
2	120.61
3	372.85

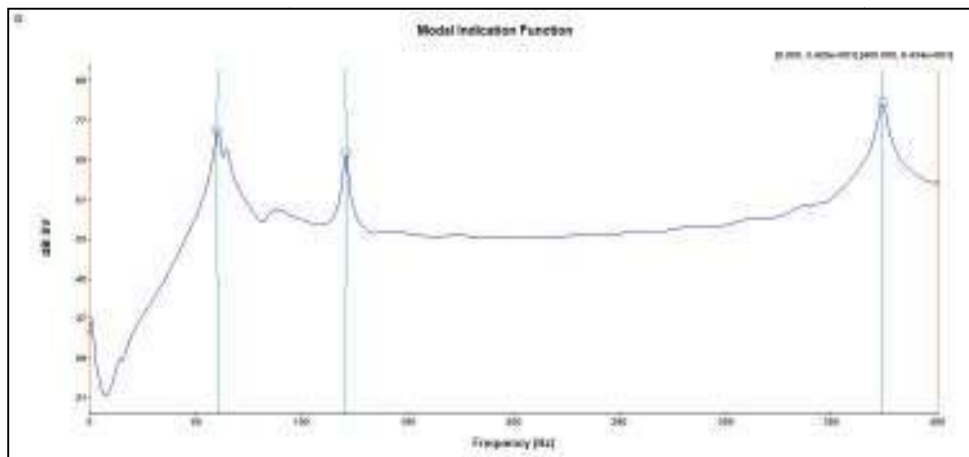


Fig. 5 Modal indication function of composite plate

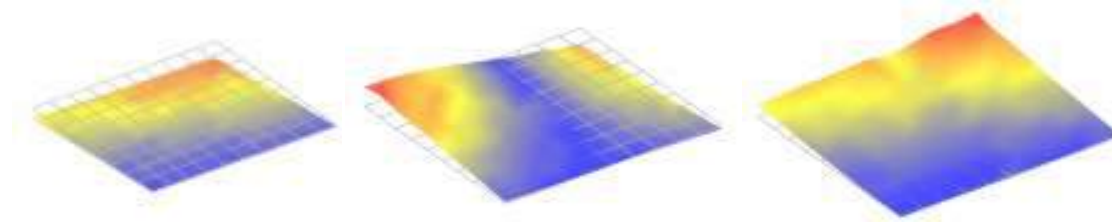


Fig. 6 First three mode shapes from EMA

A Modal Assurance Criterion (MAC) function confirms the accuracy of the natural frequencies obtained from the EMA. From the below Fig. 8, it can be observed that the MAC for all the three modes have a value of 1, which shows that the analysis is carried out with strong signals and is accurate.

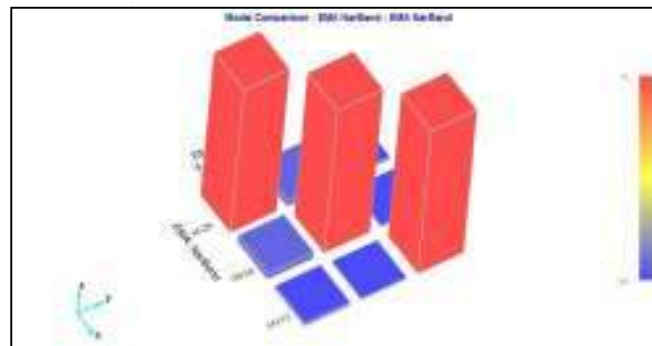


Fig. 7 MAC Function

3.2 Numerical modal analysis

The NMA has been carried out using ANSYS software. The plate is fixed at one end. The first three natural frequencies and their respective mode shapes have been obtained from the analysis. Table 3 shows the natural frequencies obtained from NMA. Fig. 8 indicates the first three mode shapes from NMA. The variation of the natural frequencies obtained by both EMA and NMA are well below the allowable range of 15%. Hence it is found that there is a good relativity between EMA and NMA. Table 4 represents the comparison of natural frequencies of EMA and NMA.

Table 3 Natural frequencies from NMA

Mode	Natural frequency in Hz
1	66.691
2	119.46
3	428.34

Table 4 Comparison of natural frequencies of NMA and EMA

	Frequency of 1 st Mode (Hz)	Frequency of 2 nd Mode (Hz)	Frequency of 3 rd Mode (Hz)
NMA	66.691	119.46	428.34
EMA	60.93	120.61	372.85
Variation in %	8.63	0.96	12.95

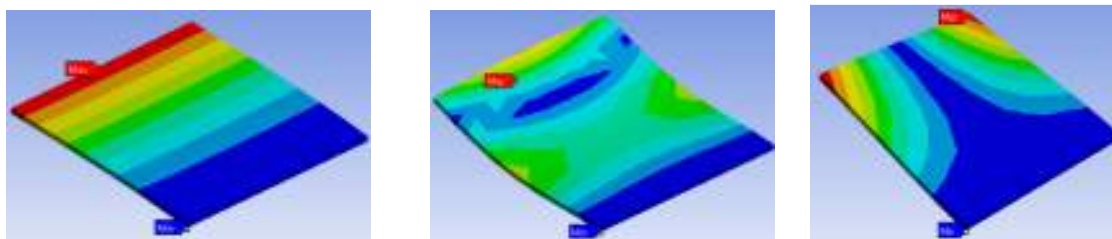


Fig. 8 First three mode shapes from NMA

3.3 Crack detection

On composite plates with and without cracks, the NMA is carried out to determine whether a crack is present. A transverse crack with a 3 mm thickness appears 50 mm from fixed end of plate. To identify the presence of crack, natural frequencies for cracked and uncracked plates are contrasted. The composite plates with and without cracks, as well as their first three natural frequencies, are displayed in the table below.

Due to the change in structural stiffness caused by the crack, the structure's vibrational characteristics, such as modal frequencies, mode shapes, and damping ratio, are affected. The difference between the natural frequencies of plates with cracks and plates without cracks is readily apparent from the table below. The deflection depends on stiffness and is inversely proportional to the natural frequencies. When compared to plates without cracks, the deflection for cracked plates is high. Because of this, the natural frequencies of cracked plates are low compared to those of uncracked plates. One can forecast the presence of a crack in the structure using this phenomenon. Fig. 9 shows the meshed cracked composite plate in ANSYS.

3.4 Crack localization

Using the data set generated from the NMA performed on cracked composite plates, the normalized mode shape curve method is trained to find the first three natural normalized frequencies intersection. In order to localize cracks in composite plates, the Normalized mode shape curve algorithm (NMSCA) is learnt. The NMSCA for composite plates is trained using the starting three natural frequencies of cracked plates in Table 5. For each crack site and crack thickness for each mode, normalized modal frequencies are determined.

For the composite plate, a similarity check is done between real crack and the estimated crack position. The interaction spot for the initial three normalized mode curves for the cracked composite plate is shown in Fig. 10 at 50.24 mm in length and 2.99 mm in thickness, this is really close to where the crack actually is i.e., at 50 mm in length and 3 mm in thickness. Table 6 compares the position and thickness of composite plate's actual and estimated cracks.

Table 6 Comparison of real and predicted crack location for composite plate

Illustration	Real	Predicted	Error (%)
Location of crack, mm	50	50.24	0.48
Thickness of crack, mm	3	2.99	0.33

Table 5 Initial three natural frequencies of healthy and cracked plate

Location of crack from fixed end mm	Thickness of crack mm	Frequency of 1 st Mode Hz	Frequency of 2 nd Mode Hz	Frequency of 3 rd Mode Hz
No Crack	No Crack	66.691	119.46	428.34
50	1	66.69	119.45	428.33
50	2	66.5575	119.285	428.19
50	3	66.425	119.12	428.05
50	4	66.388	118.975	427.635
50	5	66.351	118.83	427.22
100	1	66.69	119.45	428.33
100	2	66.6585	119.42	427.17
100	3	66.627	119.39	426.01
100	4	66.628	119.39	425.915
100	5	66.629	119.39	425.82
150	1	66.69	119.45	428.33
150	2	66.6895	119.445	428.325
150	3	66.689	119.44	428.32
150	4	66.6895	119.435	427.835
150	5	66.69	119.43	427.35

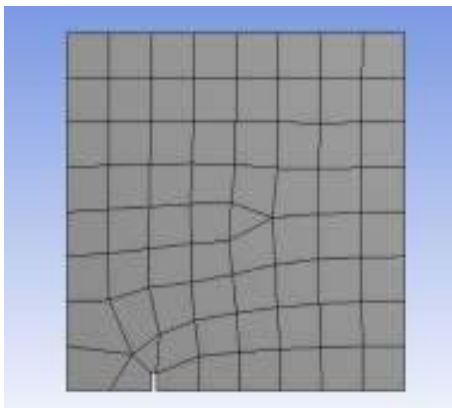


Fig. 9 Meshed cracked composite plate in ANSYS.

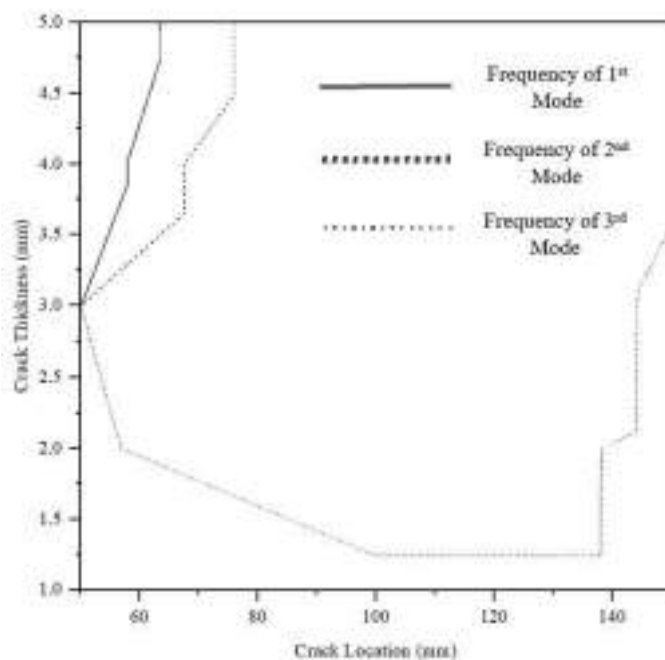


Fig. 10 First three normalized mode shape curves intersection spot for cracked plate

4 Conclusions

For healthy composite plates, the natural frequencies are computed using both EMA and NMA. Using NMA, the natural frequencies for cracked plates are determined. Changes in natural frequencies on plates with and without cracks can be used to detect the presence of

a crack in composite plates. With the set of data collected from NMA on cracked composite plates, the normalized mode shape curve algorithm is trained to produce the normalized mode shape curves. The intersection of the first three normalized mode shape curves of the damaged composite plate is utilized to determine where the crack is located. The first three normalized mode shape curve intersections provide a solid indication of the crack's location. As the difference in error between the actual and estimated crack locations is less than 1%, it is found that there is a high degree of agreement between them.

References

1. V. Meruane, S. J. Yanez, L. Quinteros and E. I. S. Flores, "Damage detection in steel-concrete composite structures by impact hammer modal testing and experimental validation", *Sensors*, vol. 2022.
2. Z. Chen, D. Zhao, Z. Chen and W. Wang, "Structural damage detection based on modal feature extraction and multi-objective optimization method for steel structures", *Frontiers in Materials*, vol. 9, 2022.
3. H. Kaushar, D. S. Barad and V. Vyas, "Crack detection in cantilever beam by frequency-based method", *Procedia Engineering*, vol. 51, pp. 770–775, 2013.
4. R. Janeliukstis, S. Rucevskis, M. Wesolowski and A. Chate, "Experimental structural damage localization in beam structure using spatial continuous wavelet transform and mode shape curvature methods", *Measurement*, vol. 102, pp. 253–270, 2017.
5. A. N. Dancygier, Y. S. Karinski and Z. Navon, "Cracking localization in tensile conventionally reinforced fibrous concrete bars", *Construction and Building Materials*, vol. 149, pp. 53–61, 2017.
6. G. R. Gillich, Z. I. Praisach, M. A. Wahab and O. Vasile, "Localization of transversal cracks in sandwich beams and evaluation of their severity", *Shock and Vibration*, vol. 2014, pp. 1–10, 2014.
7. Z. Y. Chin, P. Borghesani, Y. Mao, W. A. Smith and R. B. Randall, "Use of transmission error for a quantitative estimation of root-crack severity in gears", *Mechanical Systems and Signal Processing*, vol. 171, no. 108957, p. 108957, 2022.
8. N. F. Ortega and S. I. Robles, "Assessment of residual life of concrete structures affected by reinforcement corrosion", *HBRC Journal*, 2014.
9. Y. Lyu, J. Gao, C. Chen, Y. Jiang, H. Li, K. Chen and Y. Zhang, "Joint model for residual life estimation based on long-short term memory network", *Neurocomputing*, vol. 410, pp. 284–294, 2020.
10. Dhiraj, A. Agarwal, A. Agrawal, V. Meruane and K. S. Sangwan, "Development of a machine learning based model for damage detection, localization and quantification to extend structure life", *Procedia CIRP*, vol. 98, pp. 199–204, 2021.
11. J. Melville, K. S. Alguri, C. Deemer and J. B. Harley, "Structural damage detection using deep learning of ultrasonic guided waves", *AIP Conference Proceedings 1949*, 2018.

Development of a Machine Learning Algorithm Based on Random Forest Model for Localization of Crack in the Composite Beams

T. Rahul Mani Datta, L. Ram Ganesh, S. Ramakrishna, J. Sathish

Gayatri Vidya Parishad College of Engineering, Visakhapatnam, Andhra Pradesh, India

Abstract

The Random Forest method, widely acknowledged for its versatility, accuracy, and effectiveness in supervised machine learning, has emerged as a prominent algorithm for damage evaluation. This research paper focuses on the application of damage monitoring in composite materials, with a specific emphasis on utilizing vibration data obtained from cracked composite beams. By harnessing machine learning models trained on such data, real-time health monitoring and efficient detection of damage in composite structures can be achieved, leading to the prevention of catastrophic failures and significant cost reductions in maintenance. To enhance the precision of damage localization, this study further improves the Random Forest algorithm, which is based on decision trees, by incorporating additional features for optimized selection, processing, and hyper parameter tuning based on input features. The experimental data collected from natural frequency tests is leveraged to train the Random Forest algorithm, enabling accurate prediction of crack locations in cracked composite structures. In this paper, 80% of the experimental data is allocated for training the Random Forest model, while the remaining data is dedicated to testing and evaluating the performance of the generated model. Additionally, the efficiency of the Random Forest model is enhanced through the utilization of min-max scaling techniques to normalize the training and testing data. The developed Random Forest model exhibits exceptional performance in accurately predicting crack localization, primarily utilizing the input parameters of the first three natural frequencies of the cracked composite beam..

Keywords: *Crack localization, machine learning algorithm, Random Forest algorithm, cracked composite beam, natural frequency test, natural frequencies, composite beam.*

1. Introduction

The Random Forest method is widely recognised as a highly accurate and versatile supervised machine learning technique. It has gained popularity as an effective damage evaluation algorithm due to its ability to handle complex data and provide reliable predictions. By training multiple decision trees on different subsets of the data and averaging their predictions, the random forest method generates a robust final prediction. Composite materials, such as those used in wind turbine blades, aerospace structures, bridge decks, and pressure vessels, are susceptible to cracks and other forms of damage. Detecting and monitoring these cracks is crucial for preventing costly failures and ensuring structural safety. Machine learning (ML) algorithms based on the Random Forest model have emerged as powerful tools for crack detection and health monitoring in composite beams. These algorithms can analyse data collected from embedded sensors within the structures and accurately identify the presence of cracks. Significant contributions have

been made in previous studies focused on crack detection and structural analysis. Prashant et al. [1] conducted an experimental modal analysis on a rectangular cantilever beam to determine its natural frequencies, mode shapes, and modal damping. They utilised an impact hammer connected to an FFT analyzer and employed NI Lab VIEW software to extract the modal data. Karandikar et al. [2] performed a similar experimental modal analysis on beams with different crack configurations using a Fast Fourier Transform (FFT) analyzer. They validated their experimental results by comparing them with modal analysis conducted in ANSYS, thereby confirming the accuracy of their numerical simulations. Ashish et al. [3] investigated vibration-based crack identification methods for damage detection in fibre-reinforced composites. Their study revealed the influence of cracks on static and dynamic response attributes, emphasising the correlation between crack size, location, and changes in natural frequencies and mode shapes. Chandan Kumar et al. [4] analytically and experimentally determined the natural frequencies of various modes in cantilever beams made of different materials, including aluminium and mild steel. Their findings showcased a high level of agreement between theoretical and experimental results. Vader et al. [5] investigated the effect of crack location and depth on the natural frequencies of composite cantilever beams fabricated with glass epoxy. Through numerical simulations in ANSYS and experimental validations, they observed good concurrence between the two sets of results. Khalkar et al. [6] proposed a technique based on modal analysis in ANSYS Workbench to determine the first mode frequency of healthy cantilever beams subjected to bending. Their proposed technique exhibited good conformity with modal frequencies obtained using ANSYS Workbench. Furthermore, researchers have explored innovative approaches beyond traditional methods. Melville et al. [11] employed a deep learning interpretation of ultrasonic guided waves for fast, accurate, and automated structural damage detection. Their approach involved conducting full wavefield scans of thin metal plates. Daskalakis et al. [12] presented a framework for damage detection and localization using neural networks. Their approach, demonstrated through numerically simulated data, illustrated the effectiveness of the proposed method. Adam et al. [13] proposed a hybrid identification method based on a deep learning approach for crack identification in concrete bridge images. Their method was examined and validated, showing promising results. In this research paper, our aim is to further advance the field of crack detection and structural analysis by exploring the application of the Random Forest method and other machine learning algorithms in crack localization and health monitoring of composite beams. Our experimental approach involves conducting modal analysis on various beam configurations and comparing the results with numerical simulations. The outcomes of this study have the potential to significantly enhance the safety and reliability of composite structures while minimising maintenance costs.

1. Experimental Analysis

In this research, an experimental analysis was conducted to determine the first three natural frequencies of cracked composite beams using an impact hammer test. The composite beam selected for the study was made of E-Glass and had dimensions of 300mm×50mm×3mm. To ensure stability, one end of the cracked composite beam was rigidly fixed using a bench vice, while an accelerometer was positioned at the other end. The impact hammer was employed to induce free vibrations in the beam. Both the accelerometer and impact hammer were connected to a dynamic signal analyzer for signal acquisition and processing. The frequency range for the experiment was set to 1440 Hz. The impact hammer had a sensitivity value of 10 mv/g, while the accelerometer sensor had a sensitivity of 9.68 mv/g. Accelerometers were strategically placed at selected locations,

and the initial excitation was provided by the impact hammer. During the impact hammer test, the resulting vibrations were measured using the accelerometers. The acquired vibration data was then analyzed using EDM (Engineering Data Management) software to determine the natural frequencies of the cracked composite structure. Figure 1 illustrates the cracked composite beam with the acceleration sensor, while Figure 2 depicts the impact hammer test conducted on the cracked composite beam. The results of the first three natural frequencies of the cracked composite beams are presented in Table 1. It is important to note that the data in Table 1 was utilized to train the Random Forest algorithm. Furthermore, Figure 3 showcases the frequency response spectrum of the cracked composite beam, with the crack positioned at 50 mm from the fixed end.

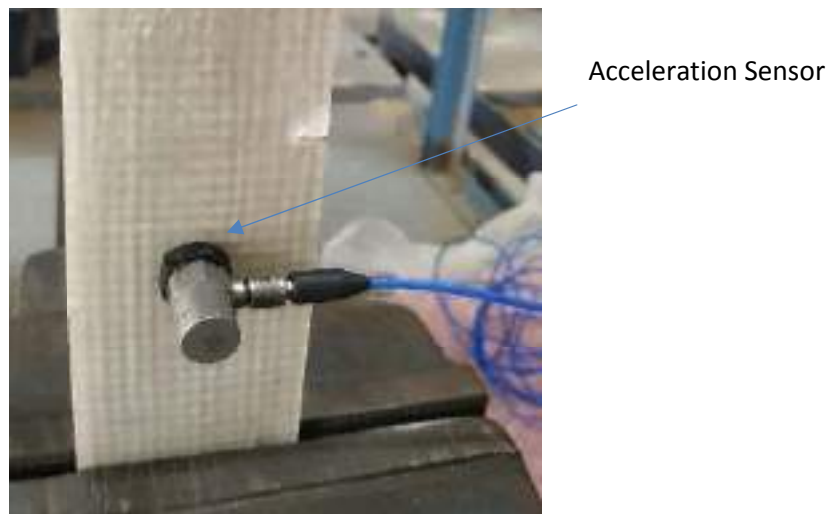


Fig. 1 Cracked composite beam with acceleration sensor



Fig. 2 Impact hammer test on cracked composite beam

Table 1. Initial three natural frequencies for a cracked composite beam

Crack Location from Fixed End (mm)	Crack Size (mm)	First mode (Hz)	Second mode (Hz)	Third mode (Hz)
50	5	20.315	135.94	169.47
50	10	20.254	133.03	168.09
50	15	20.055	129.71	165.75
50	20	19.513	129.12	162.38
100	5	20.754	130.08	169.55
100	10	20.627	129.61	168.36
100	15	20.418	128.81	166.35
100	20	20.122	127.62	163.48
150	5	20.785	129.76	169.71
150	10	20.737	128.47	168.92
150	15	20.655	126.39	167.52
150	20	20.535	123.55	165.46
200	5	20.802	129.9	169.9
200	10	20.793	128.97	169.51
200	15	20.776	127.44	168.77
200	20	20.749	125.25	167.66
250	5	20.81	130.19	170.03
250	10	20.817	130.04	169.97
250	15	20.824	129.77	169.78
250	20	20.782	129.12	162.38

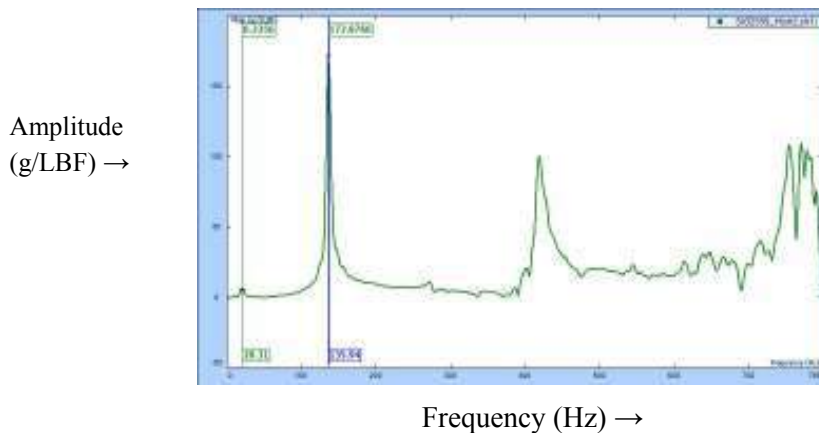


Fig. A cracked composite beam underwent frequency response spectrum analysis, revealing a 5 mm wide crack situated 50 mm away from the fixed end.

2. Random Forest Algorithm

In the paper Random Forest algorithm is employed for crack detection in composite beams. The crack location is determined using the first three natural frequencies obtained from an impact hammer test, as presented in Table 1 of the previous section (Section 2). Random Forest is a machine learning algorithm capable of both classification and regression tasks,

and in this paper, it is utilized for regression purposes. By combining multiple decision trees, this ensemble method enhances model accuracy and robustness. The Random Forest algorithm operates by creating decision trees trained on randomized subsets of the input data and features. Bagging, a process involving random sampling with replacement, is employed to create these trees. Each decision tree is trained on a distinct subset of the input data and features, which mitigates over fitting and enhances the model's generalization. The final prediction of the Random Forest algorithm is computed as the average prediction of all decision trees in the ensemble.

Fig. 4 shows the Workflow of random forest regression. This dataset shown in Table 1 used to train the Random Forest technique consists of a three sets of inputs as first three natural frequencies and corresponding outputs consists of two sets of data as crack location from clamped end and crack width. The inputs are the extracted features from impact hammer test on cracked composite specimens, while the outputs are the locations of the damage in the composite structure. The data is divided into two segments: the initial portion is used for training the model, while the remaining portion is dedicated to validating the model. Random Forest model is trained using dataset shown in Table 1. After training the model, it is to be validated with R-squared score to check its accuracy and efficiency. This can be done by using a validation dataset that was not used during the training process. Once the model is trained and validated, it can be used to locate the damage in the composite structure. The pre-processed data is input into the model, and the output is the location of the damage in the structure. Fig. 5 shows plot between the predicted and actual values of crack location.

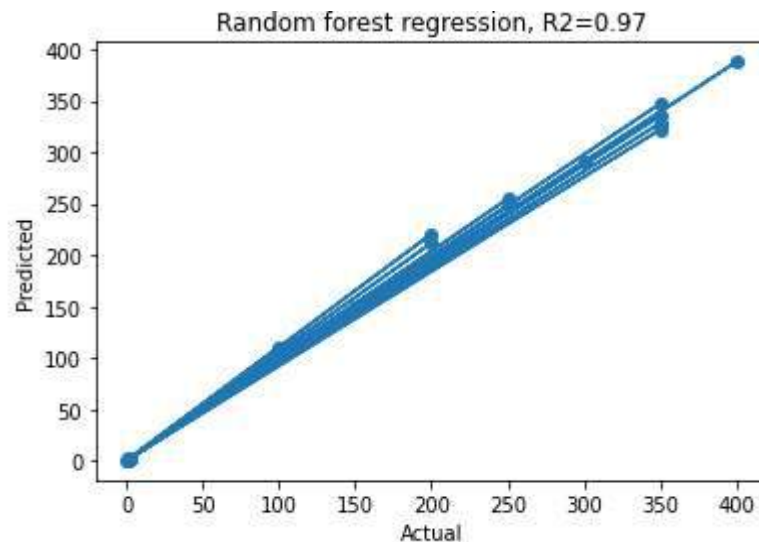


Fig. 5 Plot between the predicted and actual values of crack location

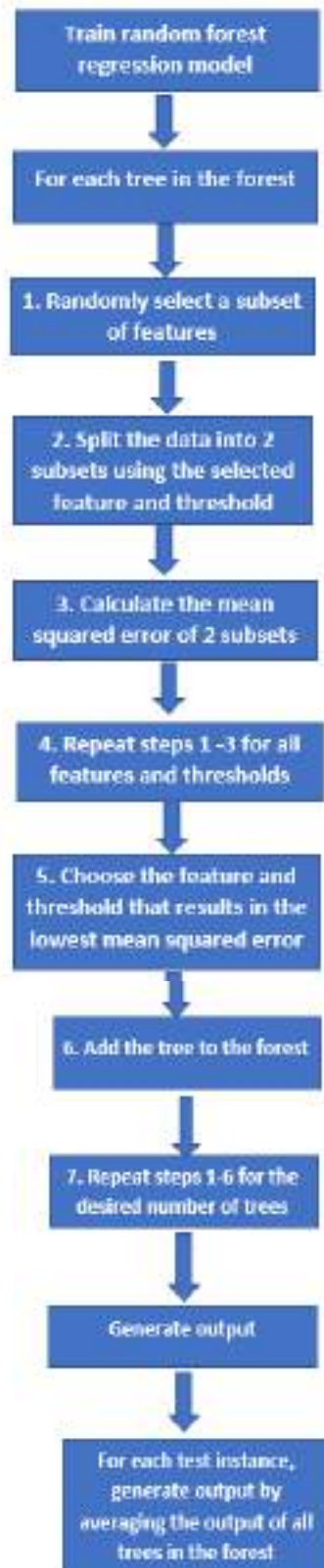


Fig. 4 Workflow of random forest regression

The model's performance was assessed using various metrics, such as the mean absolute error (MAE), mean squared error (MSE), and coefficient of determination (R² score). The results of the evaluation showed that the model performed exceptionally well in predicting

the crack location. The MAE of the model was found to be 5.547, which suggests that the average deviation between the model's predictions and the actual crack locations was small. The MSE was 92.52, further demonstrating the model's accuracy in predicting the crack location. The R2 score of 0.971 suggests that approximately 97% of the variance in the target variable, the crack location. This is an outstanding result and demonstrates the model's strong ability to accurately predict the crack location. In conclusion, the results of the performance analysis of the improvised model show that it has a mean absolute error of 5.55, a mean squared error of 92.52, and an R2 score of 0.97. This indicates a high level of accuracy in predicting the location of a crack for the three resonant frequencies as input. The study findings highlight the model's significant capability in effectively identifying cracks and various types of internal damage within composite structures, such as bridges. The use of multiple non-destructive inspection results, as inputs for the model, enhances its accuracy compared to using just one inspection result.

3. Conclusions

In conclusion, the results of this research show that the ML model developed in this study is highly effective in predicting the location of cracks in a structure based on its resonant frequencies. The high level of accuracy achieved by the model makes it a valuable tool for structural engineers and other professionals in the field. Further research may be necessary to optimize the model's performance and explore its potential applications in other areas. In conclusion, the proposed method offers a reliable and efficient way to diagnose composite structures, and could lead to more accurate inspection methods based on artificial intelligence. Future research challenges include the incorporation of additional non-destructive methods and analysing parameter measurement error and the applicable range. Overall, this research emphasizes the potential of machine learning algorithms in diagnosing composite structures and ensuring their safety.

References

1. Walunj Prashant S, V.N.Chouguleb, Anirban C. Mitrac, "Investigation on modal parameters of rectangular cantilever beam using Experimental modal analysis", *Materials Today: Proceedings*, vol.2, pp.2121-2130, 2015.
2. Pratibha M Karandikar, VaishnavVivek, and Dabhade Ganesh, "Experimental investigation of crack detection of cantilever beam-FFT analyzer", *IOSR Journal of Mechanical and Civil Engineering*, vol.13, pp. 12-17, 2016.
3. Ashish S. Apate and Nitin N. More, "Vibration analysis of cracked cantilever beam", *International Research Journal of Engineering and Technology*, vol.3, pp. 1177-1181, 2016.
4. D.P. Kamble, Chandan Kumar, Shivprasad R. Sontakke, and Ratnadip T. Gaikwad, "Analytical and experimental analysis of cantilever beam under forced vibration", *International Journal of Engineering Science and Computing*, vol.6, pp. 2168-2171, 2017.
5. Soham S. Vader and V. A. Raikar, "Crack detection in composite cantilever beam by vibration analysis and numerical method", *International Research Journal of Engineering and Technology*, vol.4, pp. 1776-1784, 2017.
6. V. Khalkar and S. Ramachandran, "Paradigm for Natural Frequency of an Un-Cracked Cantilever Beam and its Application to Cracked Beam", *ARPN Journal of Engineering and Applied Sciences*, vol.12, pp.1714-1729, 2017.

7. P. Kumar, S. Bhaduri, and A. Kumar, "Vibration Analysis of Cantilever Beam: An Experimental Study", *International Journal for Research in Applied Science & Engineering Technology*, vol.4, pp.361-369, 2016.
8. Pragnesh K. Chaudhari, Dipal Patel, Vipul Patel, "Theoretical and Software Based Comparison of Cantilever beam: Modal Analysis", *International Journal of Innovative Research in Advanced Engineering*, vol.1, pp.75-79, 2014.
9. Shishir kumar sahu and Itishree Mishra, "Modal analysis of woven fiber composite plates with different boundary conditions", *International Journal of Structural Stability and Dynamics*, vol.15, pp. 1540001-17, 2015.
10. Pushparaj Pingulkar and Suresha B, "Free vibration analysis of laminated composite plates using finite element method", *Polymers & polymer composites*, vol.24, pp. 529-538, 2016.
11. Joseph Melville, K. Supreet Alguri, Chris Deemer and Joel B. Harley, "Structural Damage Detection Using Deep Learning of Ultrasonic Guided Waves", *AIP Conference Proceedings* 1949, 230004, 2018.
12. Emmanouil Daskalakis, Christos G. Panagiotopoulos and Chrysoula Tsogka, "Stretching Method-Based Damage Detection using Neural networks", *Sensors* 22, 830, 2022.
13. Edriss Eisa Babikir Adam and A. Sathesh, "Construction of Accurate Crack Identification on Concrete Structure using Hybrid Deep Learning Approach", *JIIP*, Vol.03/No.02, 2021.

Monitoring of Power Generation for Vortex-Induced Vibrations of a Single Cylinder Using ANSYS Fluent

Johny Shaida Shaik, Srinivasa Rao. Putti , Nikhil Chaitanya Angajala

Ph.D Research scholar, Professor Department of Mechanical Engineering, Andhra University, Assistant Professor, Department of Mechanical Engineering, Vignan Institute of Information and Technology, Visakhapatnam.

Abstract

Vortex-Induced Vibration Aquatic Clean Energy (VIVACE) is a recent technology that monitors vortex-induced hydro-dynamic forces to drive the power convertor and is one many renewable ocean energy generation methods. This convertor monitors power when placed in a stream of water such as in the ocean floor or the river bed. In order to analyse its condition, a small scale geometry of the convertor of diameter (D) 60 mm, length (L) 1 m and density 2200 kg/m^3 is simulated using ANSYS Fluent for water flow velocity (U) 0.15 to 0.6 m/s (Reynolds Number range of 7.5×10^3 to 30×10^3) in cross-flow conditions. Oscillation amplitude (A), oscillation frequency (f_{osc}) and lift forces generated are monitored from the simulation of VIV phenomenon in Fluent against time scale for the spring-mounted rigid cylinder. Spring stiffness (k) values of 125 N/m and 250 N/m are used to compare the results. The oscillation amplitude/cylinder diameter ratio (A/D) and Power developed are plotted against Reynolds number and reduced velocity (U^). Amplitude variation from cycle to cycle and Power stability are monitored for each simulation case and concluded that the governing parameter for effective power extraction is the reduced velocity (U^*) which should lie between 7.0 and 8.0. The theoretical equations for power and efficiency estimation are deduced mathematically. Finally (i) the efficiency is calculated and verified with literature, (ii) power monitored from simulation is compared with theoretical value and (iii) parameters that contribute to maximize the efficiency are explained. These efficiency and power implications can further help to design the VIVACE power plant according to the power requirements.*

Keywords : ANSYS Fluent, Flow Induced Vibrations, Reynolds number, Strouhal Number, Vortex-Induced Vibrations, VIVACE.

I. Introduction:

Vortex-Induced-Vibrations for Aquatic Clean Energy, or VIVACE convertor uses the condition monitoring and fluctuations in the lift force on a circular cylinder due to cross flow of fluid (due to Karman-vortex street) to monitor the cylinder oscillations into mechanical power, which is then used to drive magnetic coil to produce electrical power. Researchers at the Marine Renewable Energy Lab, University of Michigan, Bernitsas and Raghavan [1][2]&[3], have performed experiments to monitor on various parameters that govern the VIV phenomenon by using spring-mounted cylinder in water tunnel test facilities.

Strouhal Frequency is the frequency of von-karman vortex shedding for the case of stationary cylinder and is defined in the literature (Goudarzi [4]) by (1) and the Strouhal number is taken as '0.2' for this work irrespective of the roughness from the Strouhal

Number-Reynold Number relationship as shown in Fig.1. for the Reynolds number between the range 10^3 and 10^5 .

$$f_{str} = (St \times U)/D \quad (1)$$

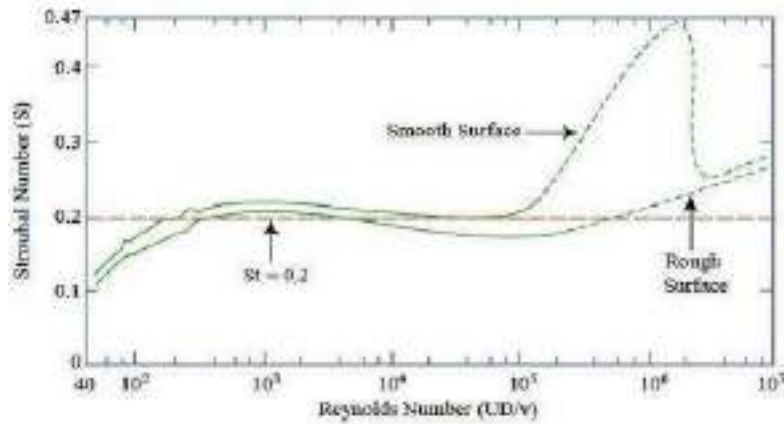


Fig. 1. Strouhal Number vs. Reynolds Number [8]&[4].

But when the cylinder is free to move in transverse direction on elastic spring, the oscillation frequency non-intuitively deviates from the Strouhal relationship (1) but still follows a linear relationship (2) that is evident from Fig.10. in [4].

$$f_{osc} \text{ approximately } = 0.75 * f_{str} \text{ to } 0.9 * f_{str} \quad (2)$$

$$= f^{\theta} * f_{str} \quad (3)$$

In this context, obvious intuition is that the amplitude of oscillation would be highest when the Strouhal frequency matches the natural frequency of the system. But in practice, the non dimensional reduced velocity (U^*) is the parameter which explains the synchronization and it is expressed in (4) [4].

$$U^* = U / (f_n \times D) \quad (4)$$

When U^* lies near 7.5, the amplitude of oscillation is maximum as found in the literature [4] & [5]. U is the fluid cross-flow fluid velocity. The natural frequency of the spring-submerged-cylinder system, f_n is given by the expression (5) as in [4],

$$f_n = \frac{1}{2\pi} \sqrt{\left(\frac{k}{mc} + ma\right)} \quad (5)$$

k is the spring stiffness, mc is the mass of the cylinder and ma is the added mass. For submersible vibrating bodies, added mass is calculated as

$$ma = cd * md \quad (6)$$

$cd = 1$ for cylinder and md is the mass of the displaced fluid

II. Condition Monitoring of Simulation Procedure

ANSYS Fluent 2D solver is used for simulating the cross flow of water around the cylinder by creating a circular void in the rectangular domain as shown in Fig.2. The built-in Six-

DOF solver is used to monitor the simulation the 2-way Fluid-Solid Interaction. The Fluent solver translates the instantaneous pressure developed on the surface of the cylinder into vertical force and gives it as input to the cylinder motion and the displacement of the cylinder thus obtained by solving the motion equation is back-propagated to the dynamic mesh and updates the mesh for the next time-step. Total simulation time is chosen as 6 s to 13 s depending on the convergence response of the instantaneous coefficient of lift. Specifications, Mesh and Schematic setup are discussed in the following sections

A. Specifications

Diameter of the cylinder is kept constant at 6 cm as in Goudarzi

[4] and cylinder length of 1 m is used since ANSYS Fluent2D solver is found to be more consistent with unit thickness (1 m). Other specifications are given in Table 1.

Table 1: Specifications of the VIVACE simulation

Parameter	Values from considered literature	Present Work
Diameter (D)	12.5 cm [1][2], 3.81 cm [8],6 cm [4], 6.35 cm [3]	6 cm
Length (L)	0.91m [1][2], 0.38 m [4], 0.3 m[6]	1 m
Mass Ratio (m^*)	1.45 [1] [2], 2.6 [8], 2.26 [4]	2.2
Damping Ratio (ξ)	0.05939 [2], 0.005 [6], 0.05 [4]	Not explicitly specified, as this can be obtained only in physical tests
Velocity (U)	0.4 – 1.2 m/s [1][2], 0.3 - 1.5 m/s [4], 0.453 m/s [6]	0.15 - 0.6 m/s
Reynolds Number (Re)	0.44–1.34x10 ³ [1][2], 15x10 ³ – 60x10 ³ [4], 10.7x10 ³ -30.4x10 ³ [6]	0.75x10 ³ - 30x10 ³

B. Mesh and ANSYS Fluent Setup

Triangular element mesh is generated in ANSYS for the fluid domain as shown in Fig.2. 20 Inflation layers starting with 0.1mm layer height are provided as shown in Fig.3. The fluid domain proportions are chosen as per the water tunnel depth in [4] and a downstream length of 1m that is just enough to show the cylinder wake.

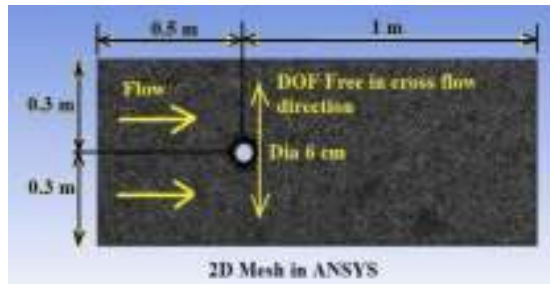


Fig. 2. 2-D Mesh with fluid domain surrounding layers

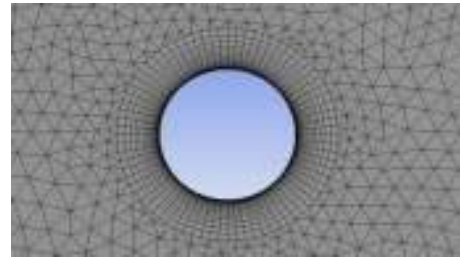


Fig. 3. Zoom-in view of inflation the cylinder

C. Schematic of VIVACE convertor

Schematic of VIVACE hydro power generator as devised by researchers in Marine Renewable Energy Lab, University of Michigan [1] is shown in a simplified manner in Fig.4.

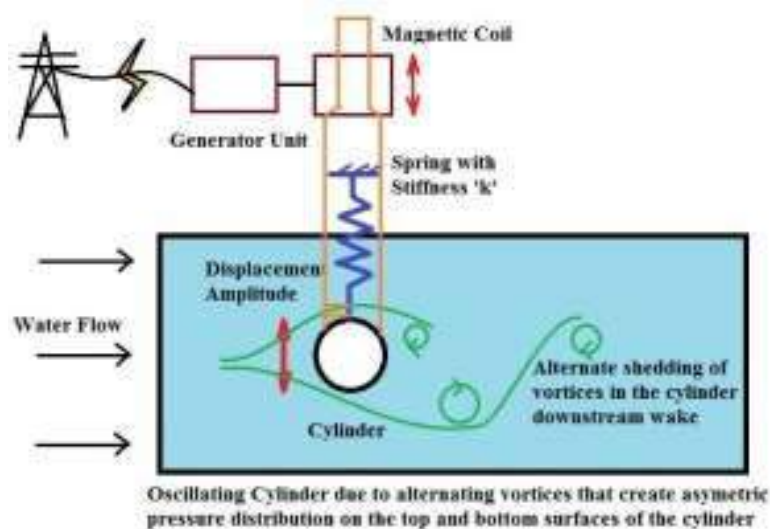


Fig.4. One-cylinder VIVACE convertor unit

A total of six simulations are monitored. Flow velocities of 0.15 m/s, 0.3 m/s and 0.6 m/s are used for 125 N/m spring stiffness and 0.2 m/s, 0.4 m/s and 0.6 m/s are used for 250 N/m spring stiffness.

Simulation 2-2 is selected and presented in Section III as an example to illustrate the lift coefficient variation with time, dynamic mesh deformation, velocity contours and displacement, velocity and power curve with time.

The summary of all the simulations is presented in results and discussions in section IV.

I. Results of Simulation-2-2

Sim 2-2 is run with a spring stiffness of 250 N/m and flow velocity of 0.4 m/s. Lift Coefficient stabilized at approximately 4 s and fluctuates between -0.65 to +0.65 approximately as shown in Fig.5 indicating the fluctuating forces generated on the cylinder due to alternate shedding of vortices on top-half and bottom-half semi-surfaces of the

cylinder. The contours of dynamic mesh deformation when the cylinder is at bottom extreme oscillation are shown in Fig.6 respectively. The Von-Karman vortex street developed in the wake of the oscillating cylinder is captured by the velocity contours shown in Fig.7. at bottom extreme of the cylinder.

The instantaneous values of lift force in N and instantaneous values of cylinder displacement amplitude in cm are plotted on a timescale as shown in Fig.8.

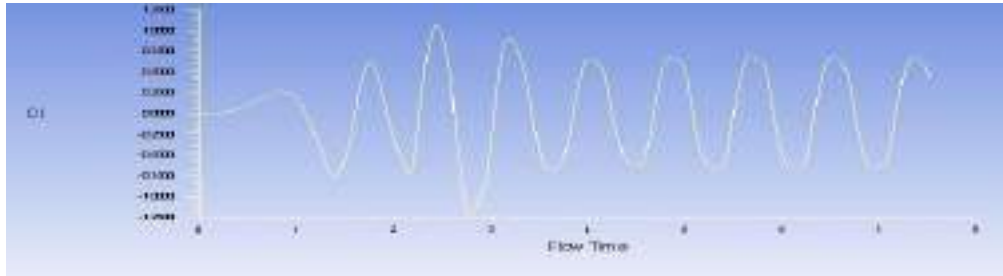


Fig.5. Lift Coefficient vs. Time - Simulation 2-2.

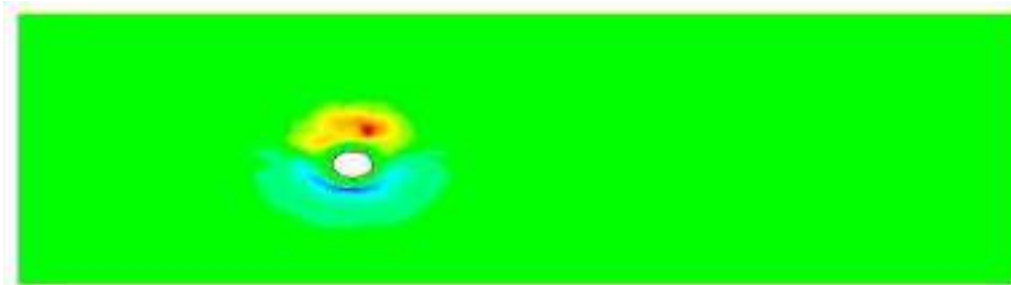


Fig.6. Dynamic cell volume change - bottom extreme point.

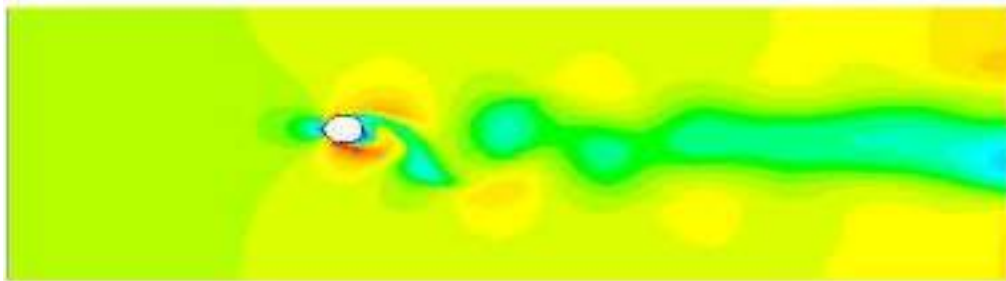


Fig.7. Velocity Contours (m/s) - bottom extreme point.

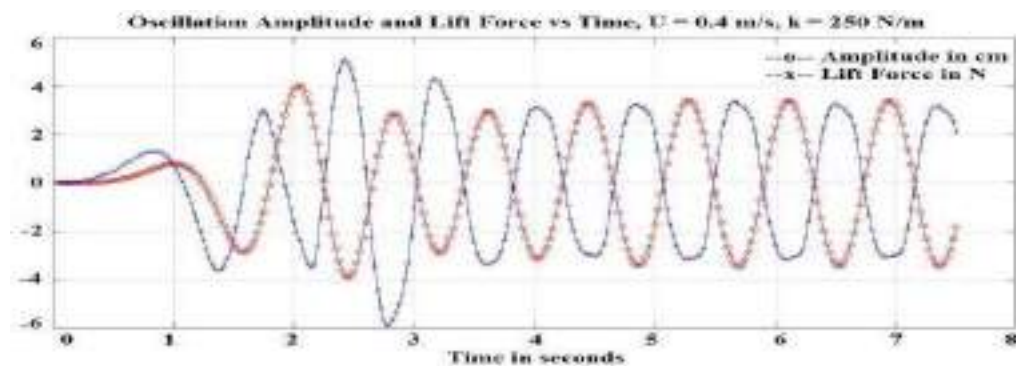


Fig.8. Oscillation amplitude and lift force versus time plot.

The power developed by the VIVACE convertor is obtained by computing the instantaneous cylinder velocity from amplitude data from time differentiation function in MATLAB. The velocity thus obtained (in m/s) is then multiplied with lift force (in N) to get the instantaneous value of mechanical power. The fluctuations of power developed, as shown in Fig.9 can be minimized by connecting 3 to 5 cylinders to the generator common line

Hence the RMS value of power as obtained from Fig.9 (excluding the beginning 3 s of instability) which is 0.3485 watts is considered as the capacity of the VIVACE convertor unit at a water flow velocity of 0.4 m/s assuming that the fluctuations of power would be compensated to a constant value by installing a group of oscillating cylinders.

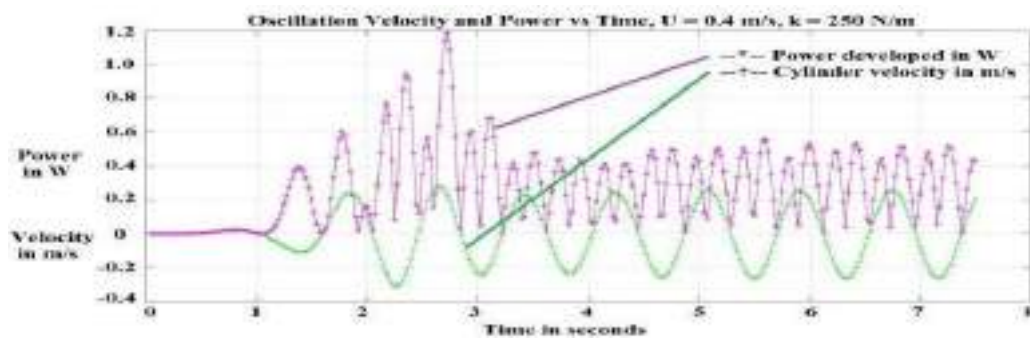


Fig. 9. Cylinder velocity and Power developed versus time

II. Results and Discussion

The simulation results are presented in Table-3. The variation of oscillation amplitude / cylinder diameter (A/D) with Reynolds number is shown in Fig.10 and with reduced velocity is shown in Fig 11. for spring stiffness of 125 N/m and 250 N/m. As the spring stiffness increases, the maximum amplitude shifts at a higher Reynolds number to the right. However, the peak amplitude occurs between Reduced velocity (U^*) of 7.0 and 8.0 irrespective of the spring stiffness (both 125 N/m and 250 N/m) as in simulation results Table-3 and similar results are obtained in Goudarzi [4].

This indicates that the diameter, density, length and spring stiffness of the VIVACE convertor should be chosen such that thereduced velocity (U^*) falls in the Uc^* range of 7.0 to 8.0.

The power developed vs Reynolds number is shown in Fig.12. and power developed vs non-dimensional reduced velocity U^* is shown in Fig 13.

7.

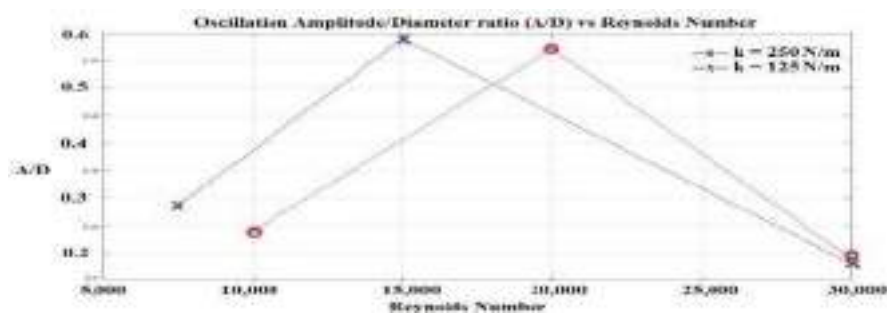


Fig.10. A/D ratio versus Reynolds number.

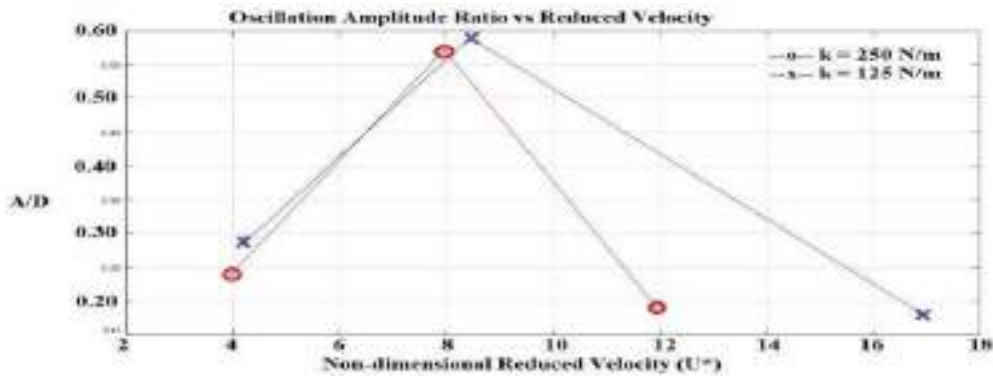


Fig.12. Power developed (in W) versus Reynolds Number.

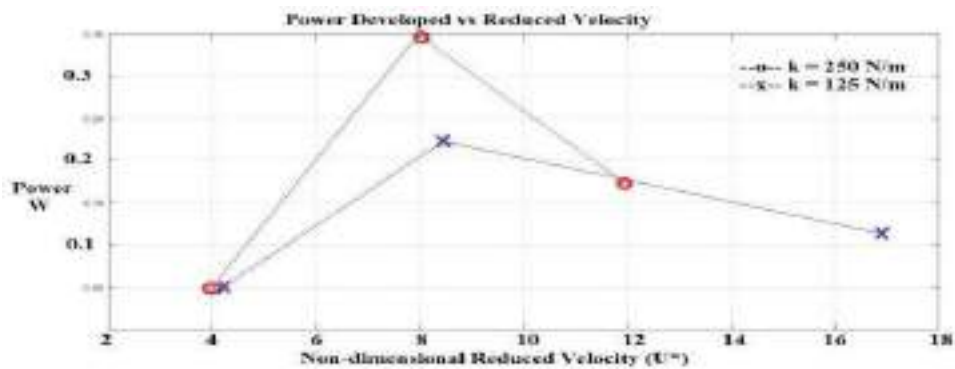


Fig.13. Power Developed (in W) versus U^* .

It is evident from Fig 12 and 13 that the power developed increases with increase in the spring stiffness.

Table 2 summarizes the results for each simulation case. Percentage variation of amplitude is least (11.59% and 8.75%) when U^* is in the vicinity of 7.0 to 8.0 and outside this range the percentage variation of amplitude between successive cycles is as large as 131.46 %. The amplitudes versus time for each value of U and U^* are shown in Fig.14. for $k = 250$ N/m respectively.

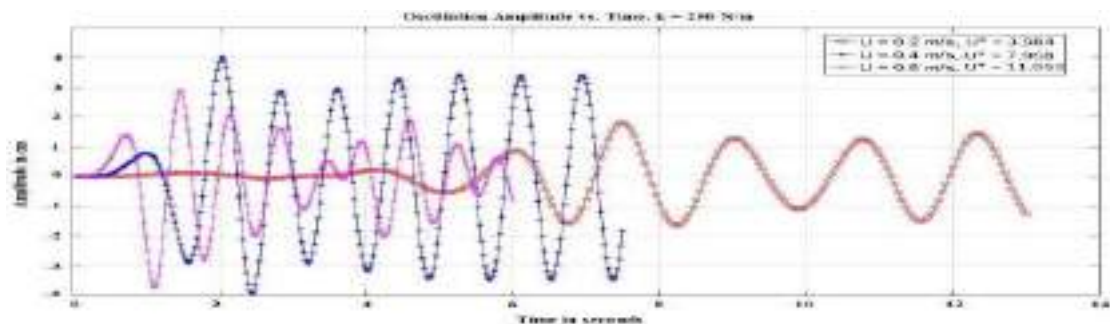


Fig.14. Oscillation amplitude versus time, $k = 250$ N/m

Table 2. Simulation Results

Sim No.	f_{str} (Hz)	f_{osc} (Hz)	f_n (Hz)	$f^* = f_{osc}/f_n$	$U^* = U/FnD$	C_L	Average Amplitude (cm)	A/D	Power Developed (in W)	% variation of amplitude	Oscillation amplitude stability
1-1	0.500	0.501	0.5915	0.8469	4.226	2.320	1.720	0.2866	0.0507	70.93%	Unstable
1-2	1.000	0.833	0.5915	1.4082	8.453	0.561	3.535	0.5891	0.2227	11.59%	Stable
1-3	2.000	1.742	0.5915	2.945	16.906	0.522	1.093	0.1822	0.1132	131.46%	Unstable
2-1	0.666	0.6218	0.8366	0.7432	3.984	1.714	1.447	0.2411	0.0489	62.8%	Unstable
2-2	1.333	1.1928	0.8366	1.4257	7.968	0.666	3.426	0.5711	0.3485	8.75%	Stable
2-3	2.000	1.6129	0.8366	1.9279	11.953	0.460	1.145	0.1908	0.1729	86.38%	Unstable

The theoretical relations that can be used to monitor the power developed are elaborated as follows: Power = Force x Velocity

$$= [C_L \cdot (A/D) \cdot 2\pi f^0 \cdot (0.2) \cdot \sin(\omega_{osc}t) \cdot \cos(\omega_{osc}t + \pi)] \times [1/2 \cdot \rho \cdot D \cdot L \cdot U^3] \quad (7)$$

So the efficiency can be formulated as :

$$\eta = [C_L \cdot (A/D) \cdot 2\pi f^0 \cdot (0.2) \cdot \sin(\omega_{osc}t) \cdot \cos(\omega_{osc}t + \pi)] \quad (8)$$

The maximum value of $\sin(\omega_{osc}t) \cdot \cos(\omega_{osc}t + \pi)$ is **0.5**.

0.4089 W and is close to the peak power of **0.5 W** in Fig. 13.

From equation (8) an **efficiency of 21.3 %** is obtained which is close to **22% efficiency** obtained in experimental tests [1] [2] and thus it can be concluded that lift coefficient (C_L), oscillation amplitude ratio (A/D) and the ratio between f_{osc} to f_{str} (f^0) are the key factors that contribute for efficiency of the convertor. Comparison is given in Table 3.

Table 3 : Comparison of Efficiency and Power data

Parameter	Theoretical	Simulation	Experimental
Efficiency	21.3 %	-	22 % [1][2]
Power	0.4089 W	0.5 W	-

V. Conclusion

The monitoring of the VIVACE cylinder is expressed in:

- i. Oscillation amplitude (A) and oscillation amplitude ratio (A/D)
- ii. Coefficient of lift force (C_L)
- iii. Ratio between f_{osc} and f_{str} (f^0)
- iv. Stability in oscillations from cycle to cycle
- v. Stability in power generated
- vi. Non-dimensional reduced velocity (U^*)

References:

1. VIVACE (Vortex Induced Vibration Aquatic Clean Energy): A New Concept In Generation Of Clean and Renewable Energy from Fluid Flow”, Bernitsas and Ragavan et.al., *OMAE 2006, 25th International Conference on Offshore Mechanics and Arctic Engineering (2006)*, and *Journal of Offshore Mechanics and Arctic Engineering*, ASME Transactions, (2008), Vol. 130, No. 4, pp. 041101-15. DOI: [10.1115/OMAE2006-92645](https://doi.org/10.1115/OMAE2006-92645)
2. “The VIVACE Converter: Model Tests at Reynolds Numbers Around 10^5 ”, Bernitsas and Raghavan, *OMAE 2006; and Journal of Offshore Mechanics and Arctic Engineering*, ASME Transactions, (2009), Vol. 131, No. 1, 1-13. DOI: [10.1115/1.2979796](https://doi.org/10.1115/1.2979796)
3. “Experimental investigation of Reynolds number effect on vortex induced vibration of rigid circular cylinder on elastic supports”, Bernitsas and Raghavan, *Ocean Engineering* 38 (2011) 719–731. DOI: [10.1016/j.oceaneng.2010.09.003](https://doi.org/10.1016/j.oceaneng.2010.09.003)
4. “Experimental Investigation of Reynolds number and spring stiffness effects on vortex induced vibrations of a rigid circular cylinder”, Goudarzi et.al., *European Journal of Mechanical/ B Fluids* 74 (2019) 34-40. DOI: [10.1016/j.euromechflu.2018.10.016](https://doi.org/10.1016/j.euromechflu.2018.10.016)
5. “Extracting energy from Vortex-Induced Vibrations: A parametric study”, Antonio Barrero et.al., *Applied Mathematical Modelling* 36 (2012) 3153–3160. DOI: [10.1016/j.apm.2011.09.085](https://doi.org/10.1016/j.apm.2011.09.085)
6. “The Effects of Spring Stiffness on Vortex-Induced Vibration for Energy Generation”, Zahari et. al., *CUTSE 2014, IOP Conf. Series: Materials Science and Engineering* 78 (2015) 012041. DOI: [10.1088/1757-899X/78/1/012041](https://doi.org/10.1088/1757-899X/78/1/012041).

Vibration analysis of an Underwater Pipeline Conveying Fluid with varying cross-section

Bala Murugan S, R K Behera, Prajjwal Anuragi

*Department of Mechanical Engineering,
National Institute of Technology Rourkela, Rourkela*

Abstract

The use of fluid-conveying pipes in engineering applications can be found in a variety of structural systems. In the case of dynamic model analysis with fluid-structure interaction (FSI) for structures in the fields of aerospace, Biomedical, and aerodynamics engineering had numerous applications. The various industrial applications in India have a vast network with non-uniform pipelines. This paper carries the vibration analysis of a non-uniform underwater pipeline with both ends fixed boundary conditions. The mathematical model is carried out using theoretical analysis. The simulation was carried out with the help of the commercial package MATLAB[®] application. The stability of the fluid in the varying cross-section is the key factor in the residual stress generation. This study focuses on the expansion and contraction effects on the pipe caused by the external force and the residual stresses. An understanding of such unstable system behaviour is required for improving the system design and analyzing the damage effects. Further, future work would focus on experimental studies.

Keywords: *non-uniform pipeline, vibrational analysis, stability, residual stress*

1. Introduction

Pipes conveying fluids are an important research subject of interest for engineers due to its widely usage in engineering applications. Pipes used in transferring fluids between equipment like in the petrochemicals processes, Fertilizer's plant, and transferring fluids for a long distance like LPG pipelines, and water pipelines between cities. In most practices pipes are exposed to vibrations caused by rotary equipment like pumps, compressors, and by wind. Also, pulsating fluid flow causes vibration which affects pipe material. These fluid forces affect the pipe and cause problems like pipe failure and plant shutdown which means money loss. So, it must be considered during the process of pipe system design. The most common configuration of a straight pipe with variable cross-sections conveying a steady-state flow with constant flow-rate and mounted on rigid supports carrying a steady flow with a constant velocity.

Stein and Togriner [1], worked on numerical solution for the equation of motion that represents the behaviour of an elastic material supported pipe of infinite length transporting an ideal pressured fluid is presented, as well as a fresh interpretation of the effects caused by internal pressure forces. Chen [2] presented a linear theory to account for the motions of extensible curved pipes conveying fluid. The natural frequency is also studied, and it is shown that with rising flow velocity, the frequency lowers. Ismael et al [3] studied the behaviours of an annular pipe transporting fluid were characterised using the transfer matrix approach. The dynamics behaviour is estimated for any point located along the annular pipe, which is separated into nodes and elements, considering the type of support and heat flux range from for different flow rate levels. Wang and Bloom [4], carried out research topic related directly to the concentric pipe system designs in silo or other mixing

units. They carried the mathematical model with Floquet evaluation method for the pulsatile flow case, and they discover that for current pipe system designs with acceptable flow rates, and the concentric pipe system is stable. Zhang et al [5] developed a mathematical model with moving pipes and flowing fluid using the Eulerian method. The effect of initial axial strain and fluid flow on the dynamic behaviour of the system is explored. Fernad et al [6] provide a simplified approach for determining the fundamental frequency of bending vibrations in fractured Euler- Bernoulli beams. The fundamental frequency is calculated using the Rayleigh approach and the approach yields closed-form formulas for the fundamental frequency in the given example. Comparing with simulation results confirms its validity Simha and Kameswara [7] created a finite element programme for rotationally constrained long tubes with internal flow that are supported by a Winkler foundation. Using the finite element method, the dynamic response of linear Bernoulli-Euler pipes rotationally controlled at either end was investigated.

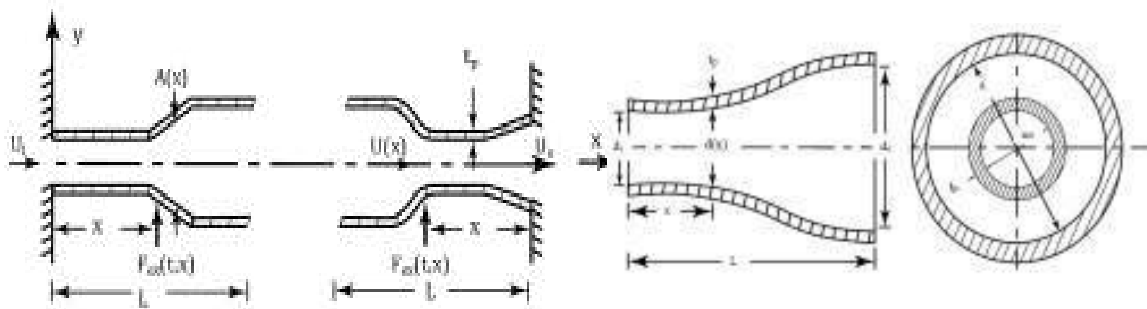
Aldraihem and Baz [8] carried out research on the stability analysis and responses of stepping tubes exposed to a stream of moving objects. The accuracy of the result is demonstrated by calculating the stability bounds of simply supported tubes and comparing the results to those described in the literature. Reddy and Wang [9] used the dynamic version of the concept of virtual displacements to derive a comprehensive system of equations of motion regulating fluid-conveying beams. The study carried for both the Euler - Bernoulli and Timoshenko beam theories, accounting for von Karman nonlinear strain, rotational inertia, forces related to the fluid flow in the beam, and kinetic energy of the flowing fluid. Yoon and Son [10] investigated the influence of an open crack and a moving mass the dynamic characteristics of a fluid-conveying pipe that is simply supported. The mathematical expression is calculated using Lagrange's equation and numerically analysed. Olunloyo et al [11] studied the energy technique and used to derive the system of equations, which contained the effects of temperature variation along the length of prestressed and pressured pipe. Yoon et. al. [12] studied the dynamic characteristics of double cracked simply supported beam. Frequency response of a simply supported beam with double cracks is measured by experiments. They find that when the crack positions are constant, the natural frequencies of a simply supported double-cracked beam are inversely proportional to the crack depth. Amabili et al. [13] studied the dynamic behaviour and instability of simply supported, circular cross section shells with in viscid incompressible fluid flow. The results reveal that divergence causes the system to lose stability.

2. Mathematical Modelling

In this chapter, a mathematical model is formulated by developing equations for the motion of a straight variable cross-section fluid conveying pipe fixed from both ends and these equations are to be solved for the response to forced sinusoidal excitation.

2.1 Equations of motion

Consider a pipe with a variable cross-section $A(x)$, a length L , an elastic modulus E , and a second moment of area $I(x)$. A fluid flows through a pipe with a density ρ_f (see Figure 1), and the pipe vibrates as a result of an exciting force $F_{ex}(t, x)$. Figure (2) shows the forces acting on fluid and pipe elements.



Layout of pipe (a) expansion, (b) contraction (c) Pipe geometry

Fig. 1: Layout of acting force and pipe geometry.

Resolving the forces on fluid element along and perpendicular to the tangent to the center line of the deflected element the following equation is obtained:

$$(AP + \frac{1}{2} \frac{\partial(AP)}{\partial x} \delta x) - (AP - \frac{1}{2} \frac{\partial(AP)}{\partial x} \delta x) + qS\delta x = 0 \quad (1)$$

Balancing the forces in the Y direction on the Fluid element for small deformation gives,

$$F\delta x - \rho_f A a_y + \left[\left(-PA \frac{\partial y}{\partial x} \right) + \frac{1}{2} \frac{\partial}{\partial x} \left(-PA \frac{\partial y}{\partial x} \right) \delta x \right] - \left[\left(-PA \frac{\partial y}{\partial x} \right) - \frac{1}{2} \frac{\partial}{\partial x} \left(-PA \frac{\partial y}{\partial x} \right) \delta x \right] \quad (2)$$

Equation (2) gets the final form as,

$$F - \rho_f A a_y - PA \frac{\partial^2 y}{\partial x^2} = 0 \quad (3)$$

The forces on the element of the pipe normal to pipe axis accelerate the pipe in Y direction element (see Fig. 2 (b)). For small deformations:

$$\begin{aligned} & - \left(Q - \frac{1}{2} \frac{\partial Q}{\partial x} \delta x \right) + \left(Q + \frac{1}{2} \frac{\partial Q}{\partial x} \delta x \right) - \left(T \frac{\partial y}{\partial x} - \frac{1}{2} \frac{\partial}{\partial x} \left(T \frac{\partial y}{\partial x} \right) \delta x \right) + \left(T \frac{\partial y}{\partial x} - \frac{1}{2} \frac{\partial}{\partial x} \left(T \frac{\partial y}{\partial x} \right) \delta x \right) \\ & + F_{ex} \delta x - F\delta x - \rho_p A_p \frac{\partial^2 y}{\partial t^2} \delta x = 0 \end{aligned} \quad (4)$$

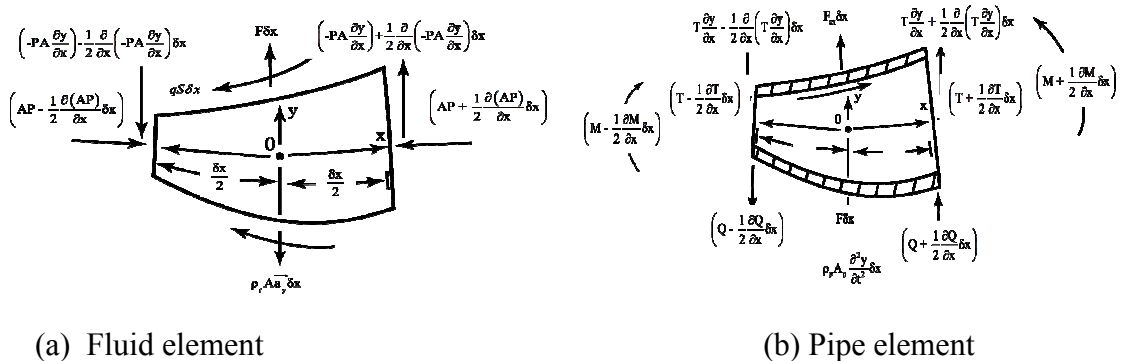


Fig. 2: Moments and forces exerted on element

Reducing F from Eq. (3) we get,

$$E \frac{\partial^2}{\partial x^2} \left(I \frac{\partial^2 y}{\partial x^2} \right) + (\rho_f A U^2 + P A - T) \frac{\partial^2 y}{\partial x^2} + (\rho_p A_p + \rho_f A) \frac{\partial^2 y}{\partial t^2} + (2U \rho_f A) \frac{\partial^2 y}{\partial x \partial t} = F_{ex} \quad (5)$$

Since Q is proportional to $\frac{\partial^3 y}{\partial x^3}$ the third term of Eq. (4), can be neglected, hence we get,

$$\frac{\partial}{\partial x} (P A - T) = 0, \text{ and here, } (P A - T) = \text{constant}$$

2.2 Calculation of Pipe Area (A_p)

Where d is inner diameter, d_i is inlet inner diameter, d_o is outlet inner diameter, t_p is thickness area, A_p outer area, A is inner area and A_i is inner area at inlet. Geometry is given in Fig. 1(c). The area of the pipe is to be calculated from:

$$A_p = \frac{\pi}{4} (d + 2t_p)^2 - \frac{\pi}{4} d^2 \quad (6)$$

$$\text{Since, } t_p \ll \frac{d_i}{2}, \quad A_p = \frac{\pi}{4} \left[\frac{4t_p}{d(x)} \right] [d(x)]^2 = A \frac{d_i}{d(x)} \left[\frac{4t_p}{d_i} \right] \quad (7)$$

$$P A - T = P_i A_i - T \quad (8)$$

2.3 Dimensionless variables

$$x^* = \frac{x}{L}, \quad y^* = \frac{y}{L}, \quad A^* = \frac{A}{A_i}, \quad A_p = 4A^* \frac{t_p^*}{d^*} \text{ or } \frac{A_p}{A_i}, \quad d_o^* = \frac{d_o}{d_i}, \quad d^* = \frac{d(x)}{d_i}, \quad t_p^* = \frac{t_p}{d_i},$$

$$\text{Since, } n = \frac{A_i}{A_o}, \text{ we get } n = \frac{1}{A_o^*} = \frac{1}{(\pi/4) d_o^{*2}}$$

By substituting all dimensionless terms in Eq. (5) gets the final form as,

$$\frac{\partial^2}{\partial x^{*2}} \left(I^* \frac{\partial^2 y^*}{\partial x^{*2}} \right) + (A^* U^{*2} + P^* A^* - T^*) \frac{\partial^2 y^*}{\partial x^{*2}} + A^* \alpha \frac{\partial^2 y^*}{\partial t^*} + 2U^* A^* \beta^{1/2} \frac{\partial^2 y^*}{\partial x^* \partial t^*} = F_{ex}^* \quad (9)$$

The exciting force F^* is a function of x^* and t^* . Hence, for sinusoidal excitation, the dimensionless exciting force may be put in the following form:

$$F_{ex}^* = F_{ex}^*(x^*, t^*) \quad (10)$$

$$F_{ex}^* = f^*(x^*) e^{(i\Omega t^*)} \quad (11)$$

Let $y^* = Y(x^*)e^{i\Omega t^*}$, and $Y(x^*)$ is the complex dimensionless amplitude.

We know: $Y(0) = Y(1) = 0$ and $\frac{dY}{dx^*}|_{x^*=0} = \frac{dY}{dx^*}|_{x^*=1} = 0$. Let $Y = y_r + iy_i$, Hence we get,

$$\frac{d^2}{dx^{*2}} \left(I^* \frac{d^2 y_i}{dx^{*2}} \right) + (A^* U^{*2} + P^* A^* - T^*) \frac{d^2 y_i}{dx^{*2}} - \Omega^2 A^* \alpha y_i + 2i\Omega U^* A^* \beta^{1/2} \frac{dy_r}{dx^*} = f^* \quad (12)$$

Assume

$$C_1 = \frac{2}{I^*} \frac{dI^*}{dx^*}; C_2 = \frac{1}{I^*} (A^* U^{*2} + \lambda + d^2 I^* dx^{*2}); C_3 = \Omega^2 \frac{A^*}{I^*} \alpha; C_4 = 2\Omega U^* \frac{A^*}{I^*} \beta^{1/2}; C_5 = \frac{f^*}{I^*}$$

Hence, the Eq. (12) becomes,

$$y_r'''' + C_1 y_r'''' + C_2 y_r'' - C_3 y_r - C_4 y_i' = C_5 \quad (13)$$

$$y_i'''' + C_1 y_i'''' + C_2 y_i'' - C_3 y_i - C_4 y_r' = 0 \quad (14)$$

The dimensionless velocity U^* can be given as,

$$U^* = U \left(\frac{L \rho_f A_i}{EI_i} \right)^{1/2}, \text{ here } U = \frac{Q_f}{A} = \frac{Q_f}{A^* A_i}, \text{ Hence } U^* = \frac{Q_f L}{A^* A_i} \left(\frac{\rho_f A_i}{EI_i} \right)^{1/2}, U^* = \frac{Q_f^*}{A^*} \quad (15)$$

The dimensionless second moment of inertia I^* can be given as,

$$I^* = \frac{[(d^* + 2t_p^*)^4 - d^{*4}]}{[(1 + 2t_p^*)^4 - 1]}, \text{ here } t_p \ll \frac{d}{2}, \text{ Now, } I^* = A^* \frac{(A^{*1/2} + 2t_p^*)}{(1 + 2t_p^*)} = \frac{(A^{*3/2} + 2t_p^* A^*)}{(1 + 2t_p^*)} \quad (16)$$

Differentiating I^* w.r.t. x^* we have,

$$\frac{dI^*}{dx^*} = \left(\frac{3}{2} A^{*1/2} + 2t_p^* \right) (1 + 2t_p^*) \frac{dA^*}{dx^*}; \frac{d^2 I^*}{dx^{*2}} = \left[\left(\frac{3}{2} A^{*1/2} + 2t_p^* \right) \frac{d^2 A^*}{dx^{*2}} + \frac{3}{4} A^{*-1/2} \left(\frac{dA^*}{dx^*} \right)^2 \right] \frac{1}{(1 + 2t_p^*)}$$

2.4 Excitation force f^*

The dimensionless exciting force f^* is, $\frac{f^*}{f_{\max}^*} = n + (1 - n) [\sin(\pi x^*)]^{2m} \quad (17)$

2.5 Solution of the equations

The equations (13) and (14) are in fourth order equation so it transformed into eight first order equation using MATLAB[®] code BVP4C for solving the boundary value problem.

$$\text{Let } \begin{array}{llll} y_r = y_1, & y_r' = y_2, & y_r'' = y_3, & y_r''' = y_4 \\ y_i = y_5, & y_i' = y_6, & y_i'' = y_7, & y_i''' = y_8 \end{array}$$

$$\text{We know, } \begin{array}{llll} y_1(0) = 0, & y_2(0) = 0, & y_5(0) = 0, & y_6(0) = 0 \quad \text{at } x = 0 \\ y_1(1) = 0, & y_2(1) = 0, & y_5(1) = 0, & y_6(1) = 0 \quad \text{at } x = 1 \end{array}$$

The solution can be given in the following form as,

$$Z = \sqrt{(y_1^2 + y_5^2)}, \text{ and Vibration velocity} = \sqrt{(y_2^2 + y_6^2)}$$

The coefficients C_1, C_2, C_3 and C_4 can be expressed as,

$$C_1 = \frac{2}{I^*} \frac{dI^*}{dx^*}; C_2 = \frac{1}{I^*} \left(\frac{Q^{*2}}{A^*} + \lambda + \frac{d^2 I^*}{dx^{*2}} \right); C_3 = \Omega^2 \frac{A^*}{I^*} \alpha; \text{ and } C_4 = 2 \frac{Q^*}{I^*} \beta^{1/2} \Omega$$

3 Results and Discussion

To obtain the numerical result we have a pipe material of steel with a modulus of elasticity of 210 GPa and density of 7850 kg/m³, length L is 10 m and thickness is 12 mm. Moreover, the fluid used for study in all cases is water having a density equal to 1000 kg/m³, pressure at entrance is 2 bars and the flow velocity is 0.48 m/s. Cases having different pipe shapes are classified as pipes with expansion cross-section and pipes with contraction cross-section. The expansion or contraction area having a varying length L_i which has three values 0.01 m, 0.1 m and 0.2 m of the pipe length L . The position of expansion or contraction cross section along the pipe L_i was varied using three values 0.2 m, 0.5 m and 0.8 m of the pipe length L . Moreover, the pipe diameter ratio was studied using three ratios. These pipe shape parameters variation allowed to study of 27 expansion pipe cases and the same number of cases for contraction pipe shape to be carried out. All cases compared with straight pipe results as a reference case.

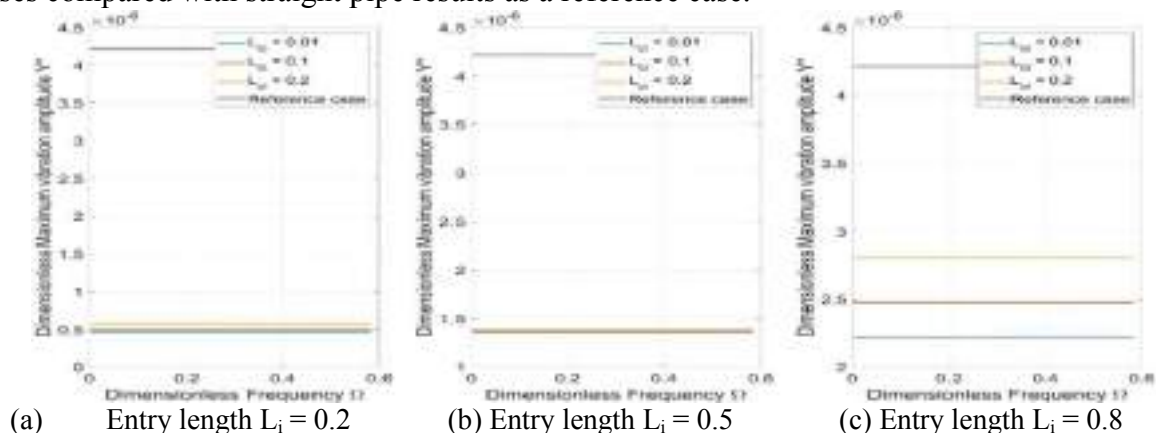
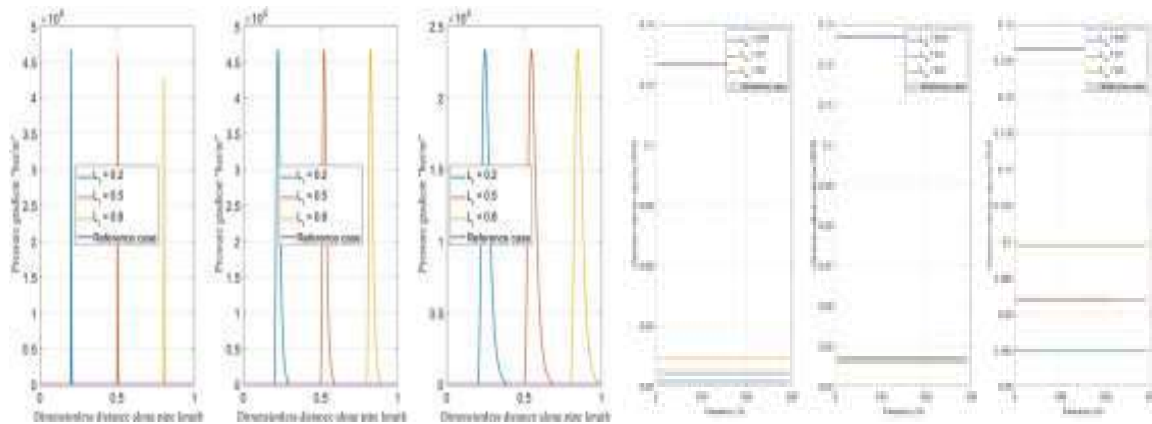


Fig. (4), Vibration amplitude Y^* versus dimensionless frequency Ω at different entry and expansion length with a diameter ratio $d_i/d_o = 0.4$

Figure (5) shows pressure gradient variation along pipe length. The Pressure gradient duration increases with increasing the expansion dimensionless length L_{ci} . An adverse pressure gradient take place over the entry expansion dimensionless length L_{ci} and it is probably the reason for increasing vibration amplitude with the expansion dimensionless length L_{ci} . Changing the entry length L_i doesn't have any similar effect on the pressure gradient, it is realized from Figs. (4) and (5) that the larger dimensionless vibration amplitude Y^* coincide with the larger L_i , is the larger. The region with zero pressure gradients is a region with constant fluid kinetic energy similar to the straight pipe values. Figure (6) shows that cases have vibration velocity within the acceptable range at all frequencies value. And all cases have vibration velocity lower that the straight pipe value.

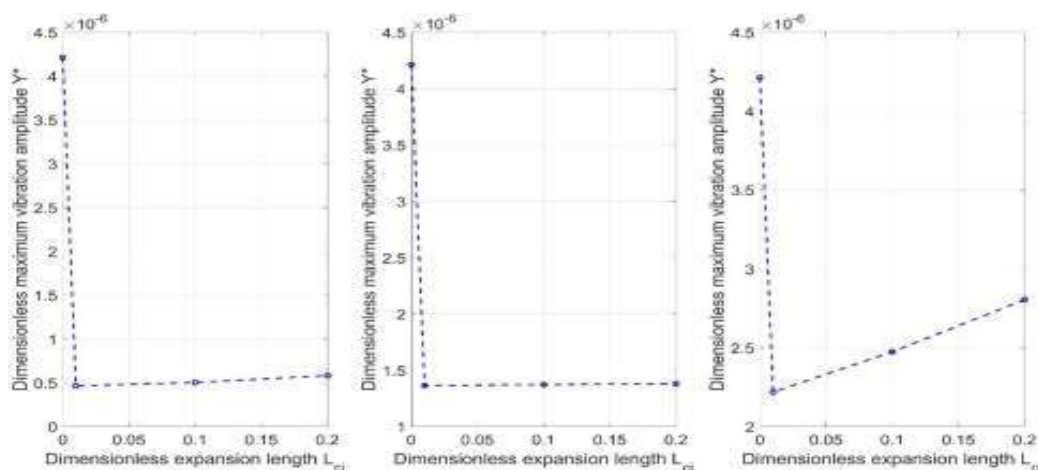


Expansion length (a) $L_{ci}=0.01$, (b) $L_{ci}=0.1$, (c) $L_{ci}=0.2$ Entry length (a) $L_i = 0.2$, (b) $L_i = 0.5$, (c) $L_i = 0.8$

Fig. (5) Pressure gradient variation with diameter ratio $(d_i/d_o) = 0.4$

Fig. (6) Vibration velocity and frequency with a diameter ratio $(d_i/d_o)=0.4$

Figure (7) shows the effect of changing expansion length L_{ci} on vibration amplitude Y^* . it is noticed that at expansion length $L_{ci} = 0$ it expresses about straight pipe. The expansion length decreases the vibration amplitude Y^* in the beginning and increases marginally.



Entry length (a) $L_i = 0.2$, (b) $L_i = 0.5$ (c) $L_i = 0.8$

Fig. (7), Effect of dimensionless expansion length L_{ci} on vibration amplitude Y^* for different expansion position with a diameter ratio $(d_i/d_o) = 0.4$

4. Conclusions

Increasing the frequency has no effect on the vibration amplitude in all cases which studied while studying expansion cases, the expansion decreasing the vibration amplitude Y^* . Also, the vibration amplitude Y^* decreased by increasing diameter ratio, increasing the dimensionless entry length L_i or decreasing the dimensionless expansion length L_{ei} . These factors have a similar effect on Vibration velocity. Pressure gradient too decreases by increasing the dimensionless expansion length L_{ei} or increasing the diameter ratio or both. So, it's clear that, the expansion should be sudden and placed at the beginning of the pipe. On the other side, contraction cases have higher vibration amplitude and vibration velocity. Many different adaptations, tests, and experiments have been left for the future which will contribute to the improvement of previous work. The following suggestions could be tested: (i) to study the effect of pipe variable geometry on its natural frequency, (ii) to carry the obtained numerical results by reliable experimental work.

Acknowledgment

The authors gratefully acknowledge financial assistance received for the study from the DST and **TIH IIT Guwahati**, Government of India (Grant No. TIH/TD/0105), with project code: SR/21/ME/080 of NIT Rourkela.

References

- [1] Stein, Robert Alfred, and M. W. Tobriner. "Vibration of pipes containing flowing fluids." (1970):
- [2] Chen, S. S. *Analysis of extensible curved pipes conveying fluid*. No. ANL-CT-75-28. Argonne National Lab., Ill.(USA), 1975.
- [3] Ismael, Kalid A., Mauwafak A. Tawfik, and Zena K. Kadhim. "A Theoretical Study of the Effect of Vibration on Heated Annulus Pipe1." *J. Chem. Phys* 74.1(1981)
- [4] Wang, Xiaodong, and Frederick Bloom. "Stability issues of concentric pipes conveying steady and pulsatile fluids. Project F004, report 7: a progress report to the member companies of the Institute of Paper Science and Technology." (1999).
- [5] Zhang, Y. L., D. G. Gorman, and J. M. Reese. "Analysis of the vibration of pipes conveying fluid." *Proceedings of the Institution of Mechanical Engineers, Part C: Journal of Mechanical Engineering Science* 213.8 (1999): 849-859.
- [6] Fernandez-Saez, J., L. Rubio, and C. Navarro. "Approximate calculation of the fundamental frequency for bending vibrations of cracked beams." *Journal of sound and vibration* 225.2 (1999): 345-352.
- [7] Simha, H., and C. Kameswara Rao. "Finite Element Analysis of Vibrations of Rotationally Restrained Fluid Conveying Pipes Resting on Soil Medium." (2001).
- [8] Ibrahim, R. A. "Overview of mechanics of pipes conveying fluids—Part I: Fundamental studies." *Journal of Pressure Vessel Technology* 132.3 (2010).
- [9] Reddy, J. N., and C. M. Wang. "Dynamics of fluid-conveying beams: governing equations and finite element models." (2004).

- [10] Yoon, Han-Ik, In-Soo Son, and Sung-Jin Ahn. "Free vibration analysis of Euler-Bernoulli beam with double cracks." *Journal of mechanical science and technology* 21.3 (2007): 476-485.
- [11] Olunloyo, Vincent OS, et al. "Dynamics and Stability of a Fluid Conveying Vertical Beam." *International Conference on Offshore Mechanics and Arctic Engineering*. Vol. 4269. 2007.
- [12] Yoon, Han-Ik, and In-Soo Son. "Dynamic behavior of cracked pipe conveying fluid with moving mass based on Timoshenko beam theory." *KSME international journal* 18.12 (2004): 2216-2224.
- [13] Amabili, M., Francesco Pellicano, and M. P. Païdoussis. "Non-linear dynamics and stability of circular cylindrical shells containing flowing fluid. Part I: stability." *Journal of sound and Vibration* 225.4 (1999): 655-699.

Performance Enhancement of Functionally Graded MEMS Accelerometer for Condition Monitoring Using Artificial Neural Network

Uttam Kumar Kar, J. Srinivas

Department of Mechanical Engineering, NIT, Rourkela, India

Abstract

The functionally graded micro electro mechanical system (FG-MEMS) sensors are widely used in various industrial applications due to its low power consumption, high sensitivity and high resolution. Recently, these sensors are being used in monitoring the condition of the machinery, dynamic certification of any intended structural components, fault prediction, structural ageing issues, and various other structural dynamics research and diagnostics. The design of such devices is challenging for engineers, since its performance depend on many parameters. To solve this problem, the present work investigated the optimal design parameters of FG-MEMS sensor to improve their performance, resolution and reliability in condition monitoring. In order to obtain the effective material and geometrical parameters of FG-MEMS sensor, a surrogate optimization methodology with artificial neural network (ANN) function estimation model is proposed. The material properties are graded using generalized power law model and modified couple stress theory is employed to capture the size effects. Finally, a case study of beam crack detection using FG-MEMS accelerometer is demonstrated.

Keywords : *FG-MEMS sensor; Condition monitoring; Artificial neural network; Optimization.*

1.Introduction

In recent years, the vibration measurement technique has been extensively used in condition monitoring of various machines[1], dynamic qualification of newly designed structural components[2], faults detection and other aging-related issues in structural components [3]. Due to their low cost and compact size, MEMS sensors and accelerometers have recently attracted attention in condition monitoring. Because of the extensive integration process, MEMS' intrinsically tiny size enables high-level functionalities. Capacitive MEMS accelerometers have wide scope in condition monitoring applications. Optimum design and material selection are the key issues in modeling for improving the performance of such accelerometer. Engesser et. al.[4] targeted to minimize the footprint area of the device, and proposed several techniques to more easily find the global minimum of optimization problems including MEMS sensors. Wang et. al. [5] proposed a design methodology using genetic algorithm (GA) with freeform geometry to enhance the sensitivity, fabrication tolerances and band width of MEMS devices. Similarly, many optimization studies have been reported in the literature to improve the performance of micro sensors [6,7]. Recently, Gu et al. [8] proposed a mode identification algorithm and machine learning (ML) technique to predict the modal shape and physical behaviour of micro-resonators. They concluded that the proposed ML-based methodology has great potential to enhance the accuracy of MEMS sensors. Sometimes the material of the micro cantilever of MEMS devices is the critical factor to improve its performance and reliability [9]. Traditionally silicon or polysilicon has been used for the fabrication of micro sensors due to its special features. Currently, functionally graded (FG) material emerges a new kind

of material for micro scale devices. Several studies on FG micro beams [10–13] and micro plates [14–16] have been found in the literature.

From the literature, a limited work has been observed on improving the performance of FG MEMS sensors/accelerometers in fault diagnosis and condition monitoring. Therefore, the present work attempted to fill this gap and proposed a novel design methodology of FG MEMS sensors to improve their performance in condition monitoring. Initially, parametric studies are carried out to understand the effects of geometrical and material parameters on the sensitivity and resolution of the capacitive accelerometer with proof mass supported with FG beam suspensions. Furthermore, a trained multi-layer perceptron neural network is used to store the relationship between the input-output features as a nonparametric model. To enhance the sensitivity, the optimum material and geometric parameters are ultimately found. The firefly optimization method with a neural network-based function estimate module are used to obtain the results.

2. Mathematical Modeling

A schematic of a capacitive MEMS accelerometer is shown in Fig. 1.

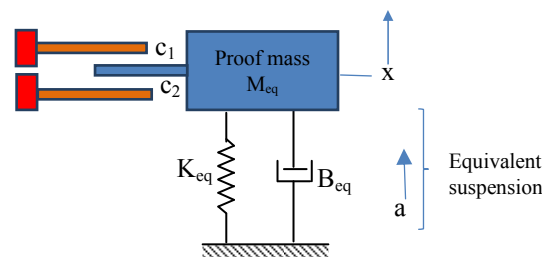


Figure 21 Capacitive accelerometer with moving mass and fixed fingers

The central part of the accelerometer is a suspended micromechanical proof mass by connecting with folded beams through anchors. The proof mass will move relative to the moving frame of reference, which serves as the sensing element, when an external acceleration is applied. By measuring the difference in capacitance (differential capacitance) between the moving finger of the proof mass and the nearby fixed electrodes, the displacements of the proof mass using the capacitive sensing approach are detected.

2.1 Material Modeling

The equivalent stiffness, damping and mass of the system is first obtained. The folded beams are made of functionally graded material consisting of Silicon carbide (SiC) as phase-1 and aluminium (Al) at phase-2 constituents with variable volume fraction distributions along length and thickness directions. The mechanical and physical properties such as elastic constant (E), Poisson's ratio (ν) and mass density (ρ) are graded in both x and z directions separately with modified power law. The modified mixture rule for effective material properties is proposed as:

$$P_{eff}(x, z) = P_1(V_1(x, z)) + P_2(V_2(x, z)) \quad (1)$$

Where P_1 and P_2 are the material properties of two constituent phases (Al and SiC), V_1 and V_2 are volume fractions of the aluminum and silicon carbide, such that

$$V_1(x, z) + V_2(x, z) = 1 \quad (2)$$

The volume fraction V_2 is calculated by the bi-directional power law distribution as

$$V_2(x, z) = \left(\frac{1}{2} + \frac{z}{h}\right)^{n_z} \left(\frac{x}{L}\right)^{n_x} \quad (3)$$

where, n_z and n_x are the volume fraction indices along the thickness and axial directions respectively. The eq. (1) can be simplified in terms of V_2 as

$$P_{eff}(x, z) = (P_2 - P_1) V_2 + P_1 \quad (4)$$

2.2 Accelerometer model

The dynamic model of the micro-accelerometer includes equivalent stiffness (K_{eq}) and mass (M_{eq}) of the springs, micro beams, and proof mass. Effective damping (B_{eq}) is provided between the micro beams. The simplified governing equation of motion of MEMS accelerometer can be written as [17]:

$$M_{eq}\ddot{x} + B_{eq}\dot{x} + K_{eq}x = M_{eq} a_{ext} \quad (5)$$

Where, x is the vibration displacement of micro beam. Also, a_{ext} indicates the input acceleration. There are four folded beam acting as four parallel springs in the system. Therefore equivalent mass, stiffness and damping can be expressed as [17–19]:

$$M_{eq} = \rho_m h_m b_m L_m + n_f \rho_f h_f b_f L_f + 4\rho_b h_b b_b L_b \quad (5a)$$

$$K_{eq} = (Gl^2 + 1) \frac{2E_b h_b b_b^3}{L_b^3} \quad (5b)$$

$$B_{eq} = n_f \mu_{eff} L_f \left(\frac{h}{g_0^3}\right) \quad (5c)$$

Where n_f is the number of moving fingers used on suspending proof mass, μ_{eff} is effective viscosity of air, G is shear modulus, l is length parameter, g_0 is nominal gap. L , b and h indicate length, width and thickness. Subscript m , f and b are used for proof mass, fingers and micro beam of MEMS system, respectively.

2.3 Performance of MEMS accelerometer

Generally, the performance of the micro sensor is observed based on the two factor, resolution and sensitivity of the system. The resolution of the MEMS accelerometer can be defined as the minimum detectable change in acceleration of the system. It can be expressed as [17]:

$$\text{Resolution } (\varphi) = a_{min} = \frac{K_{eq} d_{c1} \delta^2}{2M_{eq} c_1 (\delta^2 - 1)} \Delta c_{min} \quad (6)$$

Where $\delta = \frac{d_{c2}}{d_{c1}}$, d_{c1} and d_{c2} are the gaps of the capacitor 1 and capacitor 2 from the FG micro beam. $c_1 = \frac{\epsilon A}{g_0}$ is the capacitance of capacitor-1 and Δc_{min} is the induced capacitance change due to movement of movable finger. Similarly, sensitivity of the micro system can be expressed as [20]:

$$\text{Sensitivity (S)} = \frac{x}{a} = \frac{1}{\omega_r^2} = \frac{M_{eq}}{K_{eq}} \quad (7)$$

3. Results and discussions

A Matlab program has been developed to perform a parametric study of the MEMS accelerometer. Initially, the influence of different material and geometrical parameters on the sensitivity and resolution of micro sensor are illustrated in detail. The axial grading index value ($n_x = 0.2$) is kept constant for each investigation. The constant values of various parameters are considered as [17,20]: $L_m = 200\mu\text{m}$, $b_m = 80\mu\text{m}$, $h_m = 6\mu\text{m}$, $L_f = 160\mu\text{m}$, $b_f = 3\mu\text{m}$, $h_f = 6\mu\text{m}$, $n_f = 22$, $g_0 = 3\mu\text{m}$, $d_{c1} = 4\mu\text{m}$ and $d_{c2} = 40\mu\text{m}$. Figure 2 shows the effect of micro beam length (L_b) and grading index (n_z) on the resolution and sensitivity of micro system. The increment of both L_b and n_z leads to reduce the resolution of micro accelerometer. On the other hand with the increase of both beam length and material grading, sensitivity of the micro sensor increases gradually.

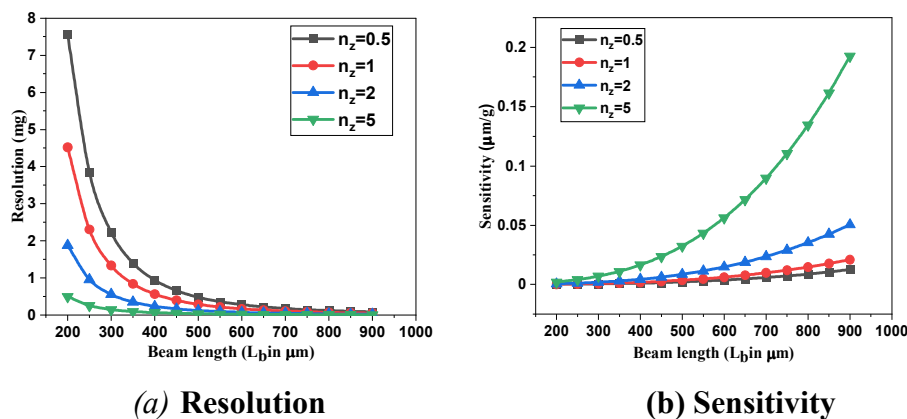


Figure 22 Influence of beam length and material gradation on the performance of micro accelerometer

It is observed that increment of n_z value and lengthening of the micro beam increases the sensitivity, but it is fact that beyond certain value, it would induce adhesion between the electrodes due to lower value of stiffness, consequently harm the stability of micro system. Therefore, it is concluded that material grading index and beam length are very critical parameter for the performance improvement of micro accelerometer.

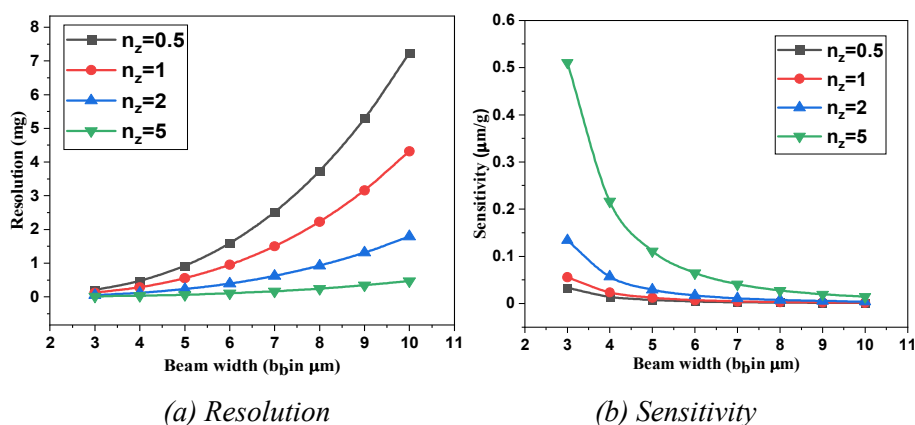


Figure 23 Influence of beam width and material gradation on the performance of micro accelerometer

Figure 3 shows the effect of micro beam width (b_b) and grading index (n_z) on the resolution and sensitivity of micro system. Increasing b_b value, from $3\mu\text{m}$ to $10\mu\text{m}$ increases the

resolution of micro accelerometer. On the other hand with the increase of material grading from 0.5 to 5, resolution decreases. Similarly, sensitivity is also significantly affected by beam width and material gradation. However, fabrication of micro system with lower beam width is very difficult. Even if fabrication is possible, the beam can easily break during measurement of external acceleration. Therefore, in order to improve the performance of the micro-accelerometer, it is essential to investigate the optimal value of the beam width and material grading index.

3.1 Performance optimization of MEMS accelerometer

From the parametric studies, it is noticed that performance of micro accelerometer significantly affected by various geometrical and material parameters. Therefore, it is necessary to determine the optimum parameters to maximize the resolution (f_1) and sensitivity (f_2) of MEMS accelerometer. For this purpose, A number weighted for the multi-objective functions was inserted into a single-objective scalar function for solving the MOO problem. Most of the optimization problems are generally formulated as a minimization problem. Therefore, Based on the weighted sum approach, the optimization problem can be formulated as follows:

$$\begin{aligned} \text{Minimize } F(Z) &= -(w_1 f_1(z) + w_2 f_2(z)) \\ \text{Subject to } Z &\in \{Z_{min}, Z_{max}\} \end{aligned} \quad (8)$$

Where $Z = [n_z, L_b, b_b]$ are the design variables, w_1 and w_2 are the weight factors for two objectives and Z_{min}, Z_{max} are the lower and upper limit on variables.

3.2 Artificial neural network model

By using the search capability of the optimization algorithm and using neural network function evaluation trained in the surrogate model framework, the optimal parameter can be found. Simulating complex issues are often solved using artificial neural networks (ANN). A well-known feed-forward ANN architecture that uses hidden layers to connect inputs and outputs is the Multilayer Perceptron (MLP). In present work, beam length, beam width and grading index are considered as input of the neural network and sensitivity and resolution are taken as output of the network. Here, all 27 (3 factor 3 level) experimental results are used for training the model. The 3-10-2 architecture model with 464 epochs gives minimum mean square error. The regression map (R^2 value) and performance plot is shown in Fig. 4(a) and Fig. 4(b), respectively.

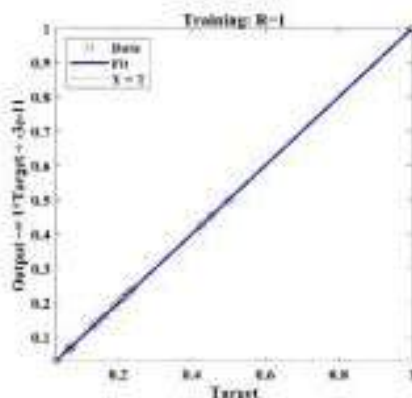
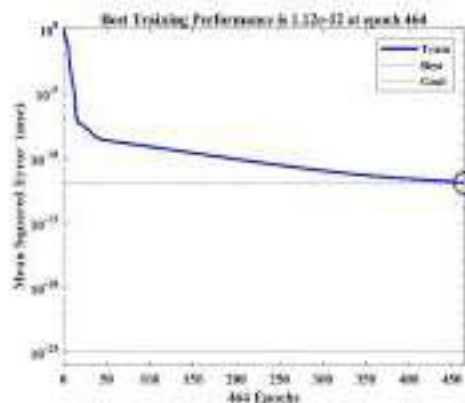


Figure 24 (a) Regression map



(b) Performance plot

3.3 Optimization result

In this section, the optimal value of geometrical and material parameters are obtained using firefly optimization algorithm with neural network function estimation model. The firefly algorithm (FA) is developed based on the flashing behaviour of fireflies.

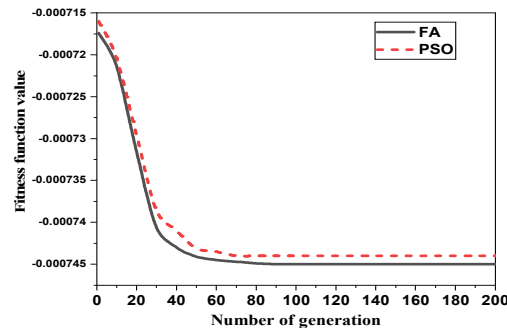


Figure 25 Convergence plot : best fitness value vs number of generation

In this algorithm, the intensity of the flashing light causes the firefly to move towards the brightest and most attractive location (objective function) to obtain the optimal solution. The optimal design variables and objective function values are obtained and compared with well-known particle swarm optimization (PSO) algorithm. The convergence plot for optimization is shown in Fig. 5. The optimum design parameters are investigated by varying weight factors such as summation of all the weights equal to one. The best solution is found by providing weight $w_1 = 0.5$ and $w_2 = 0.5$. The outcomes of the optimization are listed in Table 1.

Table 7 Optimal design variables and objective function value

Optimization Technique	Input design variable			Output function	
	n_z	$L_b(\mu m)$	$b_b(\mu m)$	$f_1(mg)$	$f_2(\mu m/g)$
FA	0.73	498.23	5.54	1.75	0.35
PSO	0.55	469.99	5.68	1.55	0.25

The optimum value of grading index, beam length and beam width is calculated as 0.73, 498.23 μm and 5.54 μm , respectively. The corresponding maximized value of resolution and sensitivity is achieved as 1.75 mg and 0.35 $\mu m/g$.

4. Case study: crack detection in a beam

In this section, the dynamic responses of a intact beam and cracked beam is analyzed by using MEMS accelerometer with optimized geometrical and material parameters.

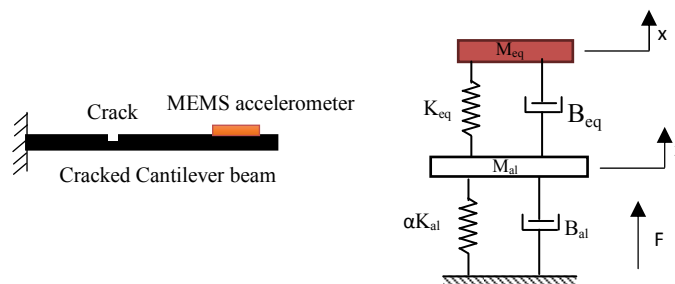


Figure 26 Cracked beam model attached with MEMS accelerometer

For this purpose, Consider an cracked aluminum (Al) cantilever beam of length $L_{al} = 200\text{mm}$, width $b_{al}=20\text{mm}$ and thickness $h_{al}=10\text{mm}$. A MEMS accelerometer is attached to the top of the beam, as shown in Fig. 6, and beam is excited by applying a force F . Let $x_1(t)$ and $x_2(t)$ are the response of cracked Al beam and accelerometer. Therefore, the dynamic model of coupled system can be formulated as:

$$M_{al}\ddot{x}_1 + B_{al}\dot{x}_1 + \alpha K_{al}x_1 + K_{eq}(x_1 - x_2) = F \quad (9)$$

$$M_{eq}\ddot{x}_2 + B_{eq}\dot{x}_2 + K_{eq}(x_2 - x_1) = 0 \quad (10)$$

Where M_{al} , B_{al} and K_{al} are the mass, damping and stiffness of cantilever beam. α indicates the crack severity factor, varies from 0 to 1. The dynamic responses of MEMS accelerometer with and without crack are investigated using Newmark average acceleration method. The optimal value of n_z , L_b and b_b is considered for analysis. Here, the crack severity factor $\alpha = 0.2$, which means 20% reduction in beam stiffness is considered due to crack. The dynamic response of intact beam and cracked beam is illustrated in Fig. 7. It is observed that when crack appears in the beam, the relative displacement of FG-MEMS accelerometer drastically increases more than conventional one. Therefore, it is concluded that proposed FG-MEMS accelerometer can detect damages in the machine components with higher accuracy.

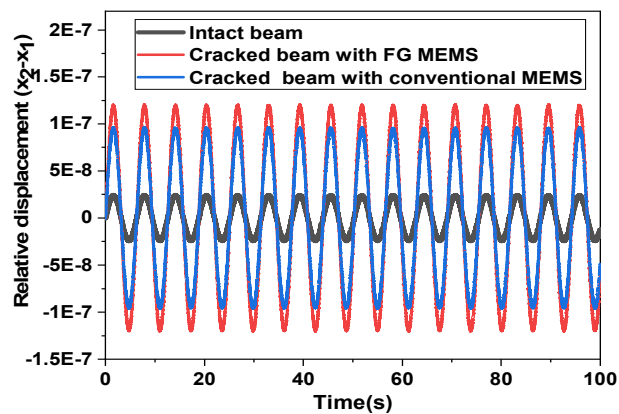


Figure 27 Dynamic response of MEMS accelerometer with and without crack

5. Conclusion

The present investigation tries to improve the performance and reliability of FG-MEMS accelerometers in condition monitoring applications. In many situations, the conventional accelerometer shows some error in vibration response when a small cracks present in the machine component due to improper design and material of folded beam and fingers. Therefore, proposed FG-MEMS accelerometer can detect the cracks accurately with lower possible cost. In this work, the optimal design variables have been obtained quickly and accurately using a non-traditional firefly scheme with an artificial neural network function estimation model. Furthermore, a case study is illustrated to understand the effectiveness of FG-MEMS accelerometer. An experimental work is required to measure the dynamic response of cracked structures using proposed micro-accelerometer, which can distinguish signals from uncracked equivalent conveniently.

References

- [1] J.K. Sinha, A.W. Lees, M.I. Friswell, Estimating unbalance and misalignment of a flexible rotating machine from a single run-down, *J. Sound Vib.* 272 (2004) 967–989.
- [2] R.I.K. Moorthy, J.K. Sinha, Dynamic qualification of complex structural components of nuclear power plants, *Nucl. Eng. Des.* 180 (1998) 147–154.
- [3] J.K. Sinha, S.K. Sinha, R.I.K. Moorthy, Diagnosis of the bearing failure in a Pilger mill, *Shock Vib. Dig.* 28 (1996) 11–14.
- [4] M. Engesser, A.R. Franke, M. Maute, D.C. Meisel, J.G. Korvink, A robust and flexible optimization technique for efficient shrinking of MEMS accelerometers, *Microsyst. Technol.* 16 (2010) 647–654.
- [5] C. Wang, X. Song, W. Fang, F. Chen, I. Zeimpekis, Y. Wang, A. Quan, J. Bai, H. Liu, G. Schropfer, C. Welham, M. Kraft, Design of freeform geometries in a MEMS accelerometer with a mechanical motion preamplifier based on a genetic algorithm, *Microsystems Nanoeng.* 6 (2020).
- [6] R. Nambisan, S.S. Kumar, B.D. Pant, Sensitivity and non-linearity study and performance enhancement in bossed diaphragm piezoresistive pressure sensor, 19th Int. Symp. VLSI Des. Test, VDAT 2015 - Proc. (2015).
- [7] V.S. Krishnasamy, A.V. Juliet, Mems accelerometer design optimization using genetic algorithm, *Adv. Mater. Res.* 705 (2013) 288–294.
- [8] L. Gu, W. Zhang, H. Lu, Y. Wu, C. Fan, Machine learning algorithm for the structural design of MEMS resonators, *Microelectron. Eng.* (2023).
- [9] M.J. Martin, Simulation of micromechanical measurement of mass accretion: Quantifying the importance of material selection and geometry on performance, *J. Vib. Acoust. Trans. ASME.* 136 (2014).
- [10] K.S. Al-Basyouni, A. Tounsi, S.R. Mahmoud, Size dependent bending and vibration analysis of functionally graded micro beams based on modified couple stress theory and neutral surface position, *Compos. Struct.* 125 (2015) 621–630.
- [11] A. Vahidi-Moghaddam, M.R. Hairi-Yazdi, R. Vatankhah, Analytical solution for nonlinear forced vibrations of functionally graded micro resonators, *Mech. Based Des. Struct. Mach.* (2021).
- [12] Z. Zhang, S. Li, Thermoelastic Damping of Functionally Graded Material Micro-Beam Resonators Based on the Modified Couple Stress Theory, *Acta Mech. Solida Sin.* 33 (2020) 496–507.
- [13] U.K. Kar, J. Srinivas, Frequency analysis and shock response studies in bidirectional functionally graded microbeam with thermal effects, *J. Brazilian Soc. Mech. Sci. Eng.* 44 (2022).
- [14] J. Zheng, C. Zhang, F. Musharavati, A. Khan, T.A. Sebaey, Thermo-mechanical buckling analysis of FG-GNPs reinforced composites sandwich microplates using a trigonometric four-variable shear deformation theory, *Case Stud. Therm. Eng.* 26 (2021).
- [15] F. Allahkarami, H. Tohidi, Size-dependent nonlinear free vibration of multilayer functionally graded graphene nanocomposite Timoshenko microbeam under different boundary conditions, *Eur. Phys. J. Plus.* 137 (2022).
- [16] M. Arefi, S. Firouzeh, E. Mohammad-Rezaei Bidgoli, Ö. Civalek, Analysis of porous micro-plates reinforced with FG-GNPs based on Reddy plate theory, *Compos. Struct.* 247 (2020).
- [17] M. Benmessaoud, M.M. Nasreddine, Optimization of MEMS capacitive accelerometer, *Microsyst. Technol.* 19 (2013) 713–720.

- [18] M. Mojahedi, Size dependent dynamic behavior of electrostatically actuated microbridges, *Int. J. Eng. Sci.* 111 (2017) 74–85.
- [19] G. Ahmed Khouqeer, S. Suganthi, N. Alanazi, A. Alodhayb, M. Muthuramamoorthy, S. Pandiaraj, Design of MEMS capacitive comb accelerometer with perforated proof mass for seismic applications, *J. King Saud Univ. - Sci.* 35 (2023) 102560.
- [20] Y. Ma, L. Xu, H. Li, Optimization design of a capacitive microaccelerometer, 2010 IEEE Int. Conf. Mechatronics Autom. ICMA 2010. (2010) 1153–1157.

Condition Monitoring of Ship Structures using Stress-Strength Model

V Srinivasa Rao

Scientist, Naval Science & Technological Laboratory, Visakhapatnam

Abstract

Ships as transport entities contribute to more than 90% of the world's trade. With the objective of realising safe shipping, the regulatory authorities are framing stringent rules and regulations. In spite of the strict norms, the global shipping sector is facing challenges in reducing maritime accidents. 30-40% of Global ship accidents are root caused to Structural failures. This paper aims to address the shortfalls of deterministic design approach and propose a new probabilistic model for condition monitoring of ship structures using the Stress-Strength model.

Key words: *Deterministic approach, Probabilistic approach, Structural integrity, Stress-Strength model, Section Modulus, Probability of Failure.*

Abbreviations and Acronyms

<i>[Symbol]</i>	<i>[Definition] [(Unit)]</i>	<i>[Symbol]</i>	<i>[Definition] [(Unit)]</i>
FoS	<i>Factor of Safety</i>	$M_{\sigma t}$	<i>Total bending moment</i>
I	<i>Moment of Inertia [m⁴]</i>	R_s	<i>Reduction Factor</i>
Z	<i>Section Modules [m³]</i>	C_w	<i>Wave Coefficient</i>
M_s	<i>Still water bending moment</i>	IMO	<i>International Maritime Organization</i>
M_w	<i>Wave bending moment</i>	$IACS$	<i>International Association of Classification Societies</i>

1. Introduction

The global shipping sector is responsible for the transportation of around 90 % of the world trade. The shipping sector has a global fleet of more than 94,171 ships with a consolidated deadweight tonnage of ~2 Billion Tons. The Maritime shipping is the major contributor to the global economy. With its advantage of competitive freight costs, the seaborne trade continues to expand by sharing the benefits to the consumers across the globe leading to economic liberalisation. Further the shipping as a mode of transport has the ability to handle oversize or heavy loads and it can also meet the demand of safe transportation of refrigerated and hazmat cargos. The low carbon foot print (CO₂ emissions) of shipping is making it as an eco-friendly and sustainable mode of transport. The shipping sector is experiencing increase in demand for the goods and raw materials to meet the need of the growing world's population. In the recent times, the accidents reported in the shipping sector are rising concerns among the different stake holders of the industry. 30-40% of Global ship accidents are root caused to structural failures. The regulatory authorities like IMO & IACS are developing advanced and complicated roles in order to establish the structural principals. The main objective of this paper is to use the Stress-Strength model for assessment of ship structural reliability.

This paper is organised as follows. Section 2 briefly touches on the statistics of accidents in the shipping sector. Section 3 addresses gist on the conventional deterministic approach being adopted in ensuring the structural integrity of ships. Section 4 addresses Probabilistic design approach in ship design philosophy. Section 5 addresses on details of the new model for condition monitoring of the ship structure. Section 6 concludes.

2. Statistics of Accidents in Shipping Sector

All the stake holders of the shipping industry are striving hard to meet the objective of transforming the maritime sector into a safe and reliable freight carrying mode. The regulatory authorities are framing stringent rules and regulations to built, maintain and operate the fleets. In spite of the strict norms, the global shipping sector is facing challenges in reducing maritime accidents. There are several factors for the maritime accidents like human errors, bad weather, technical issues, overloading capacity, heavy traffic etc.,

The figure 1 below represents the share of marine incidents by type which contribute to the shipping accidents. Out of 85% of the total failure due to failure of any machinery and technical systems, 30-40% of incidents are root caused to structural failures. The designers should focus on the remedial actions for elimination/mitigating of the different failure modes associated with the structural failures.

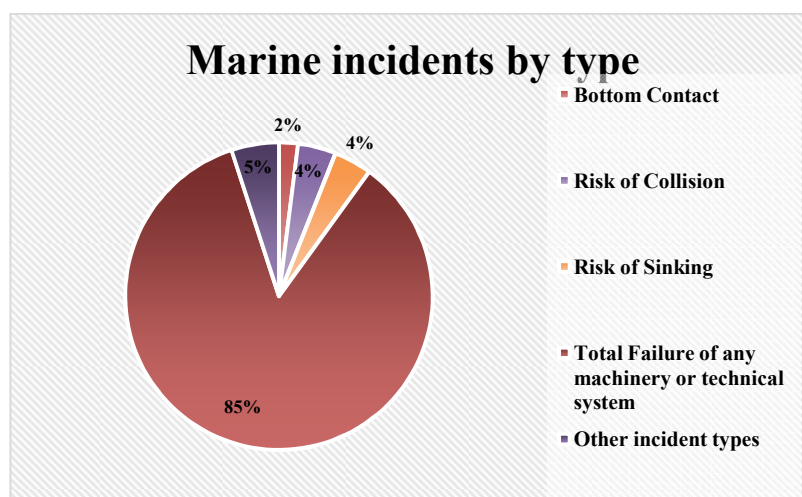


Figure 1: The percentage of marine incidents by type published by Transportation Safety board of Canada

3. Deterministic Approach in Ship Design

The conventional deterministic approach being adopted in structural design of ships considers global loads for assessing the structural integrity. Further, additional strengthening will be provided in local areas of concern. This approach considers ship as free-free beam and segregates the complete ship into individual blocks. For each of the block the weight, buoyancy, load, shear force & bending moment distributions will be computed for all the loading conditions separately. The magnitude of the maximum still water bending moment (MS) will be estimated by undertaking this exercise. In general the maximum bending moment will be experienced around amidships region.

The plots of Weight, Buoyancy, Load, Shear force & Bending Moment for a 50-meter vessel is presented here. The vessel was segregated into 4 blocks (1 to 4). The weight distribution in each of the identified block is computed and similarly the buoyancy contributed by each block was extracted from hydrostatics data. Load curve was derived by computing the difference between the weight and buoyancy. Area under the load curve results the Shear force plot and the area under the shear force curve results in the bending moment plot. The Weight, Buoyancy, Load, Shear force & Bending Moment plot was given in the figure 2 below:

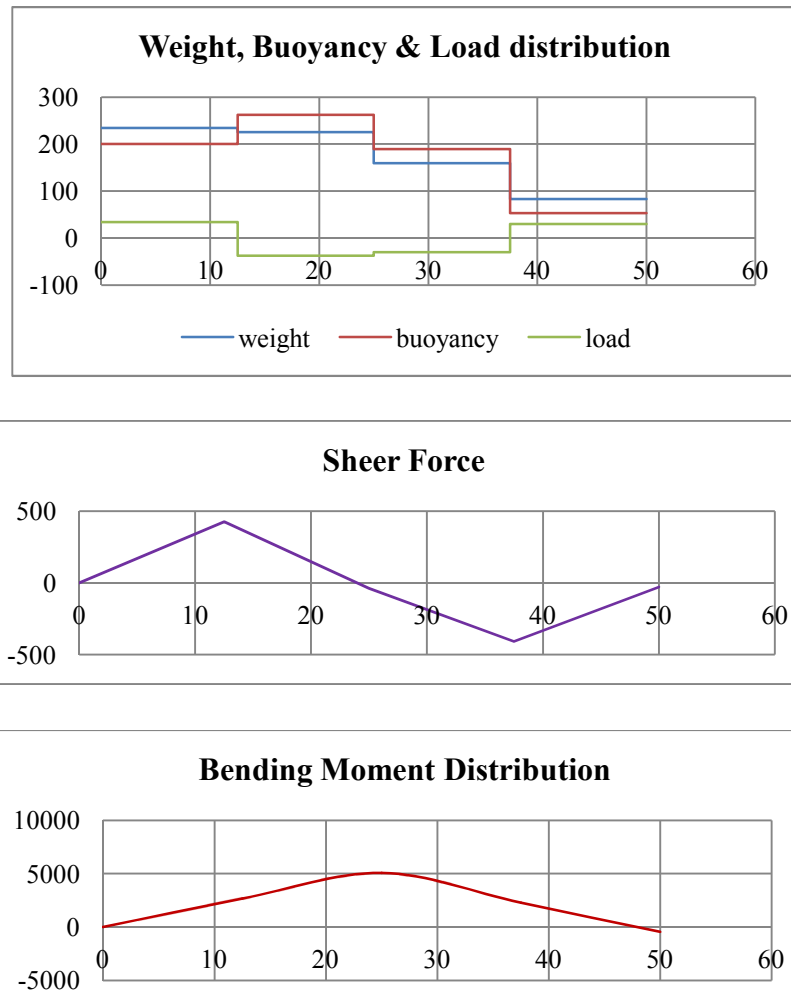


Figure 2: Weight, Buoyancy, Load, Shear force & Bending Moment distribution for a 50 m vessel.

The scantling of all the structural members falling in the mid-ship section will be frozen by adopting relevant rules formulated by classification societies. For this structural section the mass moment of inertia (I) & Section modulus (Z) will be computed. The maximum wave bending moment (M_w) will be computed from the classification society formulations. The total bending moments (M_t) will be the sum of Still water bending moment (M_s) & Wave bending moment (M_w). The working stress is calculated using the Euler's equation ($\sigma = \frac{M_t}{Z}$). The Ultimate strength of the material will be estimated based on testing of the specimen extracted from the grade of steel selected for manufacturing the ship hull. The

factor of safety ($FoS = \frac{Ultimate\ Strength}{Working\ Stress}$) is calculated by substituting the corresponding ultimate strength & working stress values.

If the computed factor of safety is greater than 1.5 the structural scantling configuration adopted will be frozen. If the FoS is less than 1.5 then the scantling will be increased and the same exercise will be undertaken until the FoS is greater than 1.5. Once the FoS criteria is met, then the mid-ship section scantlings will be considered to all the structural members that run 0.4 L either side of the mid-ship section. This will cater for the global loading / stresses being encounter by the ship and for local loading / stresses the local areas will be strengthened to have adequate structural integrity. Though the deterministic structural design approach is widely used by the ship designers by catering higher factor of safety it is having its own drawbacks. In recent times deterministic based structural designs are leading to failures, because both stress & strength are considered as fixed known values and no consideration was given to the variability of stress or strength at all. Even though designed with high factor of safety leading to unreliable designs and structures could fail, this was primarily due to the fact that no consideration was given to the variability of stress and strength with respect to time (ageing).

4. Probabilistic Approach in Ship Design

In recent times, the ship designers are shifting to probabilistic design approach for structural design of ships. The probabilistic design approach results in most reliable and economical ship designs by address the variability of stress & strength and also eliminate the risk of over-designing often being experienced with deterministic approach.

In the probabilistic model, both the stress and strength will be considered as random variables and they are modelled with their corresponding probability density functions. The subsequent paragraphs details on the modelling of working stress on the ship structure & ultimate strength of the ship girder.

Modelling of working stress acting on the ship girder:

Ship at sea experiences different kinds of global and local loads. In order to design the ship structures to have adequate structural integrity, firstly all the global and local loads have to be modelled with the governing phenomena's and then the structure have to be designed to withstand all the loads. The following are the different types of loads being experienced by the ships:

- Static load (Still water) & Wave loads (wave induced) – Global load
- Torsion loads – Global load
- Pounding, Panting, Racking loads etc., – Local loads



The total stress acting on the ship structure will be sum of all the stresses being contributed by the individual loads (both global & local). The local loads do occur for special type of ship and that to for a specific period of time. Generalised modelling of local stresses resulted due to local loads may not be feasible. Given a particular type of vessel modelling of local stress can be attempted. Most of the designers address the local stresses by provisioning additional local strengthening to counter them. The present paper considers the modelling of stress being encountered by global loads.

The stress is a function of bending moment, modelling of the bending moment is equivalent to modelling the stress. The primary total bending moment (M_t) can be divided into still water bending moments (M_s) & wave-induced bending moment (M_w). Here the time (ageing) is considered as variable. The modelled equation for total bending moment ($M_{\sigma t}$) is as follows:

$$M_{\sigma t}(t) = k_s \times M_s(t) + k_w \times x_s \times M_w(t) \quad (1)$$

K_s & K_w are random variable representing modelling uncertainty in the still-water & wave bending moments respectively. X_s accounts for the non-linearity in the wave bending.

The linear theory can be applied to simplify the time dependent functions $M_s(t)$ & $M_w(t)$ as time independent M_s & M_w [1].

Parameter	Sagging condition	Hogging condition
M_s	$-0.065 \times C_w \times L^2 \times R_s \times B(C_B + 0.7)$	$C_w \times L^2 \times B \times R_s \times (0.1225 - 0.01C_B)$
M_w	$-0.11 \times C_w \times L^2 \times R_s \times B(C_B + 0.7)$	$0.19 \times C_w \times L^2 \times B \times R_s \times C_B$

Where L is Length, B is Beam, C_B is Block coefficient of the ship under consideration, R_s is reduction factor for deciding the service limitations for type of ship. C_w is wave coefficient which can be calculated as follow:

Parameter	100<L<300	300<L<350	L>350
C_w	$10.75 - \left(\frac{300 - L}{100}\right)^{3/2}$	10.75	$10.75 - \left(\frac{L - 350}{150}\right)^{3/2}$

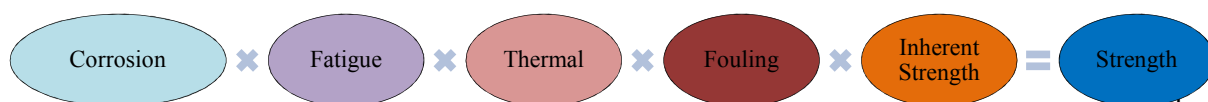
The aforementioned equations were published by most of the classification societies for calculating the still water and wave induced being moments.

Modeling of Ultimate Strength of Ship Girder:

The ultimate strength or its final strength capacity of the ship decrease overtime as the ship structure ages. The strength of the ship is a function of bending moment capacity of the ship hull and the same can be represented by the equation as follows:

$$M_s(t) = \Phi \times \sigma_u \times Z(t) \quad (2)$$

Φ is buckling knock down factor, σ_u and $Z(t)$ are the ultimate strength and section modulus of the ship's hull structural section (midship section) respectively.



There are several factors like corrosion, fatigue, thermal stresses, fouling etc., which affects the inherent strength of the ship structure. The structural degradation will affect the ship hull girder capacity by reducing the section modulus $Z(t)$ over time. The final strength of the ship can be derived by multiplying all the affects due to individual factors. The effect of each of the aforementioned factor on the section modulus of the ship hull structure has to be modeled by incorporating the critical parameters effecting the same. The present paper addresses modeling of only corrosion published in literature. Corrosion decreases the ultimate section modulus of the ship hull structure by reducing the effective thickness of the structural members. Further, it also effects the ability of the ship structure to withstand the moments caused by global and local loads. In literature there are several models to capture the effect of corrosion of the section modulus of the ship hull by considering the critical parameter as time (ageing). Câmara & Cyrino [2] has developed the following equation of predicting the hull girder section module loss due to the effect of corrosion overtime.

$$Z_c(t) = Z(t) \times \left(1 - \frac{0.8 \times (t-5)^{0.75}}{100}\right) \quad (3)$$

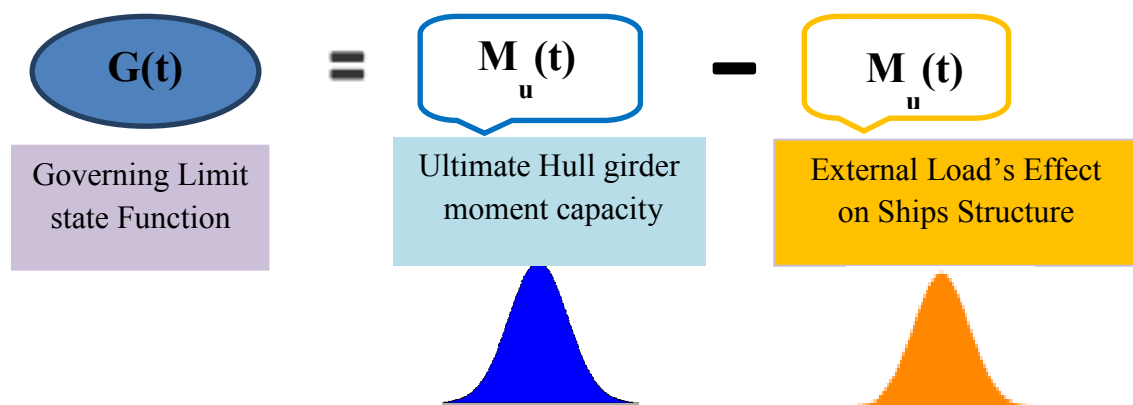
$Z_c(t)$ is the new computed section modulus due to ageing of the ship hull.

By replacing the above term in the main modelled strength equation results in the final main hull girder bending moment capacity is as follows:

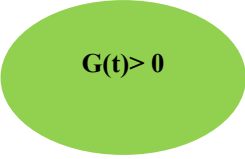
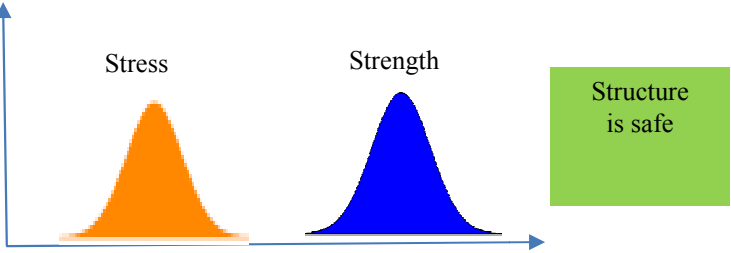
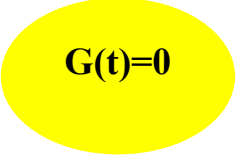
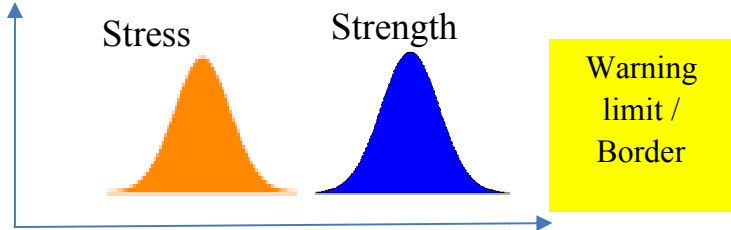
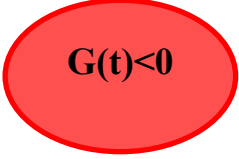
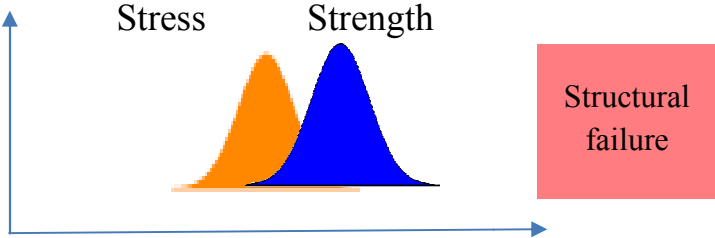
$$M_S(t) = \Phi \times \sigma_u \times Z(t) \times \left(1 - \frac{0.8 \times (t-5)^{0.75}}{100}\right) \quad (4)$$

The Stress-Strength model:

Both the modelled Stress and Strength functions are random variables with same probability space (time) and can assume several values. The Stress Strength model calls for definition of governing limit state function $G(t)$ which is joint probability distribution function as follows [3]:



The following conditions / events of the Governing limit state function can be used to interpret the condition of the ship structure:

Condition	State of the ship structure
	 <p data-bbox="584 521 1377 618">In this condition, the ultimate strength of the ship girder is more than the working stress acting on the structure. This indicates safe state / safe domain.</p>
	 <p data-bbox="584 891 1377 987">This condition represents the warning limit / border between the safe state and the failure state. The boundary between these two regions is the failure surface.</p>
	 <p data-bbox="584 1294 1377 1391">The condition represents the state of failure where the distribution of the ultimate strength overlaps with the distribution of the working stress.</p>

4. New Model for Condition Monitoring of Ship Structure

As part of preventive & predictive maintenance of ship structures, Condition Monitoring is crucial to achieve reasonably long and safe operational life with a minimal risk of catastrophic failure during the complete life cycle of the ship. The variability in stress & strength as discussed in para 4 should be completely monitored to avoid the catastrophic fracture or a complete stop. Environmental conditions in which the ship operates and the ageing (time) are two important factors to be addressed for effective design of reliable ships that can sustainably ply for the expected service life. Generally, the ships are designed for type of cargo to be handled, the specific routes and region of operation will be certain. The mean stress being experienced by the ship under consideration will be more or less remains the same with time (ageing) except for its spread (variability). On the other end the mean strength of the ship reduces over time (ageing) due to wear & tear, Corrosion, fatigue etc., and the spread (variability) will also increase its distribution. The figure 3 clearly depicts the stress, strength distributions of ships with time (ageing).

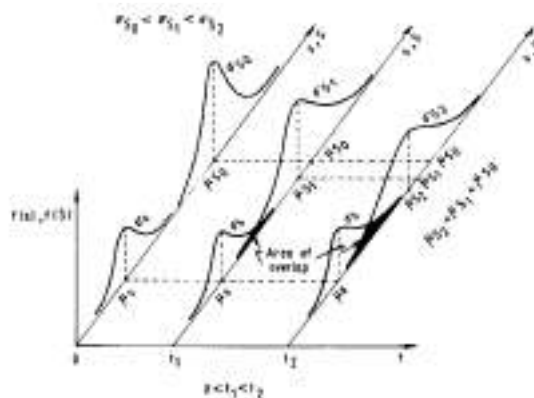


Figure 3: Stress / Strength distributions for ship with respect to ageing (time)

In figure 3, we can identify that mean value of the stress remains the same, however the spread changes due to varying environmental loads that are being experienced by the ship. The mean value of strength continuously tends to decrease and the variance (spread) increases as the ship ages. When the ships are in brand new condition ($t=0$) both the stress and strength distributions are wide apart and there will be no scope for probability of failure. But as ships ages the area of overlap between stress and strength distributions tends to increase leading to more scope for probability of failure. As discussed in para 3, the deterministic design approach fails to capture this phenomenon and leading to structural failures of the ship as ageing progresses. The probabilistic approach well captures the probable areas of overlap and necessary remedial actions can be taken to avoid occurrence of such failure. The structural reliability of ship structures can be enhanced by adopting following remedial actions [4]:

- (a) **Action 1:** By Derating the stress acting on the ship and choosing high factor of safety the gap between the stress and strength distributions can be increased. This will lead to no overlap zone thereby achieving zero probability of failure condition.
- (b) **Action 2:** By reducing the variability in stress by regulating the environmental loads being encountered by the ship. This will result in reducing the variance associated with the stress distribution this will decrease the changes of overlap region thereby reducing the probability of failure.
- (c) **Action 3:** By reducing the variability in strength by adopting better quality control procedures during the production of the ships. This will result in reducing the variance associated with the strength distribution this will decrease the changes of overlap region thereby reducing the probability of failure.

Generally, the ship operators do not have adequate understanding on the dynamics associated with the loading patterns that the hull girder experiences and the condition of the ultimate strength of the hull girder during its service life. The designers should provide adequate data which can be handy to the ship operators in decision making during ship operations. The present paper proposes for development of a software programme as future work for reliability evaluation of the ship structure during operational cycle where the operators can input the basic details of operating conditions and the software automatically computes the limiting state function and recommends the condition of the hull girder.

The ship girder is considered as free free beam. As environmental loads (global & local) act on the beam, it experiences hogging and sagging conditions. In both the conditions either in compression or in tension the midship section of the hull girder will experience the

maximum loading. The present paper proposes to select the midship section to assess the state of governing limit function. By the three criteria defined in para 4 the condition of the hull can be assessed.

5. Conclusion

The statistics associated with different incidents that cause marine accidents were discussed and the necessity for ensuring the structural integrity to reduce the marine accidents was also deliberated. The conventional deterministic structural design approach being adopted by the ship designers was discussed at length and its drawbacks were highlighted. The need for adopting the probabilistic design approach to capture the variability of stress and strength were highlighted. The complete modelling of distribution associated with the working stress being experienced by the hull girder and ultimate strength of the hull girder were elaborated. The use of Stress-Strength model for condition monitoring of the ship hull girder was discussed. By using the methodology proposed in the present paper a sophisticated software tool can be developed as a future work for assessment of ship structural reliability.

6. Acknowledgements

The author is very thankful to the Director, NSTL & Dr. HN Das, Scientist G and Dr. PC Praveen, Scientist F for extending their undue support and guidance throughout the study.

7. References

- [1] Rules and Regulations for the Construction and Classification of Steel ships (2016) by Indian Register of Shipping.
- [2] Camara, M.C. & Cyrino, J.C.R. (2012) : Structural reliability applications in design and maintenance planning of Ships subjected to fatigue and corrosion, ASME.
- [3] Mohsen, S.K., Abdollah, S. & Ahmad, I. (2018): Evaluation of ship structural reliability during design, maintenance, and repair process, MUS.
- [4] Krishna, B.M (1992): Reliability analysis and prediction



Published by

Naval Science and Technological Laboratory
DRDO, Ministry of Defence
Visakhapatnam-530027

Condition Monitoring Society of India (CMSI)
(Regd. No: 45061/ 2003)
<https://www.comsoi.org>